



Quantum Cutting Processes in Rare-earth doped fluorides for Photovoltaic applications

Diana Serrano

► To cite this version:

Diana Serrano. Quantum Cutting Processes in Rare-earth doped fluorides for Photovoltaic applications. Materials Science [cond-mat.mtrl-sci]. Université de Caen Basse-Normandie, 2012. English. NNT: . tel-01092812v2

HAL Id: tel-01092812

<https://theses.hal.science/tel-01092812v2>

Submitted on 10 Dec 2014 (v2), last revised 16 Dec 2014 (v3)

HAL is a multi-disciplinary open access archive for the deposit and dissemination of scientific research documents, whether they are published or not. The documents may come from teaching and research institutions in France or abroad, or from public or private research centers.

L'archive ouverte pluridisciplinaire **HAL**, est destinée au dépôt et à la diffusion de documents scientifiques de niveau recherche, publiés ou non, émanant des établissements d'enseignement et de recherche français ou étrangers, des laboratoires publics ou privés.



UNIVERSITE de CAEN BASSE-NORMANDIE
U.F.R. DES SCIENCES
ECOLE DOCTORALE S.I.M.E.M.

THESE

Présentée par

Diana SERRANO GARCÍA

Et soutenue

Le 28 Septembre 2012

En vue de l'obtention du

DOCTORAT de l'UNIVERSITE de CAEN

Spécialité : Milieux dilués et optique fondamentale

Arrêté du 07 août 2006

Quantum cutting processes in rare-earth doped
fluorides for photovoltaic applications

MEMBRES DU JURY:

Mme Fabienne PELLE, Dir. de Recherche CNRS, LCMCP, Chimie ParisTech (**rapporteur**)

Mr Bernard MOINE, Dir. de Recherche CNRS, LPCML, Lyon I (**rapporteur**)

Mr Xianghua ZHANG, Dir. de Recherche CNRS, EVC, Sciences Chimiques de Rennes

Mr Richard MONCORGE - Professeur, CIMAP, Université de Caen (**co-directeur**)

Mr Alain BRAUD - Maître de Conférences HDR, CIMAP, Université de Caen (**directeur**)

Contents

Remerciements	v
List of Abbreviations	vii
Résumé	1
Introduction	9
1 Current context and challenges	13
1.1 PV technologies	13
1.2 First Generation: Silicon wafers	14
1.3 Second generation: thin-film technologies	15
1.3.1 Hydrogenated amorphous Silicon based technologies	16
1.3.2 CdTe, CIS and CIGS thin films	17
1.3.3 Dye-sensitized solar cells (DSSCs) and organic photovoltaic (OPV) devices	18
1.3.4 III-V semiconductors for high-efficiency PV devices	19
1.4 Third-generation photovoltaics	20
1.4.1 Fundamental limitations of current PV technologies	21
1.4.2 Multi-bandgap approaches: high-efficiency multi-junction solar cells and Quantum wells solar cells (QWSCs)	23
1.4.3 Modifying the solar spectrum	24
1.4.4 Concentrated Photovoltaics (CPV)	27
1.5 RE based converters for silicon solar cells efficiency enhancement	28
1.5.1 Energy levels of rare-earth ions in crystals	28
1.5.2 Energy transfer processes	32
1.5.3 Rare-earth based solar up and down converters	33
1.6 Conclusions Chapter 1	44

2	Quantum Cutting in Pr^{3+}-Yb^{3+} codoped KY_3F_{10}	47
2.1	Introduction	47
2.2	Experimental methods	49
2.3	Optical spectroscopy experiments	51
2.3.1	Emission spectra	52
2.3.2	Decay curves	56
2.4	First energy transfer efficiency	58
2.5	Second energy transfer and quantum efficiency	59
2.6	Rate equation modeling	60
2.6.1	Steady-state solutions	63
2.6.2	Dynamic solutions	67
2.6.3	Conclusions	72
2.7	Other modeling approaches	73
2.7.1	Rate-equation limitations	73
2.7.2	Inokuti-Hirayama model	74
2.7.3	Monte Carlo (MC) methods	75
2.7.4	Modeling Result	77
2.7.5	MC methods incorporated to the population rate-equations	78
2.8	Conclusions Chapter 2	81
3	Clusters and energy transfers in $\text{CaF}_2\text{:Pr}^{3+}\text{-Yb}^{3+}$	83
3.1	Introduction	83
3.2	Rare-earth clustering in CaF_2 : general concepts	84
3.2.1	Single ions sites	85
3.2.2	Higher order aggregates or clusters	87
3.3	Experimental methods	90
3.4	Quantum cutting with $\text{CaF}_2\text{:Pr}^{3+}\text{-Yb}^{3+}$	91
3.4.1	$\text{CaF}_2\text{:Pr}^{3+}\text{-Yb}^{3+}$ spectroscopy	91
3.4.2	Determination of the first energy transfer efficiency	96
3.5	Preliminary conclusions and next challenges	98
3.6	Spectroscopy of the Pr^{3+} aggregates in CaF_2	98
3.6.1	Weak luminescence of Pr^{3+} ions in CaF_2	98
3.6.2	$\text{Pr}^{3+}\text{-Yb}^{3+}$ and $\text{Pr}^{3+}\text{-Lu}^{3+}$ codoping	100
3.6.3	Luminescent centers increase	102

3.7	$\text{Pr}^{3+}\text{-Yb}^{3+}$ and $\text{Pr}^{3+}\text{-Lu}^{3+}$ clusters	107
3.7.1	Elimination of Pr^{3+} clusters	107
3.7.2	Evidence of two types of clusters in the codoped samples	108
3.8	Lifetimes and ETE in the ultra-fast clusters	114
3.8.1	Super-exchange interaction	114
3.8.2	Fast Cluster to Ultrafast Cluster ratio	116
3.8.3	Consequences	118
3.9	Summary of results	119
3.10	QC with $\text{Pr}^{3+}\text{-Yb}^{3+}$ codoped CaF_2 : Yb^{3+} emission and modeling	120
3.10.1	Yb^{3+} emission and lifetimes	120
3.10.2	Rate-equation modeling	124
3.11	Conclusions Chapter 3	127
4	Cooperative Quantum Cutting in $\text{CaF}_2\text{:Tb}^{3+}\text{-Yb}^{3+}$	129
4.1	Introduction	129
4.2	Experimental methods	130
4.3	Spectroscopy of the $\text{Tb}^{3+}\text{-Yb}^{3+}$ clusters in CaF_2	131
4.3.1	Tb^{3+} aggregates	131
4.3.2	$\text{Tb}^{3+}\text{-Yb}^{3+}$ spectroscopy	133
4.3.3	Yb^{3+} emission	134
4.3.4	Lifetimes and ETE	136
4.4	Conclusions	139
4.5	Sensitization	140
4.5.1	Tb^{3+} ions sensitization	142
4.5.2	CaF_2 codoped $\text{Tb}^{3+}\text{-Ce}^{3+}$ and $\text{Tb}^{3+}\text{-Bi}^{3+}$ investigation	145
4.6	Absolute QC efficiency in $\text{Pr}^{3+}\text{-Yb}^{3+}$ and $\text{Tb}^{3+}\text{-Yb}^{3+}$ doped CaF_2	147
4.6.1	Experimental protocol	147
4.6.2	Absorbed power measurement	148
4.6.3	Downconverted Yb^{3+} emission and absolute QE	151
4.6.4	discussion	153
4.7	Conclusions Chapter 4	155
	General conclusions	157
	Bibliography	161

List of figures	191
-----------------	-----

List of tables	194
----------------	-----

Remerciements

Une thèse est sans doute un travail de recherche, mais elle constitue aussi une grande formation. C'est pour cela que je tiens à remercier tout particulièrement Alain Braud pour avoir encadré cette thèse. Le grand appui et les nombreux enseignements qu'il m'a offert depuis mon arrivée au laboratoire ont été d'un grand enrichissement autant scientifique que personnel. Je tiens également à remercier Richard Moncorgé pour m'avoir accueilli dans son équipe de recherche, pour l'intérêt porté à mon travail et pour son soutien. Je voudrais témoigner ensuite ma plus sincère gratitude pour Jean-Louis Doualan, Patrice Camy, Abdel Benayad et Vivien Ménard, dont la collaboration a été aussi nécessaire que précieuse pour qu'une thèse comme celle-ci puisse aboutir. Merci à Jean Margerie, avec qui j'ai eu l'honneur de pouvoir travailler, pour partager avec moi un peu de son immense savoir et expérience. Enfin, je voudrais remercier M. Serge Bouffard pour m'avoir accueilli dans le laboratoire CIMAP aussi que pour son soutien au projet du *Student chapter*.

Pendant ces années j'ai eu la chance de rencontrer un grand nombre d'amis, dont la présence et compagnie est devenue très importante pour moi. Ainsi, je voudrais dédier un mot à Burcu. Merci pour ta compagnie, tes réflexions et tes bons conseils dont j'espère profiter toujours. Un grand merci aussi à Thomas et Kiki. Merci pour partager avec moi votre univers de fous, pour les rires, et pour faire maintenant partie de beaucoup de moments inoubliables. Je remercie Delphine pour son amitié, Philippe pour les sourires; Julie pour les discussions et conseils; Oliv Deb pour être lui même et en générale tous ce qui m'ont accompagné pendant cette aventure. J'ai passé des moments excellents avec vous. Merci à mes amis Elsa, Bertrand, Sheila, Luis et Arantxa. Je souviendrai le temps que nous avons passé tous ensemble comme la meilleure période de ces trois ans. A Marta, Miriam et Pilar pour faire preuve chaque jour que la distance n'existe pas pour les gens qui s'apprécient. A mes parents, pour le support qui rend simple ce qui est compliqué et même des fois, possible, ce qui est impossible.

List of Abbreviations

- a-Si:H - Hydrogenated Amorphous Silicon
- c-Si - Crystalline Silicon
- CPV - Concentrated Photovoltaics
- CTB - Charge Transfer Band
- CW - Continuous waveform
- DC - Downconversion
- DSSC - Dye-Sensitized Solar Cell
- ESA - Excited State Absorption
- ET - Energy Transfer
- ETE - Energy Transfer Efficiency
- ETU - Energy Transfer Upconversion
- GSA - Ground State Absorption
- HIT - Heterojunction with Intrinsic Thin Layer
- IH - Inokuti-Hirayama
- LD - Laser Diode
- LT - Low Temperature
- LQY - Luminescence Quantum Yield
- LPE - Liquid Phase Epitaxy

- MBE - Molecular Beam Epitaxy
- mc-Si - Multicrystalline Silicon
- MC - Monte-Carlo
- MEG - Multiple Electron Generation
- MPE - Multiple Photon Emission
- MOVPE - Metalorganic Vapour Phase Epitaxy
- NIR - Near-Infrared
- nc-Si - Nanocrystalline Silicon
- μ c-Si - Microcrystalline Silicon
- OPV - Organic Photovoltaics
- PLE - Photoluminescence excitation
- PMMA - Poly(methyl methacrylate)
- PV - Photovoltaic
- QC - Quantum Cutting
- QCE - Quantum Cutting Efficiency
- QD - Quantum Dot
- QE - Quantum Efficiency
- QWSC - Quantum Well Solar Cell
- QDSC - Quantum Dot Solar Cell
- RE - Rare-earth
- SPR - Surface Plasmon Resonance
- TCO - Transparent Conducting Oxide
- RT - Room Temperature
- UC - Upconversion

Résumé

Depuis que l’existence de matériaux luminescents avec des efficacités quantiques supérieures à l’unité fut mise en évidence, de nombreuses recherches ont été consacrées à l’étude des mécanismes physiques conduisant à l’émission de plusieurs photons de faible énergie à partir de l’absorption d’un seul photon d’énergie supérieure. Ce phénomène, habituellement connu comme “quantum cutting”, a été mis en évidence dans des matériaux tels que les solides inorganiques, les semi-conducteurs et les molécules organiques. Parmi les matériaux solides luminescents, les matériaux dopés terres rares sont ceux qui présentent le plus grand potentiel pour le *quantum cutting* et ses applications. Ces ions luminescents ont été tout d’abord étudiés à cause de leurs propriétés optiques remarquables. Pourtant, cela ne fut que depuis la découverte du laser, dans les années 60, que l’intérêt pour les terres rares trivalentes augmenta jusqu’à ce qu’il fut étendu à d’autres applications dans le domaine de l’optique et la photonique. A l’heure actuelle, les ions terres rares se trouvent dans des très nombreux systèmes optiques tels que les amplificateurs, les mémoires quantiques et les guides d’onde entre autres.

Les recherches sur le *quantum cutting* ont commencé par l’étude de matériaux dopés terres rares présentant une émission en cascade. L’intérêt s’est ensuite focalisé sur des couples de terres rares où l’énergie peut-être transférée d’un des ions, appelé *donneur*, vers le deuxième (*accepteur*) par le biais d’un seul ou plusieurs processus de transferts d’énergie. Le *quantum cutting* a trouvé une de ses premières applications dans le développement de phosphores sans mercure pour des applications d’éclairage [102]. Depuis quelques années, le mécanisme du *quantum cutting* est apparu comme étant prometteur pour l’amélioration du rendement des cellules solaires à base de silicium cristallin.

Les technologies photovoltaïques sont habituellement classifiées en trois générations [6]. La première génération, qui est celle des cellules solaires à base de silicium cristallin, a été la première commercialement disponible et représente encore aujourd’hui plus de 90% du marché photovoltaïque mondial. La deuxième génération photovoltaïque, comprenant

des technologies tels que le silicium amorphe [12], les cellules CIS et CIGS [26] ou les semi-conducteurs III-V [11] est basée sur le développement des techniques de couches minces. Dans cette seconde génération, le coût de production diminue notablement par rapport à la première génération grâce à la réduction de la quantité de semi-conducteur utilisée dans les modules photovoltaïques. Malheureusement une diminution importante du rendement de conversion accompagne cette réduction de l'épaisseur du semi-conducteur. Les efficacités record sont actuellement de l'ordre de 25% [8] pour les cellules à base de silicium cristallin mais sont largement inférieures pour les technologies de deuxième génération. Afin d'augmenter les rendements de conversion tout en gardant des coûts de production faibles, la troisième génération photovoltaïque comprend plusieurs approches, une des plus importantes étant la possibilité d'utiliser des convertisseurs luminescents capables de transformer l'énergie des photons solaires incidents pour adapter le rayonnement solaire à l'absorption des cellules solaires silicium. En effet, pour toute technologie solaire basée sur une seule jonction semi-conductrice, des pertes intrinsèques limitent l'efficacité des modules. Ces pertes, qui fixent le rendement maximal pour une cellule silicium à 29% [34], sont issues d'une part de l'absence d'absorption pour les photons d'énergie inférieure au gap du semi-conducteur (1.12 eV dans le cas du silicium cristallin) et d'autre part sont liées aux effets de thermalisation qui ont lieu après l'absorption de photons d'haute énergie. Un convertisseur dit "basse-fréquence" placé en surface de la cellule (Fig.1) qui soit capable de transformer chaque photon de haute énergie en deux photons d'énergie égale à la moitié du photon original, et idéalement, de l'ordre de la bande interdite du silicium, permettrait donc de réduire les pertes provoquées par les effets de thermalisation en générant de deux électrons dans la bande de conduction par photon incident.

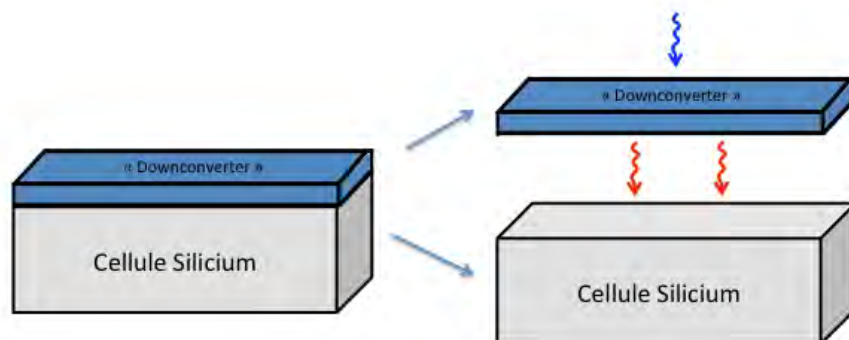


Figure 1: Cellule silicium avec convertisseur "basse-fréquence".

Dans ce travail de thèse des matériaux dopés terres rares sont étudiés en tant que *quantum cutters* efficaces pour le développement de convertisseurs solaires basse-fréquence. Avec cet objectif, le codopage $\text{Pr}^{3+}\text{-Yb}^{3+}$ a été étudié dans les matériaux hôtes KY_3F_{10} et CaF_2 . Ce codopage présente un schéma de niveaux d'énergie permettant le *quantum cutting* à partir de deux transferts d'énergie résonants et consécutifs, le premier transfert étant $\text{Pr}^{3+}({}^3\text{P}_0 \rightarrow {}^1\text{G}_4); \text{Yb}^{3+}({}^2\text{F}_{7/2} \rightarrow {}^2\text{F}_{5/2})$ et le deuxième transfert $\text{Pr}^{3+}({}^1\text{G}_4 \rightarrow {}^3\text{H}_4); \text{Yb}^{3+}({}^2\text{F}_{7/2} \rightarrow {}^2\text{F}_{5/2})$ (Fig.2).

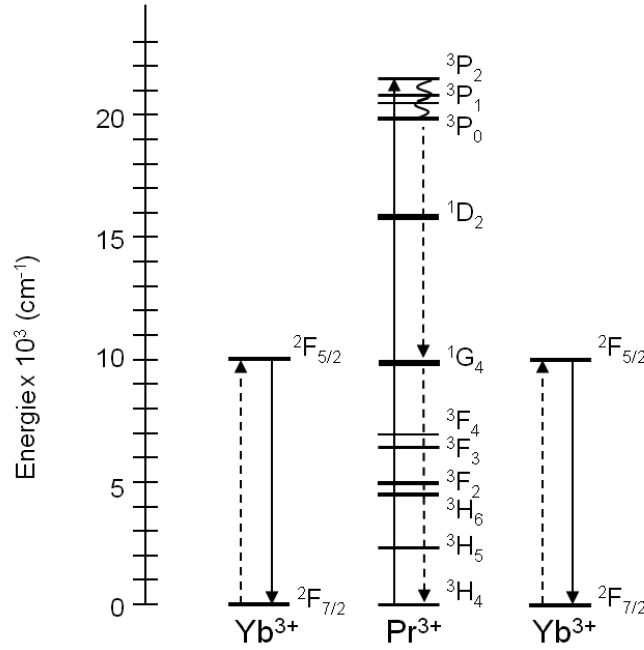


Figure 2: Schéma du quantum cutting pour le système $\text{Pr}^{3+}\text{-Yb}^{3+}$.

L'efficacité des deux transferts d'énergie décrits dépend de plusieurs paramètres parmi lesquels les plus importants sont la distance entre les ions donneurs et accepteurs et le recouvrement spectral entre l'émission du donneur et l'absorption de l'accepteur (Eq.1).

$$W_{DA} = \frac{C_{DA}^{(n)}}{R^n} \quad (1)$$

Une série d'échantillons de KY_3F_{10} et CaF_2 , avec la même concentration en Pr^{3+} (0,5%) et des concentrations en Yb^{3+} différentes ont été fabriqués en utilisant la technique de Bridgement-Stockbarger (Tableau 1). Les fluorures tels que KY_3F_{10} et CaF_2 présentent une faible énergie de phonon ($< 400 \text{ cm}^{-1}$), ce qui limite les transitions de type

non-radiative en favorisant le rendement de fluorescence des terres rares et en général, l'efficacité des mécanismes de transfert d'énergie.

Table 1: Concentration disponibles pour les échantillons de KY_3F_{10} et CaF_2 codopés Pr^{3+} - Yb^{3+} .

KY_3F_{10}	CaF_2
0.5% Pr^{3+}	0.5% Pr^{3+}
0.5% Pr^{3+} -1% Yb^{3+}	0.5% Pr^{3+} -0.5% Yb^{3+}
0.5% Pr^{3+} -5% Yb^{3+}	0.5% Pr^{3+} -1% Yb^{3+}
0.5% Pr^{3+} -10% Yb^{3+}	0.5% Pr^{3+} -2% Yb^{3+}
0.5% Pr^{3+} -20% Yb^{3+}	0.5% Pr^{3+} -4% Yb^{3+}
0.25% Pr^{3+}	0.5% Pr^{3+} -10% Yb^{3+}

Des valeurs d'efficacité de transfert d'énergie peuvent être facilement calculées pour le premier transfert d'énergie dans les différents échantillons de KY_3F_{10} (Tableau 2) à partir des valeurs expérimentales obtenues pour la durée de vie du niveau $^3\text{P}_0$:

Table 2: Efficacité du premier transfert d'énergie pour les échantillons de KY_3F_{10} codopés Pr^{3+} - Yb^{3+} .

Echantillon	Efficacité du transfert (%)
KY_3F_{10} :0.5% Pr^{3+} -5% Yb^{3+}	75,6
KY_3F_{10} :0.5% Pr^{3+} -10% Yb^{3+}	91,4
KY_3F_{10} :0.5% Pr^{3+} -20% Yb^{3+}	96,4

L'étude de l'efficacité pour le deuxième transfert d'énergie apparait quant à elle beaucoup plus compliquée. Un modèle d'équations de population classique a été développé et comparé aux expériences pour les différents échantillons de KY_3F_{10} : Pr^{3+} - Yb^{3+} . A partir de la modélisation nous pouvons déduire la valeur du taux de transfert pour les différents mécanismes de transfert d'énergie qui ont lieu dans le système (Tableau 3). La modélisation confirme d'ailleurs l'existence d'un équilibre thermique entre les niveaux $^1\text{G}_4$ and $^2\text{F}_{5/2}$ et donc, l'existence de transferts d'énergie dans les deux sens i.e. $\text{Pr}^{3+}(^1\text{G}_4) \rightarrow \text{Yb}^{3+}$ et $\text{Yb}^{3+} \rightarrow \text{Pr}^{3+}(^1\text{G}_4)$. Le modèle met de plus en évidence l'existence de mécanismes efficaces de dépeuplement de l' Yb^{3+} qui limitent la luminescence de celui-ci

et donc l'efficacité du quantum cutting pour l'émission de deux photons autour de $1\ \mu\text{m}$. En revanche, une augmentation des émission infrarouges du Pr^{3+} ($1.3\ \mu\text{m}$ et $2\ \mu\text{m}$) est observée, issue des transissions $^1\text{G}_4 \rightarrow ^3\text{H}_5$ and $^3\text{H}_6 \rightarrow ^3\text{H}_4$.

Table 3: Taux de transfert déduits de la modélisation où α représente le premier transfert d'énergie, β le deuxième transfert et γ et δ des mécanismes de dépeuplement de l' Yb^{3+} .

Echantillon	$\alpha(s^{-1})$	$\beta(s^{-1})$	$\gamma(s^{-1})$	$\delta(s^{-1})$
$\text{KY}_3\text{F}_{10}:0.5\%\text{Pr}^{3+}-5\%\text{Yb}^{3+}$	8.94×10^4	1.05×10^4	2.52×10^3	5.05×10^3
$\text{KY}_3\text{F}_{10}:0.5\%\text{Pr}^{3+}-10\%\text{Yb}^{3+}$	3.28×10^5	2.10×10^4	5.05×10^3	1.00×10^4
$\text{KY}_3\text{F}_{10}:0.5\%\text{Pr}^{3+}-20\%\text{Yb}^{3+}$	8.08×10^5	4.21×10^4	1.01×10^4	2.02×10^4

L'étude du codopage $\text{Pr}^{3+}\text{-Yb}^{3+}$ dans CaF_2 montre que les taux de transfert et les efficacités des transfert qui ont pu être mesurées sont encore beaucoup plus élevées dans ce matériau hôte (Tableau 1). Bien que des taux de transfert de 96,4% ont été mis en évidence pour le premier transfert d'énergie avec un échantillon de KY_3F_{10} codopé $0.5\%\text{Pr}^{3+}-20\%\text{Yb}^{3+}$ (Tableau 2), l'efficacité de ce même transfert d'énergie dans le cas des échantillons de $\text{CaF}_2:\text{Pr}^{3+}\text{-Yb}^{3+}$ est remarquablement supérieure (jusqu'à 99.97% pour CaF_2 codopé $0.5\%\text{Pr}^{3+}-10\%\text{Yb}^{3+}$). Cette différence est expliquée par l'existence d'une distribution de dopants complètement différente entre les deux matériaux hôtes. Ainsi, le dopage de KY_3F_{10} avec des ions terres rares donne lieu à une distribution uniforme d'ions dans la matrice tandis que dans le cas de CaF_2 , la formation de clusters de terres rares au sein desquels la distance entre les ions est très courte (seulement quelques Å) rend les transferts d'énergie plus efficaces dans ce matériau.

Les clusters résultant du codopage de CaF_2 avec Pr^{3+} et Yb^{3+} ont été analysés en détail. Les études spectroscopiques mettent en évidence l'existence de trois types de centres différents. Ces centres sont identifiés comme étant des ions Pr^{3+} isolés, des clusters de Pr^{3+} au sein desquels les mécanismes de relaxation croisée sont très efficaces ce qui rend la luminescence des ions Pr^{3+} dans ces clusters très faible, et finalement, des clusters de $\text{Pr}^{3+}\text{-Yb}^{3+}$ présentant des transferts d'énergie du Pr^{3+} vers l' Yb^{3+} extrêmement efficaces. Deux types de clusters de $\text{Pr}^{3+}\text{-Yb}^{3+}$ ont été ensuite distingués. Chaque cluster est caractérisé par un spectre d'émission différent et de plus, par des taux de transfert contrastés. Ainsi, un taux de transfert de l'ordre de $10^5\ \text{s}^{-1}$ est mesuré pour un premier type de clusters, dits "rapides", tandis qu'un taux de transfert de l'ordre de $10^7\ \text{s}^{-1}$ est calculé pour le deuxième type de clusters dits "ultra-rapides". L'interaction multipolaire,

en particulier dipôle-dipôle, rend compte du taux de transfert obtenu pour les clusters “rapides” (Eq.1). Ce n’est pas le cas pour les clusters “ultra-rapides” dont le taux de transfert ne peut pas être expliqué que par une interaction de type échange où le taux de transfert présente une dépendance exponentielle avec la distance entre les ions (Eq.2) ce qui donne lieu à des taux de transferts beaucoup plus élevés. Ce résultat indique une différence structurale importante entre les deux types de clusters, les distances entre les ions dans les clusters “ultra-rapides” étant nécessairement beaucoup plus courtes que dans les clusters “rapides”.

$$W_{ex} = \frac{1}{\tau_0} \exp\left(\gamma\left(1 - \frac{R}{R_0}\right)\right) \quad (2)$$

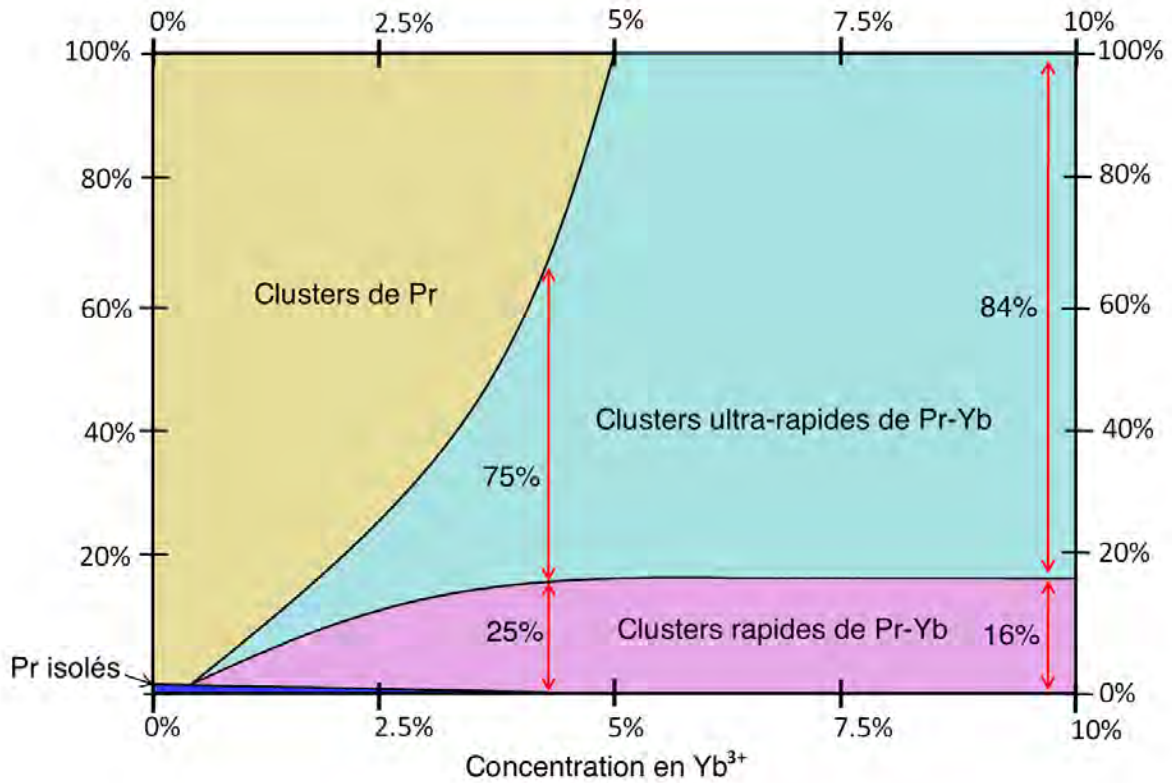


Figure 3: Evolution des espèces avec la concentration en Yb³⁺.

En utilisant de nombreux résultats expérimentaux originaux, les proportions des différents centres (Pr³⁺ isolés; clusters de Pr³⁺ et clusters de Pr³⁺-Yb³⁺) ont pu être déterminées en fonction de la concentration en Yb³⁺. Ainsi, seulement les clusters de Pr³⁺-Yb³⁺ existent pour des concentrations égales ou supérieures à 4%Yb³⁺, étant les clusters “ultra-rapides” devenant rapidement dominants avec une proportion de 84% par rapport au nombre total de centres luminescents pour une concentration de 10%Yb³⁺.

Au contraire, les clusters de Pr^{3+} dominent la structure à faibles concentrations en Yb^{3+} . Cette analyse nous permet de conclure que ce sont les échantillons avec des concentrations supérieures à 4% qui vont être finalement intéressants pour le quantum cutting (Fig.3) bien que l'extinction de la luminescence de l' Yb^{3+} soit aussi constatée dans CaF_2 à hautes concentrations en Yb^{3+} .

Les différentes études réalisées autour des clusters de $\text{Pr}^{3+}\text{-Yb}^{3+}$ ont révélé l'existence d'une équivalence spectroscopique entre le codopage $\text{Pr}^{3+}\text{-Yb}^{3+}$ et le codopage $\text{Pr}^{3+}\text{-Lu}^{3+}$ dans CaF_2 . Le codopage $\text{Pr}^{3+}\text{-Lu}^{3+}$ donne ainsi lieu au même type de clusters que le codopage $\text{Pr}^{3+}\text{-Yb}^{3+}$, ce qui est dû aux similarités existantes entre l' Yb^{3+} et le Lu^{3+} (masse et rayon atomique). Le codopage avec Lu^{3+} conduit au remplacement des clusters de Pr^{3+} par des clusters de $\text{Pr}^{3+}\text{-Lu}^{3+}$ tel qu'il est observé dans la Figure 3. Par contre, l'absence de transfert d'énergie du Pr^{3+} vers le Lu^{3+} , contrairement à l' Yb^{3+} , provoque une augmentation drastique de la luminescence dans ce codopage. En particulier, la luminescence est 400 fois plus intense dans CaF_2 codopé 0.5% Pr^{3+} -5% Lu^{3+} par rapport à CaF_2 simplement dopé 0.5% Pr^{3+} . La luminescence étant très faible dans CaF_2 simplement dopé Pr^{3+} , l'utilisation de ce matériau laser se trouve limitée, ce qui n'est pas le cas pour le codopage $\text{Pr}^{3+}\text{-Lu}^{3+}$.

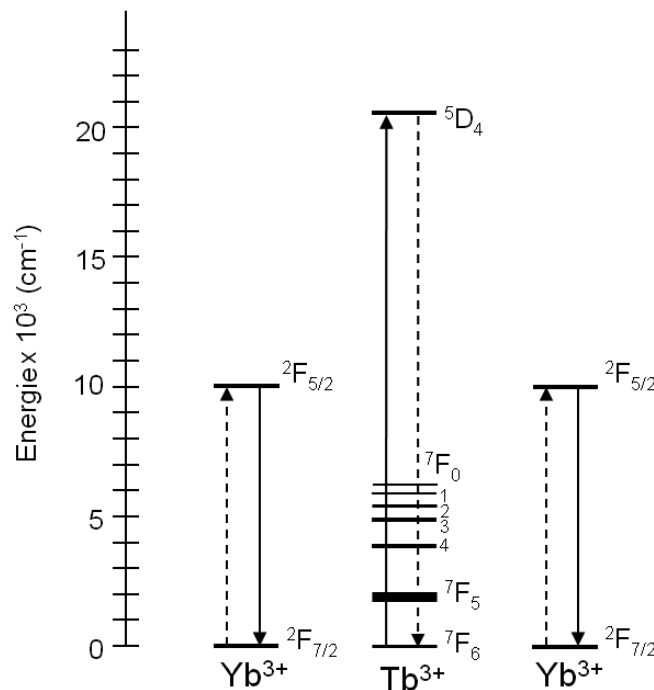


Figure 4: Schéma du quantum cutting pour le système $\text{Tb}^{3+}\text{-Yb}^{3+}$.

Le mécanisme du quantum cutting a été finalement étudié avec le codopage Tb^{3+} - Yb^{3+} dans CaF_2 . Dans ce système, l'excitation de deux Yb^{3+} a lieu par le biais d'un seul transfert d'énergie dit coopératif à partir du niveau $^5\text{D}_4$ du Tb^{3+} (Fig.4). Le mécanisme coopératif est plusieurs ordres de grandeur moins efficace qu'un transfert d'énergie résonnant. Pourtant, les études spectroscopiques réalisées accomplies avec une série d'échantillons de CaF_2 codopés Tb^{3+} - Yb^{3+} indiquent la formation de clusters de Tb^{3+} - Yb^{3+} au sein desquels le transfert coopératif est particulièrement efficace. Les valeurs obtenues pour l'efficacité du transfert coopératif ainsi que pour l'efficacité du quantum cutting sont présentées dans le Tableau 4. Contrairement au comportement observé dans le codopage Pr^{3+} - Yb^{3+} , la luminescence de l' Yb^{3+} augmente avec la concentration en Yb^{3+} pour le système Tb^{3+} - Yb^{3+} , ce qui indique l'absence de mécanismes de dépeuplement de l' Yb^{3+} dans ce matériau et confirme l'intérêt de ce système pour l'application envisagée.

Table 4: Efficacité du premier transfert d'énergie pour les échantillons de CaF_2 codopés Tb^{3+} - Yb^{3+} .

Echantillon	Efficacité du transfert (%)	Efficacité du QC
$\text{CaF}_2:0.5\%\text{Tb}^{3+}-0.5\%\text{Yb}^{3+}$	18	118
$\text{CaF}_2:0.5\%\text{Tb}^{3+}-2\%\text{Yb}^{3+}$	22	122
$\text{CaF}_2:0.5\%\text{Tb}^{3+}-10\%\text{Yb}^{3+}$	47	147
$\text{CaF}_2:0.5\%\text{Tb}^{3+}-20\%\text{Yb}^{3+}$	53	153

L'étude du rendement absolu du quantum cutting pour les échantillons de CaF_2 codopés Pr^{3+} - Yb^{3+} et Tb^{3+} - Yb^{3+} montre une efficacité 40 fois supérieure pour le codopage Tb^{3+} - Yb^{3+} . Malgré ce résultat prometteur, un défi reste à résoudre concernant la faible absorption du niveau $^5\text{D}_4$ du Tb^{3+} ($\sigma_{abs} \sim 10^{-23} \text{ cm}^2$). Différents candidats sont ainsi considérés pour la sensibilisation du Tb^{3+} dont la bande 5d du Ce^{3+} . Une étude préliminaire a été réalisée qui montre l'existence d'un transfert d'énergie efficace du Ce^{3+} vers le Tb^{3+} après absorption efficace entre 250 nm et 320 nm de la part du Ce^{3+} .

Introduction

Since the existence of luminescent materials presenting quantum efficiencies greater than unity was first demonstrated, several investigations have been devoted to the study of the physical mechanisms leading to the generation of several low-energy photons per incident high-energy photon. This phenomenon, usually referred to as *quantum cutting*, is nowadays known to occur in different materials such as inorganic solids, semiconductors and organic molecules.

Among the luminescent solids, rare-earth doped materials have shown a remarkable potential for quantum cutting applications. These luminescent ions were first studied at the beginning of the last century because of their peculiar properties. However, it was after the discovery of the laser action in the early 60s that the interest in trivalent rare earth ions grew up and was also extended to optics and photonics applications other than lasers. Therefore, rare-earth ions can be currently found in various optical systems such as optical amplifiers, quantum memories and waveguides.

Investigations on quantum cutting started with singly rare-earth doped-materials capable of a cascade emission. The focus was next shifted to the combination of two rare-earth ions where the energy of one of them, usually referred to as donor, is transferred stepwise to the other one (acceptor) through a single or a series of energy transfers. The quantum cutting mechanism found one of its first applications in the development of efficient Hg free rare-earth doped phosphors for the lighting industry which led to an intense research activity on potential quantum cutters. More recently, quantum cutters appear to be able to notably contribute to the next generation of photovoltaic (PV) technologies by converting UV-visible photons into several near-infrared (NIR) photons in order to minimize the energy losses due to thermalization of electron-hole pairs in the PV modules.

This thesis is focused on the study of rare-earth doped fluoride materials presenting a strong potential for visible to infrared quantum cutting:

In **Chapter 1**, the main photovoltaic technologies are reviewed paying particular attention to the so-called third generation approaches. The aim of the PV third-generation is to reduce production costs while increasing the efficiency of the cells. Among these approaches, improving the silicon cells efficiency is planned by using rare-earth doped luminescent converters able to shift the visible-near UV incident solar radiation to the near-infrared region so as to adapt the incident light to the silicon layer absorption.

The second half of the first chapter recalls the theoretical background leading to the determination of the energy levels of rare-earth ions in crystals. The principal energy transfer theories are next summarized finishing the chapter by a detailed review of the potential rare-earth based luminescent solar converters reported so far in the literature. These systems are presented as classified within two types, namely *upconverters* when referring to systems able to perform an energy shift from low energy to higher energy; and *downconverters*, when transforming instead high energy into lower energy.

Chapter 2 presents the investigation of the quantum cutting mechanism in $\text{Pr}^{3+}\text{-Yb}^{3+}$ codoped KY_3F_{10} . The energy transfers taking place within the $\text{Pr}^{3+}\text{-Yb}^{3+}$ system are here studied by a series of optical spectroscopy experiments, along with a classical rate equation modeling. Energy transfer rate values as well as quantum efficiency values are deduced from the rate equation modeling concluding that the energy transfers from Pr^{3+} to Yb^{3+} ions occur in an efficient way. However, the Yb^{3+} emission appears to be strongly quenched because of efficient back-transfer mechanisms taking place from Yb^{3+} to Pr^{3+} ions. A further description of the Pr^{3+} and Yb^{3+} dynamics is carried out by using modeling approaches such as the Inokuti-Hirayama model and Monte-Carlo computational methods. The Monte-Carlo methods are demonstrated to present a strong potential for modeling dynamics involving energy transfers.

In **Chapter 3**, the quantum cutting mechanism is investigated with a series of $\text{CaF}_2\text{:Pr}^{3+}\text{-Yb}^{3+}$ samples. The spectroscopic study reveals first the existence of two different Pr^{3+} centers within the $\text{CaF}_2\text{:Pr}^{3+}\text{-Yb}^{3+}$ codoped crystals. These species are identified as isolated Pr^{3+} ions and $\text{Pr}^{3+}\text{-Yb}^{3+}$ clusters. A dominance of the $\text{Pr}^{3+}\text{-Yb}^{3+}$ clusters is clearly observed when increasing the Yb^{3+} concentration in the sample. High energy transfer efficiencies for the first energy transfer are determined in $\text{CaF}_2\text{:Pr}^{3+}\text{-Yb}^{3+}$ due to the short distance between the Pr^{3+} and Yb^{3+} ions in the clusters.

The second part of this chapter presents a further insight into the rare-earth clustering in CaF_2 . Singly Pr^{3+} doped CaF_2 is dominated by non-luminescent Pr^{3+} clusters which explain the very weak emission observed for this material. On the contrary, the codoping of Pr^{3+} ions with Lu^{3+} ions avoids the formation of the Pr^{3+} clusters and instead favors the emergence of Pr^{3+} - Lu^{3+} clusters which emit light. The Pr^{3+} - Lu^{3+} codoping is then compared to the Pr^{3+} - Yb^{3+} codoping concluding that they give rise to the same type of rare-earth aggregates. Moreover, this investigation evidences the existence of two different types of Pr^{3+} - RE^{3+} clusters (with $\text{RE}^{3+} = \text{Lu}^{3+}$ or Yb^{3+}). These two types of clusters are primarily distinguished by their emission spectrum and, in the case of the Pr^{3+} - Yb^{3+} codoping, by their energy transfer rate and associated energy transfer mechanism. Indeed, the energy transfer from Pr^{3+} to Yb^{3+} in the so-called *fast* Pr^{3+} - Yb^{3+} cluster is most likely due to a dipole-dipole interaction. On the contrary, in the so-called *ultra-fast* cluster, the energy transfers are demonstrated to be far more efficient, which is attributed to a super-exchange interaction. The results derived from the detailed spectroscopic study enable a more complete evaluation of the QC mechanism in $\text{CaF}_2\text{:Pr}^{3+}\text{-Yb}^{3+}$ by taking into account the impact of the ultra-fast clusters, previously unnoticed, in the energy transfer efficiencies.

Chapter 4 is devoted to the study of the cooperative quantum cutting mechanism with Tb^{3+} - Yb^{3+} codoped CaF_2 . The spectroscopic investigations show the formation of Tb^{3+} - Yb^{3+} clusters within which the cooperative energy transfer is particularly efficient. On the other hand, the analysis of the evolution of the Yb^{3+} emission with the Yb^{3+} content reveals a promising low impact of the Yb^{3+} quenching in $\text{CaF}_2\text{:Tb}^{3+}\text{-Yb}^{3+}$. The last part of the chapter is focused on the RE^{3+} sensitization. The potential Tb^{3+} sensitizers are finally reviewed including some promising and very recent results obtained with Ce^{3+} ions.

Current context and challenges

1.1 PV technologies

Nowadays, it is widely accepted that human activities contribute to climate change. The activities devoted to energy production are those which present the highest environmental impact. Carbon dioxide emissions due to burning fossil fuels increased by 53% from 1971 to 2008 [1] and, during the same period, the world surface temperature and sea level raised [2]. Coincidence or not, these types of climate change evidences, combined with the growing global energy demand, are important incentives for the development of CO₂ neutral and renewable energy industries.

The term “solar energy” refers in a general way to any use of sunlight radiations for practical ends. The sun constitutes an endless source of energy whose applications are indeed multiple. For instance, the sun is a natural source of lighting, and also, solar radiations can be used to directly heat air, water or even cook. These solar passive technologies reduce the need for alternate resources limiting thus CO₂ emissions. However, besides these support technologies, solar active technologies are devoted to increase the world’s energy supply. Electrical power generation is possible with materials able to produce a voltage upon exposure to light. Those materials undergo the well-known *photovoltaic effect* so that, they are usually referred to as photovoltaic (PV) materials. Up until now, PV energy only represents a small contribution to the world total primary energy supply. Nevertheless, the growth rate in terms of cell production is impressive, with 27.2 GW manufactured within the year 2010, which constitutes a growth rate of 118%, the greatest annual growth in 12 years [3]. In agreement with this tendency, the *International Energy Agency* (IEA) [4] claims that solar power generators may produce most of the world’s electricity within 50 years, dramatically reducing the emissions of greenhouse gases that harm the environment. Unfortunately, in spite of these global per-

spectives, the costs associated with the PV energy production must still be reduced in order to enter areas of competitiveness so far unknown.

Since Russell Ohl accidentally discovered the first solar cell in 1940 (US Patent 2402662) [5], numerous materials have been investigated as potential PV devices giving rise to the current variety of solar technologies. One of the pioneer in solar cell technology, Professor Martin Green, classified the PV devices within three main generations, setting crystalline silicon wafer-type cells as PV first generation, thin-films technologies as a second generation, and any new concepts leading to improve the solar cells performance and competitiveness, in an heterogeneous third generation [6]. This classification is widely accepted nowadays.

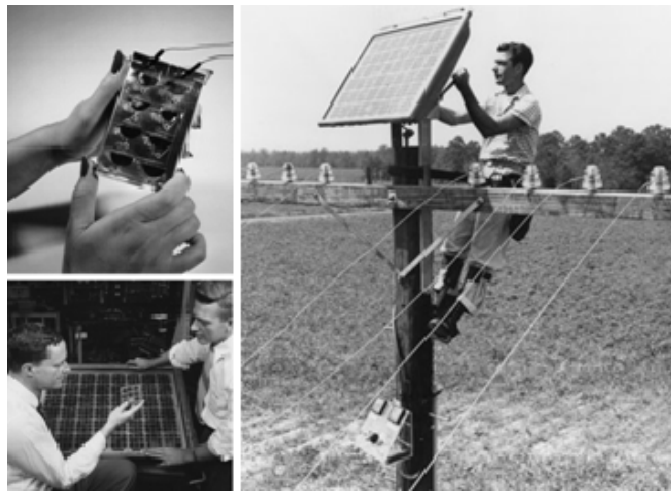


Figure 1.1: First Silicon cell by Bell laboratory [7].

1.2 First Generation: Silicon wafers

The first solar cell was developed in 1940 but it was after the 1950's semiconductors revolution that the first efficient solar cell and its first commercial application appeared [7]. That primitive device made of a silicon wafer was able to convert 6% of the sun-light radiation into electricity (Fig.1.1). Since then, wafer-type silicon cells, which can be monocrystalline (c-Si) or multicrystalline (mc-Si) depending on the manufacturing technique, have remained essential to PV technologies. From that low efficiency primitive device, the PV first generation has evolved to the current c-Si cells with 24.7% efficiency [8]. These wafer-type c-Si cells hold the world record efficiency among the overall single-junction technologies. Multicrystalline Si cells are indeed less efficient (19.3% [9]) than

those made from a Si single crystal. However, they have also known success since they are much simpler to produce and far less expensive to manufacture, presenting durability and longevity comparable to their monocrystalline counterparts.

During the past fifty years, crystalline and multicrystalline silicon have remained the main PV materials despite several studies pointing that other materials could become good PV candidates. Wafer-type crystalline silicon PV modules (consisting of a number of joint c-Si solar cells) were the first devices commercially available and still represent the most mature technology so that they continue to dominate the PV energy market with a share between 80 and 90 percent in 2010 (52.9% of monocrystalline and 33.2% of multicrystalline) even though the research and development of new PV technologies has notably intensified in recent years [3].

In general terms, the first generation of solar cells is successful. However, the c-Si wafer-type cells do not offer optimal performance, which should include stability, durability and high efficiency combined with economical viability. Within the manufacturing costs, the price of the Silicon wafer constitutes the largest cost, with more than 50% of the global expenses [10]. This is the reason why the development of thin-film technologies opened a new way to achieve low-cost PV devices.

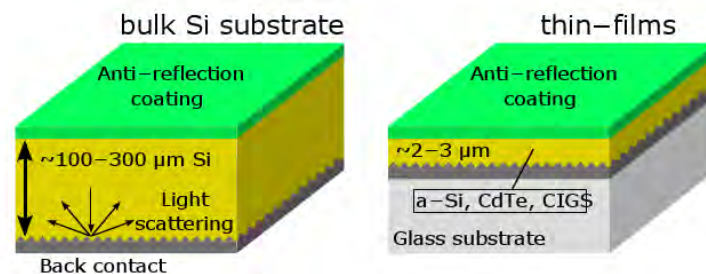


Figure 1.2: First generation cell (left). Second generation cell (right).

1.3 Second generation: thin-film technologies

First generation wafers are made from a cut of a silicon ingot. In the second generation, the semiconductor is deposited onto a substrate glass, plastic or steel (Fig.1.2). These technologies save costs by reducing the waste of the precious semiconductor. However, not only the costs but also the efficiency rates are limited in the so-called second generation (from 22.9% for a first generation c-Si module to 8.2% in a second genera-

tion 1-2 μm thin-film mc-Si submodule [11]) The balance between price and efficiency is without question the main challenge for the PV second generation.

1.3.1 Hydrogenated amorphous Silicon based technologies

Hydrogenated amorphous silicon (a-Si:H), introduced in the mid-1970's, appeared to be the best material for low-cost devices. Hydrogenated amorphous silicon cells use less than 1% of the silicon needed for a classical c-Si solar cell. Moreover, a-Si:H is a better absorber since its absorption coefficient exceeds by almost one order of magnitude that of c-Si over the 315-750 nm range [12]. Nevertheless, the adoption of this technology has been impaired by a problem of inherent instability, named the *Staebler-Wronski* effect after its discoverers [13], which provokes the cell efficiency to drop during the first six months of operation. As of this day, despite a better understanding of the effect, a solution has not been found. The current record efficiency for stabilized laboratory a-Si:H p-i-n¹ cells is around 10% [14]. In the mid-1990's, many research groups started to optimize the first stages of crystallization of their a-Si:H films. This led to the development of nanocrystalline (nc-Si) silicon and microcrystalline silicon ($\mu\text{c-Si}$) films consisting of small crystalline grains (10-500 Å) embedded in an amorphous silicon matrix. The use of these specific films to trigger the ordering process is now known to result in more stable and more efficient devices [16]. Currently, researches on a-Si are mainly focused on stacked structures such as a-Si/ $\mu\text{c-Si}$, or a-Si/nc-Si (so-called “micromorph” tandem cells) [16]. Up to date, the record efficiency for this PV technology has been achieved with an a-Si/nc-Si/nc-Si tandem cell presenting 12.5% efficiency [17].

The a-Si/c-Si heterojunction (Fig.1.3), also known as HIT (Heterojunction with Intrinsic Thin layer), constitutes an interesting alternative within the a-Si technologies. It is formed by depositing extremely thin layers of intrinsic and doped a-Si:H onto a c-Si wafer. It is a simple process with relatively low manufacturing costs which gives rise to promising solar cells with improved efficiency [18]. The potential of this technology was definitely demonstrated by Sanyo in 1991 [19]. Since then, it has been continuously developed reaching outstanding efficiency results in both research laboratory cells (22% efficiency [20]), and commercial modules (19.5% efficiency [21]).

¹A p-i-n junction is a varied form of the standard p-n junction, formed at the boundary between a p-type (lack of electrons or hole excess) and n-type (electron excess) semiconductor, in which, an intrinsic part of semiconductor is introduced between the p-zone and n-zone

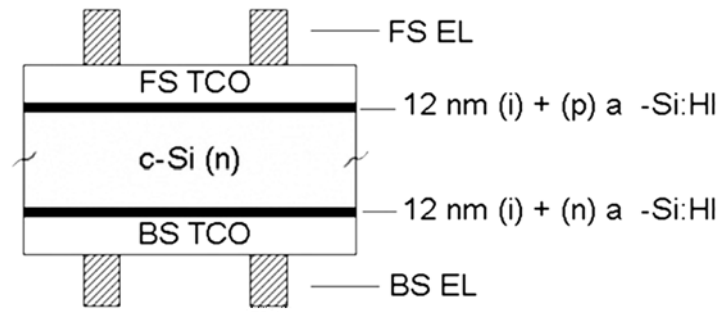


Figure 1.3: HIT cell [22].

PV technologies based on a-Si:H are low-cost, light, flexible (a 1 μm thin-film can be deposited onto a flexible substrate) and with aesthetical success so that their major applications are architectural structures (solar cell roof shingles [23]) and little devices (calculators, watches, lanterns...). In addition, the good efficiency results obtained with a-Si/c-Si heterojunctions (HIT) make this a-Si based technology a potential candidate for energy supply.

1.3.2 CdTe, CIS and CIGS thin films

CdTe cells dominated the first 25 years of thin-film PV technologies. Having a nearly ideal energy bandgap for a single-junction solar cell (1.41 eV at 300 K [24]), efficient CdTe cells were fabricated by different potentially scalable low-cost processes in the past. The best results showed efficiencies of 16.7% for CdTe research cells [11] and 10.9% for modules [25]. However, the usual problem associated with CdTe technologies is its acceptance in the market place. For the time being, cadmium and tellurium are not expensive materials but the availability of tellurium could become a serious inconvenience since it is an extremely rare element. In addition, Cd is toxic if ingested, inhaled or handled improperly so that manufacturing processes must be done in precise safety conditions, eventually rising the production costs.

The ternary alloy CuInSeCO_2 (CIS) was also found to exhibit properties well suited for PV converters. It is a direct band-gap semiconductor presenting a high optical absorption, stable electro-optical properties and energy bandgap suited for PV applications. In the seventies, the tandem $\text{CdS/CuInSeCO}_2/\text{Mo}$ showed 12% efficiency [26]. Since then, the structure has been under continuous development. Firstly, CIS evolved into an alloy, Cu(In,Ga)Se_2 (CIGS). Progressively, the CIGS layer and the other components taking

part in the tandem evolved resulting in more and more efficient devices. Currently, CIGS cells present a complex stacked structure with a record efficiency of 20% [27]. Despite the good efficiency results, CIGS manufacturing remains a complex and expensive process. Current researches on CIGS try to solve these challenges, for example, by looking for low-cost deposition methods in order to avoid expensive vacuum processes [28], with the aim of providing economical viability to this PV technology.

1.3.3 Dye-sensitized solar cells (DSSCs) and organic photovoltaic (OPV) devices

In the early 1960's, it was discovered that many common dyes had semi-conducting properties. Later, these dyes were among the first organic materials to exhibit PV effect [29]. In a dye sensitized solar cell (DSSC) (Fig.1.4) light absorption generates excitons (electron-hole pairs travelling as a unit). Then, the pair is separated when reaching a boundary which is, in this case, the interface between the dye and the TiO_2 layer [20]. So far, DSSCs have achieved efficiencies around 11% with research cells [31].

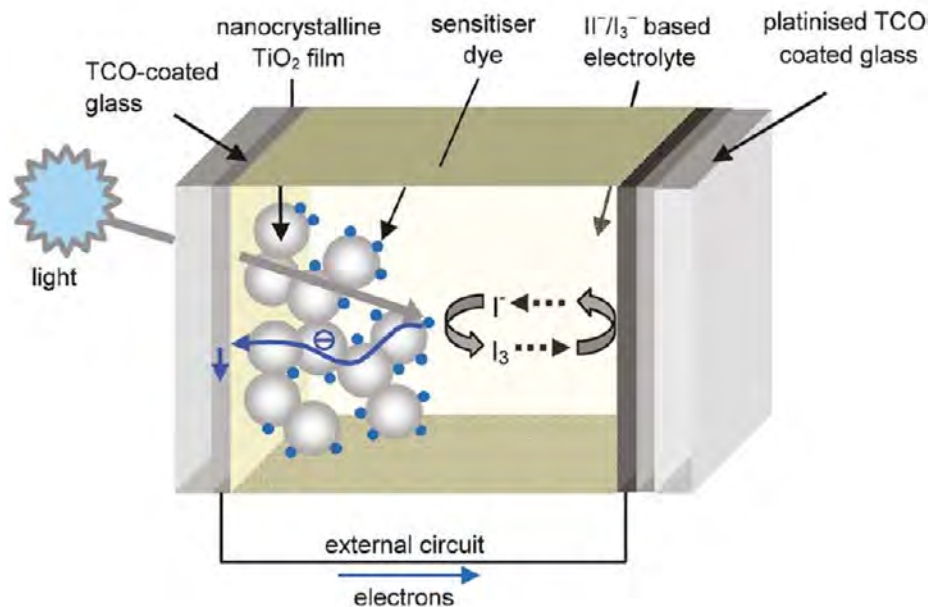


Figure 1.4: Gratzel-type DSSC scheme. Once separated, the TiO_2 layer captures the conduction electrons, while holes are conducted through the electrolyte.

DSSCs cells have been in development for a relatively long period compared to other PV approaches. Most in the PV community associate the problems and issues of DSSCs with the dye itself. Dyes are expensive and, in addition, the liquid dye and the solid-liquid interface present doubts about their long-term viability. A low cost manufacturing perspective is considered as the main advantage of this PV technology. However, DSSCs remain under development; therefore, they are still far from reaching the commercial market to be able to prove their competitiveness. Besides dyes, the PV effect has been observed in many important biological molecules such as carotenes, chlorophylls and other porphyrins [29]. Also based on excitonic processes, only a few of these organic photovoltaic (OPV) devices have validated performance and still, in a very low efficiency range (3-5%). As DSSCs, the major support of this technology has always been the possibility of reaching extremely low cost devices. Organic semiconductors are a less expensive alternative than inorganic semiconductors and, in addition, organic molecules can be processed by a large number of cheap techniques which are not available to crystalline inorganic semiconductors [32]. In spite of that, the OPV approach has many challenges to overcome before becoming a real alternative in the PV market. A very recent result (December 2011), by Heliatek, a Germany-based developer of organic photovoltaic cells, is nevertheless particularly encouraging for the future of OPV cells. Heliatek has achieved 9.8% of certified efficiency. This device shows indeed far better efficiency than any other OPV device investigated so far, pointing that the major disadvantage of OPV cells i.e. the low efficiency, might be overcome in the future.

1.3.4 III-V semiconductors for high-efficiency PV devices

Binary, ternary and quaternary alloys such as GaAs, GaAlAs and GaInAsP, have been receiving a special attention in recent years because of their potential as PV converters. According to the latest report, single junction GaAs thin-film research cells exhibit 27.6% efficiency [11], which is the absolute efficiency record within the thin-film technologies. In addition, these cells show greater conversion efficiency than the most efficient first generation c-Si wafer-type cells. On the other hand, as it happens with CIGS cells, the economical viability of this technology has always been questioned due to the expensive deposition techniques needed for their production. Nevertheless, the interest in these compounds for solar applications has been renewed since they give rise to one of the most important third generation approaches: the extremely efficient multi-junction solar cells.

1.4 Third-generation photovoltaics

The optimal PV device should present reliability, high efficiency and low cost. The PV second generation tried to reduce costs by limiting the waste of raw material and by looking for cheap processing techniques. The cost reduction resulted in less efficient PV devices (around 10% efficiency for a-Si:H, CdTe, DSSCs and OPVs). On the other hand, more efficient solutions have been proposed (CIGS, III-V single-junction cells), although they present the disadvantage of being expensive. With the aim of achieving high efficiency and low manufacturing costs at the same time (Fig.1.5), the third generation tackles new approaches. Most of these approaches are nowadays in the first steps of research and development, however, they are expected to play a fundamental role in the future PV technologies [6,33].

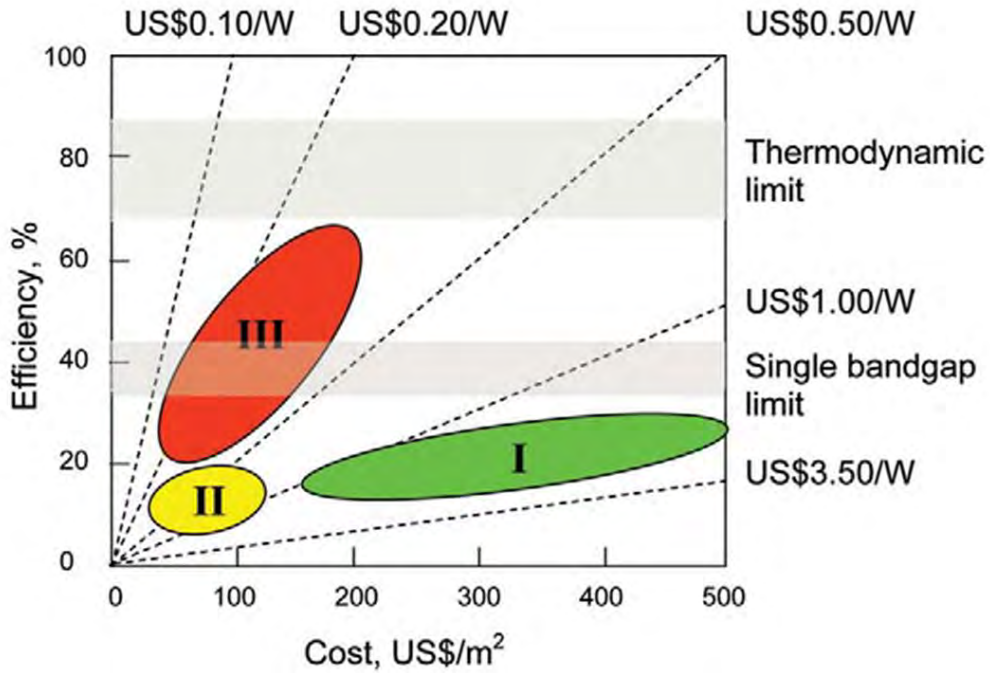


Figure 1.5: Efficiency and cost projections for first (I), second (II), and third generation (III) PV technologies (wafer-based, thin films and advanced approaches respectively). The first and second generation efficiency limit range (denoted single bandgap limit) is represented for solar concentrated power [34].

1.4.1 Fundamental limitations of current PV technologies

For any solar cell based on a single p-n junction, the upper conversion efficiency the device will be able to achieve is determined by the loss mechanisms taking place within the semiconductor. Four major loss mechanisms exist in a standard solar cell: lack of absorption for below bandgap photons; losses due to thermalization mechanisms after absorption of photons in the excited states of the conduction band; losses related to the junction and contact voltage, and finally, losses due to the recombination of electron-hole pairs within the junction (Fig.1.6). Between these four mechanisms, two of them i.e. absence of below bandgap photons absorption and thermalization, significantly limit the conversion efficiency of the resulting device. Recombination losses are indeed unavoidable, but their impact can be neglected in comparison with other loss mechanisms. On the other hand, the contact voltage and junction losses can be notably reduced with well-designed devices.

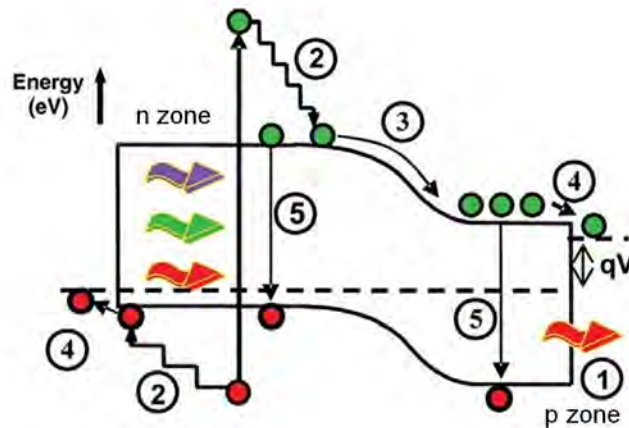


Figure 1.6: Band diagram representing the four types of loss processes in a standard p-n junction: (1) Non absorption of below bandgap photons; (2) lattice thermalization losses; (3) and (4) junction and contact voltage losses; (5) recombination losses (radiative recombination is unavoidable).

Taking in account sub-bandgap transparency and thermalization losses; assuming zero contact resistance and considering the sun as a black emitting body (Fig.1.7), Shockley and Queisser investigated the *detailed balance limit* of efficiency for single junction solar cells [34]. This limit is a theoretical upper value which establishes the maximum achievable ratio between the number of extracted electrons and the number of incident photons in a semiconductor under non concentrated sunlight radiation.

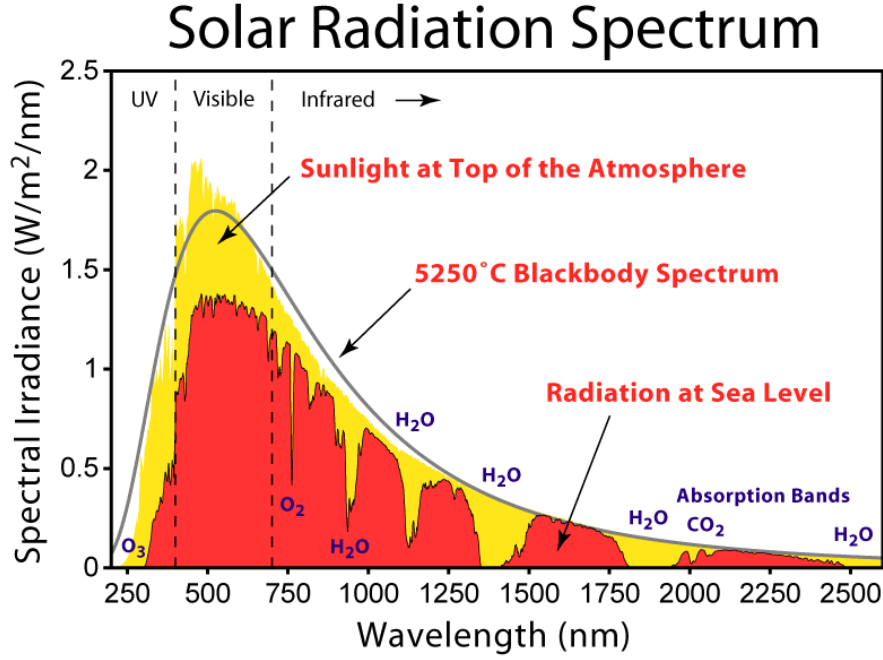


Figure 1.7: AM1.5 Solar radiation spectrum

Shockley and Queisser obtained a limiting efficiency of 31% for a 1.3 eV bandgap optimized cell. Silicon and GaAs cells, with bandgaps of 1.12 eV and 1.45 eV respectively (Table 1.1), present the same efficiency limit (29% [34]). Thus, the record efficiencies reported in each case, i.e. 24.7% for first generation c-Si cells [8] and 27.6% for second generation GaAs thin films [11], indicate well-designed and technologically developed devices approaching their upper efficiency limit.

The *detailed balance limit* eventually shows that single junction solar cells are only efficient to convert solar photons within a small energy range located around the semiconductor bandgap energy. Thus, the solar spectrum, emitting between 250 and 2500

Table 1.1: Main PV semiconductors bandgap energies.

PV cell	bandgap (eV)	λ (nm)
CdS	2.4	516
a-Si	1.75	711
CdTe	1.56	790
GaAs	1.45	860
CIGS	1.41	880
c-Si	1.12	1100

nm (Fig.1.7) is clearly underexploited by first and second generation single junction cells. The aim of the third generation PV approaches is to go through the theoretical limit and, for that, a more efficient exploitation of the solar spectrum is required.

1.4.2 Multi-bandgap approaches: high-efficiency multi-junction solar cells and Quantum wells solar cells (QWSCs)

Derived from the second-generation III-V single junction cells, multiple junction PV cells are among the few high-efficiency technologies that have been realized and commercialized. These devices, also referred to as *tandem cells*, are based on a stacking of p-n junctions, each junction, tuned to a specific energy of the solar spectrum as displayed in Fig.1.8. III-V semiconductors are particularly suitable for this technology due to their bandgap adjustability. Thus, the GaInP/GaAs/Ge triple-junction cell presents confirmed efficiency of 32% under *one-sun*² radiation [11]. A larger number of junctions assure, in principle, a better exploitation of the solar spectrum. Concepts of 4-6 junctions are now in the research stage [35] although each layer added entails tremendous technological complexities due to the lattice mismatch between the different semiconductors. Therefore, translating such a complex device from the laboratory to the commercial market, nowadays, is not a real option. This kind of technology can find its application in the spatial industry [36] for which the efficiency is a priority unlike costs.

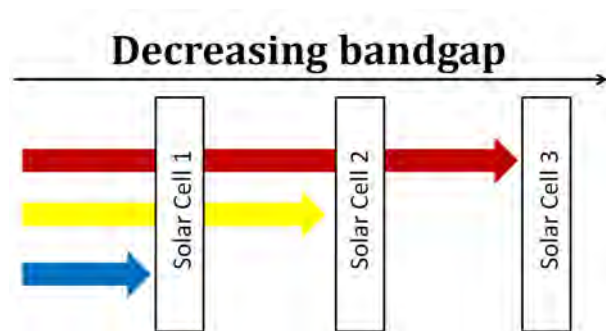


Figure 1.8: Absorption mechanism in a triple-junction solar cell. From the front side to the rare side, the layers follow a decreasing bandgap energy order. Above-bandgap photons are progressively absorbed by the consecutive layers while sub-bandgap photons reach the next layer.

²Maximum value of natural insolation.

Quantum wells solar cells (QWSCs) constitute an advanced approach to multi-bandgap solar cells derived from the recent development of semiconductor nanostructures [37,38]. The PV device is based on a single p-i-n structure with a number of narrow low bandgap regions or quantum wells (QWs), within the intrinsic zone of the junction. The QWs can be created by intercalating very narrow films (a few nanometers) of a lower bandgap semiconductor into the main semiconductor; or, by a semiconductor quantum dots (QDs) structure as displayed in Fig.1.9. These QWSCs are also referred to as Quantum dots solar cells (QDSCs). The main advantage of this structure is its enhanced absorption. Contrarily to single-junction solar cells, in QWSCs, sub-bandgap photons can be absorbed by the wells. Optimally, carriers escape next from the well (thermal escape) so that, the light absorbed by the cell in the lower bandgap regions is integrally converted into photocurrent before recombining [39]. QWSCs are based on a complex technology which could provide good efficiency results in the future. As a proof, efficiencies of 26% have been measured with a GaAsP/GaInAs nanostructured PV device [40]. Nevertheless, the biggest inconvenient of this technology is still the price of the resulting device, since it involves expensive materials and deposition methods (MBE, MOVPE...).

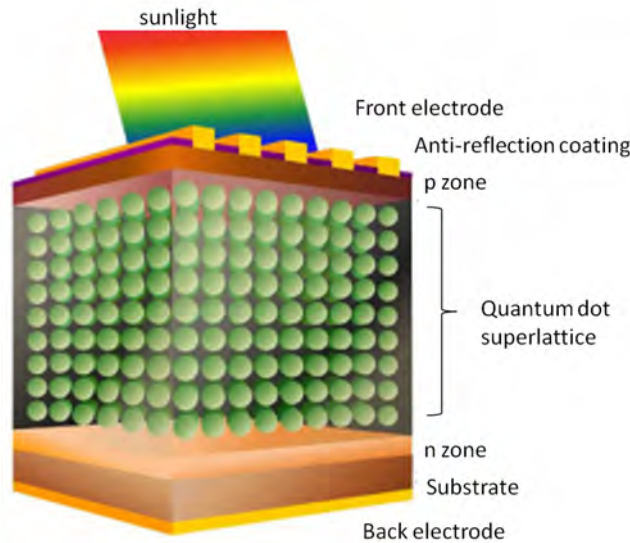


Figure 1.9: QDs solar cell.

1.4.3 Modifying the solar spectrum

So far, we have presented third-generation technologies trying to accommodate the PV cell absorption to the solar energy range. However, instead of tuning the device absorption, modifying the incoming spectrum can be realized by incorporating energy

conversion layers or spectral *converters*, into existing solar cells [41-44]. Thus, a first converter could be placed on top of the solar cell for downconversion (frequency shift from high energy to lower energy), while a second layer could be placed at the back of the cell for upconversion (frequency shift from low energy to higher energy), both layers being electronically isolated from the active semiconducting layer.



Figure 1.10: (a) solar cell with downconverter added to the front side; (b) solar cell with upconverter on the rear side.

The aim of the downconversion layer (*downconverter*) is to split high energy photons into several lower energy photons in order to create several electron-hole pair per incident photon. This splitting, usually referred to as quantum cutting, allows a more efficient use of the incident photon energy since it reduces thermalization losses. The downconverter must be placed on the front side of the cell to be able to convert the incident photons before they reach the semiconducting layer (Fig.1.10.a). On the other hand, the role of the upconversion layer (*upconverter*), is to combine several non absorbable low energy photons to create a single higher energy photon with energy above the semiconductor's bandgap energy. Since the purpose of an upconverter is to use photons transmitted by the cell, it can be placed at the rear side with a good optical coupling necessary to ensure high transmission of the low energy light to the upconverter and of the upconverted light back into the cell (Fig.1.10.b). Thus, the major loss mechanisms in single-junction solar cells (thermalization and non absorption of low energy photons), are expected to be reduced by these two layers. Indeed, the Shockley and Queisser upper efficiency limit is estimated to be increased from 29% [34] to 40.2% for a c-Si cell with an upconversion layer incorporated [45]; and from 29% to 36.6% for a c-Si cell with a downconversion layer [43]. In addition, the advantage in comparison to other PV technologies is that no modification of the active layer is needed, and neither a complicated cell structure such as that used for tandem solar cells or QWSCs. In conclusion, this alternative tries to implement already existing PV technologies, particularly c-Si based technologies, enhancing their efficiency but restraining costs by taking advantage of already developed manufacturing techniques.

In a general way, a spectral converter must fulfil characteristics such as wide absorption bands, emission peaks matching the solar cell absorption, minimum reabsorption losses due to overlap of absorption and emission spectra, luminescent quantum yield (LQY) near unity, high transmittance in the cell's high response region and low scattering. Some candidates are:

Fluorescent organic dyes

Organic luminescent materials such as perylene-based dyes exhibit near-unity LQY [46] and have been demonstrated stable for many years in a PMMA host [47]. In the eighties, multi-dye systems were proposed to increase the absorption range of solar cells [48] since they were shown to be able to absorb up to 70% of the solar spectrum energy [49]. Downconversion processes take place in these compounds by cascade emission when the emission of one molecule is absorbed and re-emitted by another molecule that has a longer emission wavelength. Thus, photons absorbed at shorter wavelengths travel through the different luminescent dyes to be finally emitted by the longest wavelength emitting dye [50]. The main disadvantage is that multidye plates exhibit narrow absorption bands as well as significant reabsorption losses [51].

Luminescent semiconductor quantum dots (QDs)

The development of spectral converters containing semiconductor nanocrystals or QDs is also investigated [52]. Semiconductor QDs present broad absorption spectra with high absorption coefficients opening the door to an extensive utilization of the solar spectrum energy [53]. In addition, QDs technologies provide spectral tunability since their absorption and emission characteristics are controlled by the QD diameter [54]. The possibility of multiple exciton generation (MEG) within the QDs also exists [55]. MEG is a process during which an electron with kinetic energy larger than the semiconductor bandgap energy excites a second electron from the valence band creating two electron-hole pairs. This phenomenon has been observed recently with PbSe QDs resulting in LQY up to 3 [56]. This means that every PbS QD in the sample produces three electron-hole pairs per incident photon so that each absorbed photon eventually results in the emission of three lower energy photons. Currently available semiconductor QDs only exhibit LQYs lower than 1, reabsorption losses and instability. However, they will present a great potential as energy converters if stable and high LQY systems become more available.

Rare-earth ions

Lanthanides or rare earth ions is the name used to refer to a group of elements with atomic number comprised between 57 (Lanthanum) and 71 (Lutetium). Usually presented as doubly or triply charged ions, these elements are also referred to as $4f$ elements since they can be recognized by their unfilled and optically active $4f$ shell. Generally, as luminescent centers within a host material, trivalent rare-earth ions exhibit stability, small reabsorption losses and high LQY. In addition, the $4f$ energy levels offer a large variety of energy transfer possibilities between different rare-earth ions [57]. Thus, rare-earth doped materials are good candidates both for upconversion and downconversion quantum cutting. Unfortunately, as a disadvantage, trivalent rare earth ions present narrow absorption peaks with low absorption coefficients. The summary of properties presented in Table 1.2, shows that rare-earths seem to be the best suited luminescent species for solar cells efficiency enhancement by energy conversion approaches [58]

Table 1.2: Comparison of the potential energy converters main properties.

Desired property	Dyes	QDs	REs
Wide absorption band	×	✓	×
Minimal reabsorption	×	×	✓
High LQY	✓	×	✓
Stability	✓	×	✓

1.4.4 Concentrated Photovoltaics (CPV)

Solar concentrators do not constitute a PV technology, however, they must be mentioned since they can be considered as a promising complement for any existing PV technology. Solar concentrators have been studied since the seventies and nowadays, they are implemented in many PV installations for power supply. Typically formed by lenses and mirrors, their purpose is to focus a large area of sunlight radiation into a small area of PV material. Therefore, solar concentrators increase the amount of incident energy consequently increasing the electric output of the device. In addition, CPV systems are not expensive and lead to a reduction of the PV cells size, which is particularly interesting to limit the costs in high-efficiency technologies such as multi-junction solar cells. For

instance, the GaInP/GaAs/InGaAs triple-junction cell holds the absolute world record of efficiency with 42.3% confirmed efficiency under 406 suns concentrated light [59]. For comparison, the upper efficiency limit for a c-Si solar cell with an upconversion layer under concentrated sunlight is calculated to be 54% [45]. This theoretical value represents an increase of almost 200% in comparison to the classical Shockley-Queisser limit (29%), which proves that solar concentrators may be playing a major role in the future when combined with third-generation PV technologies.

1.5 RE based converters for silicon solar cells efficiency enhancement

As seen in a previous section, silicon PV technologies, comprising c-Si, mc-Si and a-Si:H devices, dominate the current solar energy market with more than 90% of world trade. In addition, the research stage and high costs of other PV technologies combined with the secure supply of raw silicon for the next decades, and the possibility of making the already existing Si cells more efficient through third-generation approaches such as downconversion and upconversion layers acting under concentrated sunlight, points that silicon will remain the dominant PV technology in the future.

Among the luminescent species proposed for modifying the solar spectrum, it was shown that trivalent rare-earth ions were the ones which fitted best the required properties. In this section, we review some fundamental concepts on rare-earth ions acting as dopants within a crystalline environment, and then, we describe the different rare-earth doped systems investigated as third-generation upconverters and downconverters for silicon solar cells efficiency enhancement.

1.5.1 Energy levels of rare-earth ions in crystals

The energy states of a free-atom with n electrons are given by the time-independent Schrödinger equation:

$$H\psi(\mathbf{r}_1, \dots, \mathbf{r}_n) = E\psi(\mathbf{r}_1, \dots, \mathbf{r}_n) \quad (1.1)$$

in which $\psi(\mathbf{r}_1, \dots, \mathbf{r}_n)$ is the wavefunction of eigenvalue E , and H , is the Hamiltonian for the n -electron system which takes the form:

$$H = \sum_{i=1}^n \left(-\frac{\hbar^2}{2m} \nabla^2 - \frac{Ze^2}{4\pi\epsilon_0 \mathbf{r}_i} \right) + \sum_{i=1}^n \xi(r_i) \mathbf{l}_i \mathbf{s}_i + \frac{1}{2} \sum_{i=1}^n \sum_{j=1}^n \frac{e^2}{4\pi\epsilon_0 |\mathbf{r}_i - \mathbf{r}_j|} \quad (1.2)$$

The many-electron Hamiltonian is composed of three terms, the first term being a sum over n electrons of one-electron kinetic and potential energy operators; the second term representing the spin-orbit coupling interaction and the third one describing the inter-electron Coulomb repulsion [60]. Approximated wavefunctions can be found for the n -electron system under *central field approximation*. This approximation assumes that the inter-electron repulsion term contains a large spherically symmetric component referred to as $U(r_i)$. Thus,

$$H = H_0 + H' + H_{so} \quad (1.3)$$

in which

$$H_0 = \sum_{i=1}^n \left(-\frac{\hbar^2}{2m} \nabla^2 - \frac{Ze^2}{4\pi\epsilon_0 \mathbf{r}_i} \right) + U(\mathbf{r}_i) \quad (1.4)$$

$$H_{so} = \sum_{i=1}^n \xi(\mathbf{r}_i) \mathbf{l}_i \mathbf{s}_i \quad (1.5)$$

$$H' = \frac{1}{2} \sum_{i=1}^n \sum_{j=1}^n \frac{e^2}{4\pi\epsilon_0 |\mathbf{r}_i - \mathbf{r}_j|} - \sum_{i=1}^n U(\mathbf{r}_i) \quad (1.6)$$

For atoms with low atomic number the effect of H' is greater than that of H_{so} so that wavefunctions, namely LS terms of energy $E(^{2S+1}L)$ are found for $H_0 + H'$. The spin-orbit interaction is next taken in account (*LS coupling or Russel-Saunders coupling*), provoking the degenerated ^{2S+1}L terms to split into several $^{2S+1}L_J$ terms with $J = L + S$ and degeneracy equal to $2J + 1$ [61]. On the other hand, atoms with high atomic number, endure the effect of the spin-orbit interaction more than that of H' . In that case, we consider the coupling of the spin and orbital angular momentum on individual electrons (j states with $j = l + s$ for individual electrons) and then, the coupling of the j states through H' (*j-j coupling*).

Eventually, wavefunctions are more complicated to determine when the effect of H' is comparable to that of H_{so} since a mixing of states with the same quantum number J and different quantum numbers L and S takes place (*intermediate coupling*). The rare-earth ions belong to this group. The $4f^n$ energy levels are thus expressed as $^{2S+1}L_J$

Russel-Saunders terms, their final position is then derived from experimental data of the free-ion emission spectra. The $4f^n$ energy levels were reported by Dieke and Crosswhite in 1963, being the results summarized in the so-called Dieke diagram [57].

In the presence of a crystal environment, the $^{2S+1}L_J$ levels split into a number of sub-levels (Stark sub-levels) due to the interaction between the $4f^n$ electrons and the electric field created by the ions forming the crystal lattice. For the particular case of dopant rare-earth ions, the optically-active $4f$ electrons are only weakly affected by the crystal field since they are partially screened by the filled $5s^25p^6$ outer shells. Thus, the splitting due to the spin-orbit coupling is much stronger than the splitting provoked by the interaction with the crystal field (H_{cf}) (Fig 1.11), which is thus treated as a perturbation on the free-ion energy levels:

$$H = H_0 + H' + H_{so} + H_{cf} \quad (1.7)$$

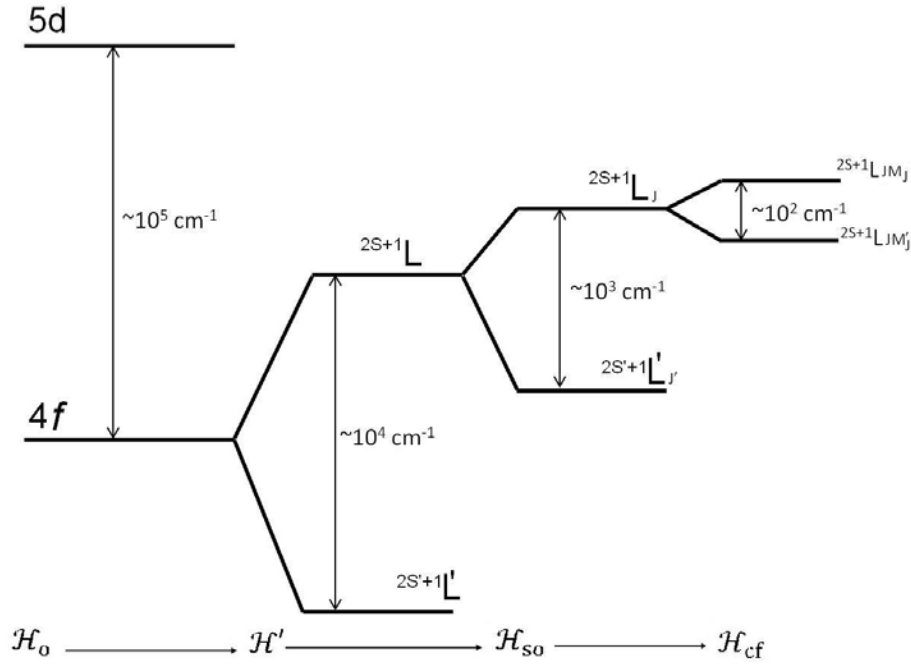


Figure 1.11: $4f$ energy levels splitting under the effect of different interactions.

The study of the crystal field is a very complex problem. The simplest description uses the point charge model, in which, the lattice ions causing the electrostatic crystal field are represented by point charges supposed fixed in their lattice position. The crystal-field Hamiltonian takes then the form:

$$H_{cf} = \frac{1}{4\pi\epsilon_0} \sum_{i=1}^n \sum_{l=1}^n \frac{Z_l e^2}{|\mathbf{R}_l - \mathbf{r}_i|} \quad (1.8)$$

where the summations is done over all $4f$ electrons and ligands. The development of $|\mathbf{R}_l - \mathbf{r}_i|^{-1}$ in a base of spherical harmonics leads to:

$$H_{cf} = \sum_{k,q} \sum_l B_q^k C_q^k(\theta, \phi) \quad (1.9)$$

which is the form of the crystal field usually employed for rare-earth ions, with B_q^k the crystal field parameters. The crystal field experienced by the optically-active $4f$ electrons notably reflects the symmetry of the crystalline environment, especially the symmetry regarding the nearest ligands (local symmetry). The splitting of the $^{2S+1}L_J$ energy levels is for instance more important when the local site symmetry is low as shown in Table 1.3.

Table 1.3: Expected splitting for a $^{2S+1}L_J$ level with integer (up) and half-odd-integer (down) J depending on local site symmetry.

J=n	J=0	J=1	J=2	J=3	J=4	J=5	J=6	J=7	J=8
2J+1	1	3	5	7	9	11	13	15	17
Cubic	1	1	2	3	4	4	6	6	7
Hexagonal	1	2	3	5	6	7	9	10	11
Trigonal	1	2	3	5	6	7	9	10	11
Tetragonal	1	2	4	5	7	8	10	11	13
Orthorhombic	1	3	5	7	9	11	13	15	17
Monoclinic	1	3	5	7	9	11	13	15	17
Triclinic	1	3	5	7	9	11	13	15	17
J=n/2	J= $\frac{1}{2}$	J= $\frac{3}{2}$	J= $\frac{5}{2}$	J= $\frac{7}{2}$	J= $\frac{9}{2}$	J= $\frac{11}{2}$	J= $\frac{13}{2}$	J= $\frac{15}{2}$	J= $\frac{17}{2}$
2J+1	2	4	6	8	10	12	14	16	18
Cubic	1	1	2	3	3	4	5	5	6
Hexagonal	1	2	3	4	5	6	7	8	9
Trigonal	1	2	3	4	5	6	7	8	9
Lower sym.	1	2	3	4	5	6	7	8	9

1.5.2 Energy transfer processes

The theoretical background for the phenomenon where an impurity (acceptor or activator) is able to emit light upon light absorption by a different type of center (donor or sensitizer) was established by Förster (1948) and Dexter (1953). This phenomenon, usually referred to as energy transfer, occurs through three different ways represented in Fig.1.12.

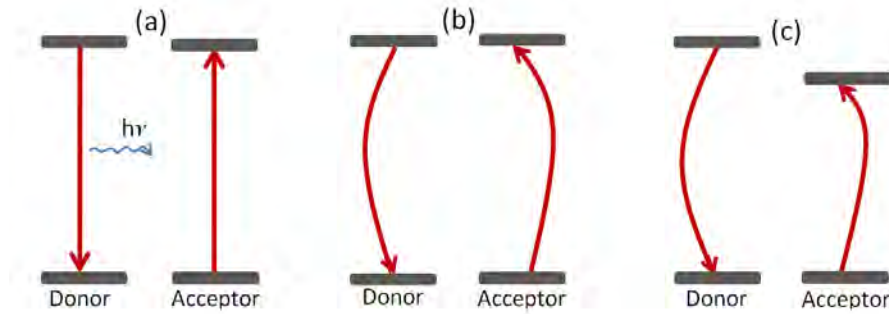


Figure 1.12: Energy transfer processes (a) Radiative resonant energy transfer; (b) Non-radiative resonant energy transfer; (c) Phonon-assisted energy transfer.

In the first process, the depopulation of the donor takes place by emitting a photon which is then absorbed by the acceptor (Fig.1.12.a). In the second process, the energy transfer takes place without any radiative emission (Fig.1.12.b). In the case of a non-resonant energy transfer, the excess or lack of energy between the donor emission and the acceptor absorption is compensated by phonon exchange with the host material (Fig.1.12.c). The non-resonant energy transfer becomes more and more efficient as the number of phonons needed is low. As seen in Fig.1.12, radiative and non-radiative energy transfers lead to the same final state; however, there is no modification of the donor lifetime for the radiative process in contrast to what happens with the non-radiative one in which the donor lifetime can be drastically reduced.

The energy transfer processes were described by Dexter (1953) [62] as being able to take place between impurity centers in condensed media, for instance, with rare-earth ions or transition-elements acting as dopants within a crystalline host; or, directly between the host and the impurity, in which case they are referred to as *host-sensitized energy transfers*. The type of interaction leading to the energy transfer process has also been discussed by different authors [62,63]. The classical approach considers the non-radiative energy transfers to occur by direct electric multipole interaction between donors and

acceptors [64]. Under this assumption, the energy transfer rate [61] is given by:

$$W_{DA} = \frac{3c\pi^4 n^2}{R^n} \int \sigma_A(E) \sigma_E(E) \quad (1.10)$$

So, W_{DA} depends on the spectral overlap between the donor emission spectrum and the acceptor absorption spectrum as well as the donor-acceptor distance (R), with $n=6$ for dipole-dipole interactions, $n=8$ for dipole-quadrupole interactions and $n=10$ for quadrupole-quadrupole interactions; being with n the refractive index and c the light speed. Eq.1.10 is usually presented using an abbreviate notation:

$$W_{DA} = \frac{C_{DA}^{(n)}}{R^n} \quad (1.11)$$

in which $C_{DA}^{(n)}$ is the *transfer microparameter*:

$$C_{DA}^{(n)} = 3c\pi^4 n^2 \int \sigma_A(E) \sigma_E(E) \quad (1.12)$$

Besides multipole interactions, the energy transfer processes have also been described as occurring by exchange mechanisms [63,65]. The energy transfer rate takes then the form:

$$W_{ex} = \frac{1}{\tau_0} \exp\left(\gamma\left(1 - \frac{R}{R_0}\right)\right) \quad (1.13)$$

where τ_0 is the intrinsic donor lifetime (i.e. without energy transfer), γ is equal to $2R_0/L$, with L the effective average Bohr radius (usually taken as 1 Å) [66]; and R_0 is the critical interaction distance at which the energy transfer becomes equal to the intrinsic de-excitation rate τ_0^{-1} . Studies show that the interaction responsible for energy transfer among rare-earth ions is generally electric multipolar: dipole-dipole; dipole-quadrupole or quadrupole-quadrupole. However, exchange transfers have also been reported, usually coinciding with systems in which the distance between donors and acceptors is especially short [67,68].

1.5.3 Rare-earth based solar up and down converters

As seen in section 1.5.1, each trivalent rare-earth ions present a complex and well-defined energy-level structure [57] giving rise to a number of narrow optical transitions.

Within the $4f$ configuration, a large variety of energy transfer paths exists and indeed, numerous efficient energy transfers have been reported within a single rare earth ion [69-72], and also between two different rare-earth ions [73-75]. Energy transfer processes have been widely investigated due to the important role they play in the design of laser and optoelectronic devices. Recently, the energy transfers between rare-earth ions have been studied for solar applications due to the possibility of developing rare-earth based upconverters and downconverters. Among the rare-earth ions, trivalent ytterbium is an optimal candidate for taking part in spectral converters devoted to Si-based PV technologies. Trivalent ytterbium has a single excited state around 10000 cm^{-1} ($\sim 1.24\text{ eV}$), just above the silicon bandgap energy ($\sim 1.12\text{ eV}$ (Table 1.1)). Therefore, the Yb^{3+} infrared emission can be efficiently absorbed by silicon solar cells without significant thermalization losses. In addition, with only presenting two energy levels ($^2F_{5/2}$ and $^2F_{7/2}$), Yb^{3+} shows luminescent quantum yield near unity. Thus, trivalent ytterbium is, in principle, an excellent activator for this application, needing then a good sensitizer to accomplish the energy conversion process.

Upconversion of below-bandgap photons

Photons with energy lower than the silicon bandgap energy can be exploited by using upconversion processes. According to the basic principle, two or more incoming photons react with the upconverter, which re-emits a single photon with energy higher than the incoming photons.

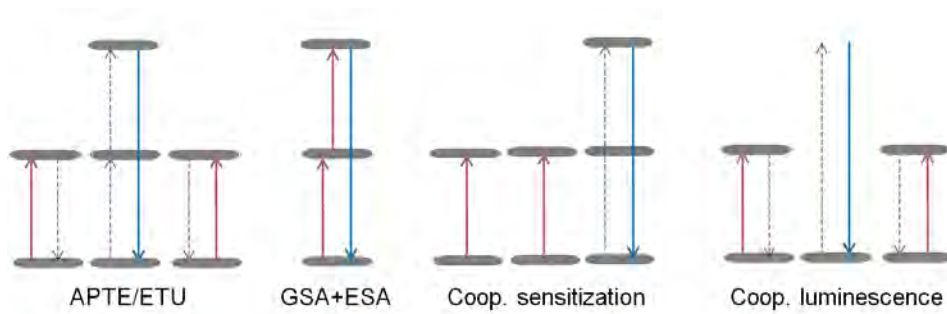


Figure 1.13: Overview of upconversion mechanisms [78]. Absorption and emission processes are indicated by solid arrows. Energy transfers are indicated by dashed arrows. Vertical lines are real energy levels. The efficiency of the processes decreases from left to right.

Upconversion can be achieved by different mechanisms (Fig.1.13). Among them, the most efficient ones are the so-called ETU (energy transfer upconversion) or APTE (“Addition de Photons par Transfert d’Energie”, name attributed by F. Auzel after discovering the mechanism in 1966 [76]) processes. Other mechanisms consist of 2-photon absorption with a first absorption from the ground-state followed by an excited-state absorption (GSA+ESA). Less efficient, although non-negligible there are also the so-called cooperative sensitization and cooperative luminescence second-order processes [77].

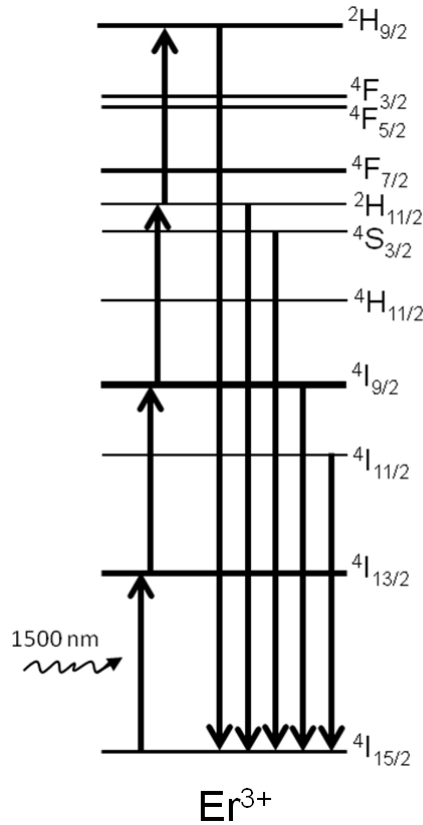


Figure 1.14: GSA+ESA within Er^{3+} ions resulting in several visible upconverted emissions. Solid arrows represent excitation transitions and radiative emissions.

Upconversion of infrared into visible light has been widely investigated in order to develop infrared-pumped visible lasers and for their potential applications such as color display, optical storage, optoelectronics, and medical applications [79-88]. Indeed, upconversion from the near-infrared to the visible spectral regions has been receiving much more attention than upconversion from infrared wavelengths to $1\ \mu\text{m}$ [41,89-92]. Nevertheless, upconversion applied to silicon solar cells requires absorbing photons at wavelengths longer than $1.1\ \mu\text{m}$ (Si bandgap) in order to get upconverted emission within the sili-

con absorption range ($\lambda < 1.1\mu\text{m}$). Thus, two types of rare-earth doping fulfilling this condition have been investigated which are single Er^{3+} doping and Er^{3+} - Yb^{3+} codoping.

Erbium is a very promising sensitizer for a solar upconverter because of its ground state absorption at about 1500 nm ($^4\text{I}_{15/2} \rightarrow ^4\text{I}_{13/2}$). It can also play the role of active ion since, under 1500 nm excitation, it may exhibit multiple photon absorption (GSA+ESA) or ETU processes giving rise to visible emissions from higher excited states (Fig.1.14). Thus, Er^{3+} upconverted emissions are located at approximately 980 nm ($^4\text{I}_{11/2} \rightarrow ^4\text{I}_{15/2}$), 810 nm ($^4\text{I}_{9/2} \rightarrow ^4\text{I}_{15/2}$), 660 nm ($^4\text{S}_{3/2} \rightarrow ^4\text{I}_{15/2}$), 550 nm ($^2\text{H}_{11/2} \rightarrow ^4\text{I}_{15/2}$) and 410 nm ($^2\text{H}_{9/2} \rightarrow ^4\text{I}_{15/2}$), all of them comprised within the silicon absorption range.

Er^{3+} doped materials such as ZBLAN, YAG, YF_3 , LiYF_4 , SrF_2 and CaF_2 [93-98] have been investigated in terms of upconversion efficiency under 1500 nm pumping. Regarding solar applications, one of the most remarkable results was obtained with $\text{NaYF}_4:\text{Er}^{3+}$. The addition of a $\text{NaYF}_4:20\%\text{Er}^{3+}$ upconversion layer onto the rear side of a bifacial silicon solar cell resulted in a combined device (cell-upconverter) showing a slight improved response in the infrared region [98].

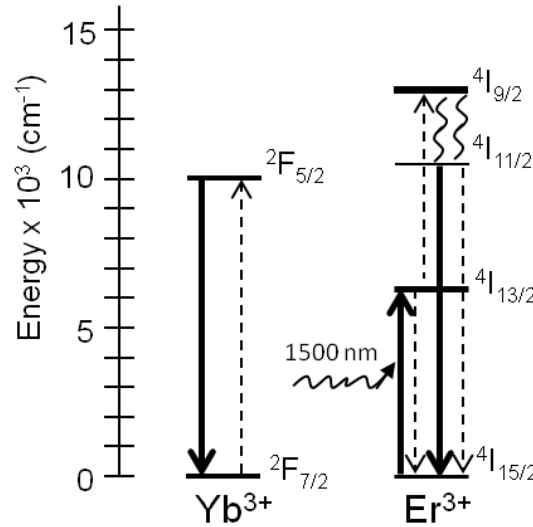


Figure 1.15: Upconversion mechanism with Er^{3+} and Yb^{3+} ions. The absorption takes place at 1500 nm ($^4\text{I}_{15/2} \rightarrow ^4\text{I}_{13/2}$). Solid arrows represent excitation and emission transitions; dashed arrows represent energy transfer processes and curved lines represent non-radiative relaxations.

As mentioned before, Yb^{3+} ions are promising activator ions for Si-based PV applications due to the spectral match between the Yb^{3+} emission and the silicon cell absorption. Thus, the codoping with Er^{3+} and Yb^{3+} ions has also been investigated for solar upcon-

verters [96,97]. Erbium acts as a sensitizer absorbing photons at 1500 nm ($^4I_{15/2} \rightarrow ^4I_{13/2}$) to eventually transfer its energy to Yb^{3+} ions (Fig.1.14). For that, a succession of energy transfers is needed. After absorption at the $^4I_{13/2}$ level, a first energy transfer takes place between Er^{3+} ions [$\text{Er}^{3+}(^4I_{13/2} \rightarrow ^4I_{15/2})$ to $\text{Er}^{3+}(^4I_{13/2} \rightarrow ^4I_{9/2})$]. This first transfer is then followed by multiphonon relaxation ($^4I_{9/2} \rightarrow ^4I_{11/2}$) and consecutive energy transfer to Yb^{3+} ions [$\text{Er}^{3+}(^4I_{11/2} \rightarrow ^4I_{15/2})$ to $\text{Yb}^{3+}(^2F_{7/2} \rightarrow ^2F_{5/2})$]. Therefore, codoping with Yb^{3+} leads to an increase of the upconversion luminescence in the near-infrared spectral region (around 1 μm). This is indeed the advantage of the codoping in comparison to the single Er^{3+} doping [96].

Downconversion of high energy photons

The same way that long wavelengths can be accessed through upconversion mechanisms, the UV-visible solar spectral range can be used in a more efficient way by associating downconverters to silicon cells. Downconversion is a term describing the shift of a light radiation from high energy to lower energy. Some authors use “downconversion” to denote the splitting of a high energy photon into several lower energy photons (processes with luminescent quantum yield $\text{LQY} > 1$). We understand, nevertheless, the concept in a broader sense, i.e. referring to any down shifting mechanism including those with quantum efficiency lower than 1. The splitting of a high energy photon into several lower energy photons is therefore a particular case of downconversion usually known as multiple photon emission (MPE) or *downconversion quantum cutting*.

The use of downconversion mechanisms to improve the Si solar cells efficiency can be envisioned in two ways. On the one hand, the use of downconversion as simple downshift could be useful to enhance the poor response of the Si cells in the blue and UV region [41] (Fig.1.16). This poor response is not due to the silicon absorption profile but to the absorption of the short-wavelength photons by the TCO (transparent conducting oxide), a film located in the front side of the cell playing the role of ohmic contact for carrier transport.

Kawano et al. showed an improvement of 5% in the efficiency of a CdS/CdTe cell when combining a Si solar cell with a downconversion layer of $\text{KMgF}_3:\text{Eu}^{3+}$ [99,100]. In spite of this result, the response of the cells is expected to be enhanced by the development of new ohmic contacts showing good transparency in the blue and VUV region.

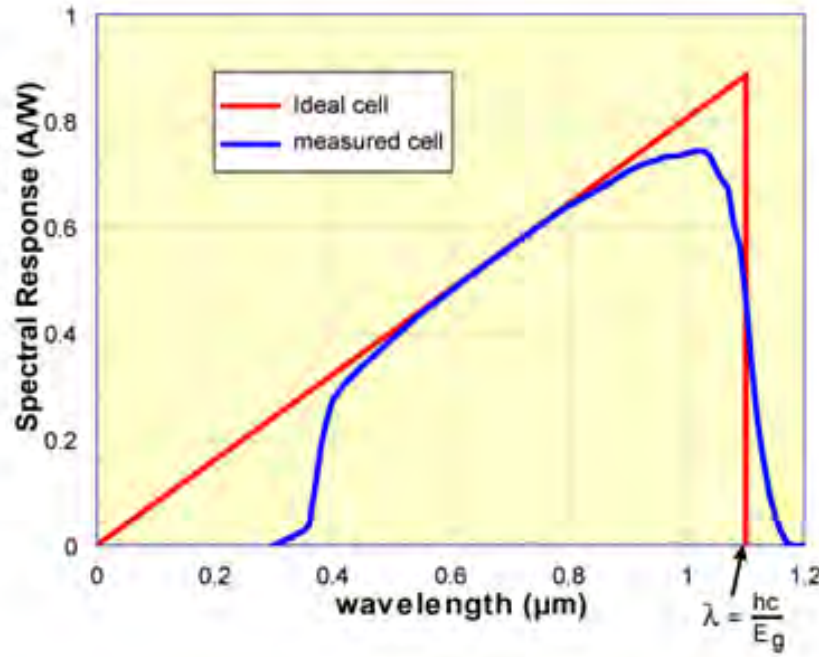


Figure 1.16: Silicon cell response.

On the other hand, the interest of dividing the upcoming photons into several lower energy photons by downconversion quantum cutting is evident since it leads to the generation of multiple electron-hole pairs per incident photon reducing, at the same time, thermalization losses. The possibility of quantum yields greater than unity was firstly suggested by Dexter in 1957 [101].

Most systems showing multiple photons emission consist of host-materials doped with one or more impurity ions. Absorption takes place either via the host-material or within the impurities and then, the energy absorbed can lead to the direct emission of several lower energy photons by the same luminescent center (photon cascade emission (PCE)); energy transfer (ET) to a different center and emission from both donor and acceptor; emission to an intermediate level and subsequent energy transfer (ET) to another impurity; excitation of two acceptors through two consecutive energy transfers (2-ET); or even, excitation of two acceptors simultaneously through a single cooperative energy transfer. Fig.1.17 reviews the main MPE processes.

Early examples of quantum cutting in rare-earth doped materials resulted from the research on new phosphors for mercury-free fluorescent tubes and plasma display panels [102-104]. In both applications, a noble gas discharge is used to generate VUV radiation, which is then converted into visible light by a luminescent material or phosphor. However,

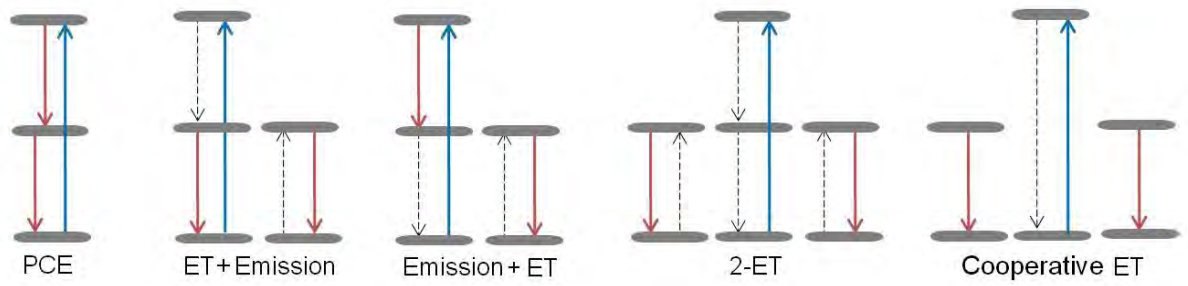


Figure 1.17: Overview of downconversion quantum cutting mechanisms. Absorption and emission processes are indicated by solid arrows and energy transfers by dashed arrows. Horizontal lines are real existing energy levels. The efficiency of the processes decreases from left to right.

during the energy conversion, half of the energy of the VUV photon is lost. Quantum cutting appeared then as a promising mechanism to reduce these energy losses since it allows to split the VUV photons into two visible photons. One of the first quantum cutters to be reported was $\text{YF}_3\text{:Pr}^{3+}$ [105,106]. In this material, upon VUV excitation in the $4f5d$ levels of Pr^{3+} , it was observed that the relaxation of Pr^{3+} could take place in two steps, both resulting in the emission of a visible photon (PCE). The most successful VUV to visible quantum cutters were nevertheless obtained with systems showing two consecutive energy transfers. This is the case of $\text{LiGdF}_4\text{:Eu}^{3+}$ and $\text{BaF}_2\text{:Gd}^{3+}\text{-Eu}^{3+}$, with quantum efficiencies (QE) of 190% and 194% respectively [69,104]. In both cases, upon VUV excitation of Gd^{3+} , two visible photons are emitted by Eu^{3+} ions as a result of an efficient two-step energy transfer process $\text{Gd}^{3+} \rightarrow \text{Eu}^{3+}$. The $\text{Gd}^{3+}\text{-Eu}^{3+}$ couple remains thus nowadays among the most successful quantum cutting systems.

In recent years, the promising prospect of downconverters for silicon solar cells has intensified investigations on quantum cutting systems. In contrast with the case of phosphors, this application requires converting UV and visible photons into near-infrared (NIR) photons. For that purpose, energy transfer processes within several ($\text{RE}^{3+}\text{-Yb}^{3+}$) couples have been investigated. As mentioned earlier, the choice of trivalent ytterbium as the acceptor in a downconverter devoted to Si solar cells has been widely justified. However, the choice of a suitable donor able to transfer efficiently its energy so as to obtain two excited Yb^{3+} ions appears to be far more complicated. We are now going to review the most remarkable examples of $\text{RE}^{3+}\text{-Yb}^{3+}$ codoped quantum cutters.

First order quantum cutting processes

Praseodymium appears to be an interesting candidate to transfer its energy to neighboring Yb^{3+} ions (Fig.1.18) since $^3\text{P}_0$ is located at 20000 cm^{-1} approximately and $^1\text{G}_4$ around 10000 cm^{-1} . Once excited, the depopulation of the $^3\text{P}_0$ level can take place through two consecutive energy transfers from Pr^{3+} to Yb^{3+} :

- $\text{Pr}^{3+}(^3\text{P}_0 \rightarrow ^1\text{G}_4)$ to $\text{Yb}^{3+}(^2\text{F}_{7/2} \rightarrow ^2\text{F}_{5/2})$
- $\text{Pr}^{3+}(^1\text{G}_4 \rightarrow ^3\text{H}_4)$ to $\text{Yb}^{3+}(^2\text{F}_{7/2} \rightarrow ^2\text{F}_{5/2})$.

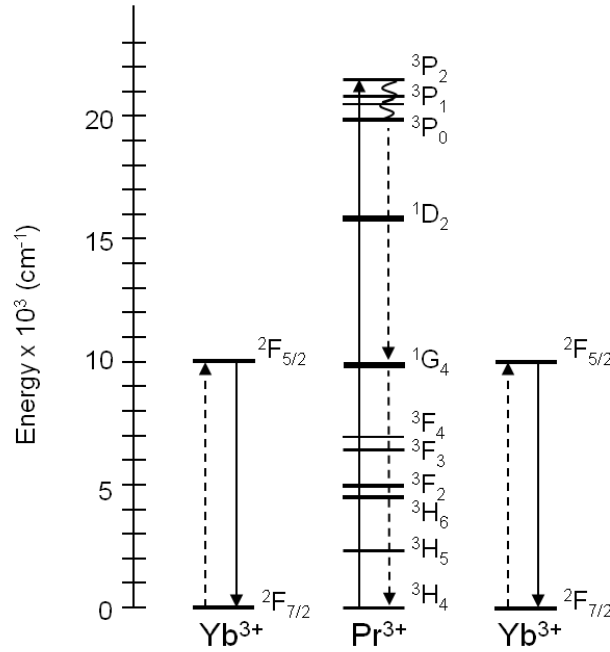


Figure 1.18: Quantum cutting with Pr^{3+} - Yb^{3+} .

The absorption of a blue photon in the $^3\text{P}_J$ levels leads, in an ideal situation, to the excitation of two Yb^{3+} ions and to the emission of two NIR photons. The energy transfers in the Pr^{3+} - Yb^{3+} system have been investigated in different host materials such as SrF_2 [107], LaF_3 [108] YF_3 [109], LiYF_4 [110], $\text{GdAl}_3(\text{BO}_3)_4$ [111], $\text{La}_2\text{BaZnO}_5$ [112] and glasses [113]. These studies reveal an efficient first step of the process (1), depopulating the $^3\text{P}_0$ level and transferring energy to Yb^{3+} ions. However, in most cases, very little information about the second step (2) is provided. The efficiency of the second energy transfer will be discussed in details in Chapter 2 along with the efficiency of the whole quantum cutting process for the Pr^{3+} - Yb^{3+} codoping.

The rare-earth couples $\text{Er}^{3+}\text{-Yb}^{3+}$ and $\text{Nd}^{3+}\text{-Yb}^{3+}$ have been also investigated as candidates for visible to NIR cutting. $\text{Er}^{3+}\text{-Yb}^{3+}$ is a well-known codoping which has been used for various applications such as EDFA (Erbium Doped Fiber Amplifiers) or upconversion as discussed in the previous section (1.5.3). For downconversion, Er^{3+} ions present a level scheme allowing, in principle, two resonant energy transfers from Er^{3+} to Yb^{3+} ions i.e. $\text{Er}^{3+}(^4\text{F}_{7/2} \rightarrow ^4\text{I}_{11/2})$ to $\text{Yb}^{3+}(^2\text{F}_{7/2} \rightarrow ^2\text{F}_{5/2})$ and $\text{Er}^{3+}(^4\text{I}_{11/2} \rightarrow ^4\text{I}_{15/2})$ to $\text{Yb}^{3+}(^2\text{F}_{7/2} \rightarrow ^2\text{F}_{5/2})$ (Fig.1.19.a). However, the small energy gap between the $^4\text{F}_{7/2}$ and the $^4\text{H}_{11/2}$ levels is such that multiphonon relaxation is a much more efficient relaxation path for Er^{3+} ions than the energy transfer to Yb^{3+} ions [114]. Thus, in order to get reasonable efficiency results, quantum cutting with the $\text{Er}^{3+}\text{-Yb}^{3+}$ codoping requires extremely low-phonon hosts as it was demonstrated with $\text{Er}^{3+}\text{-Yb}^{3+}$ codoped $\text{Cs}_3\text{Y}_2\text{Br}_9$ [115]. In the case of $\text{Nd}^{3+}\text{-Yb}^{3+}$, similar conclusions can be drawn. A two-step quantum cutting process is in theory possible with Nd^{3+} and Yb^{3+} ions (Fig.1.19.b). However, very low energy transfer efficiencies have been reported so far because of the very strong multiphonon relaxations endured by Nd^{3+} ions from the $^4\text{G}_{9/2}$ level [116].

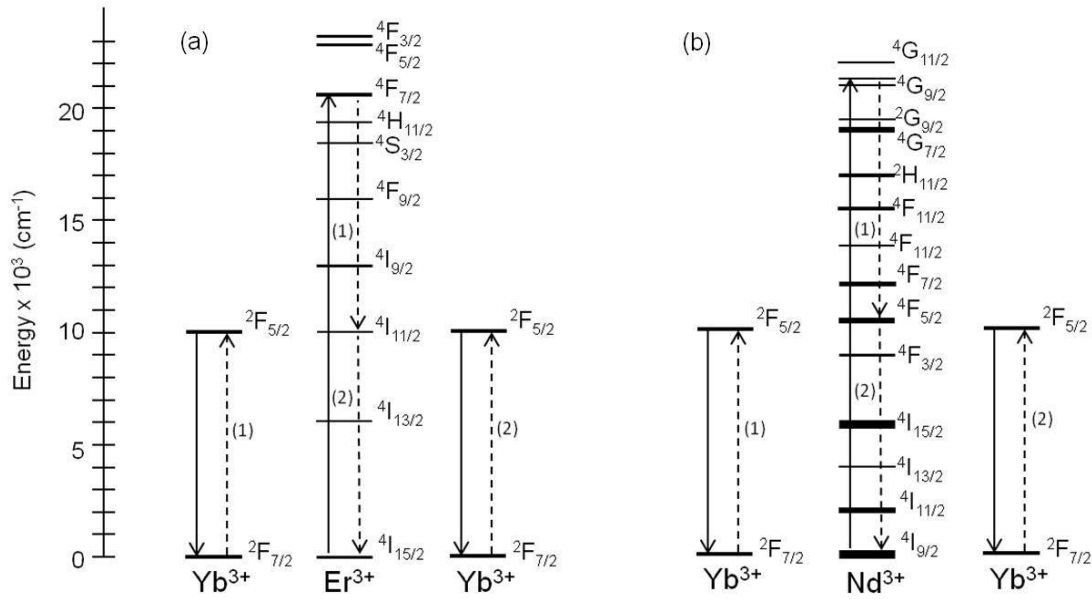


Figure 1.19: (a) QC with $\text{Er}^{3+}\text{-Yb}^{3+}$ ions; (b) QC with $\text{Nd}^{3+}\text{-Yb}^{3+}$ ions.

Second order quantum cutting processes

Among the rare-earth doped systems which have been considered suitable to get two NIR photons per visible photon, the $\text{Tb}^{3+}\text{-Yb}^{3+}$ codoping was the first to be proposed

[117] and still remains one of the most investigated [118-121]. The $\text{Tb}^{3+} {}^5\text{D}_4 \rightarrow {}^7\text{F}_6$ transition is located at approximately twice the energy of the $\text{Yb}^{3+} {}^2\text{F}_{5/2} \rightarrow {}^2\text{F}_{7/2}$ transition and, as displayed in Fig.1.20.a, there are no Tb^{3+} levels energetically resonant with the Yb^{3+} transition. Thus, the depopulation of one Tb^{3+} ion at the ${}^5\text{D}_4$ level can take place through three different paths: phonon-assisted energy transfer, accretive energy transfer and cooperative energy transfer [117]. Among them, the cooperative mechanism was demonstrated to be dominant. The spectral mismatch between the $\text{Tb}^{3+} {}^5\text{D}_4 \rightarrow {}^7\text{F}_6$ emission and the $\text{Yb}^{3+} {}^2\text{F}_{7/2} \rightarrow {}^2\text{F}_{5/2}$ absorption is too large for a phonon-assisted energy transfer. On the other hand, through the accretive and cooperative mechanisms two Yb^{3+} ions get excited simultaneously after relaxation of one Tb^{3+} ion at the ${}^5\text{D}_4$ level. There is however a difference which is that the energy transfer occurs through a virtual energy level located at the donor ion in the case of the cooperative process, while, for the accretive process the virtual level is located at one of the acceptor ions so that two transfer paths are possible in this case. Cooperative quantum cutting has been demonstrated in different host materials such as $\text{YPO}_4:\text{Tb}^{3+}-\text{Yb}^{3+}$ [117] and $\text{Y}_2\text{O}_3:\text{Tb}^{3+}-\text{Yb}^{3+}$ [122]. Besides, it has been reported with other codopings as for example Tm^{3+} and Yb^{3+} ions [75,113] (Fig.1.20.b).

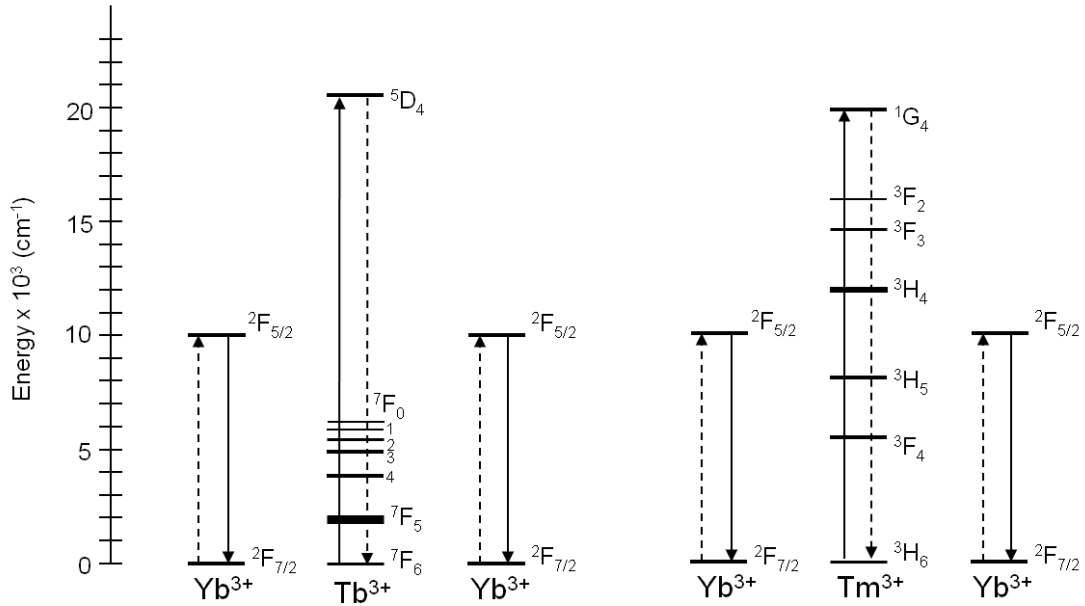


Figure 1.20: (left) Cooperative QC with $\text{Tb}^{3+}-\text{Yb}^{3+}$ ions and (right) $\text{Tm}^{3+}-\text{Yb}^{3+}$ ions.

In a general way, the main disadvantage of any cooperative system is precisely the fact that it is based on a second order process involving a three-body interaction. The cooperative processes are between four and five orders of magnitude less efficient than any

two-step first-order process [110]. Thus, they only take place in systems such as Tb^{3+} - Yb^{3+} for which, first-order two-step processes are forbidden or impossible because of the absence of resonant energy transfer paths (1.20.a).

On the other hand, there are also advantages associated to the cooperative mechanism. As seen, an efficient cooperative energy transfer assures the excitation of acceptors per photon absorbed by the donors. On the contrary, in first-order processes, the existence of two steps may create situations in which one of the steps is extremely efficient but not the other one. Thus, in spite of having a lower probability, an effective cooperative process might be eventually more interesting for real applications than an inefficient first-order system. This explains the fact that cooperative systems have been attracting as much attention as first order systems for quantum cutting applications.

Besides the Tb^{3+} - Yb^{3+} couple, cooperative quantum cutting has been investigated with codopings such as Ce^{3+} - Yb^{3+} [123-127] and Bi^{3+} - Yb^{3+} [128-130]. The system Ce^{3+} - Yb^{3+} uses the $4f \rightarrow 5d$ absorption of Ce^{3+} assuming subsequent cooperative energy transfer from one Ce^{3+} to two neighboring Yb^{3+} ions. The scheme is very similar with Bi^{3+} and Yb^{3+} ions. Therefore, upon VUV absorption by a broad excitation band owing to the $6s^2(^1S_0) \rightarrow 6s6p(^3P_1)$ transition of Bi^{3+} ions, cooperative energy transfer to Yb^{3+} is expected. The main advantage of these two codopings in comparison with the Tb^{3+} - Yb^{3+} codoping is that they show enhanced absorption. The absorption cross-section of the rare-earth $4f \rightarrow 5d$ transitions is several orders of magnitude greater than the absorption cross-section of the $4f \rightarrow 4f$ transitions. Moreover, the absorption spectrum of Bi^{3+} ions is also much wider than that of the narrow $4f \rightarrow 4f$ transitions of rare-earth ions. However, in spite of this advantage, the occurrence of a cooperative transfer from Ce^{3+} or Bi^{3+} to Yb^{3+} seems unclear since the possibility of charge transfer cannot be excluded. The Ce^{3+} 5d states have a higher energy than that usually attributed to the ytterbium charge transfer band (CTB) [131] and the same occurs with the 6s6p states of Bi^{3+} . Thus, the energy transfer from Ce^{3+} and Bi^{3+} to the ytterbium charge transfer band would be, in principle, more favorable than a cooperative energy transfer to the Yb^{3+} 4f states. In consequence, the NIR emission from Yb^{3+} upon VUV excitation does not constitute a conclusive proof for the cooperative mechanism since, as seen, this emission can be also related to other transfer paths.

1.6 Conclusions Chapter 1

A review of the principal PV technologies has been performed in this chapter concluding that the Si-based PV technologies are the most developed nowadays so as to the ones presenting a greater potential to assure solar power supply in the near future. The so-called third generation of solar cells, devoted to the development of more efficient and less expensive PV devices, points two main approaches in order to overcome the challenges confronted by the current PV technologies. The first one is the development of ultra-high efficiency multiple junction cells from a stacking of different semiconductors (typically III-V). As second approach, implementing the already existing PV technologies with efficient conversion layers is proposed with the aim of adapting the energy of the solar radiations to the cell absorption.

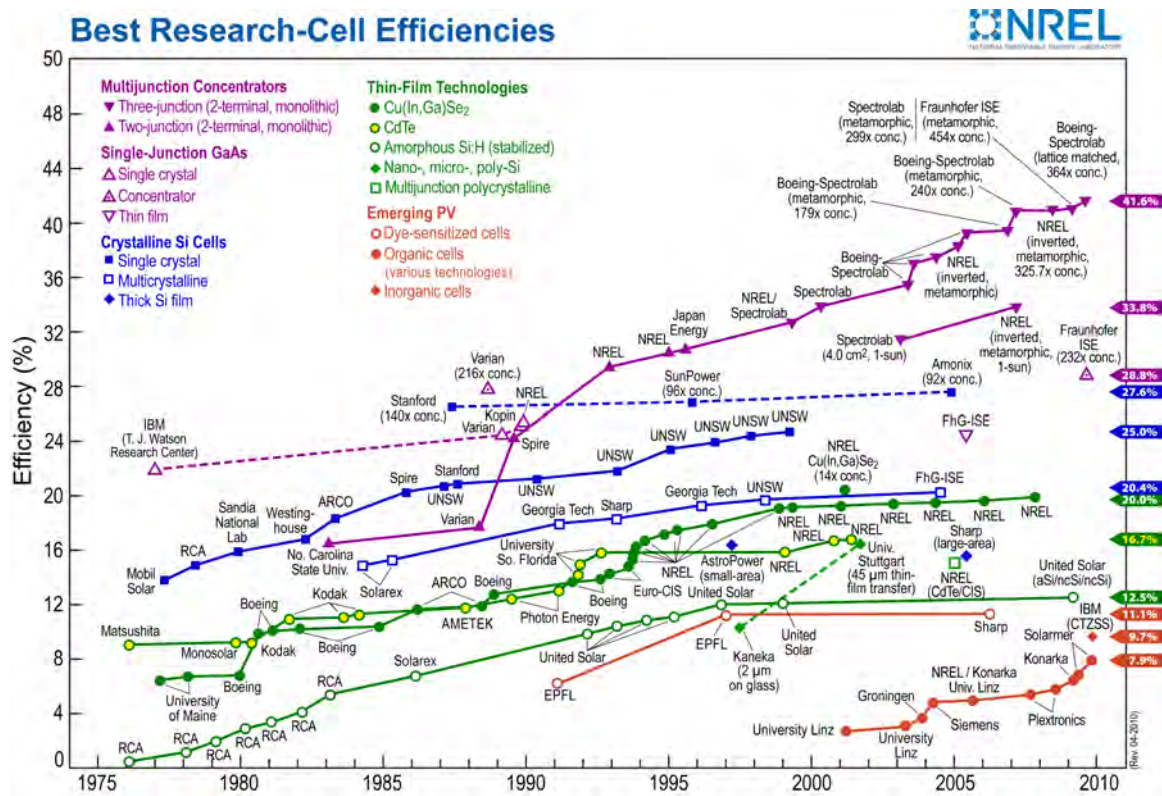


Figure 1.21: Research cells efficiency (updated results).

Both approaches are planned to reach high efficiencies under concentrated sunlight. The multi-junction research cells already hold the world record efficiency among the PV technologies as displayed in Fig.1.21. On the other hand, achieving efficiencies around 50%

is planned under concentrated sunlight by combining a classical Si cell with performing upconverters and downconverters.

Among several types of luminescent centers, the trivalent rare-earth ions have been shown suitable to take part in luminescent solar converters (Table 1.2). In particular, the potentiality for upconversion and downconversion quantum cutting applications of rare-earth systems such as $\text{Er}^{3+}\text{-Yb}^{3+}$, $\text{Pr}^{3+}\text{-Yb}^{3+}$ or $\text{Tb}^{3+}\text{-Yb}^{3+}$ was discussed.

Quantum Cutting in Pr^{3+} - Yb^{3+} codoped KY_3F_{10}

2.1 Introduction

In this chapter, we present spectroscopic investigations along with the corresponding simulations of the two-step quantum cutting process with Pr^{3+} and Yb^{3+} ions using KY_3F_{10} as the host material. The unit cell of KY_3F_{10} is a fluorite-related $2 \times 2 \times 2$ face centered cubic structure in which the $[\text{KY}_3\text{F}_8]^{2+}$ and $[\text{KY}_3\text{F}_{12}]^{2-}$ ionic complexes alternate along the cube axes. As displayed in Fig.2.1, Y^{3+} ions occupy cube face centre positions which coincide with the vertices of a regular octahedron; K^+ ions are at the cube corners and F^- ions are positioned within the K^+ cubes giving rise to the $[\text{KY}_3\text{F}_8]^{2+}$ and $[\text{KY}_3\text{F}_{12}]^{2-}$ complexes alternatively (Fig.2.1). The lattice constant is found to be 11.544 Å at room temperature [132], with the side of the K^+ cubes being half of the lattice constant i.e. 5.772 Å. Trivalent rare-earth ions introduced into the KY_3F_{10} lattice replace the Y^{3+} ions resulting in a C_{4v} symmetry centre. The lattice is transparent over a wide spectral range (0.2-8 μm [133]), thermally and chemically stable as well as isotropic [134]. Thus, it is an ideal host for optical studies and laser applications. Comprehensive spectroscopic studies on trivalent rare-earth ions within KY_3F_{10} crystals have been performed including for instance Pr^{3+} [135-141], Sm^{3+} [73], Eu^{3+} [142-144], Er^{3+} [145], Tm^{3+} [70,146], Ho^{3+} [147] and Yb^{3+} [148,149]. Energy transfer processes between rare-earth ions in KY_3F_{10} have also been reported [150-154]. As a fluoride material, its relatively low phonon energy (420 cm^{-1}) makes it particularly suitable for applications involving energy transfers. Thus, a low phonon energy host lattice reduces non-radiative relaxations via multiphonon emissions which favours high fluorescence quantum yields and efficient energy transfers.

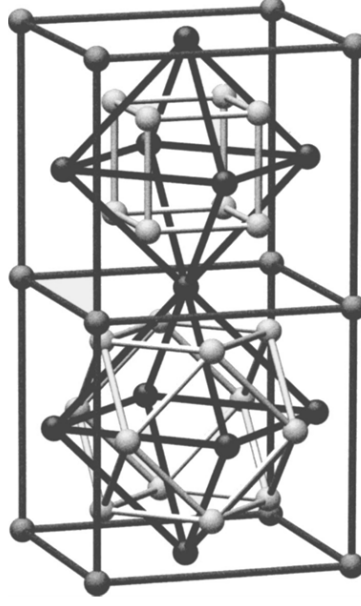


Figure 2.1: KY_3F_{10} primitive cell. The darkest spheres represent yttrium or rare-earth ions, the lightest ones fluorine, and the intermediate ones potassium. The structural modules $[\text{KY}_3\text{F}_8]^{2+}$ and $[\text{KY}_3\text{F}_{12}]^{-2}$ appear in the upper and lower cubes respectively. Four primitive cells placed so as to alternate the $[\text{KY}_3\text{F}_8]^{2+}$ and $[\text{KY}_3\text{F}_{12}]^{-2}$ ionic complexes are needed to form the KY_3F_{10} unit cell.

The codoping of KY_3F_{10} with Pr^{3+} and Yb^{3+} ions is here investigated as a promising candidate for visible to near-infrared quantum cutting through two consecutive energy transfers from Pr^{3+} to Yb^{3+} . In a general way, the level structure associated with Pr^{3+} and Yb^{3+} ions offers several energy transfer paths that have been analysed for different applications. For instance, Pr^{3+} ions present a $1.3\ \mu\text{m}$ infrared emission ($^1\text{G}_4 \rightarrow ^3\text{H}_5$) which is highly attractive for the development of new optical amplifiers [155]. Direct pumping of the Pr^{3+} ions at the $^1\text{G}_4$ level is inefficient because of the extremely low $^3\text{H}_4 \rightarrow ^1\text{G}_4$ absorption. Nevertheless, the $1.3\ \mu\text{m}$ emission from Pr^{3+} can be exploited by using Yb^{3+} ions as sensitizers [156,157].

On the other hand, exciting the Yb^{3+} ions can lead to upconverted emissions from Pr^{3+} ions as displayed in Fig.2.2. Upconversion with Pr^{3+} and Yb^{3+} ions has been reported in various host materials such as YLiF_4 [80], KPbCl_5 [87], BaY_2F_8 [79] or glasses [158]. Pr^{3+} - Yb^{3+} codoped KY_3F_{10} has also been previously investigated as a promising upconversion material. The study accomplished by Kim et al. [85] revealed fluorescence signal from $^3\text{P}_0$ under strong infrared (IR) excitation.

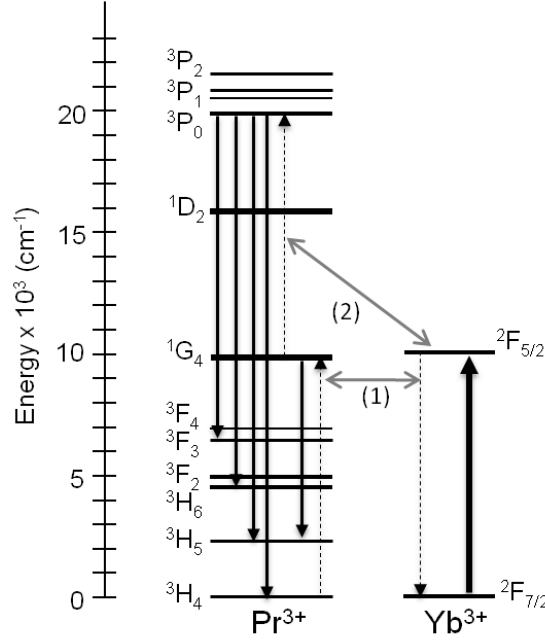


Figure 2.2: Selection of energy transfer processes within the Pr^{3+} - Yb^{3+} system: (1) Yb^{3+} sensitized $1.3 \mu\text{m}$ praseodymium emission. (2) Resonant energy transfer leading to up-converted emissions from Pr^{3+} upon Yb^{3+} excitation. Solid arrows represent absorption and emission transitions. Dashed arrows indicate energy transfer paths.

As shown in Chapter 1, downconversion quantum cutting can be obtained with Pr^{3+} and Yb^{3+} ions through two consecutive energy transfers from Pr^{3+} to Yb^{3+} and subsequent emission from the excited Yb^{3+} ions (Fig.1.18). As mentioned earlier, the mechanism was previously investigated with a variety of host materials (Section 1.5.3). Nevertheless, to our knowledge, this study is the first investigation of the quantum cutting mechanism with Pr^{3+} and Yb^{3+} ions using KY_3F_{10} as host material.

2.2 Experimental methods

A series of Pr^{3+} - Yb^{3+} doped KY_3F_{10} single crystals were grown in our laboratory by using the Bridgman-Stockbarger technique [159]. Pure KF , YF_3 and PrF_3 and YbF_3 powders were used as raw materials. The starting powders are introduced in a cylindrical graphite crucible within the growth chamber. A reasonable vacuum ($<10^{-5}$ mbar) is achieved and then, a mixture of Argon and CF_4 gases is injected to reduce oxygen and water pollution. The temperature, which had been raised during the vacuum process, is next increased beyond the raw materials melt temperature. Once a homogeneous melt

is achieved, the graphite crucible moves through an axial temperature gradient to start the crystal growth. The cylindrical graphite crucible presents a conic edge finished by a narrow tube (2 mm diameter). This tube assures the growth of a single crystal from the beginning of the pulling process since the crystallization starts on it. The pulling rate is about of 4-5 mm/h. After growth, the crystals are cooled down to room temperature within the growth chamber in order to avoid thermal shock.

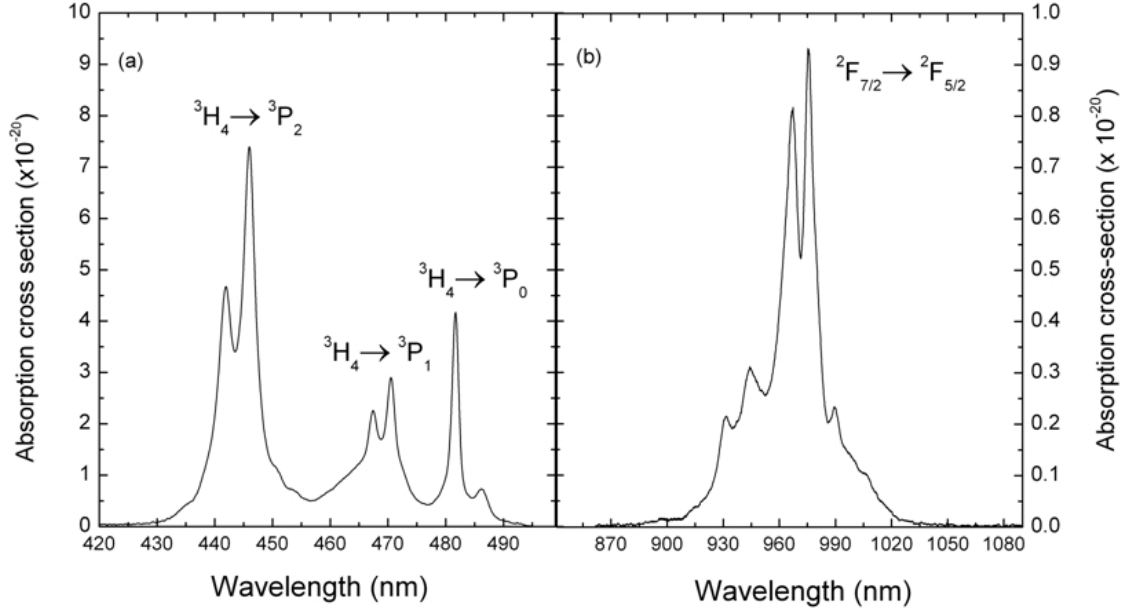


Figure 2.3: Room temperature absorption spectra in $\text{KY}_3\text{F}_{10}:\text{Pr}^{3+}\text{-Yb}^{3+}$ (a) $^3\text{H}_4 \rightarrow ^3\text{P}_J$ ($J = 0, 1, 2$) absorptions within the 420-500 nm wavelength range (b) Yb^{3+} absorption spectrum.

The dopant concentration was measured by inductively coupled plasma (ICP) technique, in the CNRS Analyse Central Service (SCA, Vernaison). Another method to assess the dopant concentrations in the crystals was by absorption measurements using calibrated reference samples as displayed in Fig.2.3. Both methods demonstrated real concentrations very close to the nominal concentrations in the melt as displayed in Table 2.1. The crystals were afterwards prepared as powder samples for spectroscopic experiments.

The absorption spectra were performed with a Perkin-Elmer Lambda 1050 spectrophotometer with a wide wavelength range going from 285 to 3300 nm. For the emission spectra, Pr^{3+} ions were excited into the $^3\text{P}_2$ level with a blue laser diode (Nichia-NDHB510APAE1 50 mW) emitting at 442 nm while Yb^{3+} ions were pumped at 940 nm ($^2\text{F}_{5/2}$) by using a Ti-Sa laser (Coherent 890). The sample fluorescence was dispersed by

Table 2.1: $\text{KY}_3\text{F}_{10}:\text{Pr}^{3+}\text{-Yb}^{3+}$ investigated samples. 1%at. represents 1.57×10^{20} at/cm³.

Nominal concentrations	Real concentrations
0.5%Pr ³⁺	0.5%Pr ³⁺
0.5%Pr ³⁺ -1%Yb ³⁺	0.45%Pr ³⁺ -1.0%Yb ³⁺
0.5%Pr ³⁺ -5%Yb ³⁺	0.45%Pr ³⁺ -5.0%Yb ³⁺
0.5%Pr ³⁺ -10%Yb ³⁺	0.50%Pr ³⁺ -10.5%Yb ³⁺
0.5%Pr ³⁺ -20%Yb ³⁺	0.45%Pr ³⁺ -19.5%Yb ³⁺

a Jobin-Yvon HSR2 monochromator (grating with 1200 l/mm and blazed at 500 nm; 600 l/mm and blazed at 1 μm ; or 300 l/mm blazed at 2 μm) and detected using a standard lock-in amplifier technique. Fluorescence decays and time-resolved spectra were carried out using an optical parametric oscillator (OPO GWU C-355) pumped by the third harmonic (355 nm) of a Nd:YAG laser (Spectron 404G). After dispersion by a 0.25m monochromator (Oriel 77200 series), the luminescent transient signals obtained after pulsed excitation, were fed into a digital oscilloscope (Tektronix TDS 3032) and averaged out to improve the signal-to-noise ratio. Different detectors were used depending on the detection requirements. Hamamatsu R9110 and R5108 photomultipliers were employed to detect the luminescence signals in the visible and NIR regions while a Peltier-cooled InGaAs detector (Hamamatsu G5852-01) was used in the IR range, beyond 1.1 μm . Detectors were associated to preamplifiers if needed in order to increase the output signal. All the experimental recordings were afterwards corrected from the setup spectral response.

2.3 Optical spectroscopy experiments

In order to have a good understanding of the downconversion quantum cutting mechanism in $\text{KY}_3\text{F}_{10}:\text{Pr}^{3+}\text{-Yb}^{3+}$, two series of experiments were performed. On the one hand, praseodymium emission spectra from $^3\text{P}_0$ and $^1\text{G}_4$, as well as the downconverted ytterbium emission were recorded upon $\text{Pr}^{3+}(^3\text{P}_2)$ excitation at 442 nm. A direct comparison of the evolution of the emission spectra could be performed since the excitation and detection geometry were kept identical for all samples and that all samples were prepared as powders having the exact same geometry. The evolution of the $^3\text{P}_0$, $^1\text{G}_4$ and Yb^{3+} emission spectra displayed in Fig.2.4 with the Yb^{3+} concentration provided the first signs of energy transfer in the $\text{Pr}^{3+}\text{-Yb}^{3+}$ system.

The second series of experiments was performed by pumping the Yb^{3+} ions at 940 nm. Under IR pumping, Yb^{3+} emission along with Pr^{3+} infrared emissions are observed. This series of experiments provides extra information about the second step of the quantum cutting process, $\text{Pr}^{3+}({}^1\text{G}_4 \rightarrow {}^3\text{H}_4)$ to $\text{Yb}^{3+}({}^2\text{F}_{7/2} \rightarrow {}^2\text{F}_{5/2})$, as well as the reciprocal $\text{Yb}^{3+}({}^2\text{F}_{5/2} \rightarrow {}^2\text{F}_{7/2})$ to $\text{Pr}^{3+}({}^3\text{H}_4 \rightarrow {}^1\text{G}_4)$ energy transfer. The existence of a back-transfer is clear since the $\text{Yb}^{3+}({}^2\text{F}_{5/2} \rightarrow {}^2\text{F}_{7/2})$ emission and the $\text{Pr}^{3+}({}^3\text{H}_4 \rightarrow {}^1\text{G}_4)$ absorption transitions present good spectral overlap.

The study of the Pr^{3+} and Yb^{3+} dynamics was also performed by exciting the samples both at 442 nm and 940 nm. The evolution of the fluorescence lifetimes for the ${}^3\text{P}_0$, ${}^1\text{G}_4$ and Yb^{3+} levels can then be used to discuss the overall quantum efficiency (QE) of the quantum cutting process.

2.3.1 Emission spectra

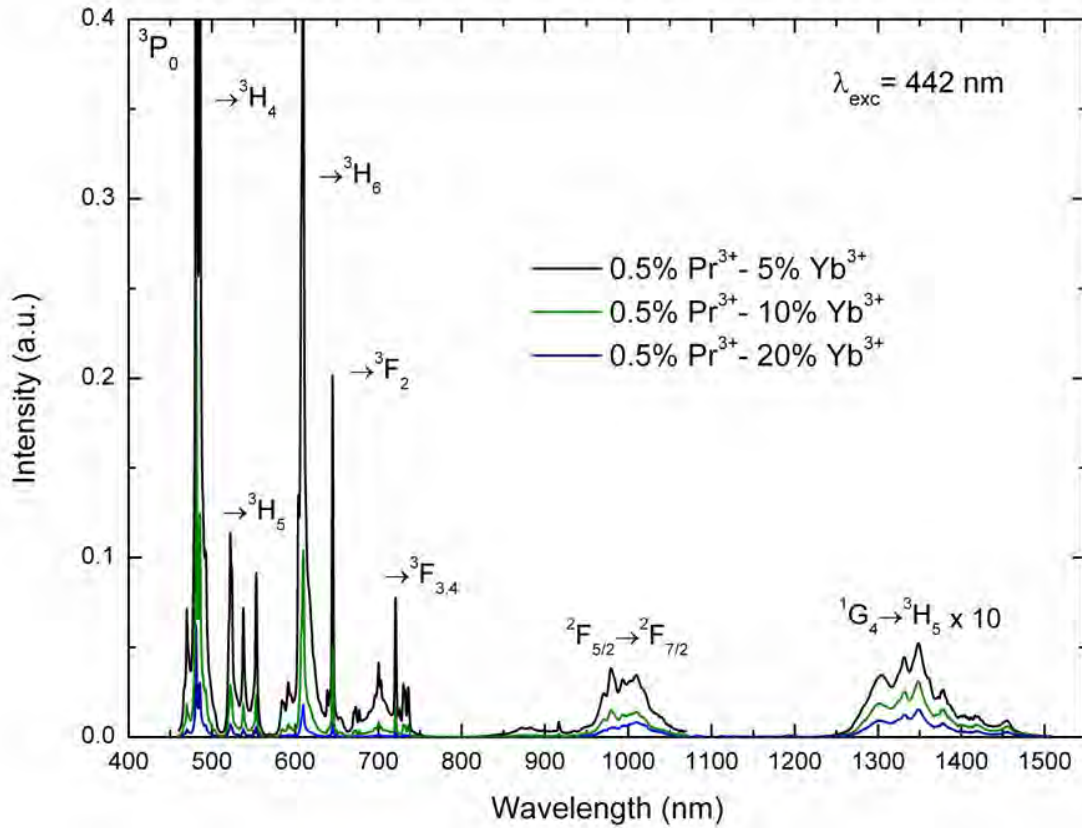


Figure 2.4: Room temperature emission spectra under laser diode excitation at 442 nm in KY_3F_{10} codoped 0.5% Pr^{3+} -5% Yb^{3+} (black); 0.5% Pr^{3+} -10% Yb^{3+} (green) and 0.5% Pr^{3+} -20% Yb^{3+} (blue).

Typical $\text{KY}_3\text{F}_{10}:\text{Pr}^{3+}-\text{Yb}^{3+}$ fluorescence spectra were recorded under laser diode excitation at 442 nm for different samples with the same 0.5%at. Pr^{3+} concentration and different Yb^{3+} concentrations. Once excited, ions in $^3\text{P}_2$ undergo a fast multiphonon decay to $^3\text{P}_0$. In Fig.2.4, the main transitions from the $^3\text{P}_0$ level can be observed. A larger band around 1 μm is assigned to the $\text{Yb}^{3+}:^2\text{F}_{5/2} \rightarrow ^2\text{F}_{7/2}$ emission and a weak band around 1.3 μm (with a 10 times factor) is identified as the $\text{Pr}^{3+}:^1\text{G}_4 \rightarrow ^3\text{H}_5$ transition. The infrared emission from Yb^{3+} under non resonant 442 nm excitation already constitutes a first evidence of energy transfer from Pr^{3+} to Yb^{3+} . For more details, Fig.2.5 presents normalized $^3\text{P}_0$ emission spectra between 580 and 670 nm. Two typical Pr^{3+} transitions can be easily identified peaking at 612 nm ($^3\text{P}_0 \rightarrow ^3\text{H}_6$) and at 644 nm ($^3\text{P}_0 \rightarrow ^3\text{F}_2$).

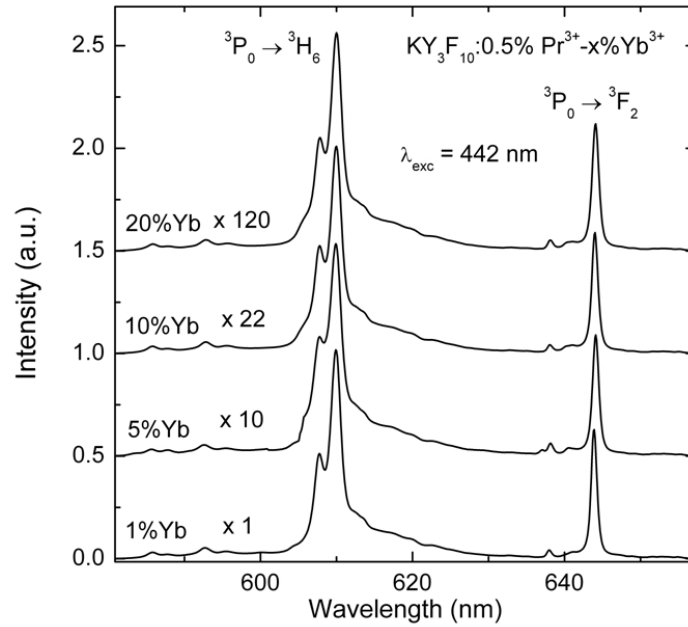


Figure 2.5: Room temperature $^3\text{P}_0$ emission spectra under blue excitation at 442 nm ($^3\text{P}_2$) in $\text{KY}_3\text{F}_{10}:0.5\%\text{Pr}^{3+}-x\%\text{Yb}^{3+}$ ($x=1, 5, 10, 20$). The spectra are normalized for the sake of clarity.

As expected for a single-site structure, the shape of the spectra remains the same even for a high Yb^{3+} concentration (20%) indicating that the Yb^{3+} doping does not distort the Pr^{3+} incorporation site significantly. The emission spectra displayed in Fig.2.5 are normalized and the evolution of the normalization factors (10, 22 and 120) shows a progressive quenching of the $^3\text{P}_0$ luminescence with the Yb^{3+} concentration. This large decrease of the Pr^{3+} emission intensity is clearly due to the cross-relaxation energy transfer from $\text{Pr}^{3+}(^3\text{P}_0 \rightarrow ^1\text{G}_4)$ to $\text{Yb}^{3+}(^2\text{F}_{7/2} \rightarrow ^2\text{F}_{5/2})$.

Regarding the Yb^{3+} emission, an important quenching of the luminescence intensity is also observed when the Yb^{3+} content increases (Fig.2.4). This Yb^{3+} quenching is usually associated to concentration-related processes resulting in the depopulation of the Yb^{3+} excited state. At high Yb^{3+} concentrations, concentration quenching due to energy migration among the Yb^{3+} ions followed by energy transfer to defects or other impurities in the host (*quenching centers*), is a well-known mechanism already reported in Yb^{3+} singly-doped KY_3F_{10} [160]. In a similar way in our system, energy migration among the Yb^{3+} ions may significantly increase the probability of Yb^{3+} to Pr^{3+} back-transfer since, according to the migration-assisted energy transfer models [161-163], the excitation energy jumps from one excited ytterbium to a neighboring one until it reaches a quenching center (in our case praseodymium ions) close enough to allow an efficient energy transfer. Thus, the quenching of the Yb^{3+} emission in the Pr^{3+} - Yb^{3+} system can be reasonably considered as partially due to migration-assisted back-transfer from Yb^{3+} to Pr^{3+} ions.

Considering finally the $^1\text{G}_4$ emission spectra at $1.3\ \mu\text{m}$ (Fig.2.4), the emission intensity is also observed to decrease with the Yb^{3+} concentration. The quenching of the $^1\text{G}_4$ emission can be related, in principle, to the second energy transfer $\text{Pr}^{3+}(^1\text{G}_4 \rightarrow ^3\text{H}_4)$ to $\text{Yb}^{3+}(^2\text{F}_{7/2} \rightarrow ^2\text{F}_{5/2})$ of the quantum cutting process leading to the excitation of a second Yb^{3+} ion. This result is a first-hand indication that the second energy transfer does take place despite the fact that the back-transfer from Yb^{3+} to Pr^{3+} is more probable when taking into account simple thermodynamic considerations. Indeed, the $^1\text{G}_4$ level is at lower energy than the $^2\text{F}_{5/2}$ level. Therefore, the back-transfer is more likely to occur than the second energy transfer of the QC process. However, this thermodynamic point of view does not encompass the acceptor concentrations which are very different for both energy transfers. An energy transfer rate W is usually described as $W = P \times N_A$ where N_A is the acceptor concentration and P the energy transfer parameter in $\text{cm}^{-3}\text{s}^{-1}$. If the parameter P is for instance 20 times smaller for the second energy transfer than for the back-transfer from Yb^{3+} to Pr^{3+} , the overall rate W will still be twice larger for the second energy transfer than for the back-transfer in a $\text{KY}_3\text{F}_{10}:0.5\%\text{Pr}^{3+}-20\%\text{Yb}^{3+}$ sample since the acceptor concentration is then 40 times larger for the Pr^{3+} to Yb^{3+} energy transfer.

In a general way, the transfer and back-transfer between $\text{Yb}^{3+}(^2\text{F}_{5/2})$ and $\text{Pr}^{3+}(^1\text{G}_4)$ in fluorides is similar to the case of the Tm^{3+} - Ho^{3+} codoping in which the $\text{Tm}^{3+}(^3\text{F}_4)$ and $\text{Ho}^{3+}(^5\text{I}_7)$ are coupled through back and forth energy transfers creating a thermal equilibrium between the two levels [164-166]. The coupling is even stronger in the case of the Pr^{3+} - Yb^{3+} codoping since the energy gap between the two levels of interest is smaller

than in the case of $\text{Tm}^{3+}\text{-Ho}^{3+}$. As a consequence, the forward and back energy transfer between $^1\text{G}_4$ and $^2\text{F}_{5/2}$ make the analysis of the emission from $^1\text{G}_4$ complicated as will be discussed further in the text.

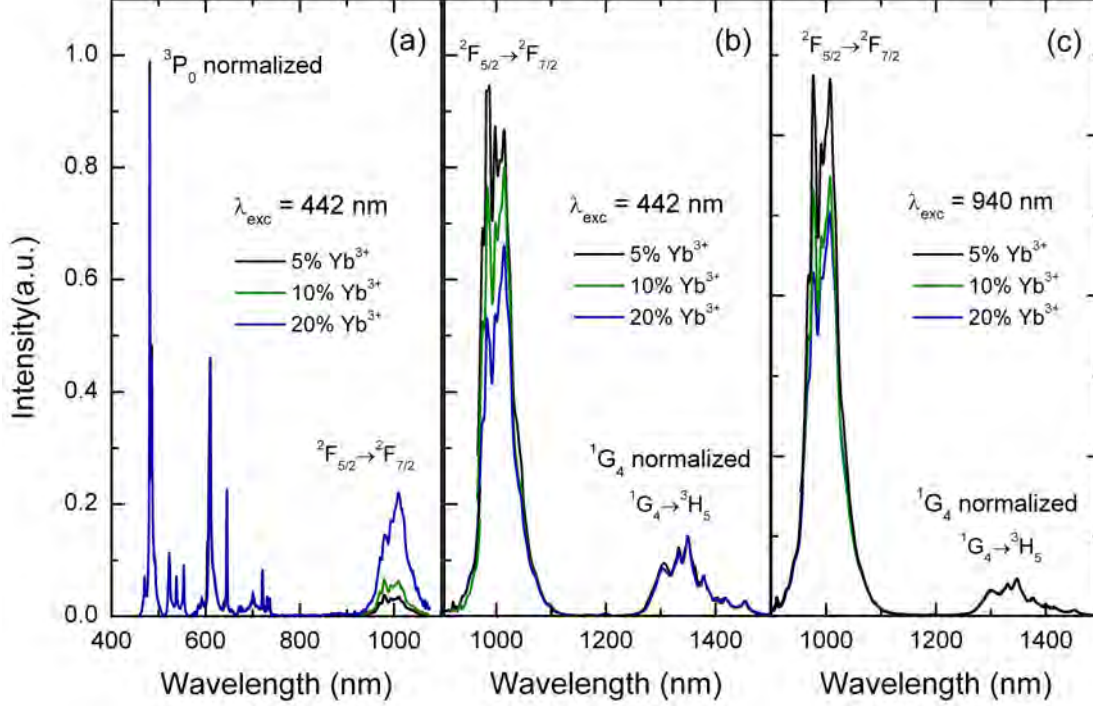


Figure 2.6: $\text{KY}_3\text{F}_{10}:0.5\%\text{Pr}^{3+}-x\%\text{Yb}^{3+}$ ($x = 5, 10, 20$) normalized emission spectra (a) $^3\text{P}_0$ and Yb^{3+} emissions with a normalization on the emission spectra from $^3\text{P}_0$, (b) Yb^{3+} and $^1\text{G}_4$ emissions under 442 nm excitation with a normalization on the spectra from $^1\text{G}_4$ and (c) Yb^{3+} and $^1\text{G}_4$ emissions under 940 nm excitation with a normalization on the spectra from $^1\text{G}_4$.

In order to get further insight into the effects of the first, second, and back transfers, the evolution of the Pr^{3+} and Yb^{3+} emissions were compared by normalizing the $^3\text{P}_0$ and $^1\text{G}_4$ emissions in all samples (Fig.2.6). As shown in Fig.2.6.a, the Yb^{3+} emission increases in comparison with the $^3\text{P}_0$ emission when increasing the Yb^{3+} concentration. This can be explained by the increasing efficiency of the first energy transfer. On the opposite, the Yb^{3+} emission decreases in comparison with the $^1\text{G}_4$ emission (Fig.2.6.b). This would indicate that the back-transfer could be more efficient than the second energy transfer. Very similar results were found for the Yb^{3+} and $^1\text{G}_4$ infrared emissions under 940 nm excitation (Fig.2.6.c). From these results, it appears that an energy balance exists between the forward and backward $^2\text{F}_{5/2} \leftrightarrow ^1\text{G}_4$ energy transfers whether the excitation occurs at 940 nm (Yb^{3+}) or at 442 nm (Pr^{3+}).

2.3.2 Decay curves

The 3P_0 , 1G_4 and Yb^{3+} fluorescence decays are presented in Fig.2.7 and the corresponding fluorescence lifetimes are summarized in Table 2.2. The study of the dynamics shows a decrease of all lifetimes with the Yb^{3+} content for the 3P_0 , 1G_4 and $^2F_{5/2}$ energy levels, both upon 442 nm and 940 nm excitations. This result is in agreement with the emission decrease observed previously in Fig.2.4 for the 3P_0 , 1G_4 and Yb^{3+} emission spectra. A special care was taken in the case of the Yb^{3+} excitation at 940 nm to keep the excitation density at a low level in order to avoid possible upconversion phenomena between ions in the 1G_4 and $^2F_{5/2}$ levels which would affect the dynamics. As mentioned earlier, the 3P_0 lifetime decrease is due to the first energy transfer while migration-assisted back-transfer processes participate to the quenching of the Yb^{3+} lifetime. The decrease of the 1G_4 lifetime (Fig.2.7) is another indication that the second step of the QC process from 1G_4 towards Yb^{3+} ions takes place despite previously discussed basic thermodynamic considerations. If this 1G_4 towards Yb^{3+} energy transfer did not take place, one should see in the simple case of Yb^{3+} excitation at 940 nm a rise time and a decay time in the 1G_4 dynamics reflecting the Yb^{3+} lifetime and the 75 μs intrinsic lifetime of the 1G_4 level. Fig.2.7 shows that it is not the case and that instead under Yb^{3+} excitation at 940 nm the 1G_4 and Yb^{3+} lifetimes are very much alike (Table 2.2).

Table 2.2: Experimental lifetimes. “rt” corresponds to the estimated rise times.

Sample	$\lambda_{exc} = 442 \text{ nm}$			$\lambda_{exc} = 940 \text{ nm}$	
level	$\tau_{3P0} (\mu s)$	$\tau_{1G4} (\mu s)$	$\tau_{2F5/2} (\mu s)$	$\tau_{1G4} (\mu s)/\text{rt} (\mu s)$	$\tau_{2F5/2} (\mu s)$
0.5%Pr $^{3+}$	34	75	-	75	-
0.5%Pr $^{3+}$ -5%Yb $^{3+}$	8.3	55	154	164/9.4	157
0.5%Pr $^{3+}$ -10%Yb $^{3+}$	3.0	38	94	95/6.5	80
0.5%Pr $^{3+}$ -20%Yb $^{3+}$	1.2	19	45	45/2.3	42
%0.5Yb $^{3+}$	-	-	-	-	1770
%20Yb $^{3+}$	-	-	-	-	1200

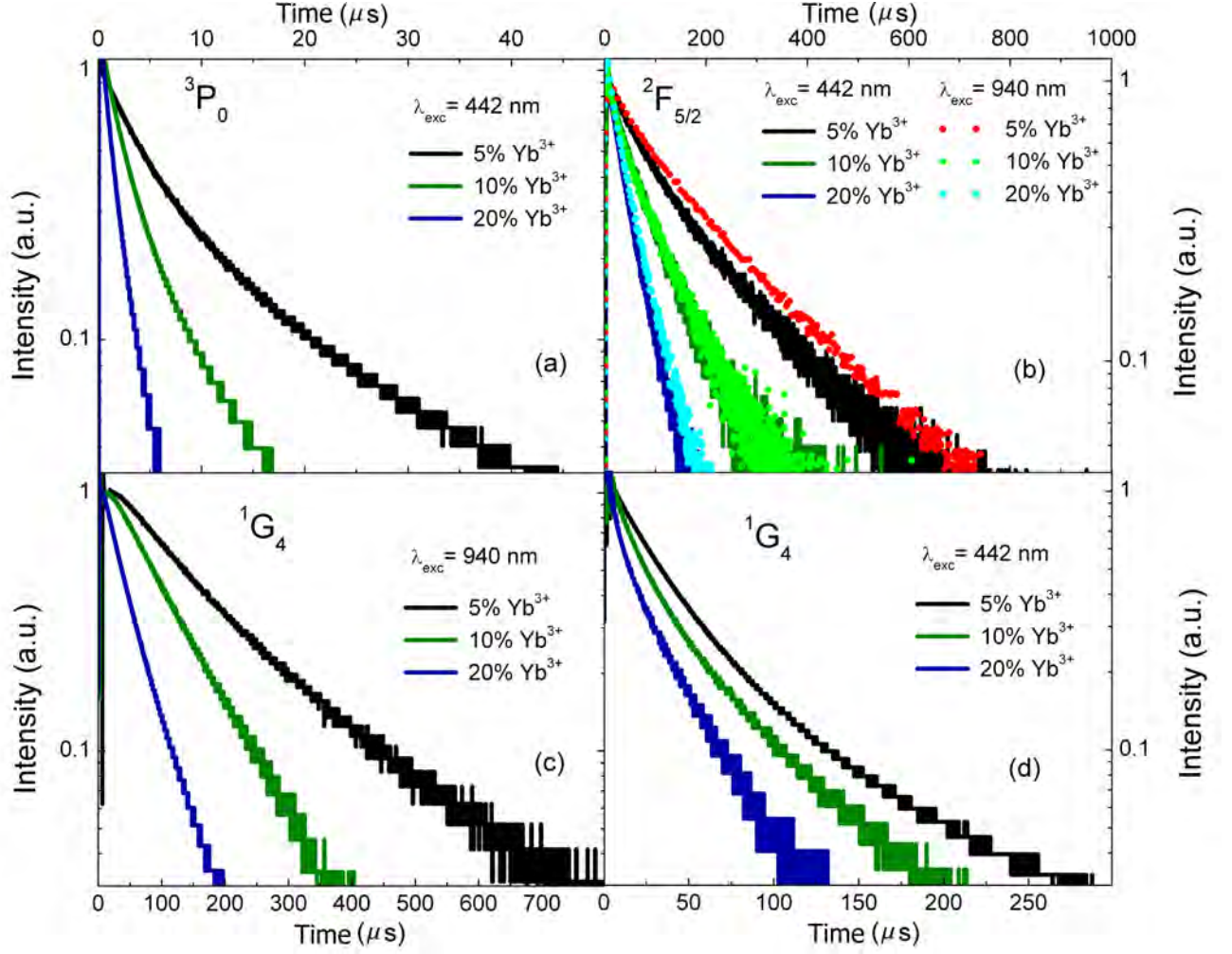


Figure 2.7: Experimental 3P_0 , 1G_4 and $^2F_{5/2}$ decay curves in $KY_3F_{10}:0.5\%Pr^{3+}-x\%Yb^{3+}$ ($x = 5, 10, 20$).

Due to the non-exponential character of some of the decay curves, average 3P_0 , 1G_4 and $^2F_{5/2}$ lifetimes were determined by normalizing to unity the fluorescence decay curves at $t = 0$ and by integrating the entire decay curves according to the expression:

$$\tau = \frac{1}{I_0} \int_0^\infty I(t) dt \quad (2.1)$$

in which I_0 is the fluorescence intensity at $t = 0$. Table 2.2 shows that the decrease of both the Yb^{3+} and 1G_4 lifetimes is very strong as both lifetimes reach values equal or below $45 \mu s$ in $KY_3F_{10}:0.5\%Pr^{3+}-20\%Yb^{3+}$. In other words, it shows that both the Yb^{3+} and 1G_4 lifetimes become shorter than the intrinsic 1G_4 lifetime ($\tau = 75 \mu s$) in singly Pr^{3+} doped KY_3F_{10} . This result has a direct impact on the simulations as will be discussed further in the text.

2.4 First energy transfer efficiency

The determination of the 3P_0 lifetime in the different samples enables to quantify the energy transfer efficiency for the first energy transfer. The energy transfer efficiency (ETE) is defined in a general way as the ratio between the energy transfer rate and the total relaxation rate comprising possible energy transfer rates, the radiative decay rate and the multiphonon relaxation rate [167]. In the particular case of 3P_0 , the total relaxation rate is given by:

$$\tau_{3P0-x\%Yb}^{-1} = \alpha + \tau_{3P0-0\%Yb}^{-1} \quad (2.2)$$

in which $\tau_{3P0-x\%Yb}$ and $\tau_{3P0-0\%Yb}$ are the 3P_0 lifetimes with $x\%Yb^{3+}$ and without any Yb^{3+} respectively, and α is the energy transfer rate. The multiphonon relaxation rate from 3P_0 is neglected in fluoride materials since the nearest lower level 1D_2 is located 3800 cm^{-1} below 3P_0 [109]. The ETE can then be expressed as a function of the Yb^{3+} concentration:

$$ETE(1) = \eta_{x\%Yb} = \frac{\tau_{3P0-x\%Yb}^{-1} - \tau_{3P0-0\%Yb}^{-1}}{\tau_{3P0-x\%Yb}^{-1}} = 1 - \frac{\tau_{3P0-x\%Yb}}{\tau_{3P0-0\%Yb}} \quad (2.3)$$

Results obtained with Eq.2.3 and presented in Table 2.3 show a very efficient energy transfer $Pr^{3+}(^3P_0 \rightarrow ^1G_4)$ to $Yb^{3+}(^2F_{7/2} \rightarrow ^2F_{5/2})$ for high Yb^{3+} concentrations with efficiency up to 96% in $KY_3F_{10}:0.5\%Pr^{3+}-20\%Yb^{3+}$. When comparing this result with other ETEs reported in the literature (Table 2.4), we see that KY_3F_{10} is a promising host for this type of energy transfer.

Table 2.3: Experimental 3P_0 lifetimes and derived energy transfer efficiencies.

Sample	$\tau_{3P0} (\mu s)$	ETE(1) (%)
0.5%Pr ³⁺	34	-
0.5%Pr ³⁺ -5%Yb ³⁺	8.3	75.6
0.5%Pr ³⁺ -10%Yb ³⁺	3.0	91.4
0.5%Pr ³⁺ -20%Yb ³⁺	1.2	96.4

Table 2.4: Reported ETEs.

Sample	Doping concentration	ETE (%)	Reference
SrF ₂ :Pr ³⁺ -Yb ³⁺	0.1%Pr ³⁺ -17%Yb ³⁺	99	[107]
LaF ₃ :Pr ³⁺ -Yb ³⁺	0.005%Pr ³⁺ -10%Yb ³⁺	61.6	[108]
YF ₃ :Pr ³⁺ -Yb ³⁺	0.5%Pr ³⁺ -17%Yb ³⁺	2.9	[109]
GdAl ₃ (BO ₃) ₄ :Pr ³⁺ -Yb ³⁺	1%Pr ³⁺ -30%Yb ³⁺	95.4	[111]
La borogermanate glass	0.5%Pr ³⁺ -20%Yb ³⁺	65	[113]
KY ₃ F ₁₀ :Pr ³⁺ -Yb ³⁺	0.5%Pr ³⁺ -20%Yb ³⁺	96.5	[168]

2.5 Second energy transfer and quantum efficiency

When evaluating a system based on energy transfers for a potential application, as it is the case for a solar downconverter, an accurate determination of the quantum efficiency of the system becomes essential. In our case, it implies a good knowledge of the efficiency of both the first and second energy transfers. In section 2.4, the efficiency of the first step of the quantum cutting process: Pr³⁺(³P₀→¹G₄) to Yb³⁺(²F_{7/2}→²F_{5/2}), was easily derived. Unfortunately, the efficiency of the second-step cannot be calculated as simply as the ratio between the energy transfer rate and the total relaxation rate of the ¹G₄ level since, because of the back-transfer, the total relaxation rate can not be directly obtained from the ¹G₄ lifetimes. Indeed, the efficiency of the second energy transfer appears rather complicated to determine experimentally.

Confronted with this problem, some reports use the ETE of the first step to derive the quantum efficiency of the whole quantum cutting process by assuming implicitly that the second step has a 100% efficiency or that the QC is merely a cooperative process [111,113]. With these types of assumptions, the QC efficiency can be easily expressed as follows:

$$\eta_{QC} = \eta_{r(3P0)}(1 - \eta_{x\%Yb}) + 2\eta_{x\%Yb} \quad (2.4)$$

in which $\eta_{x\%Yb}$ is the ETE for the first energy transfer and $\eta_{r(3P0)}$ is the intrinsic quantum efficiency of the praseodymium ³P₀ level, which is usually set to 1. The assumptions needed to use Equation 2.4 seem however excessive. A cooperative process only takes place when the first order processes can be neglected, and this is not the case of the

$\text{Pr}^{3+}\text{-Yb}^{3+}$ system. The very few investigations trying to discuss the efficiency of the second step indicate that indeed the real efficiency appears to be far from 100% [112,169]. The experimental results shown so far, especially the normalized spectra in Fig.2.6 also seem to indicate that the efficiency of the second energy transfer is fairly low. Thus, quantifying the QC efficiency for a two-step process requires to take into account the efficiency of both first, $\text{Pr}^{3+}({}^3\text{P}_0 \rightarrow {}^1\text{G}_4)$ to $\text{Yb}^{3+}({}^2\text{F}_{7/2} \rightarrow {}^2\text{F}_{5/2})$, and second, $\text{Pr}^{3+}({}^1\text{G}_4 \rightarrow {}^3\text{H}_4)$ to $\text{Yb}^{3+}({}^2\text{F}_{7/2} \rightarrow {}^2\text{F}_{5/2})$, energy transfers. The QC efficiency for a two-step process can be thus written as follows:

$$\eta_{QC} = \eta_{r(3P0)}(1 - \eta_{x\%Yb(1)}) + \eta_{x\%Yb(1)} + \eta_{x\%Yb(1)}(\eta_{r(1G4)}(1 - \eta_{x\%Yb(2)}) + \eta_{x\%Yb(2)}) \quad (2.5)$$

in which, $\eta_{x\%Yb(1)}$ and $\eta_{x\%Yb(2)}$ are the ETEs for the first and second energy transfers respectively. One can note that Equation 2.5 does not take into account the back-transfer from Yb^{3+} to Pr^{3+} ions which would even complicate the definition of the quantum efficiency.

The investigation of the different energy transfers efficiency can be attempted by comparing the experimental results with adequate simulations. A rate equation model showing a good agreement with the experiments can provide a further insight into the second energy transfer efficiency along with a better comprehension of the whole system. To our knowledge, very few modeling of the downconversion process in the $\text{Pr}^{3+}\text{-Yb}^{3+}$ system have been reported. Moreover, the few modeling which have been developed focus on the first-step of the quantum cutting process [110]. In the next sections we are going to present two types of modeling. The system was first analyzed with a classical rate-equation model. Secondly, the fluorescence decays were compared to simulated fluorescence decays derived from a random Monte Carlo method. The pertinence of each approach will be discussed.

2.6 Rate equation modeling

The $\text{Pr}^{3+}\text{-Yb}^{3+}$ system involves 15 energy levels [57] which is clearly too complex for a rate equation analysis. The Pr^{3+} diagram, with 13 levels, can be reduced to 3 relevant levels ${}^3\text{P}_0$, ${}^1\text{G}_4$ and ${}^3\text{H}_4$ provided that some assumptions are verified. First, the ${}^1\text{D}_2$ level can be omitted since the energy gap between ${}^3\text{P}_0$ and ${}^1\text{D}_2$ is high enough ($> 3000 \text{ cm}^{-1}$) to avoid multiphonon relaxation in a host with low phonon frequency such as KY_3F_{10} .

The radiative relaxation ${}^3P_0 \rightarrow {}^1D_2$ is also known to be very weak so that no population is expected in 1D_2 when exciting the 3P_J multiplet. We also verified experimentally that no emission from 1D_2 could be recorded when exciting the 3P_2 multiplet at 442 nm. The levels 3P_2 and 3P_1 can be also ignored since they undergo fast multiphonon decay to 3P_0 so that, the 3P_J multiplet is exclusively represented by the 3P_0 level within the model. Moreover, in order to avoid eventual upconversion phenomena, the experiments were performed with low excitation density. The low excitation density allows neglecting any depletion of the ${}^2F_{7/2}$ and 3H_4 ground states. Thus, n_{3H4} and $n_{2F7/2}$ can be considered equal to the concentration of Pr^{3+} and Yb^{3+} ions respectively. The three energy levels under consideration i.e. 3P_0 , 1G_4 and ${}^2F_{5/2}$, are labeled “1”, “2” and “3” respectively in the simulations.

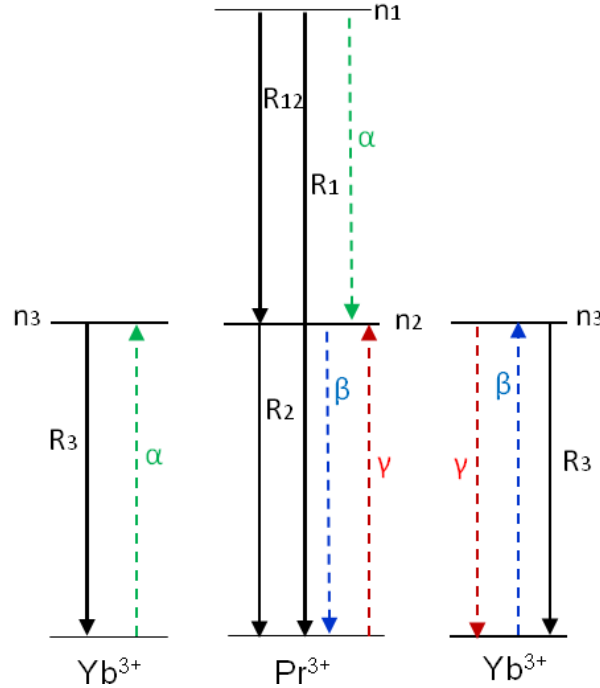


Figure 2.8: Energy levels and processes involved in downconversion quantum cutting with Pr^{3+} and Yb^{3+} ions. Solid arrows represent the radiative transitions and dashed arrows the energy transfers.

Experiments were compared to a set of two rate equations when pumping the Yb^{3+} ions (2.6) and a set of three rate equations when pumping the Pr^{3+} ions (2.7).

$$\begin{aligned} \frac{dn_2}{dt} &= -(R_2 + \beta)n_2 + \gamma n_3 \\ \frac{dn_3}{dt} &= -(R_3 + \gamma + \delta)n_3 + \beta n_2 + \sigma \phi N_{Yb} \end{aligned} \quad (2.6)$$

$$\begin{aligned}
\frac{dn_1}{dt} &= -(R_1 + \alpha)n_1 + \sigma\phi N_{Pr} \\
\frac{dn_2}{dt} &= -(R_2 + \beta)n_2 + \gamma n_3 + \alpha n_1 + R_{12}n_1 \\
\frac{dn_3}{dt} &= -(R_3 + \gamma + \delta)n_3 + \beta n_2 + \alpha n_1
\end{aligned} \tag{2.7}$$

in which n_i is the population of level i ; $\sigma\phi$ represents the pumping rate with σ the absorption cross-section and ϕ the excitation photon flux in $\text{cm}^{-2}\text{s}^{-1}$. R_i is the decay rate from level i which is equal to τ_i^{-1} , with τ_i the intrinsic lifetime of level i . The parameter R_{ij} corresponds to the radiative decay rate from level i to level j , with $R_{ij} = \beta_R^{ij}\tau_i^{-1}$, and β_R^{ij} the $i \rightarrow j$ transition branching ratio. α , β and γ are the energy transfer rates for the first, second and back transfers respectively (Fig.2.8). We will further refer to γ as a back-transfer even when considering the excitation at the Yb^{3+} ions (2.6) to avoid any confusion. Energy transfer rates α , β and γ exhibit the following dependences with the Pr^{3+} and Yb^{3+} concentrations:

$$\alpha = P_\alpha N_{Yb} \tag{2.8}$$

$$\beta = P_\beta N_{Yb} \tag{2.9}$$

$$\gamma = K_\gamma N_{Yb} N_{Pr} \tag{2.10}$$

with P_α , P_β and K_γ the corresponding transfer parameters. In the case of the two energy transfers from Pr^{3+} to Yb^{3+} (α and β), the transfer rates are classically proportional to the acceptor concentration, i.e the Yb^{3+} concentration. The back-transfer rate γ in Eq.2.10 is however based on migration assisted energy-transfer models which establish a direct dependence of the transfer probability with both the acceptor concentration and the donor concentration [170]. Indeed, the Yb^{3+} concentration in our samples ranges from 5 to 20% Yb^{3+} . As mentioned earlier, it is well-known that at high Yb^{3+} concentration energy migration takes place among Yb^{3+} ions and enhances possible energy transfer towards other impurities.

An important problem to address within the modeling is the fact that, $\text{Yb}^{3+}(^2\text{F}_{5/2})$ and $\text{Pr}^{3+}(^1\text{G}_4)$ lifetimes in Table 2.2 show a drastic decrease of both lifetimes down to 45 μs when exciting Yb^{3+} ions at 940 nm. Such a result cannot be explained by only a transfer (β) from $\text{Pr}^{3+}(^1\text{G}_4)$ to Yb^{3+} and a back-transfer (γ). When two energy levels

are coupled by a reciprocal exchange of energy, the decays cannot be shorter than the shortest of both intrinsic $\text{Yb}^{3+}({}^2\text{F}_{5/2})$ and $\text{Pr}^{3+}({}^1\text{G}_4)$ lifetimes, in our case the ${}^1\text{G}_4$ level with a lifetime of $75 \mu\text{s}$. This point will be discussed in details in section 2.6.1 dealing with the dynamics. Dynamics can thus only be described by adding, besides α , β and γ , a fourth energy transfer mechanism draining the Yb^{3+} excited state which can be viewed as a concentration quenching process. This fourth mechanism is labeled δ and is proportional to the Yb^{3+} content as follows:

$$\delta = P_{\delta} N_{\text{Yb}} \quad (2.11)$$

The proportionality with the Yb^{3+} concentration shows that this energy transfer is assisted by energy migration among Yb^{3+} ions and ends on quenching centers. The difference between δ and γ is the fact that the energy lost by the Yb^{3+} ions through δ do not feed the ${}^1\text{G}_4$ level. The δ process can thus be considered as a concentration quenching process. However, the real nature of the quenching centers is not obvious. Indeed, we measured the Yb^{3+} lifetime in a singly-doped $\text{KY}_3\text{F}_{10}:20\%\text{Yb}^{3+}$ sample and found 1.3 ms. This is not a great reduction in comparison with the intrinsic 1.77 ms Yb^{3+} radiative lifetime in KY_3F_{10} [151]. It indicates that the concentration quenching in singly-doped $\text{KY}_3\text{F}_{10}:20\%\text{Yb}^{3+}$ remains rather weak. Possible explanations for the origin of the δ concentration quenching will be discussed in the next section along with a comparison between the modeling (Systems 2.6 and 2.7) and the lifetimes presented in (Table 2.2), and also intensity ratios obtained under CW excitation.

2.6.1 Steady-state solutions

Systems 2.6 and 2.7 were solved under steady-state conditions i.e. $\frac{dn_i}{dt} = 0$, with $i = 1, 2, 3$. The steady-state equations are used to derive on the one hand the ratio n_1/n_3 between the ${}^3\text{P}_0$ and the Yb^{3+} populations and, on the other hand the ratio n_2/n_3 between the ${}^1\text{G}_4$ and the Yb^{3+} populations. These ratios can be described with rather simple expressions. Indeed, when calculating the ratios with systems 2.6 and 2.7, simplifications occur as for instance the n_1 , n_2 and n_3 dependence with the pumping rate, which appear in both sides of the ratio and therefore cancel each other out. When exciting the Yb^{3+} ions at 940 nm (System 2.6), one can derive:

$$\frac{n_2}{n_3} = \frac{\gamma}{R_2 + \beta} \quad (2.12)$$

When exciting the $\text{Pr}^{3+}({}^3\text{P}_0)$ ions at 442 nm (System 2.7), we obtain:

$$\frac{n_1}{n_3} = \frac{R_2 R_3 + \gamma R_2 + \delta R_2 + \beta R_3}{\alpha R_2 + \beta R_1 R_{12} + 2\alpha\beta} \quad (2.13)$$

$$\frac{n_2}{n_3} = \frac{R_{12} R_2 R_3 + \gamma R_{12} R_2 + \delta R_{12} R_2 + \alpha R_3 + 2\delta\alpha + 2\gamma\alpha}{\gamma R_2 + \beta R_1 R_{12} + 2\gamma\beta} \quad (2.14)$$

The dependence with the Yb^{3+} concentration can be introduced in Equations 2.12, 2.13 and 2.14 by using the definitions 2.8, 2.9, 2.10 and 2.11 of the energy transfer rates α , β , γ and δ .

$$\frac{n_2}{n_3} = \frac{K_\gamma N_{Pr} N_{Yb}}{R_2 + P_\beta N_{Yb}} \quad (2.15)$$

$$\frac{n_1}{n_3} = \frac{R_2 R_3 + K_\gamma R_2 N_{Pr} N_{Yb} + P_\delta R_2 N_{Yb} + P_\beta R_3 N_{Yb}}{P_\alpha R_2 N_{Yb} + P_\beta R_1 R_{12} N_{Yb} + 2P_\alpha P_\beta N_{Yb}^2} \quad (2.16)$$

$$\frac{n_2}{n_3} = \frac{R_{12} R_2 (R_3 + K_\gamma N_{Pr} N_{Yb} + P_\delta N_{Yb}) + P_\alpha N_{Yb} (R_3 + 2K_\gamma N_{Pr} N_{Yb} + 2P_\delta N_{Yb})}{K_\gamma R_2 N_{Pr} N_{Yb} + P_\beta R_1 R_{12} N_{Yb} + 2K_\gamma P_\beta N_{Yb}^2} \quad (2.17)$$

Using equations 2.15, 2.16 and 2.17, the dependence of the population ratios with the Yb^{3+} content can be compared to the experimental ratios. The population ratio between two levels is proportional to the corresponding ratio of emission intensities. Therefore we determined experimental intensity ratios by dividing the integrated area of the ${}^3\text{P}_0$ and ${}^1\text{G}_4$ emissions to that of the Yb^{3+} 1 μm band (Fig.2.6). In addition, several spectroscopic parameters values are needed for the modeling. The ${}^3\text{P}_0$, ${}^1\text{G}_4$ and ${}^2\text{F}_{5/2}$ intrinsic lifetimes, i.e without Yb^{3+} codopant (namely τ_1 , τ_2 and τ_3), are known values (Table 2.2) equal to 34 μs , 75 μs and 1.77 ms respectively. The branching ratio for the ${}^3\text{P}_0 \rightarrow {}^1\text{G}_4$ transition needed for the R_{12} decay rate was experimentally estimated to 3% by recording the ${}^3\text{P}_0$

entire emission spectrum from 480 nm to 1100 nm which was then corrected for the spectral response of the setup. The transition from $^3P_0 \rightarrow ^1D_2$ in the infrared was not taken into account as it only gives a small contribution to the overall emission spectrum. The branching ratio β was then calculated as the ratio between the spectral integral of the $^3P_0 \rightarrow ^1G_4$ transition of interest and the spectral integral of the entire emission spectrum.

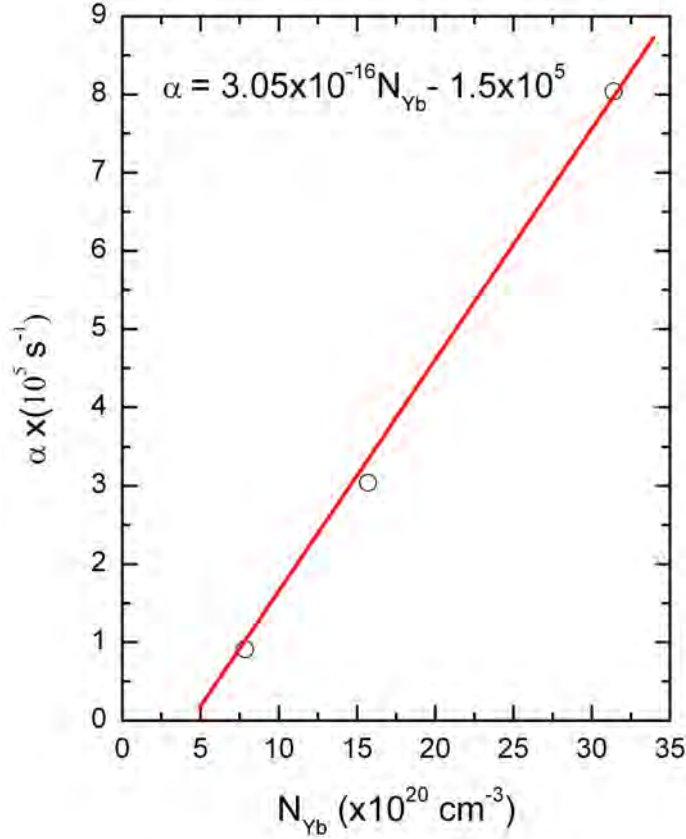


Figure 2.9: Calculation of P_α from Eq.2.18.

Contrarily to P_β , K_γ and P_δ , the transfer parameter P_α can be determined quite easily. Eq.2.2 shows that the energy transfer rate α can be calculated from the experimental data as the difference between the 3P_0 total relaxation rate with Yb^{3+} ions $(\tau_{1-x\%Yb})^{-1}$ and without Yb^{3+} ions $R_1 = (\tau_{1-0\%Yb})^{-1}$. Then, according to the definition of α given in Eq.2.8, P_α can be derived by a linear regression.

$$\tau_{1-x\%Yb}^{-1} - \tau_{1-0\%Yb}^{-1} = P_\alpha C_{Yb} N_T \quad (2.18)$$

We obtained $P_\alpha = 3.05 \times 10^{-16} \text{ cm}^{-3} \text{ s}^{-1}$ (Fig.2.9). One can notice that the γ -intercept is not exactly 0, showing that the “traditional” linear dependence of the energy transfer rate

with the acceptor concentration is not totally accurate. The three other parameters P_β , K_γ and P_δ were determined by adjusting the modeling (Eq.2.15 in Fig.2.10.c, Eq.2.16 in Fig.2.10.b, and Eq.2.17 in Fig.2.10.a) to the experimental results.

The simulated curves shown in Fig.2.10 show a good agreement with the experimental ratios versus the Yb^{3+} content with, $P_\beta=1.34\times 10^{-17} \text{ cm}^{-3}\text{s}^{-1}$; $K_\gamma=4.10\times 10^{-38} \text{ cm}^{-6}\text{s}^{-1}$ and $P_\delta=6.56\times 10^{-18} \text{ cm}^{-3}\text{s}^{-1}$. Importantly, these values are the same which will be used to describe the dynamics in the next section 2.6.2. In other words, these energy transfer parameters values describe both the experimental results under CW excitation and under pulsed excitation.

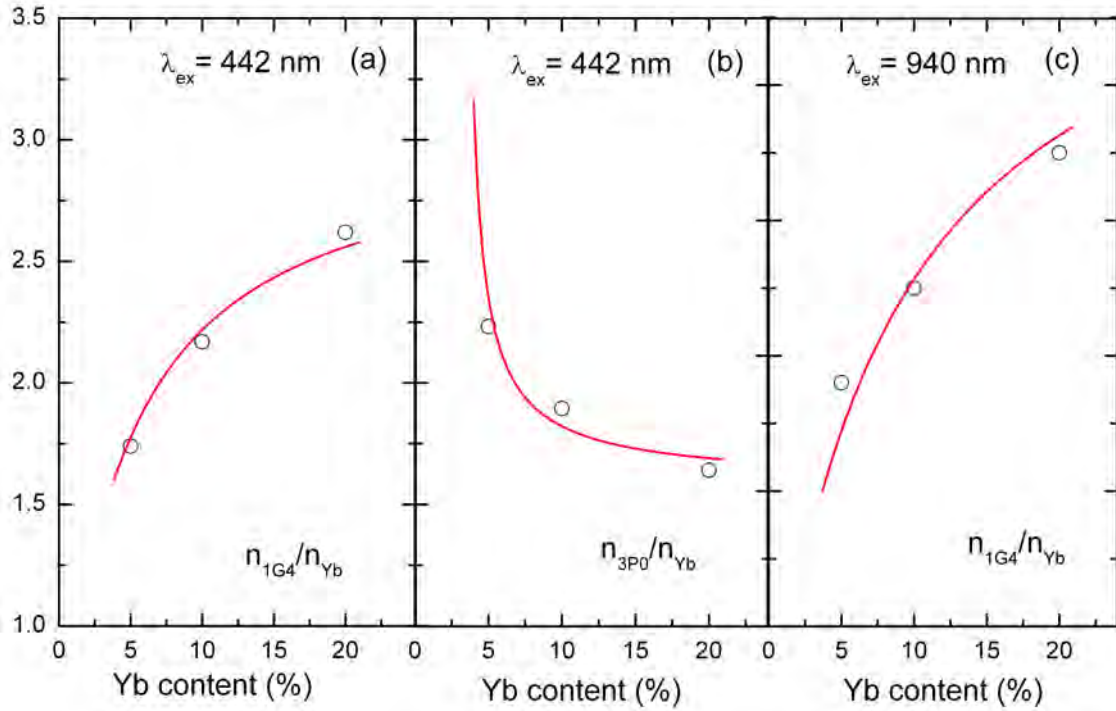


Figure 2.10: Experimental intensity ratios compared to the simulated population ratios as a function of the Yb^{3+} content.

The case of $n(^1G_4)/n(^2F_{5/2})$ under Yb^{3+} excitation (Fig.2.10.c) is interesting since it confirms the need to consider energy migration among Yb^{3+} ions within the rate equation model. Without migration, the back-transfer γ would only depend on the Pr^{3+} concentration so that Eq.2.15 would become:

$$\frac{n_2}{n_3} = \frac{P_\gamma N_{Pr}}{R_2 + P_\beta N_{Yb}} \quad (2.19)$$

Eq.2.19 shows that the n_2/n_3 ratio is then expected to decrease with the Yb^{3+} concentra-

tion for any values of β and γ . However, as observed in Fig.2.10.c, experimental results clearly show an increase of the n_2/n_3 ratio with the Yb^{3+} content which can be accurately described when considering energy migration among the Yb^{3+} ions.

2.6.2 Dynamic solutions

Time-dependent solutions of the rate equations systems 2.6 and 2.7 were compared to the experimental decay curves (Fig.2.7). The experimental decay curves were obtained under nanosecond pulsed excitation so that the pumping rate $\sigma\Phi$ was considered infinitely short in systems 2.6 and 2.7.

In the case of Yb^{3+} excitation (System 2.6) the set of two coupled rate equations can be solved analytically. Closed-form solutions can be then written as follows:

$$n_2(t) = \frac{\gamma}{\sqrt{\Delta}} (e^{-\frac{1}{2}(R_2+R_3+\beta+\gamma+\delta-\sqrt{\Delta})t} - e^{-\frac{1}{2}(R_2+R_3+\beta+\gamma+\delta+\sqrt{\Delta})t}) \quad (2.20)$$

$$n_3(t) = \frac{R_3 - R_2 + \gamma + \delta - \beta + \sqrt{\Delta}}{2\sqrt{\Delta}} e^{-\frac{1}{2}(R_2+R_3+\beta+\gamma+\delta+\sqrt{\Delta})t} - \frac{R_3 - R_2 + \gamma + \delta - \beta - \sqrt{\Delta}}{2\sqrt{\Delta}} e^{-\frac{1}{2}(R_2+R_3+\beta+\gamma+\delta-\sqrt{\Delta})t} \quad (2.21)$$

in which

$$\sqrt{\Delta} = (R_2 + R_3 + \beta + \gamma + \delta) \sqrt{1 - \frac{4(R_2(R_3 + \delta + \gamma)) + \beta(R_3 + \delta)}{(R_2 + R_3 + \beta + \gamma + \delta)^2}} \quad (2.22)$$

Eq.2.20 was then used to simulate the experimental $^1\text{G}_4$ decays (Fig.2.7.c) while Eq.2.21 was used to describe the experimental Yb^{3+} decays (Fig.2.7.b) as shown in Fig.2.11-right, both of them obtained upon Yb^{3+} excitation at 940 nm. Eq.2.20 for the $^1\text{G}_4$ decay exhibits two components: a fast build-up time with a rate constant $\frac{1}{2}(R_2 + R_3 + \beta + \gamma + \delta + \sqrt{\Delta})$ and a decay time with a time constant as follows:

$$\tau = \left(\frac{1}{2}(R_2 + R_3 + \beta + \gamma + \delta - \sqrt{\Delta})\right)^{-1} \quad (2.23)$$

This decay time is given in Table 2.2 for the 1G_4 level. Interestingly, the same time constant appears for the Yb^{3+} decay in Eq.2.21 and represents the long time part of the decay. This common decay time (Eq.2.23) is therefore important and needs to be further discussed. We will first show that Eq.2.23 cannot describe the lifetime values of Table 2.2 without the introduction of an additional energy transfer δ .

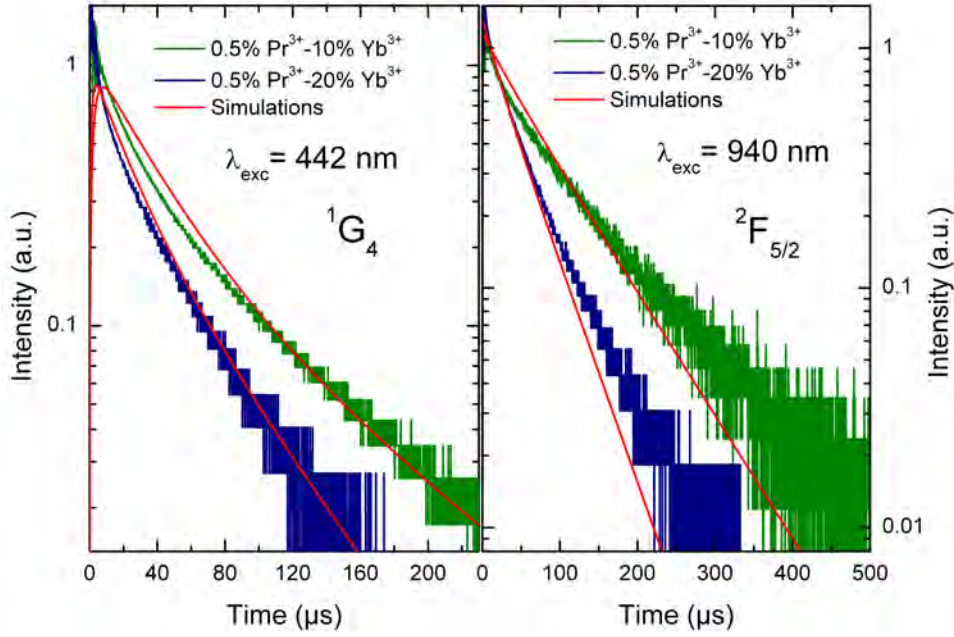


Figure 2.11: Comparison between experimental and simulated decay curves (left) 1G_4 decays under 442 nm excitation for the samples codoped with 10% Yb^{3+} and 20% Yb^{3+} ; (right) $^2F_{5/2}$ decays under 940 nm excitation for the samples codoped with 10% Yb^{3+} and 20% Yb^{3+} .

If one considers that the δ energy transfer does not exist ($\delta = 0$), Eq.2.22 becomes:

$$\sqrt{\Delta} = (R_2 + R_3 + \beta + \gamma) \sqrt{1 - \frac{4(R_2 R_3 + R_2 \gamma + \beta R_3)}{(R_2 + R_3 + \beta + \gamma)^2}} \quad (2.24)$$

The term $\sqrt{\Delta}$ (Eq.2.24) can be simplified since $(R_2 + R_3 + \beta + \gamma)2 \gg 4(R_2 R_3 + R_3 \gamma + \beta R_3)$. This approximation is valid for any values of β and γ except when β is equal to 0 which would contradict the fact that the $\text{Yb}^{3+}(^2F_{5/2})$ and $\text{Pr}^{3+}(^1G_4)$ energy levels are coupled by a reciprocal exchange of energy previously discussed. Taking into account

this approximation, Eq.2.24 can be expanded in Taylor series and then becomes:

$$\sqrt{\Delta} \cong (R_2 + R_3 + \beta + \gamma) \left(1 - \frac{2(R_2 R_3 + R_2 \gamma + \beta R_3)}{(R_2 + R_3 + \beta + \gamma)^2} \right) \quad (2.25)$$

Replacing then Eq.2.25 in Eq.2.23 the decay rate becomes:

$$\tau^{-1} = \frac{R_2 R_3 + R_2 \gamma + \beta R_3}{R_2 + R_3 + \beta + \gamma} \quad (2.26)$$

Asymptotic values can be easily derived from Eq.2.26. If $\beta \rightarrow 0$ and $\gamma \rightarrow \infty$, τ^{-1} becomes equal to R_2 , while if $\beta \rightarrow 0$ and $\gamma \rightarrow 0$, the rate τ^{-1} is simply $(R_2 \times R_3)/(R_2 + R_3)$ and if $\beta \rightarrow \infty$ and $\gamma \rightarrow \infty$, the rate τ^{-1} is then $(R_2 + R_3)/2$.

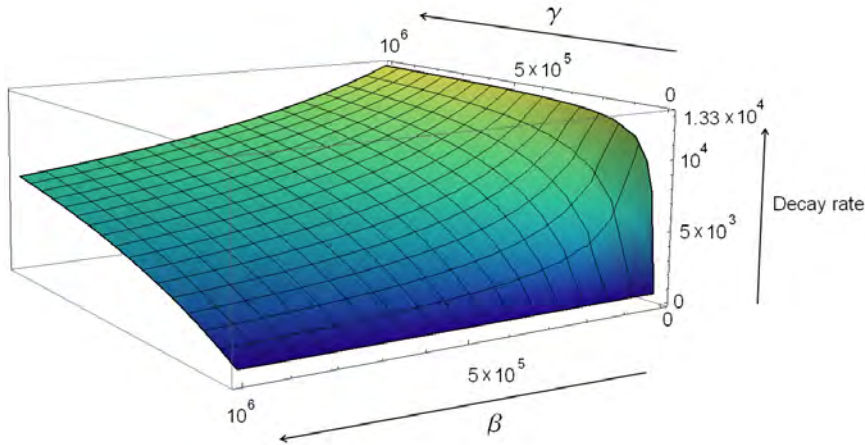


Figure 2.12: Evaluation of Eq.2.26 with β and γ varying from 0 to 10^6 s^{-1} . The decay rate reaches asymptotic values equal to 13333 s^{-1} (R_2) and 6949 s^{-1} $((R_2 + R_3)/2)$ and 542 s^{-1} $((R_2 \times R_3)/(R_2 + R_3))$ at the limits $(\beta \rightarrow 0, \gamma \rightarrow \infty)$, $(\beta \rightarrow \infty, \gamma \rightarrow \infty)$ and $(\beta \rightarrow 0, \gamma \rightarrow 0)$ respectively.

Fig.2.12 shows the dependence of the decay rate (Eq.2.26) with the energy transfer parameters β and γ . One can see that the maximum value of the decay rate is 13333 s^{-1} which is the $^1\text{G}_4$ intrinsic decay rate, i.e. $R_2 = (75 \mu\text{s})^{-1}$. In other words, the shortest $^1\text{G}_4$ decay time which can be derived from the model with $\delta = 0$ (Eq.2.23) is equal to the $^1\text{G}_4$ intrinsic lifetime i.e. $75 \mu\text{s}$. This limitation makes the model with $\delta = 0$ unable to explain the measured lifetimes of $45 \mu\text{s}$ in $\text{KY}_3\text{F}_{10}:0.5\%\text{Pr}^{3+}-20\%\text{Yb}^{3+}$ (Table 2.2). The overall meaning of the closed expressions 2.20 and 2.21 is that when two energy levels are coupled by back and forth energy transfer, the long time part of their respective dynamics will

reflect the values of their intrinsic (meaning without codopant) lifetimes. This long time part of their decays cannot be shorter than the shortest of the two intrinsic lifetimes.

The introduction into the modeling of the δ mechanism, which does not take part in the mutual energy exchange, reduces the Yb^{3+} lifetime and consequently the $^1\text{G}_4$ decay time. With a proper set of energy transfer parameters, Eqs. 2.20 and 2.21 can successfully reproduce the experimental $^1\text{G}_4$ and $^2\text{F}_{5/2}$ lifetimes upon IR excitation at 940 nm.

Table 2.5: Compared theoretical and experimental lifetimes.

Sample	$\lambda_{exc} = 442 \text{ nm}$			$\lambda_{exc} = 940 \text{ nm}$	
	$\tau_{^3P_0}(\mu s)$	$\tau_{^1G_4}(\mu s)$	$\tau_{^2F_{5/2}}(\mu s)$	$\tau_{^1G_4}(\mu s)$	$\tau_{^2F_{5/2}}(\mu s)$
	Th/ Exp	Th/ Exp	Th / Exp	Th / Exp	Th / Exp
0.5%Pr ³⁺ -5%Yb ³⁺	8.4/ 8.3	54/ 55	155/ 154	155/ 164	151/ 157
0.5%Pr ³⁺ -10%Yb ³⁺	2.8/ 3.0	42/ 38	94/ 94	94/ 95	85/ 80
0.5%Pr ³⁺ -20%Yb ³⁺	1.3/ 1.2	28/ 19	49/ 45	49/ 45	40/ 42

In the case of $^3\text{P}_0$ excitation at 442 nm closed expressions could not be easily found as it involves a set of three-coupled rate equations (2.7). Numerical solutions were thus found. The same values of the four energy transfer parameters (P_α , P_β , K_γ and P_δ) as in the modeling of the intensity ratios were used to simulate the decays both under $^3\text{P}_0$ excitation at 442 nm and Yb^{3+} excitation at 940 nm. Again the first parameter P_α was not adjusted but kept at a fixed value of $3.05 \times 10^{-16} \text{ cm}^{-3}\text{s}^{-1}$ obtained with Eq.2.18 (Fig.2.9). Table 2.5 presents the lifetime values obtained with the set of three adjusting parameters $P_\beta=1.34 \times 10^{-17} \text{ cm}^{-3}\text{s}^{-1}$; $K_\gamma=4.10 \times 10^{-38} \text{ cm}^{-6}\text{s}^{-1}$ and $P_\delta=6.56 \times 10^{-18} \text{ cm}^{-3}\text{s}^{-1}$. A general good agreement is found between the experimental values and the modeling (Table 2.5). The modeling is able to derive the average lifetimes of the different levels, but the exact form of the decays is more difficult to reproduce as illustrated in Fig.2.11 in two different cases, especially when the decays are non-exponential. The three energy transfer parameters values (P_β , K_γ and P_δ) are remarkable in the sense that they allow us to have a good description of all our experiments description: intensity ratios under CW excitation and dynamics under pulsed excitation, both under Yb^{3+} and Pr^{3+} excitations.

The need of introducing a concentration quenching process δ was clearly evidenced by the analysis of the dynamics. Without this process, it is impossible to explain the short decay values found in the Yb^{3+} concentrated samples such as $\text{KY}_3\text{F}_{10}:\text{0.5\%Pr}^{3+}\text{-20\%Yb}^{3+}$.

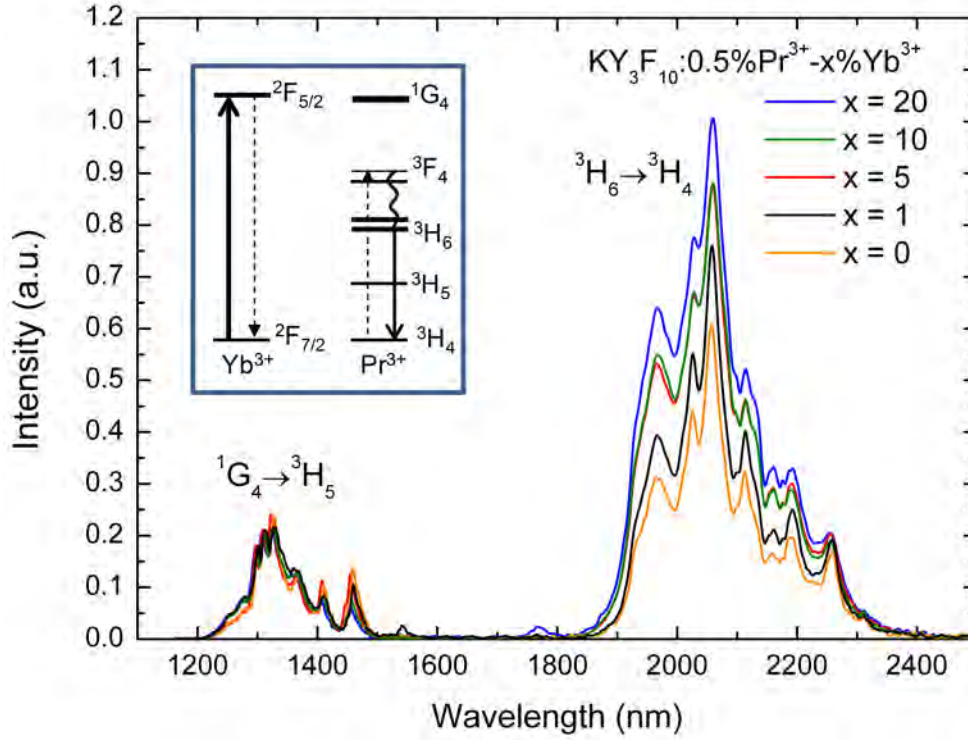


Figure 2.13: Room temperature Pr^{3+} emission spectra in the range 1.1 to 2.5 μm for a 980 nm excitation.

However, the exact nature of the δ mechanism deserves a discussion. The δ process is described as a migration assisted energy transfer where the migration takes place among Yb^{3+} ions and transfer Yb^{3+} energy to impurities or defects. Our investigations show that part of the δ process can be assigned to an energy transfer from $\text{Yb}^{3+} ({}^2\text{F}_{5/2} \rightarrow {}^2\text{F}_{7/2})$ to $\text{Pr}^{3+} ({}^3\text{H}_4 \rightarrow {}^3\text{F}_4)$ despite the energy gap between the ${}^2\text{F}_{5/2}$ and the ${}^3\text{F}_4$ levels. We recorded infrared emissions from Pr^{3+} between 1.1 μm and 2.5 μm upon Yb^{3+} excitation at 980 nm. Within this spectral range, two infrared transitions can be observed which are ${}^1\text{G}_4 \rightarrow {}^3\text{H}_5$ around 1.3 μm and ${}^3\text{H}_6 \rightarrow {}^3\text{H}_4$ around 2.1 μm (Fig.2.13). The recorded spectra were normalized to the ${}^1\text{G}_4 \rightarrow {}^3\text{H}_5$ emission. As displayed in Fig.2.13, the emission from the ${}^3\text{H}_6$ level is found to increase with the Yb^{3+} content in comparison with the emission from ${}^1\text{G}_4$. When comparing the integrated emission from ${}^3\text{H}_6$ to that of ${}^1\text{G}_4$ we found that the corresponding ratio (R) is twice larger in the case of the codoped 0.5% Pr^{3+} -20% Yb^{3+} sample ($R = 4.16$) compared to the 0.5% Pr^{3+} singly doped one ($R = 2.09$). This result shows that a non-resonant energy transfer $\text{Yb}^{3+} ({}^2\text{F}_{5/2} \rightarrow {}^2\text{F}_{7/2})$ to $\text{Pr}^{3+} ({}^3\text{H}_4 \rightarrow {}^3\text{F}_4)$ followed by multiphonon relaxation from ${}^3\text{F}_4$ to ${}^3\text{H}_6$ is taking place and even in a fairly important way. This energy transfer is without any doubt a part of the δ mechanism and constitutes

a second migration-assisted back-transfer mechanism from Yb^{3+} to Pr^{3+} ions, in addition to the first back-transfer γ from Yb^{3+} towards $^1\text{G}_4$.

2.6.3 Conclusions

A rate equation modeling was developed to describe the different dynamics of Pr^{3+} and Yb^{3+} ions, along with the intensity ratios recorded under CW excitation. Besides the three obvious energy transfer mechanisms, a fourth energy transfer mechanism labeled δ which depletes the $^2\text{F}_{5/2}$ level, was evidenced by the study of the Pr^{3+} - Yb^{3+} codoping under Yb^{3+} excitation and the related system of two coupled rate equations. The modeling was used to estimate the energy transfer rates of the different mechanisms within the Pr^{3+} - Yb^{3+} system upon Pr^{3+} excitation at 442 nm ($^3\text{P}_2$ level). The results are summarized in Table 2.6.

Table 2.6: Energy transfer rates derived by modeling.

Sample	$\alpha(s^{-1})$	$\beta(s^{-1})$	$\gamma(s^{-1})$	$\delta(s^{-1})$
0.5% Pr^{3+} -5% Yb^{3+}	8.94×10^4	1.05×10^4	2.52×10^3	5.05×10^3
0.5% Pr^{3+} -10% Yb^{3+}	3.28×10^5	2.10×10^4	5.05×10^3	1.00×10^4
0.5% Pr^{3+} -20% Yb^{3+}	8.08×10^5	4.21×10^4	1.01×10^4	2.02×10^4

The α energy transfer parameter for the first energy transfer was deduced by direct calculation from the $^3\text{P}_0$ fluorescence decays (Eq.2.18). The resulting energy transfer rate is found equal to $8.08 \times 10^5 \text{ s}^{-1}$ in the case of the 0.5% Pr^{3+} -20% Yb^{3+} codoped sample. The energy transfer parameters corresponding to the second transfer β , back-transfer γ and fourth transfer δ were adjusted to fit the experimental data. These two latter γ and δ energy transfers explain the strong quenching of the Yb^{3+} emission which causes the Yb^{3+} lifetime to go down from 1.77 ms [151] in Yb^{3+} singly-doped KY_3F_{10} to 50 μs in KY_3F_{10} : 0.5% Pr^{3+} -20% Yb^{3+} under Pr^{3+} pumping at 442 nm. This drop in the Yb^{3+} lifetime is a very pessimistic sign for the practical application of KY_3F_{10} : Pr^{3+} - Yb^{3+} in solar downconverters as the overall efficiency of the system will decrease with the Yb^{3+} emission quenching. However, the interpretation of the $^2\text{F}_{5/2}$ dynamics must be handled with care as it is the result of not only a back-transfer γ towards the $^1\text{G}_4$ level, but of 4 energy transfers with two feeding transfers (α from the $^3\text{P}_0$ level and β from the $^1\text{G}_4$ level) and two quenching processes (γ and δ). The system is made even more complicated

as the β and γ energy transfer go back and forth between the 1G_4 and the $^2F_{5/2}$ levels creating a thermodynamic equilibrium between these two levels. Therefore, the definition of a quantum efficiency of the whole quantum cutting process is complicated.

The overall agreement between the experiments and the modeling is very much satisfying despite the fact that the modeling was confronted to a wide range of experiments both under CW and pulsed excitations. Interestingly, Table 2.6 shows that the second energy transfer β appears to be more efficient than its reciprocal γ energy transfer from the $^2F_{5/2}$ back to the 1G_4 level. This result is in apparent contradiction with basic thermodynamic considerations under which the γ process should be more efficient than the β energy transfer. As mentioned earlier, the difference in acceptor concentrations for both energy transfers is likely to explain the results of Table 2.6 since the acceptor concentration plays a key role in the energy transfer rates. Indeed, in the samples of our study, the Yb^{3+} concentration is between 10 to 40 times larger than the Pr^{3+} concentration. Therefore, on average a Pr^{3+} ion is surrounded by Yb^{3+} ions while a random Yb^{3+} ion is far from a Pr^{3+} ion making the transfer from $^2F_{5/2}$ to the 1G_4 level less efficient.

However, limitations within the modeling appear which are related to the assumptions we made. The assumption that the back-transfer γ and concentration quenching δ are assisted by migration among Yb^{3+} ions was verified by the experiments, but it does not mean that direct energy transfer from Yb^{3+} to Pr^{3+} ions or impurities does not take place. To take into account both direct and migration assisted energy transfer, one would have to implement separate energy transfer parameters. We have chosen to limit the number of adjusting parameters to the minimum in order to keep a realistic modeling.

2.7 Other modeling approaches

2.7.1 Rate-equation limitations

When dealing with luminescence dynamics, fundamental limitations are inherent with the use of classical rate-equations to describe the temporal evolution of donor ions enduring direct donor-acceptor energy transfer. A good example can be found with the 3P_0 decay which is derived from 2.7:

$$I_1(t) \propto n_1(t) = n_1(0)e^{-(R_1+\alpha)t} \quad (2.27)$$

In this simple case, a classical rate-equation model predicts exponential 3P_0 decay curves notably contrasting with the non-exponential experimental behavior as displayed in Fig.2.14.

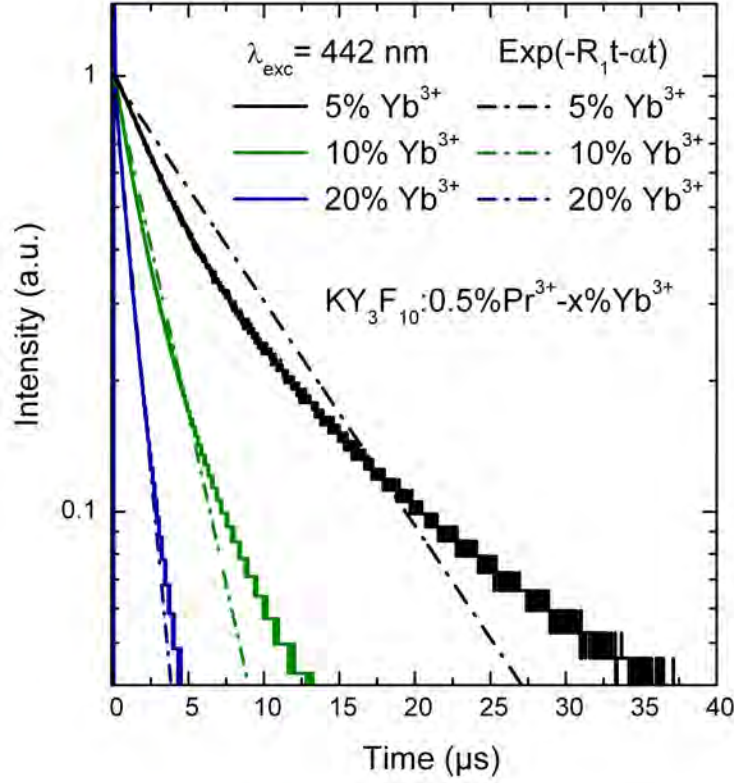


Figure 2.14: Experimental 3P_0 decay curves compared to the exponential curves resulting from the rate-equation model. The greatest difference is observed for the sample codoped $0.5\%Pr^{3+}$ - $5\%Yb^{3+}$.

The exponential character of the theoretical curves is indeed the consequence of considering that the energy transfer rate remains constant in time throughout the decay. In other words, it is like considering that the energy transfer takes place at a fixed averaged interaction distance. Therefore the energy transfer rate α would then be constant for a given acceptor concentration (Eq.2.8) which consequently would lead to a single exponential luminescence decay for 3P_0 .

2.7.2 Inokuti-Hirayama model

Numerous experimental studies reveal the necessity of energy transfer theories or methods able to interpret non-exponential experimental results. Inokuti and Hirayama [63] extended the Förster-Dexter model deriving a formula which establishes a non-

exponential time-dependent emission of donor ions in a system presenting energy transfers. Thus,

$$I(t) = I(0)e^{-(\frac{t}{\tau} + KC_{DA}t^{3/s})} \quad (2.28)$$

where τ is the intrinsic lifetime of the donor, C_{DA} is the energy transfer microparameter (section 1.5.2) and $s = 6$ for dipole-dipole (d-d), 8 for dipole-quadrupole (d-q) and 10 for quadrupole-quadrupole (q-q) inter-ionic interactions. The parameter K is given by the following equation:

$$K = \frac{4\pi}{3} N_A \Gamma(1 - \frac{3}{s}) \quad (2.29)$$

with N_A the acceptor concentration. The non-exponentiality of the Inokuti-Hirayama fluorescence decay arises from taking into account a distribution of donor-acceptor interaction distances. As shown by Eq.2.28, the beginning of the decay is dominated by the non-exponential term representing the emission of donor ions actively transferring energy to nearby acceptor ions. In contrast, the end of the decay presents the exponential decay of non-interacting donors (isolated). The Inokuti-Hirayama equation has been used in numerous occasions to reproduce non-exponential luminescence decays with quite successful results [171-173].

2.7.3 Monte Carlo (MC) methods

Approaches based on computational methods have been used in order to manage the distribution of distances between donor and acceptor ions within energy transfer models [174,175]. On a microscopic scale, the energy transfer rate for a direct donor-acceptor dipole-dipole interaction is given by the Förster-Dexter formula:

$$W_{DA} = \frac{C_{DA}}{R_{ij}^6} \quad (2.30)$$

in which R_{ij} is the distance between the donor “ i ” and the acceptor “ j ”. The total energy transfer rate is then the sum of energy transfer rates over all acceptors in the crystal [176]:

$$W_{DA} = \sum_{j=1}^n \frac{C_{DA}}{R_{ij}^6} \quad (2.31)$$

When considering the dopants as occupying random positions in the crystal lattice, the randomness makes that each donor may be surrounded by a particular environment of dopants referred to as *configuration*. Thus, each configuration gives rise to a transfer rate value based on all the donor-acceptor distances existing within the configuration (Eq.2.31). According to the notation used in the previous sections, the 3P_0 decay for a particular configuration of Yb^{3+} ions around a Pr^{3+} ion is given by Eq.2.32:

$$I_1(t)_{conf} \propto e^{-(R_1 + \alpha_{conf})t} \quad (2.32)$$

Then, taking into account the contribution of a large range of possible configurations in the crystal, the final 3P_0 luminescence decay is obtained by averaging over n exponential decays, ideally, with $n \rightarrow \infty$ [176].

$$\langle I_1(t)_{conf} \rangle \propto \langle e^{-(R_1 + \alpha_{conf})t} \rangle_n \quad (2.33)$$

Monte Carlo (MC) methods are used to place the dopants randomly at allowed lattice positions [176,177] and generate then a large number of configurations in order to simulate averaged 3P_0 luminescence decay curves (Eq.2.33). This technique has been previously used to describe the luminescence decay curves of donor ions in different crystalline systems [110,117,176]. A limited volume of crystal containing $7 \times 7 \times 7$ K^+ cubes (Fig.2.1), i.e. 1029 yttrium sites, was considered as the simulation box. The Y^{3+} sites were randomly filled with Y^{3+} or Yb^{3+} ions so as to keep the Yb^{3+} content equal to the Yb^{3+} concentration in the sample. The interaction distances were measured between a Pr^{3+} ion (donor) placed at the simulation box center and the Yb^{3+} ions (acceptors) forming the random configuration. The size of the simulation box is wide enough to provide meaningful results since interactions up to 33 Å are taken into account, and one can consider that the contribution to the global energy transfer rate of energy transfers over longer distances is negligible (Eq.2.31). The final decay curves were obtained from averaging over 30000 random configurations. The number of configurations chosen was found high enough to ensure the convergence of the result, knowing that the limit of convergence is given by the central limit theorem¹.

¹The central limit theorem (CLT) states that a set of independent random variables is sufficiently large when the variables are approximately normally distributed.

2.7.4 Modeling Result

Simulated praseodymium 3P_0 decay curves were obtained for Yb^{3+} dopant concentrations equal to 5%, 10% and 20% by using MC methods and the Inokuti-Hirayama model. Only dipole-dipole interactions were considered ($s=6$) since the dipole-dipole description already provides satisfying results. As displayed in Fig.2.15.a, the behavior of the MC simulations is particularly interesting, since it gives a simulated decay very close to the experimental decay. The energy transfer microparameter C_{DA} in Eq.2.31 was determined by fit and found equal to $5 \times 10^9 \text{ s}^{-1} \text{ \AA}^6$. The Inokuti-Hirayama model (IH) (Eq.2.28) also shows decent results, but not as accurate of the MC method (Fig.2.15.b). In the IH case, the energy transfer microparameter (C_{DA} in Eq.2.28) was found equal by fit to $3.7 \times 10^9 \text{ s}^{-1} \text{ \AA}^6$. The agreement in terms of lifetime values is excellent for the MC simulations but notably lower with the Inokuti-Hirayama model (Table 2.7).

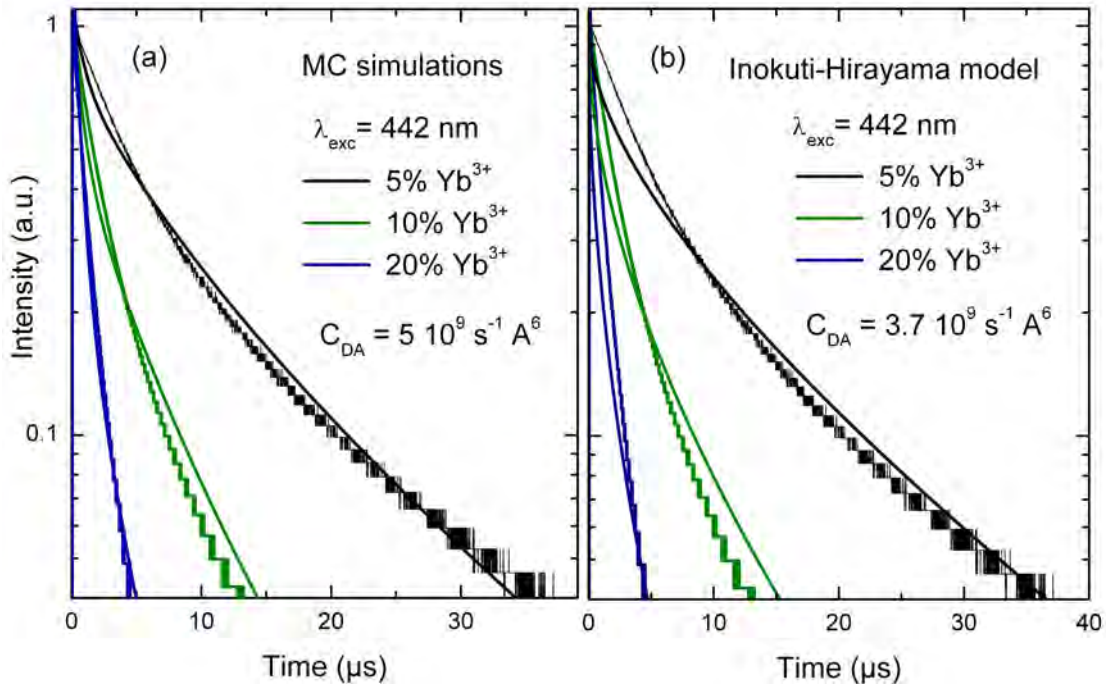


Figure 2.15: Experimental 3P_0 decay curves in $KY_3F_{10}:Pr^{3+}-Yb^{3+}$ compared to the simulated decays obtained by using (a) MC methods; (b) Inokuti-Hirayama equation (Eq.2.28).

The transfer microparameter C_{DA} for the energy transfer $Pr^{3+}(^3P_0 \rightarrow ^1G_4)$ to $Yb^{3+}(^2F_{7/2} \rightarrow ^2F_{5/2})$ was directly calculated with the spectral overlap between the donor emission spectrum (here $^3P_0 \rightarrow ^1G_4$) and the acceptor absorption ($^2F_{7/2} \rightarrow ^2F_{5/2}$) (Fig.2.16) and using the definition given by Eq.1.12. The result was $1.36 \times 10^9 \text{ s}^{-1} \text{ \AA}^6$. This value is notably lower than those obtained by fit from the MC simulations and the Inokuti-Hirayama

Table 2.7: Simulated and experimental 3P_0 lifetimes.

Sample	Exp (μs)	MC (μs)	IH (μs)
0.5%Pr ³⁺ -5%Yb ³⁺	8.3	8.2	9.4
0.5%Pr ³⁺ -10%Yb ³⁺	2.8	2.9	2.7
0.5%Pr ³⁺ -20%Yb ³⁺	1.2	1.2	0.9

model. Eq.1.12 provides a value of energy transfer microparameter which corresponds to a purely resonant energy transfer since it is directly derived from the spectral overlap (Fig.2.16). It does not take into account phonon-assisted energy transfer processes which could significantly contribute to the energy transfer efficiency.

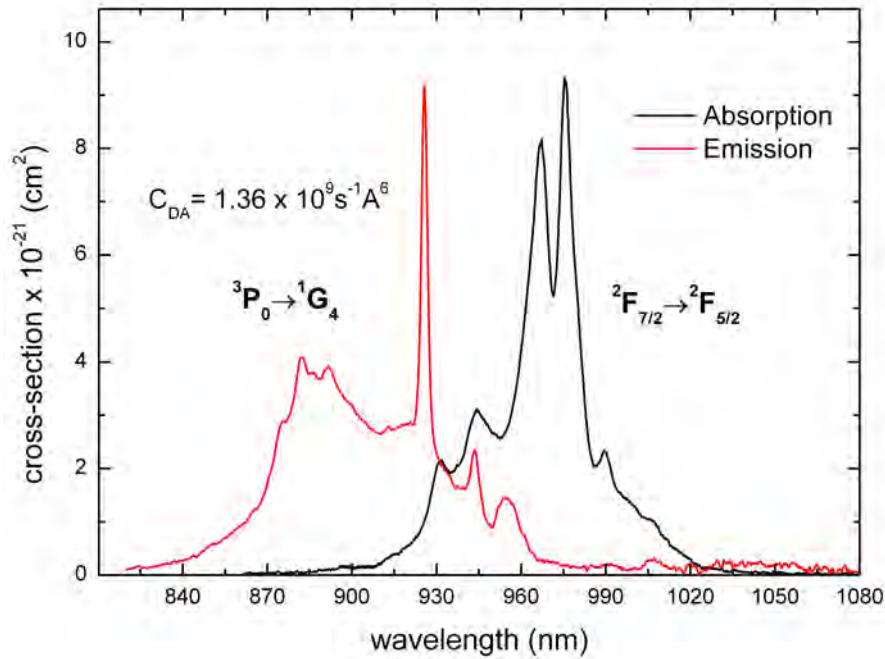


Figure 2.16: Spectral overlap between the Pr³⁺ $^3P_0 \rightarrow ^1G_4$ emission and Yb³⁺ $^2F_{7/2} \rightarrow ^2F_{5/2}$ absorption.

2.7.5 MC methods incorporated to the population rate-equations

Besides the good results obtained for the 3P_0 decays, MC methods may be used to simulate all the decay curves in the Pr³⁺-Yb³⁺ system including those of 1G_4 and $^2F_{5/2}$. This versatility is an additional advantage of the MC method in comparison with the

Inokuti model which can be only applied to single direct energy transfers. Thus, instead of using the classical definitions for the energy transfer rates β , γ and δ (Eq.2.8-2.11), these rates can be calculated for different configurations and so take into account the distribution of distances and the geometry of the crystal. The energy transfer with rate β is, like α , a direct donor-acceptor energy transfer $\text{Pr}^{3+}({}^1\text{G}_4 \rightarrow {}^3\text{H}_4)$ to $\text{Yb}^{3+}({}^2\text{F}_{7/2} \rightarrow {}^2\text{F}_{5/2})$. Thus, it can be also derived from Eq.2.31 in which C_{DA} is this time labeled as C_β referring to the second energy transfer. The energy transfer rates for the back-transfer γ and the concentration quenching process δ require taking into account the energy migration process. The migration process has been treated by MC methods in a variety of ways [178-181]. In our case, we used a simple approach which consists in summing over all the donor-donor and donor-acceptor distances in Eq.2.31 so as to take into account the donor-donor interaction given by the migration process.

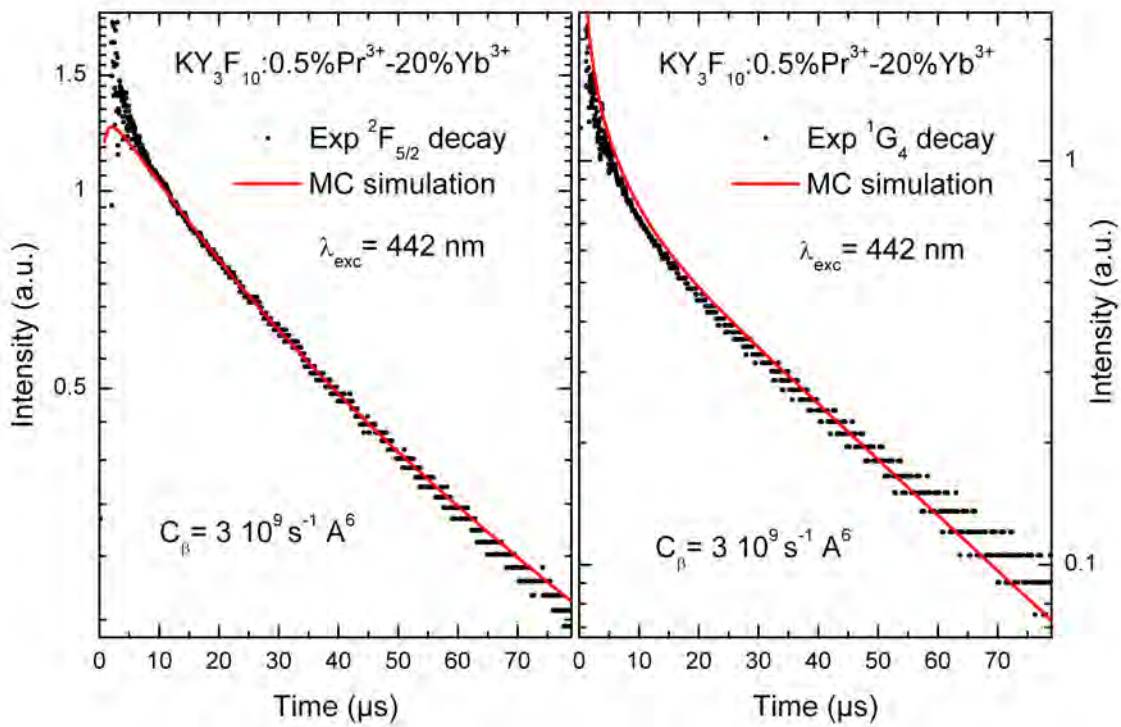


Figure 2.17: MC simulations of the ${}^2\text{F}_{5/2}$ (left) and ${}^1\text{G}_4$ decays (right) compared to the experimental curves for the $0.5\%\text{Pr}^{3+}\text{-}20\%\text{Yb}^{3+}$ codoped sample.

The energy transfer rates α , β , γ and δ , are calculated as previously described for a single random configuration and then, the three equations system 2.7, is solved in order to obtain the set of solutions $(n_1(t), n_2(t), n_3(t))_{conf}$ corresponding to the configuration. The operation is repeated over n configurations to finally obtain the averaged solutions

$\langle n_1(t) \rangle_n$, $\langle n_2(t) \rangle_n$, $\langle n_3(t) \rangle_n$ from which, the time-dependent luminescence of the 3P_0 , 1G_4 and $^2F_{5/2}$ levels are afterwards deduced.

Unlike, the case of 3P_0 , the fact that analytical solutions can not be found for the time-dependent 1G_4 and $^2F_{5/2}$ emissions involves a great computational complexity which may be even increased by using sophisticated approaches for the migration process. Good results for the 1G_4 and $^2F_{5/2}$ decays are obtained by combining the MC approach with the population rate-equations as displayed in Fig.2.17. Nevertheless, it involves a great calculation complexity without significantly improving the results in comparison with the classical rate-equation modeling solutions when the decays are exponential. Indeed, the migration process provides single exponential experimental decays [164] as it is verified for $^2F_{5/2}$ (Fig.2.7.b). Thus, unlike 3P_0 , the $^2F_{5/2}$ decays can be reproduced quite satisfyingly by the classical rate-equation model. The 1G_4 decays were found exponential under excitation at 940 nm (Fig.2.7.c) but non-exponential under excitation at 442 nm (Fig.2.7.d). The description of the non-exponential 1G_4 decays is improved by using MC methods (Fig.2.17) even when the classical rate-equation model also gives rise to non-exponential decay curves for 1G_4 upon 442 nm excitation. The possibility of using MC methods to model multiple energy transfer systems remains interesting in spite of the computational complexity since it is a very powerful technique which may provide good results beyond the classical rate equation model.

2.8 Conclusions Chapter 2

The quantum cutting mechanism within the $\text{Pr}^{3+}\text{-Yb}^{3+}$ system using KY_3F_{10} as host material was studied in this chapter. A series of $\text{KY}_3\text{F}_{10}\text{:}0.5\%\text{Pr}^{3+}\text{-}\times\%\text{Yb}^{3+}$ samples (with $\times = 0, 5, 10, 20$) were investigated. The analysis of the evolution with the Yb^{3+} content of the $^3\text{P}_0$, $^1\text{G}_4$ and $^2\text{F}_{5/2}$ emission spectra and fluorescence decays provided the first conclusions concerning the energy transfer efficiencies. A complete rate equation modeling was then developed and used to derive the energy transfer rates for the four energy transfer processes taking place in the $\text{Pr}^{3+}\text{-Yb}^{3+}$ system. We showed that the dynamics, especially for the $^1\text{G}_4$, and $^2\text{F}_{5/2}$ levels, are not simple and must be interpreted with special care as they result from the interactions of four different energy transfers. In addition, two of the energy transfers go back and forth between the $^1\text{G}_4$, and $^2\text{F}_{5/2}$ levels and thus create a thermal equilibrium between these two levels making the system even more complicated.

In terms of possible application, while the downconversion process is efficient in $\text{KY}_3\text{F}_{10}\text{:Pr}^{3+}\text{-Yb}^{3+}$, a great part of the infrared emissions do not come from the Yb^{3+} ions but from the Pr^{3+} ions because of the efficient back-transfer processes from Yb^{3+} to Pr^{3+} ions. The strong quenching of the Yb^{3+} lifetime is thus a major obstacle for a possible application of $\text{KY}_3\text{F}_{10}\text{:Pr}^{3+}\text{-Yb}^{3+}$ in solar downconverters.

The rate-equation modeling was further developed by incorporating Monte-Carlo methods achieving good descriptions of the experimental decays. The limits of the assumptions within the classical rate-equations were discussed to show the importance of taking explicitly into account the lattice positions within the modeling.

Clusters and energy transfers in $\text{CaF}_2:\text{Pr}^{3+}-\text{Yb}^{3+}$

3.1 Introduction

CaF_2 is a well-known fluoride material that has been used for a long time in optical components due to its wide transparency spectral range extending into the UV, and its good thermal conductivity. The possibility of fabricating rare-earth doped CaF_2 bulk crystals by using standard techniques such as Bridgman, Czochralski, and thin films by molecular beam epitaxy (MBE) [182] or liquid phase epitaxy (LPE) [183] increases the current interest for this material for laser and optical applications [184-186].

CaF_2 shows several remarkable properties when it is doped with trivalent rare-earth ions. As a fluoride material, it shares with KY_3F_{10} the property of having relatively low maximum phonon frequency ($<495 \text{ cm}^{-1}$). Non radiative relaxations between adjacent rare-earth energy levels are thus very much reduced allowing many visible and infrared optical transitions as well as efficient energy transfers. In addition, it is well known that the incorporation of trivalent rare-earth ions into the CaF_2 structure is accompanied by charge-compensating defects which give rise to different types of centers either comprising one rare-earth ion or several rare-earth ions within a cluster.

In terms of photonic applications, the presence of a large number of rare-earth clusters in rare-earth doped CaF_2 can be beneficial or not depending on the intended application. On the one hand, the complex site structure generally leads to optical transitions characterized by broad bands. Therefore, CaF_2 presents the same advantages as glasses since these broad-bands can be used advantageously for the production of broadly tunable ultra-fast diode-pumped solid-state lasers but keeping, at the same time, the advantages

of single crystals. A remarkable example of this is found with Ytterbium doped CaF_2 . Ytterbium ions experience important clustering in CaF_2 giving rise to large absorption and emission bands which are now used to develop very efficient high power laser amplifier systems and femtosecond lasers [186]. Thus, CaF_2 is a very attractive host for laser and optical applications, combining advantages of fluoride crystals and glass-like spectroscopic properties.

Another interesting consequence of rare-earth clustering is the occurrence of very efficient energy transfer processes between rare-earth ions because of the short distance between the ions forming the cluster. These energy transfers can be advantageously exploited for upconversion and downconversion applications. For instance, cross-relaxation processes among Tm^{3+} ions are used to excite two Tm^{3+} ions per pump photon for the development of efficient $2\ \mu\text{m}$ lasers in Tm^{3+} doped CaF_2 [184]. Also, efficient upconversion with Er^{3+} and Yb^{3+} ions using CaF_2 as fluoride host has been reported [96]. On the other hand, the rare-earth clustering might present important disadvantages depending on the application. In several cases, cross-relaxation processes within clusters are a major source of optical losses and can lead to the quenching of the optical emission under consideration as it happens for Nd^{3+} for which, the cross-relaxation processes in the Nd^{3+} clusters impair Nd^{3+} doped CaF_2 to be used as a laser material [187].

3.2 Rare-earth clustering in CaF_2 : general concepts

CaF_2 , the same that SrF_2 and BaF_2 , present an optically isotropic *fluorite* structure in which the Ca^{2+} ions form a face-centered cube (FCC) lattice with lattice parameter equal to $5.462\ \text{\AA}$, and the F^- ions are placed in a simple cubic arrangement at the tetrahedral holes. Another view, as displayed in Fig.3.1, is that the structure consists of a simple cubic lattice of fluorine ions with every other body-center position occupied by divalent calcium.

When trivalent rare-earth ions are introduced into the lattice, they replace the divalent Ca^{2+} sites. Thus, charge compensation is required in order to balance the additional positive charge introduced by the dopant. Following a wide number of structural studies based on experimental techniques such as electron paramagnetic resonance spectroscopy (EPR) [188-197], nuclear magnetic resonance (NMR) [198], dielectric relaxation spectroscopy (DRS) [199-201], ionic thermocurrent measurements (ITM) [202-204], electron-nuclear double resonance (ENDOR) [205], [206], optical spectroscopy [77],

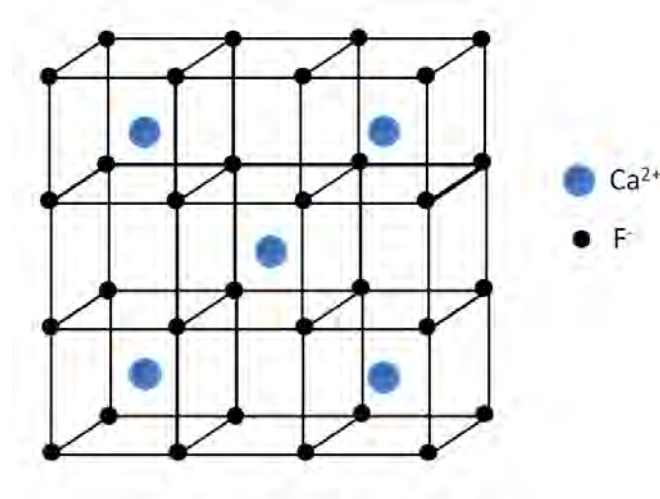


Figure 3.1: CaF_2 crystal structure.

[94,187,207-209], selective laser excitation [71,210-214], extended X-ray absorption fine structure (EXAFS) [215] or transmission electron microscopy (TEM) [216] as well as detailed calculations and computer simulations [217-219], it was concluded that charge compensation could be achieved in several ways depending on the rare-earth size, the lattice parameter (progressively increasing from CaF_2 to SrF_2 and BaF_2) [218], the doping concentration and the sample thermal treatments [220].

The main sites resulting from the different charge compensation mechanisms are the following:

3.2.1 Single ions sites

Cubic symmetry (O_h)

Cubic symmetry is observed when charge compensation is not achieved locally (Fig.3.2). In the late fifties [189], trivalent rare-earths were proved to be able to occupy cubic sites in CaF_2 and since then, cubic symmetry has been reported in a large number of studies concerning RE^{3+} doped CaF_2 , with the second half of the rare-earth ions series (number of $4f$ over 7) more usually found in cubic sites than the first half ones [221]. The formation of these sites has been demonstrated to be strongly dependent on the thermal treatment of the sample. Thus, at elevated temperatures, dissociation of ion-defect pairs occurs, generating cubic sites [220]. Moreover, the existence of cubic sites in the sample appears to be favored by the presence of other chemical species in the host, for instance Na^+ or Li^+ , since they balance the overall charge excess [222,223].

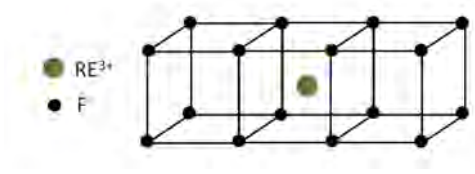
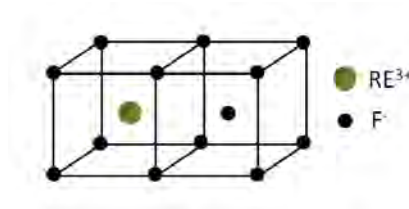


Figure 3.2: Uncompensated cubic symmetry.

Tetragonal symmetry (C_{4v})

Charge compensation can be achieved by the presence of a F^- ion in one of the nearest-neighbor (NN) interstitial sites (Fig.3.3). Evidence of this compensation mechanism was first reported by Bleaney et al. in 1956 for $\text{CaF}_2:\text{U}^{3+}$ [188]. Currently, it is known that the so-called NN aggregates are particularly stable [217], especially for rare-earth ions larger than Gd^{3+} (the ionic radius progressively decreases from Ce^{3+} to Yb^{3+} in the lanthanide series). This mechanism is usually considered as the dominant charge compensation mechanism in rare-earth doped CaF_2 for all trivalent rare-earth ions.

Figure 3.3: Next neighbor (NN) C_{4v} symmetry cluster.

Trigonal symmetry (C_{3v})

Several trigonal symmetry sites related to different charge compensation mechanisms have been reported so far [190,205,224-226]. Some authors suggested that C_{3v} sites could be produced by the replacement of one of the eight nearest-neighbor F^- ions by an O^{2-} as shown in Fig.3.4-left. On the other hand, Ranon et al. [227] proposed a trigonal site in which charge compensation is ensured by an interstitial fluorine ion occupying one of the next-nearest neighbors (NNN) interstitial sites (Fig.3.4-right). The NNN aggregates are expected to be commonly found in rare-earth doped CaF_2 since they were demonstrated to be stable and even dominant in comparison to the NN aggregates when the considered rare-earth dopant presents a small radius [228].

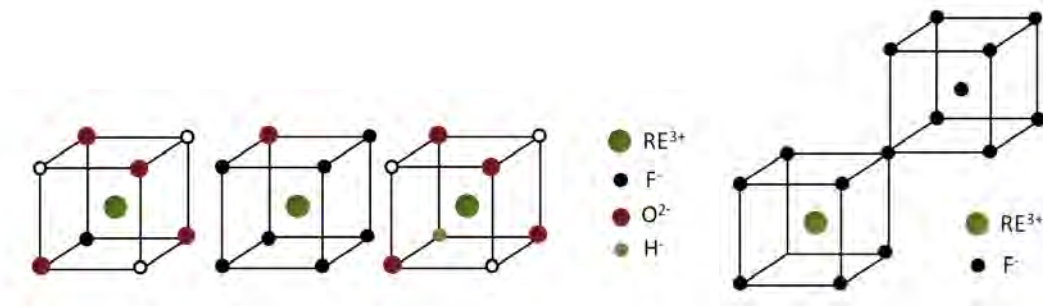


Figure 3.4: (Left) O^{2-} compensated C_{3v} sites, from left to right: T_1 configuration, T_2 configuration, T_3 configuration; (Right) Next-nearest neighbor (NNN) C_{3v} symmetry cluster.

Lower symmetry sites

A variety of low symmetry configurations such as rhombic sites (C_{2v}) have been reported in the literature [211], [229]. However, these are minor configurations regarding the before described tetragonal, cubic and trigonal sites.

3.2.2 Higher order aggregates or clusters

It has become clear that clustering is significant in rare-earth-doped calcium fluoride even for small concentrations of dopants, as for instance 0.05% Pr^{3+} [230]. In 1964, the possible formation of energetically favored aggregates or RE clusters in CaF_2 was firstly suggested [221]. Since then, a large number of experimental evidences of clustering have been found [231]. Theoretical calculations were performed in the eighties with the aim of determining the lowest energy configurations in $CaF_2:RE^{3+}$. These calculations were shown to be useful to get a better understanding of the clustering process [217,218,232]. Indeed, the conclusions obtained from the theoretical calculations are still considered as a reference.

Two distinct ranges of doping are necessary in order to classify the high-order aggregates:

Slightly doped ($< 0.1\%at$) and moderately doped ($< 1\%at$.) CaF_2

The simplest cluster, a dimer, (two coupled rare-earth ions), has been identified even in slightly doped CaF_2 crystals [233,234]. These experimental results are in agreement with the theoretical calculations of Catlow et al. [217], which showed that dimers are very stable in CaF_2 even at small rare-earth concentrations. Moreover, two different symmetries are possible as represented in Fig.3.5: a dimer structure originating from the

aggregation of two NN monomers (Fig.3.5-left), and a dimer resulting from the aggregation of two NNN monomers (Fig.3.5-right). The NN dimers are expected to be dominant when composed of large size rare-earth ions. On the contrary, the presence of NNN dimers increases when doping with small rare-earth ions.

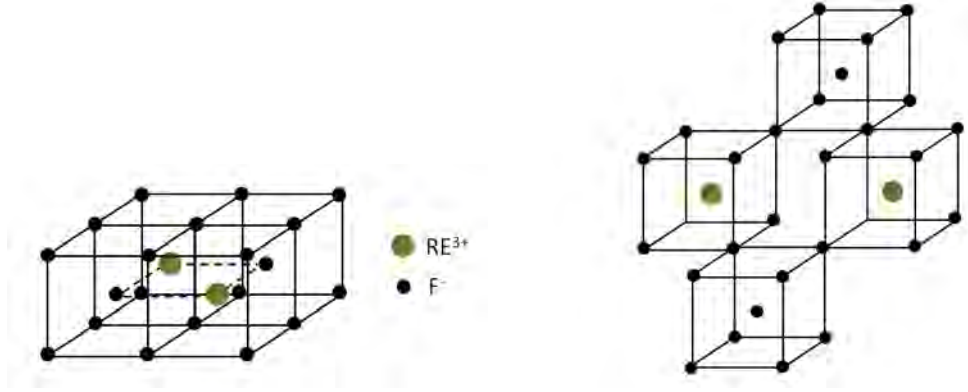


Figure 3.5: NN type dimer (left) and NNN type dimer (right).

The rare-earth aggregates were also investigated in the SrF_2 and BaF_2 fluorite structures [217]. The different lattice parameter (progressively increasing from CaF_2 to SrF_2 and BaF_2) also plays a role in the clustering tendency. Besides the decreasing ionic radius, the NNN dimers are also favored by an increasing lattice parameter. Thus, in SrF_2 and BaF_2 , NNN dimers are expected to be more stable and so more abundant than in CaF_2 .

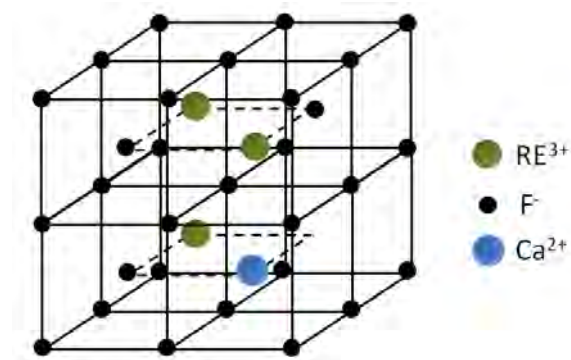


Figure 3.6: Trimer structure.

When the rare-earth concentration is increased, the formation of trimers i.e. three associated rare-earth ion aggregates (Fig.3.6), is supposed to be more probable. However, Moore et al. already identified clusters greater than dimers in CaF_2 doped 0.01% Er^{3+} [235]. Theoretically, the energy of formation of a trimer from a monomer and a dimer

indicates that trimers can be indeed as stable as dimers [218]. It also means that trimers must be expected in CaF_2 at relatively low concentrations.

For small rare-earth ions such as Yb^{3+} , higher order aggregates or superstructures are also possible within this concentration range. In a general way it is concluded that the smaller the rare earth ion is, the more stable are the high-order structures it creates.

Heavily doped CaF_2 ($>1\% \text{at.}$)

Rare-earth heavily doped CaF_2 crystals usually present a complicated multiple site structure related to a variety of cluster sites. The theoretical studies performed by Bendall et al. in 1984 [218], established the configuration of the most stable clusters at high rare-earth concentrations in the CaF_2 , SrF_2 and BaF_2 lattices.

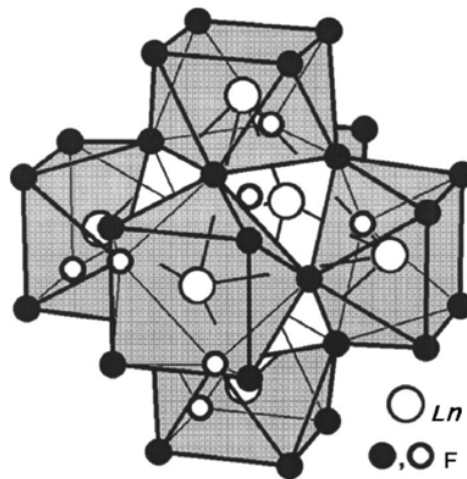


Figure 3.7: Hexameric cluster Ln_6F_{36} [195].

As mentioned previously, the stability of the high-order clusters increases when the ionic radius of the rare-earth ion decreases. Thus, for large rare-earth ions such as Ce^{3+} or Nd^{3+} , at high concentrations, the predominance of small clusters such as dimers or trimers is expected. On the contrary, in the case of small rare-earth ions, superstructures may become stable or even dominant. Indeed, according to the calculations, superstructures start to occur with trivalent Y^{3+} . Y^{3+} ions show a tremendous ability to form clusters of any kind, which is probably related to its small ionic radius. When considering the formation of high-order structures it is important to take into account the stability of the lower order structures from which the superstructures are, in principle, originated. Thus,

for instance, a stable tetramer will be the one originating from two stable dimers (NN or NNN), and the same for hexamers (Fig.3.7), which may derive from three stable dimers, or even two trimers.

Several experimental studies have been undertaken in order to identify the different rare-earth incorporation sites including cluster superstructures. However, to get information about the higher-order clustering process is a very difficult task [216,219,233,236,237]. The tendency obtained from theoretical estimations is mostly in agreement with the experiments. A majority of dimers and trimers sites was suggested for Pr^{3+} in CaF_2 with a doping concentration of 0.1% [211]. On the contrary, for the same concentration, the presence of hexamers was shown in the case of CaF_2 : Er^{3+} [235] and was also reported by Kazanskii et al., for Er^{3+} , Tm^{3+} and Yb^{3+} doped CaF_2 [195].

3.3 Experimental methods

A series of Pr^{3+} - Yb^{3+} and Pr^{3+} - Lu^{3+} codoped CaF_2 crystals were grown in our laboratory by using the *Bridgman-Stockbarger* technique. The growth technique was briefly described in the previous chapter (section 2.2). After growth, the samples were prepared for experiments in three different ways which are: plates with a 3 mm thickness; thin disks with a 200 μm thickness and powders. Like in the case of the KY_3F_{10} : Pr^{3+} - Yb^{3+} codoped samples (Table 2.1), the real dopant concentrations in the CaF_2 crystals were measured by using the inductively coupled plasma (ICP) technique and assessed by absorption measurements using calibrated reference samples. Both methods demonstrated real dopant concentrations very close to the nominal concentrations in the melt as shown in Table 3.1.

Table 3.1: CaF_2 : Pr^{3+} - X^{3+} ($\text{X}=\text{Yb}^{3+}$ or Lu^{3+}) investigated samples.

Nominal concentrations	Real concentrations
0.5% Pr^{3+}	0.48% Pr^{3+}
0.5% Pr^{3+} -0.5% Yb^{3+}	0.51% Pr^{3+} -0.50% Yb^{3+}
0.5% Pr^{3+} -1% Yb^{3+}	0.46% Pr^{3+} -0.98% Yb^{3+}
0.5% Pr^{3+} -2% Yb^{3+}	0.55% Pr^{3+} -2.05% Yb^{3+}
0.5% Pr^{3+} -4% Yb^{3+}	0.5% Pr^{3+} -4% Yb^{3+}

Low temperature and room temperature absorption spectra were carried out with a Perkin-Elmer Lambda 1050 spectrophotometer. The low temperature absorption experiments were performed by mounting the samples in a closed-cycle helium cryostat and by cooling them down to 11 K. Pr^{3+} emission spectra were recorded by exciting the samples with a continuous wave laser diode (Nichia-NDHB510APAE1) at 442 nm. The light emitted by the different samples was dispersed by a 0.5m Jobin-Yvon HRS2 monochromator (gratings of 1200 l/mm blazed at 500 nm and 600 l/mm blazed at 1 μm) and detected using a standard lock-in amplifier technique associated to different detectors (PM tubes or InGaAs photodiodes) depending of the detection wavelength. Emission decays and time-resolved spectra were carried out using an OPO (GWU) pumped by the third harmonic (355 nm) of a Nd:YAG nanosecond pulsed laser. After dispersion by a 0.25m ORIEL monochromator, the luminescent transient signals obtained after pulsed excitation were fed into a digital oscilloscope. All the experimental recordings were corrected afterwards from the setup response.

3.4 Quantum cutting with CaF_2 : Pr^{3+} - Yb^{3+}

The energy transfers between Pr^{3+} and Yb^{3+} ions in CaF_2 are investigated in the next section for the different Pr^{3+} - Yb^{3+} codoped CaF_2 samples presented in Table 3.1.

3.4.1 CaF_2 : Pr^{3+} - Yb^{3+} spectroscopy

Room temperature Pr^{3+} emission spectra in the 590-650 nm range were recorded under blue light excitation at 442 nm ($^3\text{H}_4 \rightarrow ^3\text{P}_2$) for all samples. The Pr^{3+} emissions recorded around 605 nm and 640 nm are presented in Fig.3.8. The peaks around 640 nm can be ascribed unambiguously to the $^3\text{P}_0 \rightarrow ^3\text{F}_2$ transition. On the contrary, this is not the case of the peaks between 600 nm and 608 nm which can arise not only from the $^3\text{P}_0 \rightarrow ^3\text{H}_6$ transition but also from the $^1\text{D}_2 \rightarrow ^3\text{H}_4$ transition. The doubt is nevertheless easily solved since the same luminescence decay is observed both around 605 nm and around 640 nm for all samples whether they are codoped with Pr^{3+} and Yb^{3+} ions or singly doped with Pr^{3+} ions (Fig.3.9). In consequence, the peaks around 600 nm clearly correspond for all samples to the $^3\text{P}_0 \rightarrow ^3\text{H}_6$ transition and not to the $^1\text{D}_2 \rightarrow ^3\text{H}_4$ transition. Furthermore, the $^1\text{D}_2$ level decay recorded at 828 nm ($^3\text{H}_4 \rightarrow ^1\text{D}_2$) under direct excitation at 590 nm ($^3\text{H}_4 \rightarrow ^1\text{D}_2$) is clearly different from the $^3\text{P}_0$ level recorded at 640 and 605 nm as illustrated in Fig.3.9 for CaF_2 :0.5% Pr^{3+} and CaF_2 :0.5% Pr^{3+} -4% Yb^{3+} .

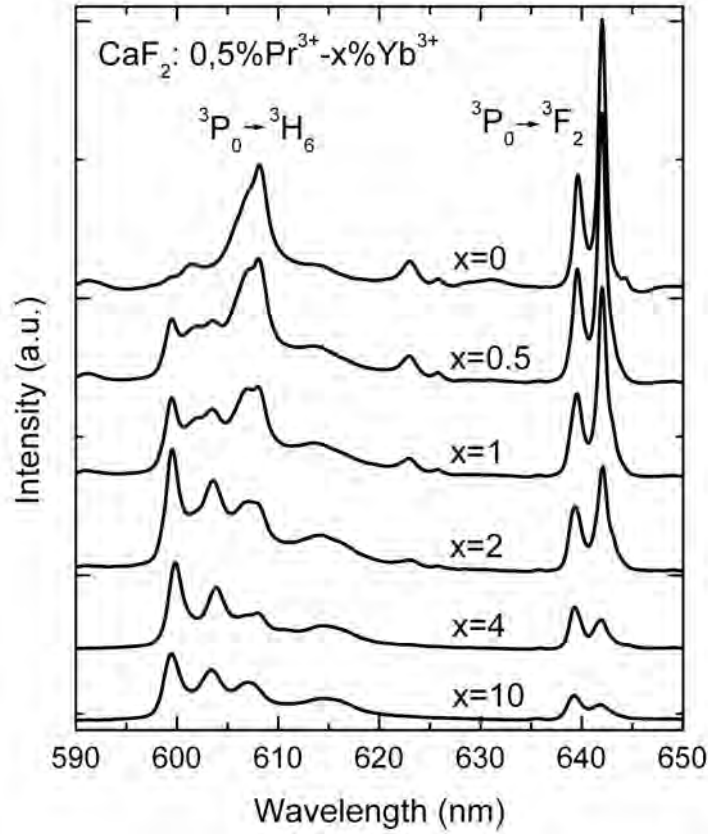


Figure 3.8: Room temperature Pr^{3+} emission spectra under blue excitation at 442 nm ($^3\text{P}_2$) in $\text{CaF}_2:0.5\%\text{Pr}^{3+}-x\%\text{Yb}^{3+}$ ($x = 0, 0.5, 1, 2, 4, 10$).

A significant emission from $^1\text{D}_2$ under $^3\text{P}_2$ excitation around 442 nm can be observed in materials having a large maximum phonon energy [238] (700 cm^{-1} and more) in which case the excited Pr^{3+} ions relax non-radiatively by multiphonon emission from the $^3\text{P}_0$ level down to the $^1\text{D}_2$ level located around 4000 cm^{-1} below. On the contrary, in fluoride materials the maximum phonon energy is rather small ($\sim 450\text{ cm}^{-1}$) making the multiphonon relaxation from $^3\text{P}_0$ to $^1\text{D}_2$ very unlikely.

The $^3\text{P}_0$ luminescence decays under blue excitation are presented in Fig.3.10 for all samples having the same $0.5\%\text{Pr}^{3+}$ concentration. The $^3\text{P}_0$ decay becomes shorter and shorter as the Yb^{3+} concentration is raised because of the $\text{Pr}^{3+} \rightarrow \text{Yb}^{3+}$ energy transfer. The efficiency of the $\text{Pr}^{3+} \rightarrow \text{Yb}^{3+}$ energy transfer appears to be remarkable since the $^3\text{P}_0$ lifetime decreases by a factor of 120 from $150\text{ }\mu\text{s}$ for singly Pr^{3+} doped CaF_2 , down to $1.3\text{ }\mu\text{s}$ with only $10\%\text{Yb}^{3+}$ in $\text{CaF}_2:0.5\%\text{Pr}^{3+}-10\%\text{Yb}^{3+}$. For comparison, a decrease by a factor of 30 (four times less than in $\text{CaF}_2:0.5\%\text{Pr}^{3+}-10\%\text{Yb}^{3+}$) of the $^3\text{P}_0$ lifetime because of the $\text{Pr}^{3+} \rightarrow \text{Yb}^{3+}$ energy transfer was observed with $20\%\text{Yb}^{3+}$ in $\text{KY}_3\text{F}_{10}:0.5\%\text{Pr}^{3+}-20\%\text{Yb}^{3+}$ (see in Chapter 2), KY_3F_{10} being a fluoride material with a random distribution of dopants

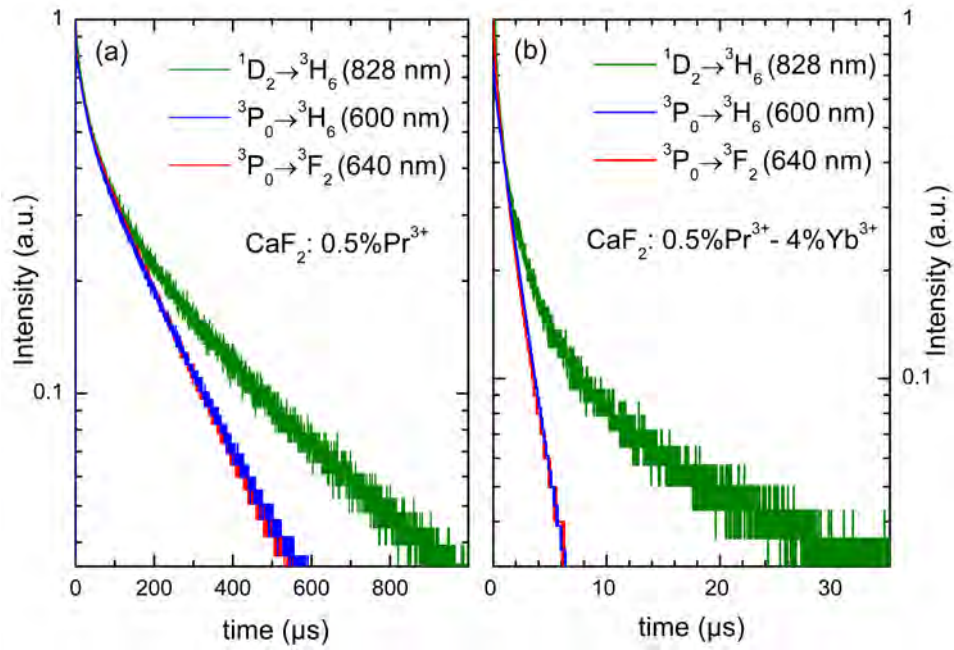


Figure 3.9: 3P_0 decay curves recorded at 605 nm ($^3P_0 \rightarrow ^3H_6$) and 640 nm ($^3P_0 \rightarrow ^3F_2$) with $\lambda_{exc}=442$ nm and 1D_2 decay curve recorded at 828 nm ($^1D_2 \rightarrow ^3H_6$) with $\lambda_{exc}=590$ nm: (a) $\text{CaF}_2:0.5\%\text{Pr}^{3+}$ and (b) $\text{CaF}_2:0.5\%\text{Pr}^{3+}-4\%\text{Yb}^{3+}$.

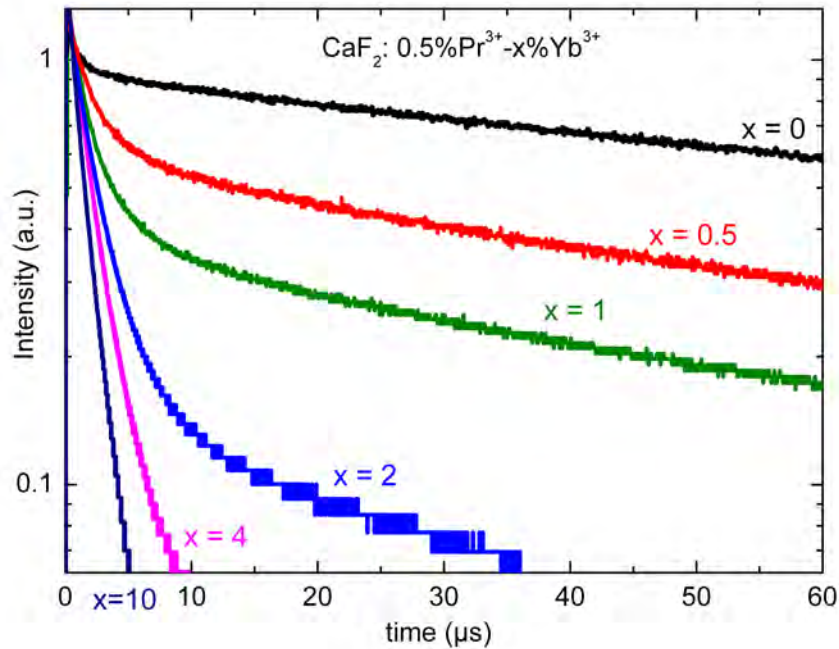


Figure 3.10: 3P_0 decay curves recorded at 607 nm ($^3P_0 \rightarrow ^3H_6$) in $\text{CaF}_2:0.5\%\text{Pr}^{3+}-x\%\text{Yb}^{3+}$ ($x=0, 0.5, 1, 2, 4, 10$) under blue excitation at 442 nm (3P_2).

unlike CaF_2 . This unusual efficiency of Pr^{3+} to Yb^{3+} energy transfer in CaF_2 is due to the rare-earth ion clustering effect taking place in this host enabling a very short distance between rare-earth ions and thus very efficient energy transfers.

The $^3\text{P}_0$ decay in CaF_2 :0.5% Pr^{3+} -4% Yb^{3+} and CaF_2 :0.5% Pr^{3+} -10% Yb^{3+} is exponential (Fig.3.10) while the other decays for the Pr^{3+} - Yb^{3+} codoped samples clearly exhibit non-exponential features. As will be discussed further in the text, this non-exponential character of the decays is due to the presence of two Pr^{3+} luminescent centers. These two Pr^{3+} centers already appear in the monotonic change observed in the shape of the Pr^{3+} emission spectra with the Yb^{3+} concentration in Fig.3.8. The first center, whose emission spectrum appears for singly doped Pr^{3+} samples ($\times=0\%$ in Fig.3.8), corresponds to “isolated” Pr^{3+} ions, in other words Pr^{3+} ions non-coupled to Yb^{3+} ions. When codoping with Yb^{3+} ions, a change in the emission spectrum is clearly seen for the $^3\text{P}_0 \rightarrow ^3\text{H}_6$ transition with new emission peaks appearing at 600 nm and 604 nm and can be also observed for the $^3\text{P}_0 \rightarrow ^3\text{F}_2$ transition. This new Pr^{3+} emission spectrum emerging in addition to the first spectrum is likely due to the incorporation of Yb^{3+} ions in the vicinity of Pr^{3+} ions forming Pr^{3+} - Yb^{3+} clusters. As the Yb^{3+} concentration increases, the Pr^{3+} - Yb^{3+} cluster emission spectrum becomes more and more prominent and for an Yb^{3+} concentration equal to 4%at., the Pr^{3+} - Yb^{3+} cluster emission spectrum dominates. This result shows that when the Yb^{3+} concentration reaches 4%at., the emission spectrum related to non-coupled Pr^{3+} ions can no longer be observed meaning that the majority of Pr^{3+} ions are coupled to Yb^{3+} ions.

Evidence that most Pr^{3+} ions are within Pr^{3+} - Yb^{3+} clusters for an Yb^{3+} concentration of 4% or higher is found when recording the emission from the $^1\text{G}_4$ level. Fig.3.11 shows the Pr^{3+} emission spectrum around 1.3 μm ($^1\text{G}_4 \rightarrow ^3\text{H}_5$ transition) obtained under direct Pr^{3+} excitation at 457 nm ($^3\text{H}_4 \rightarrow ^3\text{P}_1$) and under Yb^{3+} excitation at 920 nm in CaF_2 :0.5% Pr^{3+} -0.5% Yb^{3+} and CaF_2 :0.5% Pr^{3+} -4% Yb^{3+} . The direct Pr^{3+} excitation excites all Pr^{3+} ions whether they are coupled to Yb^{3+} ions or not. On the contrary, the Yb^{3+} excitation only leads to the emission from Pr^{3+} ions which are coupled to Yb^{3+} ions and therefore excited by energy transfer from Yb^{3+} to Pr^{3+} ions. Interestingly, in CaF_2 :0.5% Pr^{3+} -0.5% Yb^{3+} , the Pr^{3+} emission spectrum (Fig.3.11.a) is different under direct Pr^{3+} excitation and under Yb^{3+} excitation indicating that some Pr^{3+} ions are effectively coupled to Yb^{3+} ions while some Pr^{3+} ions remain isolated. In contrast, for CaF_2 :0.5% Pr^{3+} -4% Yb^{3+} both spectra are identical (Fig.3.11.b), meaning that the same Pr^{3+} ions are excited when directly exciting all Pr^{3+} ions or going through Yb^{3+} ions. In

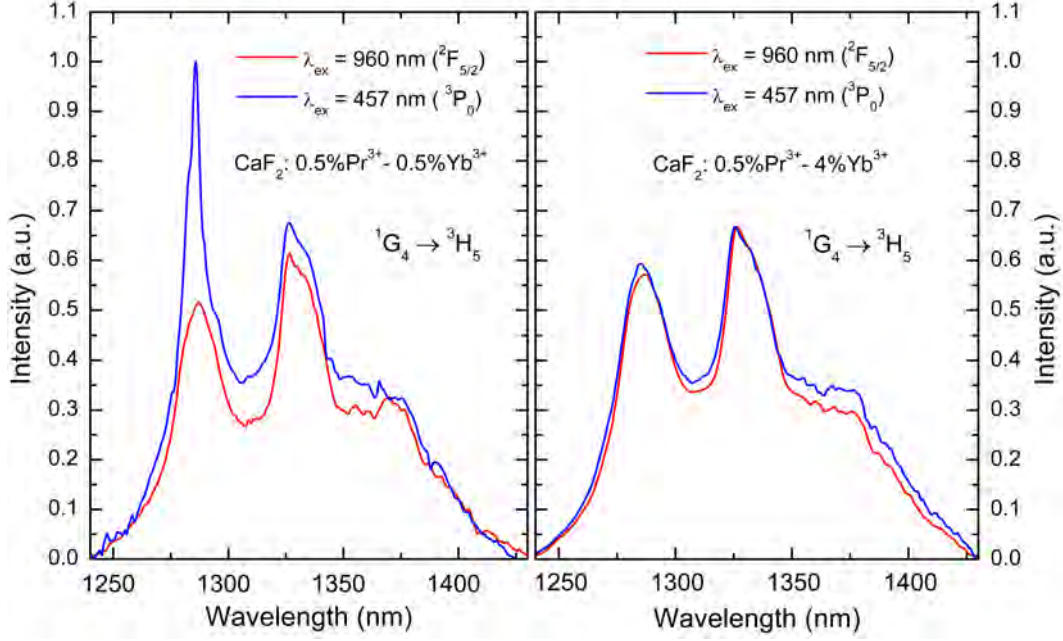


Figure 3.11: Room temperature Pr^{3+} emission spectra around $1.3 \mu\text{m}$ ($^1G_4 \rightarrow ^3H_5$) under Pr^{3+} excitation at 457 nm (3P_1) and under Yb^{3+} excitation in (a) $\text{CaF}_2:0.5\%\text{Pr}^{3+}-0.5\%\text{Yb}^{3+}$ (b) and $\text{CaF}_2:0.5\%\text{Pr}^{3+}-4\%\text{Yb}^{3+}$.

other words, this result shows again that the majority of Pr^{3+} ions are coupled to Yb^{3+} ions in $\text{CaF}_2:0.5\%\text{Pr}^{3+}-4\%\text{Yb}^{3+}$.

In a remarkable way, time-resolved spectroscopy experiments enable us to clearly dissociate contributions from non-coupled Pr^{3+} ions and $\text{Pr}^{3+}\text{-Yb}^{3+}$ clusters in samples where both centers coexist. The non-exponential features of the 3P_0 decays observed in Fig.3.12 for codoped samples (except $\text{CaF}_2:0.5\%\text{Pr}^{3+}-4\%\text{Yb}^{3+}$ and $\text{CaF}_2:0.5\%\text{Pr}^{3+}-10\%\text{Yb}^{3+}$) consist of two components: a very fast component dominating in the first microseconds and a slow component. Time-resolved spectra were recorded within the corresponding time windows as displayed in Fig.3.12 for $\text{CaF}_2:0.5\%\text{Pr}^{3+}-2\%\text{Yb}^{3+}$. For the fast component (Fig.3.12.a), the resulting spectrum recorded within the first $10 \mu\text{s}$ is the $\text{Pr}^{3+}\text{-Yb}^{3+}$ cluster emission spectrum observed with $x=4\%$ and $x=10\%$ in Fig.3.8 with no visible contribution from the non-coupled Pr^{3+} ions emission spectrum. On the contrary, for the long part of the decay (Fig.3.12.b) the non-coupled Pr^{3+} emission spectrum is solely observed and is identical to $x=0\%$ in Fig.3.8. The very rapid 3P_0 decay associated with $\text{Pr}^{3+}\text{-Yb}^{3+}$ clusters indicates a very efficient energy transfer from Pr^{3+} to Yb^{3+} ions within the clusters while the long 3P_0 decay of non-coupled Pr^{3+} ions shows that their coupling with Yb^{3+} ions is very weak.

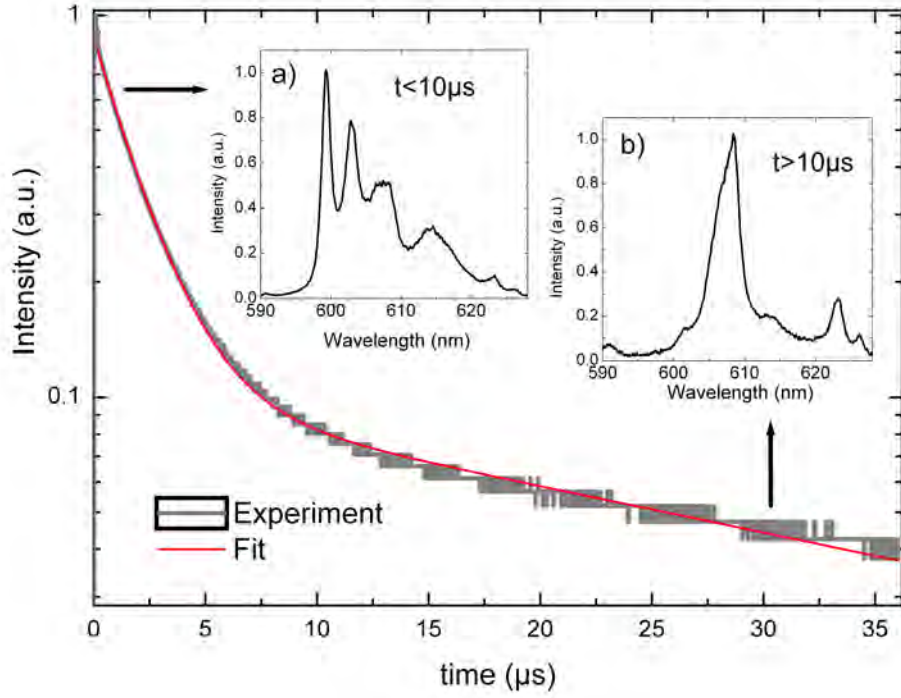


Figure 3.12: $^3\text{P}_0$ decay curve recorded at 607 nm ($^3\text{P}_0 \rightarrow ^3\text{H}_6$) with $\lambda_{exc}=442$ nm in $\text{CaF}_2:0.5\%\text{Pr}^{3+}-2\%\text{Yb}^{3+}$. The solid line represents a two-exponential fit of the decay. Insets: time-resolved spectra for the first 10 μs (a) and for the long part of the decay ($t > 10 \mu\text{s}$).

3.4.2 Determination of the first energy transfer efficiency

The experimental decays shown in Fig.3.10 were accurately adjusted with a double exponential fit to determine the values of the fast and slow decay components (Fig.3.12). The $^3\text{P}_0$ lifetime for Pr^{3+} - Yb^{3+} clusters derived from the fast decay component (Table 3.2) enables to quantify the energy transfer efficiency (ETE) from $\text{Pr}^{3+}(^3\text{P}_0 \rightarrow ^1\text{G}_4)$ to $\text{Yb}^{3+}(^2\text{F}_{7/2} \rightarrow ^2\text{F}_{5/2})$ within the clusters. The ETE for the first energy transfer was defined in Chapter 2 as the ratio between the energy transfer rate and the total relaxation rate comprising the energy transfer rate, the radiative decay rate and the multiphonon relaxation rate (Eq.2.3). The ETE was calculated by applying Eq.2.3 separately to the two decay components. Furthermore, an accurate ETE calculation must take into account the fact that the intrinsic lifetime in Pr^{3+} - Yb^{3+} clusters is not the same as for the “isolated” Pr^{3+} ions ($\tau=150 \mu\text{s}$) since both centers have different local environments. A detailed investigation, which will be described in section 3.6, shows that the intrinsic lifetime in the Pr^{3+} - Yb^{3+} clusters is actually 80 μs and not 150 μs .

Table 3.2: 3P_0 lifetime and ETE for the $\text{Pr}^{3+}(^3P_0 \rightarrow ^1G_4)$ to $\text{Yb}^{3+}(^2F_{7/2} \rightarrow ^2F_{5/2})$ ET as a function of the Yb^{3+} concentration. “fc” and “lc” stand for the fast and long components of the fluorescence decays respectively. The decrease of the long component with the Yb^{3+} concentration shows that energy transfer, although not very efficient, takes place between “isolated” Pr^{3+} ions and Yb^{3+} ions.

$\text{CaF}_2:0.5\%\text{Pr}^{3+}-\times\%\text{Yb}^{3+}$	$\times=0$	$\times=0.5$	$\times=1$	$\times=2$	$\times=4$	$\times=10$
$\tau_{^3P_0}$ (μs) single ions (lc)	150	120	105	75	-	-
$\tau_{^3P_0}$ (μs) $\text{Pr}^{3+}\text{-Yb}^{3+}$ clusters (fc)	80	8.5	4.5	3.7	2.3	1.3
ETE (%) single ions (from lc)	-	20	30	50	-	-
ETE (%) clusters with (fc) $\tau_0=80 \mu\text{s}$	-	89.3	94.3	95.4	97.1	98.3

ETE values displayed in Table 3.2, show a very efficient energy transfer from Pr^{3+} to Yb^{3+} in CaF_2 for low Yb^{3+} concentrations (ETE=89.4% for $\text{CaF}_2:0.5\%\text{Pr}^{3+}-0.5\%\text{Yb}^{3+}$) clearly demonstrating the clustering of Pr^{3+} and Yb^{3+} ions occurring even at low Yb^{3+} concentrations. Moreover, the 3P_0 lifetime within the $\text{Pr}^{3+}\text{-Yb}^{3+}$ clusters decreases with the Yb^{3+} concentration and as a result, the corresponding ETE increases. This result is likely due to the energy transfer from a given Pr^{3+} ion to not only the closest Yb^{3+} ion within the cluster, but also to Yb^{3+} ions possibly in the second nearest neighbour shell. The high ETE values obtained in $\text{CaF}_2:\text{Pr}^{3+}\text{-Yb}^{3+}$ can be achieved in other hosts, but requires a much higher Yb^{3+} concentration. Using the same calculation as for CaF_2 , we derived an ETE value of 97% for $\text{KY}_3\text{F}_{10}:0.5\%\text{Pr}^{3+}-20\%\text{Yb}^{3+}$ in Chapter 2, while the same ETE is achieved in CaF_2 with only 4% Yb^{3+} (Table 3.2). The ETE has also been calculated in other hosts by using Eq.2.3. The main results were previously summarized in Table 2.4. As a comparison, ETE in doubly Pr^{3+} and Yb^{3+} doped lanthanum borogermanate glasses reaches 65% with 20% Yb^{3+} [113]. Another host of interest is SrF_2 which shares strong similarities with CaF_2 , both hosts having the fluorite structure and a comparable Pr^{3+} 3P_0 intrinsic lifetime ($\tau(\text{CaF}_2)=150 \mu\text{s}$ in Fig.3.10 and $\tau(\text{SrF}_2)=148 \mu\text{s}$ in [107]). The clustering of Pr^{3+} ions with Yb^{3+} ions appears to be more pronounced in CaF_2 since it exhibits a stronger ETE. An efficiency of 77% was reported for $\text{SrF}_2:0.1\%\text{Pr}^{3+}-5\%\text{Yb}^{3+}$ while it reaches 97.1% for a similar Yb^{3+} concentration in $\text{CaF}_2:0.5\%\text{Pr}^{3+}-4\%\text{Yb}^{3+}$ (Table 3.2).

Besides the Pr^{3+} clusters, the isolated Pr^{3+} ions also transfer their energy to Yb^{3+} ions. This is illustrated by a decrease of the long decay component with the Yb^{3+} concentration (Table 3.2). However, the corresponding energy transfer rate remains low. Therefore, for QC applications, only samples with Yb^{3+} concentrations high enough to assure that all Pr^{3+} ions are coupled to Yb^{3+} ions within clusters (4% Yb^{3+} or higher) are interesting.

3.5 Preliminary conclusions and next challenges

In this section, two different types of rare-earth centers have been identified in Pr^{3+} - Yb^{3+} codoped CaF_2 . The first one, referred to as “isolated” Pr^{3+} ions, was found to be present in Pr^{3+} singly doped CaF_2 and at low Yb^{3+} contents in the codoped samples. The second one was identified as Pr^{3+} - Yb^{3+} clusters within which, as displayed in Table 3.2, very efficient energy transfers take place.

A more detailed investigation of the rare-earth clustering in Pr^{3+} - Yb^{3+} codoped CaF_2 is nevertheless necessary since the literature shows that different rare-earth structures can be expected. In the next sections, the Pr^{3+} - Yb^{3+} codoping will be compared to the Pr^{3+} - Lu^{3+} codoping with the aim of getting a further insight into the clusters structure. The strong similarities between Yb^{3+} and Lu^{3+} allow us to expect the formation of similar aggregates for the two types of codoping. Using Lu^{3+} as codopant instead of Yb^{3+} presents the advantage of investigating a system without energy transfer since Pr^{3+} and Lu^{3+} ions do not interact. This property will be shown to be extremely useful for a better comprehension of the rare-earth clustering in the Pr^{3+} - Lu^{3+} , and Pr^{3+} - Yb^{3+} doped systems.

3.6 Spectroscopy of the Pr^{3+} aggregates in CaF_2

3.6.1 Weak luminescence of Pr^{3+} ions in CaF_2

The sites occupied by Pr^{3+} ions in CaF_2 have been investigated in the past by using different experimental techniques [212,214,233,236,239]. Tissue and Wright [211] performed the most complete investigation on this matter describing up to 22 different sites in $\text{CaF}_2:0.1\%\text{Pr}^{3+}$, from which, only three of them were assigned to single ions. The 20 sites left were therefore labeled as cluster sites composed of two (pairs or dimers) or

three (trimers) ions, proving the presence of a large number of cluster sites of Pr^{3+} ions in CaF_2 . This important Pr^{3+} clustering in $\text{CaF}_2:\text{Pr}^{3+}$ leads to a decrease of the Pr^{3+} visible luminescence quantum yield when increasing the Pr^{3+} content.

The negative impact of the Pr^{3+} clustering on the Pr^{3+} luminescence is here experimentally assessed. Praseodymium $^3\text{P}_0$ emission spectra recorded between 570 and 660 nm under blue excitation at 442 nm ($^3\text{H}_4 \rightarrow ^3\text{P}_2$) are shown in Fig.3.13 for $\text{KY}_3\text{F}_{10}:0.25\%\text{Pr}^{3+}$ (Fig.3.13.a) and $\text{CaF}_2:0.5\%\text{Pr}^{3+}$ (Fig.3.13.d). Within this spectral range, the red ($^3\text{P}_0 \rightarrow ^3\text{F}_2$) and orange ($^3\text{P}_0 \rightarrow ^3\text{H}_6$) transitions are clearly observed. The spectra were recorded with identical excitation and detection geometry. A special care was taken to design samples with the same shape as they were all prepared with a 200 μm thickness. Since the samples may exhibit different absorption cross-sections at the excitation wavelength, the small thickness of the samples is important in order to have an identical excitation beam profile within each sample. Keeping the same experimental conditions for all samples allows a direct comparison of emission intensities from the different samples. Emission intensities were integrated over the 570 to 660 nm range for both samples.

The ratio I_2/I_1 between the integrated intensities is given in Fig.3.13.a, where sample “1” is $\text{CaF}_2:0.5\%\text{Pr}^{3+}$ and sample “2” is $\text{KY}_3\text{F}_{10}:0.25\%\text{Pr}^{3+}$. An intensity ratio, I_2/I_1 , of 460 is observed between the two samples showing that $\text{KY}_3\text{F}_{10}:\text{Pr}^{3+}$ is 460 times brighter than $\text{CaF}_2:\text{Pr}^{3+}$. This result cannot be explained by a difference in absorption since the absorption coefficients ($\alpha = \sigma_{\text{abs}} N$) at the pumping wavelength are 0.16 cm^{-1} and 0.13 cm^{-1} in $\text{KY}_3\text{F}_{10}:0.25\%\text{Pr}^{3+}$ and $\text{CaF}_2:0.5\%\text{Pr}^{3+}$ respectively.

This result arises indeed from the fundamental difference between the rare-earth incorporation sites in the two hosts. As seen in Chapter 2, KY_3F_{10} is a single-site fluoride host with a uniform distribution of dopants within the lattice. Therefore, unlike CaF_2 , no strong emission quenching due to the clustering of Pr^{3+} ions is to be expected. A great majority of excited Pr^{3+} ions in KY_3F_{10} contribute thus to the luminescence of the sample. On the opposite, the very weak Pr^{3+} emission observed in $\text{CaF}_2:\text{Pr}^{3+}$ in comparison to $\text{KY}_3\text{F}_{10}:\text{Pr}^{3+}$ illustrates the fact that most Pr^{3+} ions sit in clusters and that within these clusters the Pr^{3+} emission is quenched. The short distance between the Pr^{3+} ions in clusters clearly favor cross-relaxation processes. Several cross-relaxation paths exist for Pr^{3+} ions, and consist of an energy transfer between an excited Pr^{3+} ion in the $^3\text{P}_0$ energy level and a Pr^{3+} ion in the $^3\text{H}_4$ ground state (Fig.1.18). In particular, the cross-relaxation ($^3\text{P}_0, ^3\text{H}_4 \rightarrow ^1\text{G}_4, ^1\text{G}_4$) [68] is the most probable mechanism responsible for the $^3\text{P}_0$ emission quenching. In conclusion, the Pr^{3+} emission in $\text{CaF}_2:\text{Pr}^{3+}$ (Fig.3.8)

discussed in the previous section exclusively arises from a minority of “isolated” Pr^{3+} ions. More precisely, when comparing with the literature, the $^3\text{P}_0$ luminescence spectrum in Fig.3.13, and in Fig.3.8, in singly Pr^{3+} doped CaF_2 can be identified as corresponding to the C_{4v} single ion sites [211].

In general, the efficient cross-relaxation between Pr^{3+} ions in Pr^{3+} clusters, which leads to the weak luminescence intensity of $\text{CaF}_2:0.5\%\text{Pr}^{3+}$, constitutes a major obstacle for most optical applications. Therefore, solutions to avoid the formation of rare-earth clusters are very attractive for cases like Pr^{3+} in order to extend the use of rare-earth doped CaF_2 to different photonic applications. In the next sections, the codoping of Pr^{3+} with Yb^{3+} or Lu^{3+} will be shown to be an effective way to avoid the formation of Pr^{3+} clusters in CaF_2 .

3.6.2 $\text{Pr}^{3+}\text{-Yb}^{3+}$ and $\text{Pr}^{3+}\text{-Lu}^{3+}$ codoping

Ytterbium and lutetium ions present a different clustering tendency than Pr^{3+} ions, primarily forming high-order aggregates even at low doping concentrations (3.2). Lutetium is the last element of the $4f$ series ($Z=71$) just after Ytterbium ($Z=70$), and both have almost the same ionic radius and mass. As the size of the rare-earth ion is a decisive factor in the formation of rare-earth clusters, it is not surprising that the doping of CaF_2 with Lu^{3+} or Yb^{3+} gives the same type of cluster structures [240]. The difference between the $\text{Pr}^{3+}\text{-Yb}^{3+}$ and $\text{Pr}^{3+}\text{-Lu}^{3+}$ codopings arises from the fact that no energy transfer can occur between Pr^{3+} and Lu^{3+} ions since trivalent lutetium presents a complete $4f$ shell and so, does not exhibit $4f$ excited states. The intensity ratio presented earlier between $\text{KY}_3\text{F}_{10}:\text{Pr}^{3+}$ and $\text{CaF}_2:\text{Pr}^{3+}$ was also calculated between the codoped samples $0.5\%\text{Pr}^{3+}\text{-}5\%\text{Lu}^{3+}$ and $0.5\%\text{Pr}^{3+}\text{-}10\%\text{Yb}^{3+}$, and the singly doped $\text{CaF}_2:\text{Pr}^{3+}$ sample (Fig.3.13.b and Fig.3.13.c). A tremendous increase of the Pr^{3+} luminescence is observed for $\text{CaF}_2:0.5\%\text{Pr}^{3+}\text{-}5\%\text{Lu}^{3+}$ (Fig.3.13.b). The Pr^{3+} emission is 200 times brighter in the $\text{Pr}^{3+}\text{-Lu}^{3+}$ codoped sample than in a singly Pr^{3+} doped sample ($I_2/I_1=200$) while the absorbed pump power is about the same in both samples as evidenced by the absorption cross-sections and Pr^{3+} concentration values in Table 3.3. This result is a firsthand evidence that the number of non-luminescent Pr^{3+} clusters is much smaller in $\text{CaF}_2:0.5\%\text{Pr}^{3+}\text{-}5\%\text{Lu}^{3+}$ than in $\text{CaF}_2:0.5\%\text{Pr}^{3+}$. Thus, the incorporation of Lu^{3+} as codopant somehow modifies the clustering structure of Pr^{3+} ions with the consequence of preventing the formation of Pr^{3+} clusters.

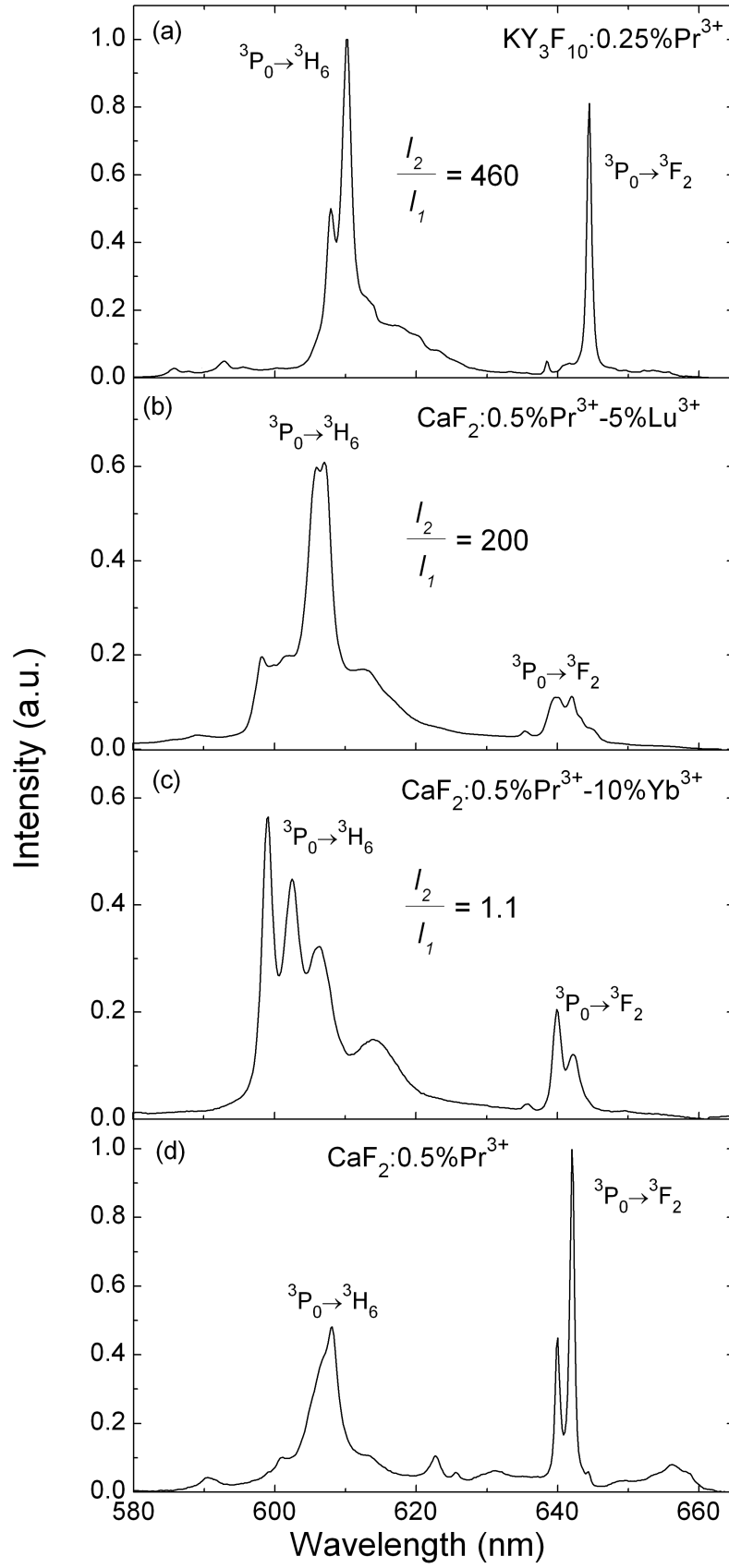


Figure 3.13: Pr^{3+} $^3\text{P}_0$ emission spectra when exciting at 442 nm. All spectra are normalized to have an integrated intensity equal to one for sake of clarity. (a) $\text{KY}_3\text{F}_{10}:0.25\%\text{Pr}^{3+}$ (b) $\text{CaF}_2:0.5\%\text{Pr}^{3+}-5\%\text{Lu}^{3+}$ (c) $\text{CaF}_2:0.5\%\text{Pr}^{3+}-10\%\text{Yb}^{3+}$ (d) $\text{CaF}_2:0.5\%\text{Pr}^{3+}$.

The codoping with Yb^{3+} ions (Fig.3.13.c) offers an apparently different result since the emission of $\text{CaF}_2:0.5\%\text{Pr}^{3+}-10\%\text{Yb}^{3+}$ is as weak as the emission from $\text{CaF}_2:0.5\%\text{Pr}^{3+}$ ($I_2/I_1=1.1$). However one would expect an even smaller intensity in the $\text{Pr}^{3+}\text{-Yb}^{3+}$ sample since the $^3\text{P}_0$ emission is quenched by energy transfer towards ytterbium i.e. $\text{Pr}^{3+}(^3\text{P}_0 \rightarrow ^1\text{G}_4); \text{Yb}^{3+}(^2\text{F}_{7/2} \rightarrow ^2\text{F}_{5/2})$ [241].

3.6.3 Luminescent centers increase

The ratio of intensities I_2/I_1 is directly related to the ratio of emitting centers concentrations N_2/N_1 , with N_i the concentration of emitting centers in sample i . The exact relationship between emission intensity and the number of emitting centers can be easily described provided that the concentration of excited ions remains small so as to avoid any depletion of the ground state. The rate equation for the concentration of luminescent centers in the excited state n_{3P0} evolves like:

$$\frac{dn_{3P0}}{dt} = -\frac{n_{3P0}}{\tau_{3P0}} + \sigma_{abs}\phi N_{Pr} \quad (3.1)$$

Under CW excitation ($\frac{dn_{3P0}}{dt} = 0$), the concentration of emitting centers in the excited state n_{3P0} is then simply given by

$$n_{3P0} = \sigma_{abs}\phi N_{Pr}\tau_{3P0} \quad (3.2)$$

where N_{Pr} represents the total concentration of emitting centers, σ_{abs} the absorption cross-section; ϕ the excitation photon flux and τ_{3P0} the emitting level lifetime. On the other hand, the emission intensity is proportional to the concentration of emitting centers in the excited state (n_{3P0}) as follows:

$$I_{3P0} \propto \frac{\beta \times n_{3P0}}{\tau_{rad}} \quad (3.3)$$

where β is the branching ratio of the transition, or transitions, being considered and τ_{rad} is the emitting level radiative lifetime. Combining expressions Eq.3.2 and Eq.3.3 one can obtain the ratio of emitting centers concentrations as a function of the intensity ratio I_2/I_1 knowing that the photon flux Φ remains constant for all samples:

$$\frac{N_2}{N_1} = \frac{I_2\beta_1\sigma_{abs1}\tau_1\tau_{rad2}}{I_1\beta_2\sigma_{abs2}\tau_2\tau_{rad1}} \quad (3.4)$$

The values needed to carry out the calculations in Eq.3.4 were measured experimentally and are summarized in Table 3.3. The branching ratio β of the red ($^3P_0 \rightarrow ^3F_2$) and orange ($^3P_0 \rightarrow ^3H_6$) transitions together was derived by recording the 3P_0 entire emission spectrum from 480 nm to 1100 nm which was then corrected for the spectral response of the experimental setup. The $^3P_0 \rightarrow ^1D_2$ infrared transition was not taken into account as it only gives a small contribution to the overall emission spectrum. The branching ratio β was then calculated as the ratio between the spectral integral of the red and orange transitions of interest and the spectral integral of the entire emission spectrum.

An effective σ_{abs} absorption cross-section value was calculated using the Pr^{3+} absorption spectra of Fig.3.14 and taking into account the 1 nm spectral linewidth of the laser diode used as excitation source. One can notice that the absorption spectra of both Pr^{3+} - Lu^{3+} and Pr^{3+} - Yb^{3+} samples are very much alike (Fig.3.14.c and Fig.3.14.d) while their emission spectrum are very different (Fig.3.13.b and Fig.3.13.c). This apparent discrepancy will be discussed in details further in the text.

Table 3.3: Spectroscopic parameters used for the calculations with Eq.3.4. β is the branching ratio of the red ($^3P_0 \rightarrow ^3F_2$) and orange ($^3P_0 \rightarrow ^3H_6$) transitions together; σ_{abs} the effective absorption cross-section, and τ and τ_{rad} the measured and radiative lifetimes respectively.

Sample	β	σ_{abs}	τ_{3P0} (μs)	$\tau_{rad-3P0}$ (μs)	ion/cm ³
0.25% Pr^{3+} : KY_3F_{10}	43%	$4.08 \cdot 10^{-21}$	40	40	$0.39 \cdot 10^{20}$
0.5% Pr^{3+} -5% Lu^{3+}	36%	$1.21 \cdot 10^{-21}$	31	80	$1.46 \cdot 10^{20}$
0.5% Pr^{3+} -10% Yb^{3+}	46%	$1.21 \cdot 10^{-21}$	1.3	80	$1.17 \cdot 10^{20}$
0.5% Pr^{3+}	39%	$1.13 \cdot 10^{-21}$	150	150	$1.17 \cdot 10^{20}$

The 3P_0 lifetimes, shown in Fig.3.15, were determined by normalizing to unity the fluorescence decay curves at $t = 0$ and by integrating the entire decay curves (Eq.2.1). The radiative lifetimes are usually derived using the Judd-Ofelt formalism. However, this calculation does not give satisfying results in the case of Pr^{3+} [242,243]. Therefore, we derived the 3P_0 radiative lifetimes by looking at the long time portion of the decays (after 100 μs) so as to avoid taking in account possible cross-relaxation processes. This estimation of the radiative lifetime is valid provided that migration assisted energy transfer

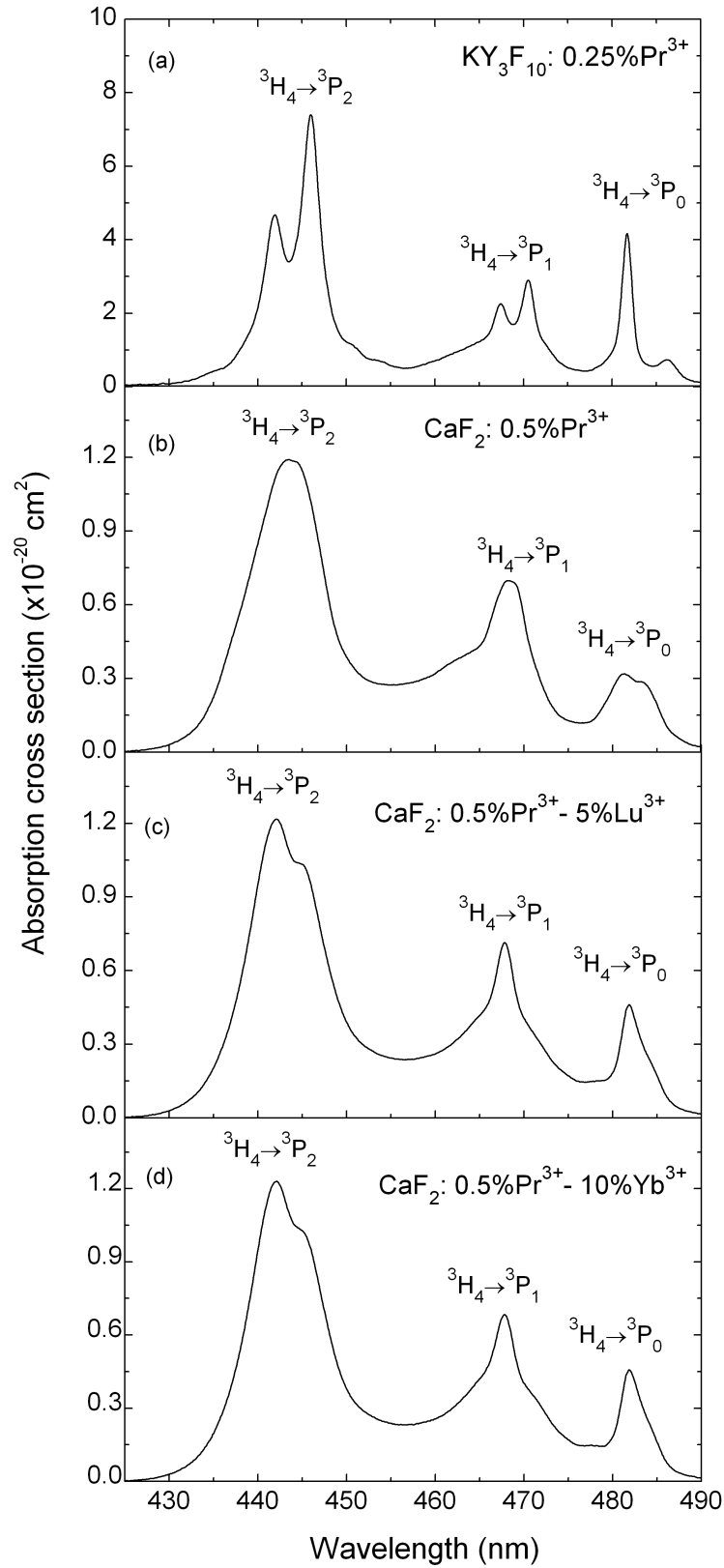


Figure 3.14: Room temperature absorption spectra recorded between 420 and 490 nm for the samples (a) $\text{KY}_3\text{F}_{10} : 0.25\% \text{Pr}^{3+}$ (b) $\text{CaF}_2 : 0.5\% \text{Pr}^{3+}$ (c) $\text{CaF}_2 : 0.5\% \text{Pr}^{3+} - 5\% \text{Lu}^{3+}$ (d) $\text{CaF}_2 : 0.5\% \text{Pr}^{3+} - 10\% \text{Yb}^{3+}$.

does not exist since it would also affect the long time portion of the decay [162]. The $0.5\%\text{Pr}^{3+}$ concentration used in all the CaF_2 samples is small enough to avoid energy migration among Pr^{3+} ions. For $\text{CaF}_2:0.5\%\text{Pr}^{3+}-10\%\text{Yb}^{3+}$ the $^3\text{P}_0$ lifetime is reduced to $1.3\ \mu\text{s}$ (Table 3.3) due to the energy transfer from $\text{Pr}^{3+}(^3\text{P}_0 \rightarrow ^1\text{G}_4)$ ions, which makes it very challenging to derive the $^3\text{P}_0$ radiative lifetime as said above. In order to overcome this difficulty, the radiative lifetime in $\text{CaF}_2:0.5\%\text{Pr}^{3+}-10\%\text{Yb}^{3+}$ is estimated to be equal to the radiative lifetime in $\text{CaF}_2:0.5\%\text{Pr}^{3+}-5\%\text{Lu}^{3+}$. This hypothesis is based on the strong spectroscopic similarities observed between $\text{CaF}_2:0.5\%\text{Pr}^{3+}-10\%\text{Yb}^{3+}$ and $\text{CaF}_2:0.5\%\text{Pr}^{3+}-5\%\text{Lu}^{3+}$ which will be detailed in the next section.

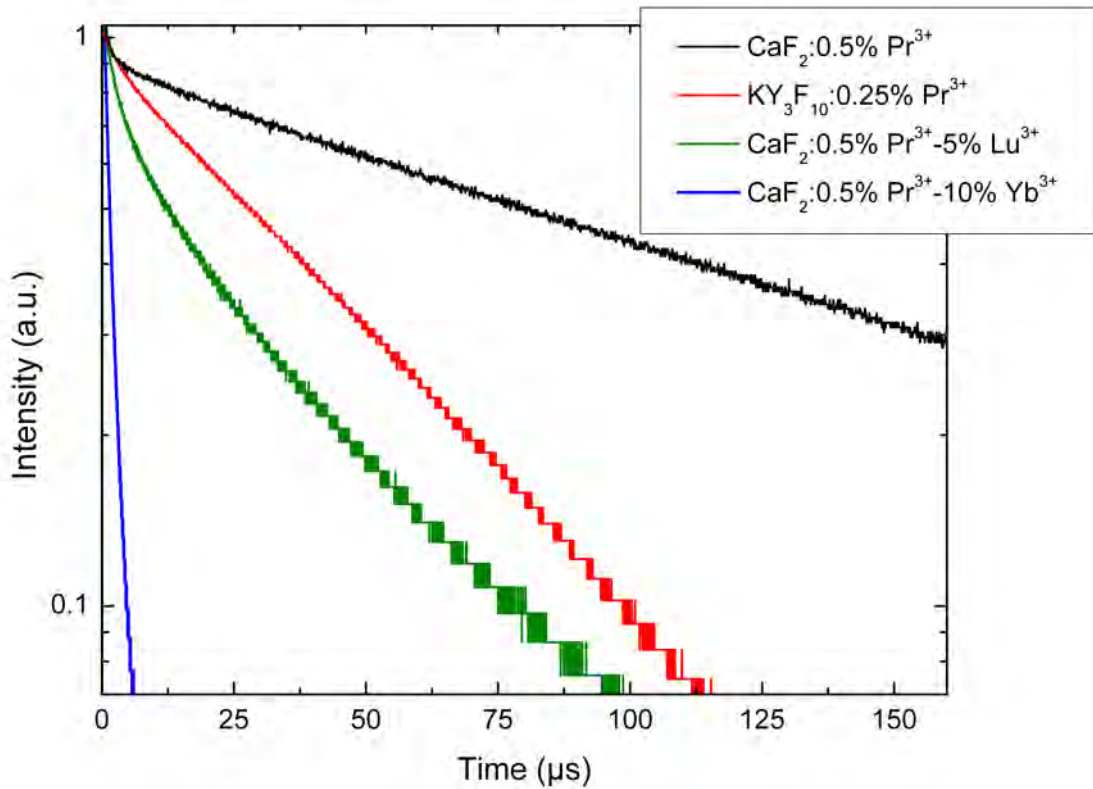


Figure 3.15: $\text{Pr}^{3+} \ ^3\text{P}_0$ decay curves under pulsed excitation at 468 nm ($^3\text{H}_4 \rightarrow ^3\text{P}_1$). (a) $\text{CaF}_2:0.5\%\text{Pr}^{3+}$ (b) $\text{KY}_3\text{F}_{10}:0.25\%\text{Pr}^{3+}$ (c) $\text{CaF}_2:0.5\%\text{Pr}^{3+}-5\%\text{Lu}^{3+}$ (d) $\text{CaF}_2:0.5\%\text{Pr}^{3+}-10\%\text{Yb}^{3+}$.

The ratio of luminescent centers N_2/N_1 derived from Eq.3.4 must be further corrected to take into account the total concentration of rare-earth ions per unit volume (Table 3.3) so as to be able to consider equal the concentration of Pr^{3+} dopant in each sample. The correction is mostly needed for $\text{KY}_3\text{F}_{10}:0.25\%\text{Pr}^{3+}$ which has a 3 times lower

Pr^{3+} concentration than the other samples. Therefore, for this sample the ratio is simply multiplied by 3 going from 118 to 354. The results obtained from Eq.3.4 with the correction regarding the number of rare earth ions per unit volume are presented in Table 3.4.

Table 3.4: Emission intensities ratios and their corresponding luminescent centers ratio corrected for the Pr^{3+} concentration.

Samples compared	I_2/I_1	N_2/N_1	N_2/N_1 corrected (% Pr^{3+})
$\text{KY}_3\text{F}_{10}:0.25\%\text{Pr}^{3+}/\text{CaF}_2:0.5\%\text{Pr}^{3+}$	466	118	354
$\text{CaF}_2:0.5\%\text{Pr}^{3+}-5\%\text{Lu}^{3+}/\text{CaF}_2:0.5\%\text{Pr}^{3+}$	200	522	418
$\text{CaF}_2:0.5\%\text{Pr}^{3+}-10\%\text{Yb}^{3+}/\text{CaF}_2:0.5\%\text{Pr}^{3+}$	1.1	54	54

Results in Table 3.4 show that the number of Pr^{3+} luminescent centers is 354 times larger in KY_3F_{10} than in CaF_2 for an equal concentration of Pr^{3+} ions confirming the large number of non-emitting Pr^{3+} clusters in Pr^{3+} doped CaF_2 . When codoping Pr^{3+} with either Lu^{3+} or Yb^{3+} ions in CaF_2 , the number of luminescent centers increases drastically (by a factor of 418 for Lu^{3+} and 54 for Yb^{3+}) indicating that the codopant substitutes for Pr^{3+} ions within the Pr^{3+} clusters enabling previously non-emitting Pr^{3+} centers to emit visible light. Considering the experimental uncertainties associated with the determination of the different spectroscopic parameters needed for Eq.3.4, one can consider that the number of emitting centers in $\text{CaF}_2:0.5\%\text{Pr}^{3+}-5\%\text{Lu}^{3+}$ ($N_2/N_1 = 418$) is similar (or even larger) to the number of emitting centers in $\text{KY}_3\text{F}_{10}:\text{Pr}^{3+}$ ($N_2/N_1 = 354$). This result shows clearly that when codoping with 5% Lu^{3+} ions all Pr^{3+} ions become emitting centers, i.e the elimination of all Pr^{3+} clusters.

The largest difference between the intensities ratio I_2/I_1 and the ratio of luminescent centers N_2/N_1 appears then for $\text{CaF}_2:0.5\%\text{Pr}^{3+}-10\%\text{Yb}^{3+}$. The low emission intensity of this codoped sample ($I_2/I_1 = 1.1$) does not reflect the actual increase of number of luminescent centers due to the Yb^{3+} codoping because of the drastic reduction of the $^3\text{P}_0$ lifetime observed in this sample. The $^3\text{P}_0$ lifetime is 150 μs in $\text{CaF}_2:\text{Pr}^{3+}$, but only 1.3 μs in $\text{CaF}_2:0.5\%\text{Pr}^{3+}-10\%\text{Yb}^{3+}$ (Table 3.3) which is attributed to the efficient energy transfer from $\text{Pr}^{3+}(^3\text{P}_0 \rightarrow ^1\text{G}_4)$ to $\text{Yb}^{3+}(^2\text{F}_{7/2} \rightarrow ^2\text{F}_{5/2})$ ions. Therefore, while the actual number of emitting centers has increased by a factor of 54 (Table 3.4) in $\text{CaF}_2:0.5\%\text{Pr}^{3+}-10\%\text{Yb}^{3+}$ in comparison to $\text{CaF}_2:0.5\%\text{Pr}^{3+}$, the emission of these new centers is very weak.

3.7 Pr^{3+} - Yb^{3+} and Pr^{3+} - Lu^{3+} clusters

3.7.1 Elimination of Pr^{3+} clusters

The codoping of Pr^{3+} with Yb^{3+} and Lu^{3+} ions appears to efficiently eliminate Pr^{3+} clusters in CaF_2 . Previous studies had already tried to use different codopants to alter the rare-earth clustering in CaF_2 . For instance, the codoping of rare-earth doped CaF_2 with monovalent impurities such as Na^+ , Li^+ or K^+ is known to favor the creation of centers of cubic symmetry and to limit the formation of clusters consequently increasing the number of emitting centers in the crystal. In these systems, new emitting centers result from combining a trivalent rare-earth ion and a monovalent cation in the vicinity [208,222,244] since the charge compensation is preserved by the substitution of the monovalent ion at a divalent calcium site which provides a net negative charge. However, to the best of our knowledge, it has not been clearly shown that these monovalent codopants prevent in a significant way the formation of rare-earth clusters.

Interestingly, Nd^{3+} clusters have been investigated in $\text{SrF}_2:\text{Nd}^{3+}$ showing that a large number of non-emitting clusters limit the use of this material for lasers and photonic applications. Nevertheless, investigations carried out by Payne et al. [187] suggest that the incorporation of Lanthanum (La^{3+}) or Yttrium (Y^{3+}) as codopants in $\text{SrF}_2:\text{Nd}^{3+}$ may give rise to new clusters formed by Nd^{3+} ions and Y^{3+} or La^{3+} ions. These new structures would eventually create new emitting centers where a Nd^{3+} ion would be surrounded by $\text{Y}^{3+}/\text{La}^{3+}$ ions instead of other Nd^{3+} ions. In consequence, the cross-relaxation paths would be drastically reduced since neighboring Nd^{3+} ions would not be present.

The results presented in the previous section, obtained with $\text{CaF}_2:\text{Pr}^{3+}-\text{Lu}^{3+}$ and $\text{CaF}_2:\text{Pr}^{3+}-\text{Yb}^{3+}$ seem to indicate that a very similar situation to that observed in $\text{SrF}_2:\text{Nd}^{3+}-\text{Y}^{3+}/\text{La}^{3+}$ is taking place. In other words, the codoping with Yb^{3+} or Lu^{3+} ions leads to the formation of $\text{Pr}^{3+}-\text{Yb}^{3+}$ or $\text{Pr}^{3+}-\text{Lu}^{3+}$ clusters within which a Pr^{3+} ion is surrounded by several Yb^{3+} or Lu^{3+} ions. This hypothesis seems particularly logical given the unbalance between the concentrations of codopants as there is 10 times more Lu^{3+} than Pr^{3+} ($\text{CaF}_2:0.5\%\text{Pr}^{3+}-5\%\text{Lu}^{3+}$) and 20 times more Yb^{3+} than Pr^{3+} ($\text{CaF}_2:0.5\%\text{Pr}^{3+}-10\%\text{Yb}^{3+}$) in the investigated samples.

3.7.2 Evidence of two types of clusters in the codoped samples

As seen in the previous discussion, the incorporation of Lu^{3+} or Yb^{3+} as codopants appears to give rise to new cluster centers containing both codopants. The analysis of low temperature absorption spectra provides important information regarding these cluster centers. Fig.3.16 shows the low temperature absorption spectra (12 K), for the singly Pr^{3+} doped CaF_2 and the $\text{Pr}^{3+}\text{-Lu}^{3+}$ and $\text{Pr}^{3+}\text{-Yb}^{3+}$ codoped samples in the 445-490 nm spectral range, in which, the transitions $^3\text{H}_4 \rightarrow ^3\text{P}_0$ and $^3\text{H}_4 \rightarrow ^3\text{P}_1$ are observed. The absorption spectrum of the singly Pr^{3+} doped sample is clearly different from the spectra recorded for the two codoped samples which are on the contrary both very similar. The similarity between the spectra of the two codoped samples (Fig.3.16.a and Fig.3.16.b) is in agreement with the hypothesis that Yb^{3+} and Lu^{3+} ions, presenting almost the same radius and atomic mass, behave in the same way during the aggregation process and give the same type of rare-earth clusters. On the contrary, the singly doped sample spectrum is characterized by numerous narrow lines around 468 nm for the $^3\text{H}_4 \rightarrow ^3\text{P}_1$ transition (Fig.3.16.c), while the spectra of the codoped samples exhibit a broad peak at this same wavelength (Fig.3.16.a and Fig.3.16.b). This contrast between the absorption spectra clearly indicates a different arrangement of the Pr^{3+} ions in the singly doped $\text{CaF}_2\text{:Pr}^{3+}$ crystal in comparison with the $\text{Pr}^{3+}\text{-Lu}^{3+}$ and $\text{Pr}^{3+}\text{-Yb}^{3+}$ codoped CaF_2 crystals.

The analysis of the $^3\text{H}_4 \rightarrow ^3\text{P}_0$ transition, gives further details concerning these different rare-earth incorporation sites. The $^3\text{P}_0$ level having $J = 0$ has a single Stark level while the $^3\text{H}_4$ ground state can have up to $2J + 1 = 9$ Stark levels. However, at low temperature (12 K), only the lowest Stark level of the $^3\text{H}_4$ multiplet is populated. Therefore, a single absorption line is expected for the $^3\text{H}_4 \rightarrow ^3\text{P}_0$ transition in the case of a single site structure. In the $\text{CaF}_2\text{:Pr}^{3+}$ absorption spectrum (Fig.3.16.c, inset) sharp lines can be observed sitting on top of a broader line centered at 479.5 nm. Each sharp line can be associated with a specific site with a well defined symmetry while the broad line evidences a strong inhomogeneous broadening most likely related to Pr^{3+} clusters.

In contrast to the singly doped sample, the $^3\text{H}_4 \rightarrow ^3\text{P}_0$ transition exhibits a very different absorption spectrum with two rather broad lines at 478 and 481 nm in both codoped samples (Fig.3.16.a and Fig.3.16.b). This result is a first indication that, indeed, two different types of $\text{Pr}^{3+}\text{-Yb}^{3+}$ or $\text{Pr}^{3+}\text{-Lu}^{3+}$ clusters might coexist in the codoped samples. Moreover, the two broad lines at 478 and 481 nm observed in the codoped samples are not present in the Pr^{3+} singly doped sample but seem to replace the Pr^{3+}

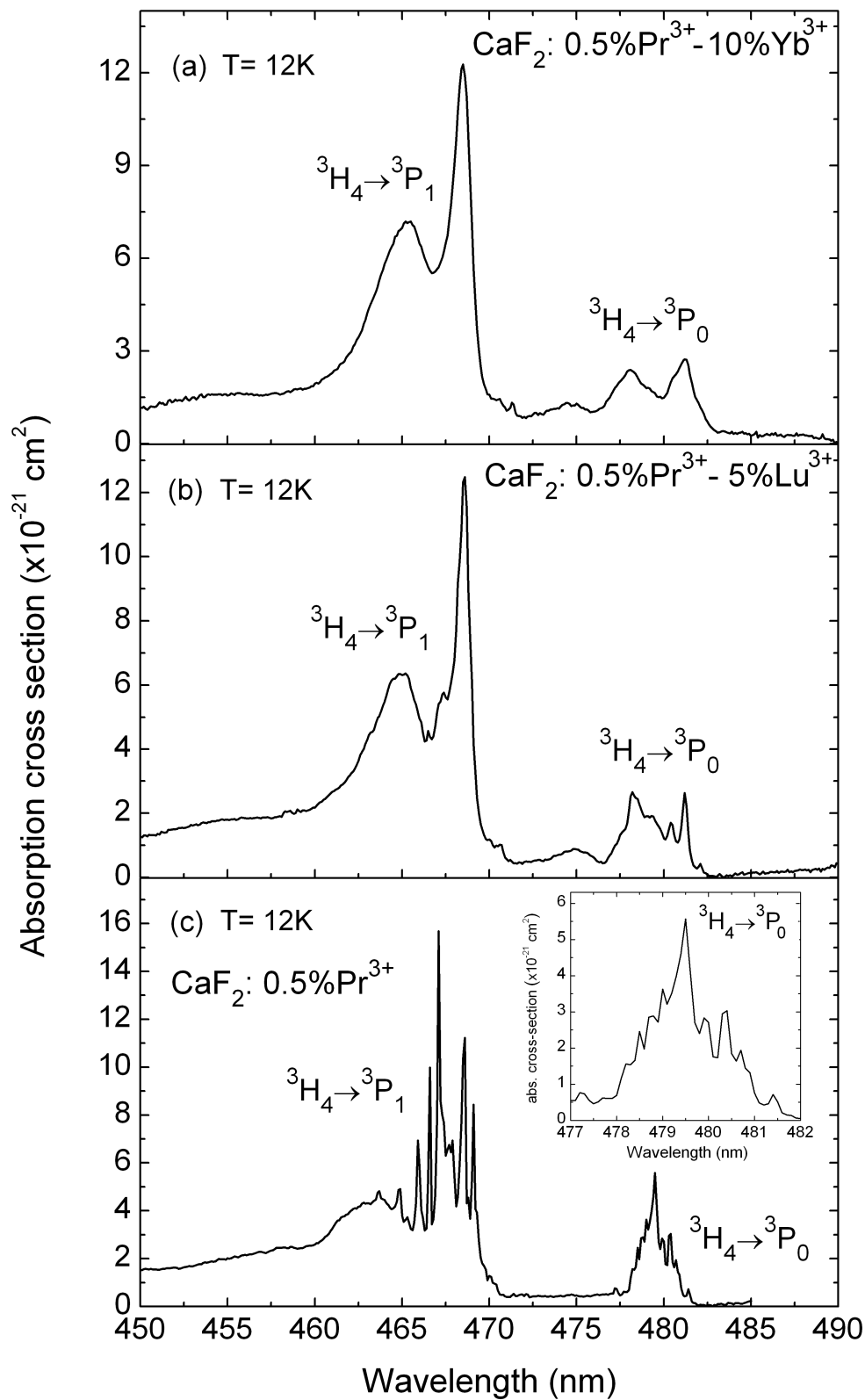


Figure 3.16: Low temperature absorption spectra between 450 and 490 nm. The ${}^3\text{H}_4 \rightarrow {}^3\text{P}_1$ and ${}^3\text{H}_4 \rightarrow {}^3\text{P}_2$ are shown for (a) $\text{CaF}_2:0.5\% \text{Pr}^{3+}-10\% \text{Yb}^{3+}$; (b) $\text{CaF}_2:0.5\% \text{Pr}^{3+}-\text{Lu}^{3+}$; (c) $\text{CaF}_2:0.5\% \text{Pr}^{3+}$.

cluster absorption spectrum when going from the singly Pr^{3+} doped sample to the codoped samples. Thus, this result supports the idea that codoping indeed avoids the formation of non-emitting Pr^{3+} clusters and favor the creation of two different types of $\text{Pr}^{3+}\text{-Yb}^{3+}/\text{Lu}^{3+}$ clusters. The existence of two types of $\text{Pr}^{3+}\text{-RE}^{3+}$ ($\text{RE}^{3+}=\text{Lu}^{3+}$ or Yb^{3+}) clusters is convincingly confirmed by investigating the $^3\text{P}_0$ time-resolved emission spectra in the codoped samples at room temperature.

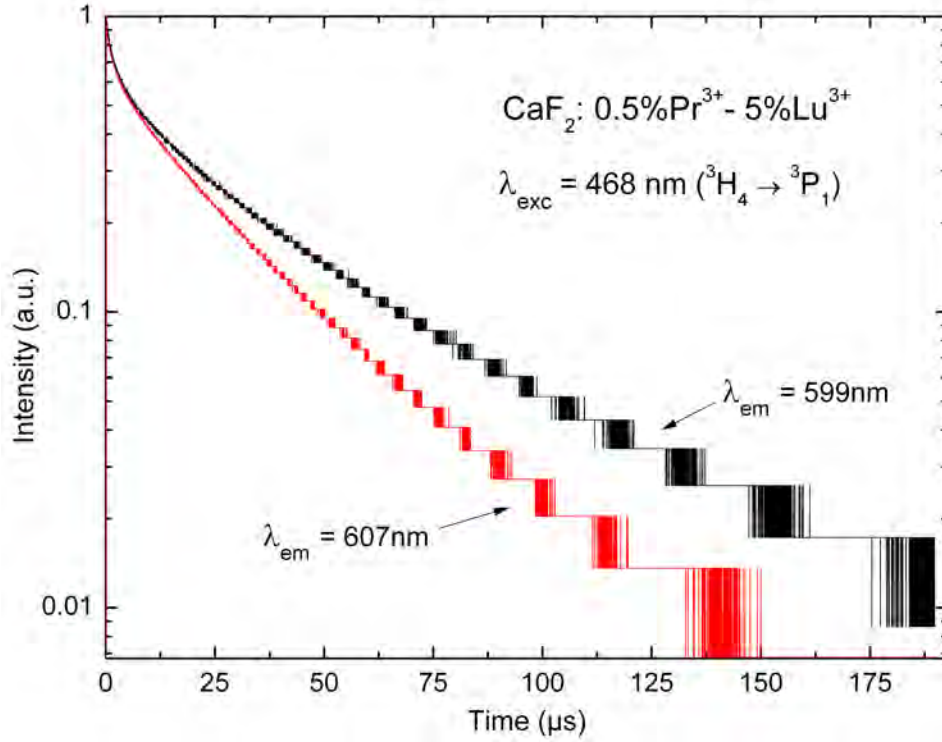


Figure 3.17: $^3\text{P}_0$ decays in $\text{CaF}_2\text{:}0.5\%\text{Pr}^{3+}\text{-}5\%\text{Lu}^{3+}$ at 599 nm and 607 nm under pulsed excitation at 468 nm ($^3\text{H}_4 \rightarrow ^3\text{P}_1$). At longer times ($t > 150 \mu\text{s}$), the two decays exhibit the same intrinsic lifetime of $80 \mu\text{s}$.

We recorded the $^3\text{P}_0$ decay in $\text{CaF}_2\text{:}0.5\%\text{Pr}^{3+}\text{-}5\%\text{Lu}^{3+}$ at two different emission wavelengths namely 599 nm and 607 nm (Fig.3.17). The decays are different ($\tau_{599}=31 \mu\text{s}$) and ($\tau_{607}=21 \mu\text{s}$) indicating that two different clusters coexist. Both decays exhibit some non-exponential features most likely due to energy transfers, in all likelihood cross-relaxation processes among Pr^{3+} ions which quench the $^3\text{P}_0$ level. As illustrated in Fig.3.18.a it is possible to isolate the emission spectrum related to the slowest center by recording the time-resolved emission spectrum with a time window starting at the end of the decay around $200 \mu\text{s}$.

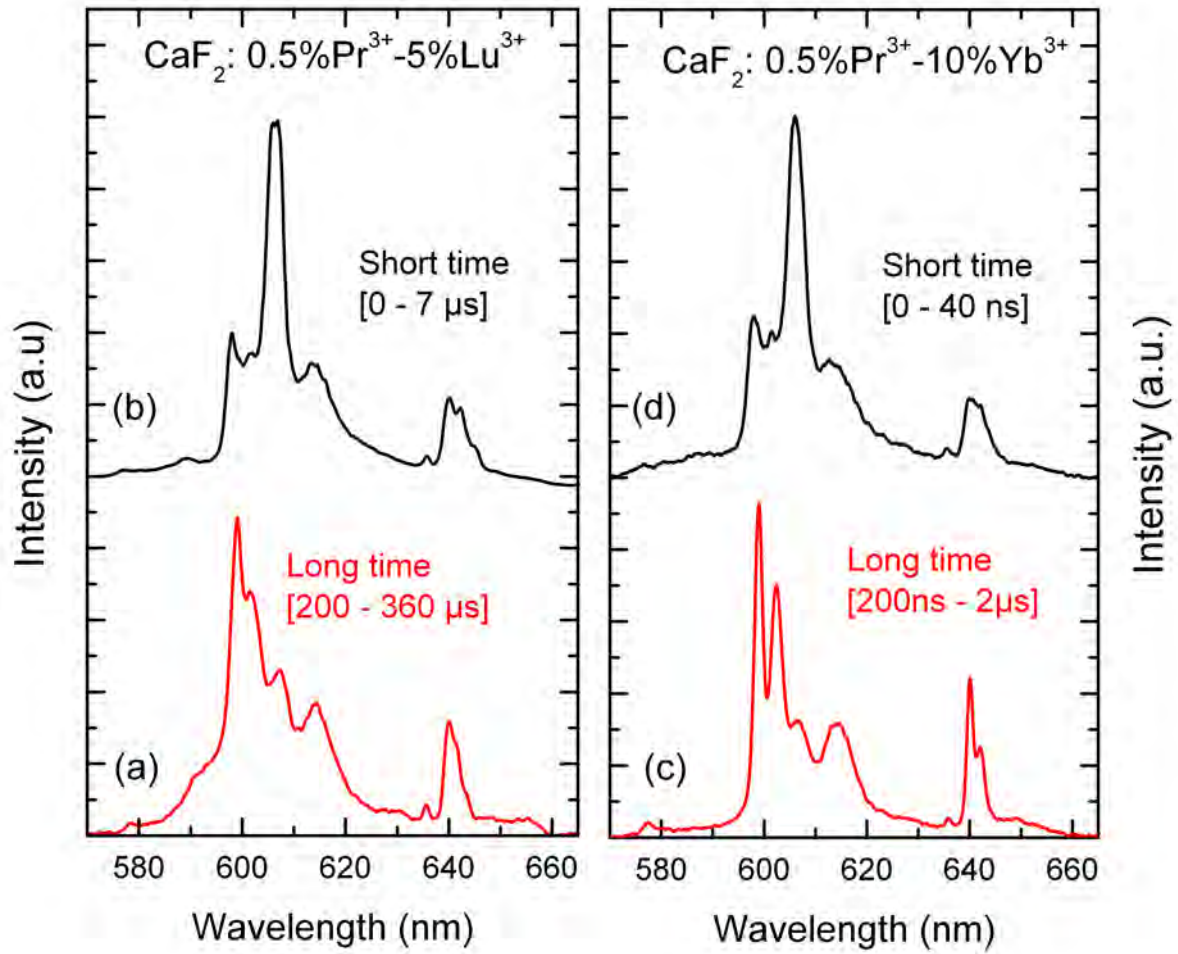


Figure 3.18: Pr^{3+} time-resolved spectra in $\text{CaF}_2:0.5\%\text{Pr}^{3+}-5\%\text{Lu}^{3+}$: (a) long time [200 - 360 μs]; (b) short time [0 - 7 μs]; and $\text{CaF}_2:0.5\%\text{Pr}^{3+}-10\%\text{Yb}^{3+}$: (c) long time [200ns - 2 μs] and (d) short time [0 - 40ns].

The emission spectrum of this first cluster (Fig.3.18.a) is characterized by a main emission peak at 599 nm which is consistent with the fact that the slowest decay was recorded at this wavelength (Fig.3.17). Another time window set during the first 7 μs of the decay gives a very different emission spectrum which is a combination of contributions from both types of clusters (Fig.3.18.b). This new spectrum exhibits a prominent emission peak at 607 nm which is characteristic of the second Pr^{3+} - Lu^{3+} cluster. Interestingly, this emission spectrum is identical to the spectrum recorded under CW laser diode excitation at 442 nm displayed in Fig.3.13.b. The fact that the emission spectrum of the first cluster (Fig.3.18.a) can hardly be seen in the emission spectrum of Fig.3.13.b is an indication that the second cluster (Fig.3.18.b) is the dominant emitting center in $\text{CaF}_2:0.5\%\text{Pr}^{3+}-5\%\text{Lu}^{3+}$.

When looking now at the $\text{Pr}^{3+}\text{-Yb}^{3+}$ codoped sample, the time-resolved emission spectra enable us to identify the same two clusters as for the $\text{Pr}^{3+}\text{-Lu}^{3+}$ codoping. However, because of the $\text{Pr}^{3+}(^3\text{P}_0 \rightarrow ^1\text{G}_4)$ to $\text{Yb}^{3+}(^2\text{F}_{7/2} \rightarrow ^2\text{F}_{5/2})$ energy transfer, the $^3\text{P}_0$ decay in $\text{CaF}_2\text{:}0.5\%\text{Pr}^{3+}\text{-}10\%\text{Yb}^{3+}$ is very short ($1.3\ \mu\text{s}$) as displayed in Fig.3.15. Therefore, a first time-window was placed within the first 40 nanoseconds of the decay, matching up with an almost unnoticed ultrafast component of the decay which can be seen in Fig.3.19. A second time window was set at longer times between 200 ns and $2\ \mu\text{s}$.

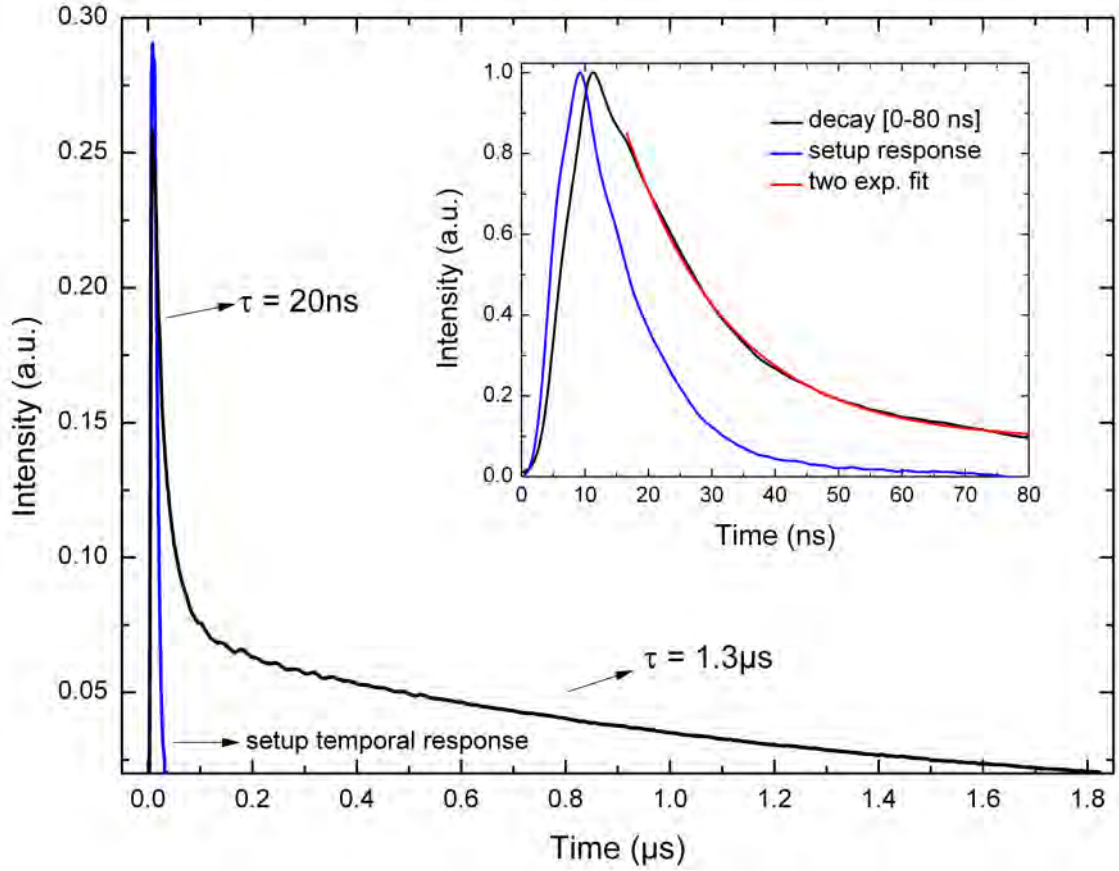


Figure 3.19: $^3\text{P}_0$ decay in $\text{CaF}_2\text{:}0.5\%\text{Pr}^{3+}\text{-}10\%\text{Yb}^{3+}$ under pulsed excitation at 468 nm ($^3\text{H}_4 \rightarrow ^3\text{P}_1$) (black line) and setup transient response to a 6 ns excitation pulse (blue line). Inset: close-up of the first 80 ns.

Fig.3.18.d shows that during the first 40 nanoseconds of the decay, we observe an emission spectrum identical to Fig.3.18.b ($\text{CaF}_2\text{:} \text{Pr}^{3+}\text{-Lu}^{3+}$) and thus dominated by the second cluster. From now on, this cluster will be labeled as “ultra-fast” cluster (UFC) because of its extremely short decay in the case of the $\text{Pr}^{3+}\text{-Yb}^{3+}$ codoping. Furthermore, Fig.3.18.a and Fig.3.18.c show that the same emission spectrum (attributed to the first cluster labeled as “fast” center or “fast” cluster (FC)) is recorded at longer times for both

codopings. These results reveal that the two major structures (fast cluster and ultra-fast cluster), created when codoping Pr^{3+} with Yb^{3+} or Lu^{3+} ions, are definitely equivalent for the two codopings in CaF_2 .

As evidenced by the fast $^3\text{P}_0$ decay (Fig.3.19), the interaction between Pr^{3+} and Yb^{3+} is efficient in the case of the fast cluster and extremely efficient in the case of the ultra-fast cluster, indicating once again that the investigated structures are in fact aggregates in which a Pr^{3+} ion is very close to one or more Yb^{3+} or Lu^{3+} ions. However, the real distance between the ions is most likely not the same in the two types of clusters. Ions have to be especially close to each other in the case of ultra-fast cluster to create a shortening of the $^3\text{P}_0$ lifetime down to a scale of tens of nanoseconds. The exact value of the $^3\text{P}_0$ lifetime for the ultra-fast cluster is indeed very short and thus not easy to estimate. The time response of our fluorescence decay experimental setup was assessed by recording the transient response following a 6 ns excitation pulse. As shown in the inset of Fig.3.19, the Full Width at Half Maximum (FWHM) duration of the recorded pulse is 10 ns. The inset of Fig.3.19 also displays a close-up of the first 80 ns of the $^3\text{P}_0$ decay in $\text{CaF}_2:0.5\%\text{Pr}^{3+}-10\%\text{Yb}^{3+}$. The setup time response appears to be fast enough to convincingly show the existence of an ultra-short decay component.

A double exponential fit was performed with a fixed value of $1.3 \mu\text{s}$ for the long part of the decay in the inset of Fig.3.19. The fit is in good agreement with the experimental decay and gives an estimate of 20 ns for the $^3\text{P}_0$ lifetime of the ultra-fast cluster in $\text{CaF}_2:0.5\%\text{Pr}^{3+}-10\%\text{Yb}^{3+}$. Such a short $^3\text{P}_0$ lifetime implies an ultra-fast energy transfer from Pr^{3+} to Yb^{3+} with a rate W of the order of $5 \times 10^7 \text{ s}^{-1}$ ($W = \tau^{-1} - \tau_0^{-1}$ with $\tau=20$ ns and $\tau_0=80 \mu\text{s}$). In other words, the Pr^{3+} emission arising from the ultra-fast cluster is essentially quenched and cannot be observed under CW excitation. Therefore, the only possibility to observe the emission of the ultra-fast cluster in $\text{CaF}_2:0.5\%\text{Pr}^{3+}-10\%\text{Yb}^{3+}$ is to record the emission spectrum within the first 40 ns of the decay after which time this emission vanishes. Consequently, the lifetime of $1.3 \mu\text{s}$ (Table 3.3) that was used up until now for the Pr^{3+} - Yb^{3+} clusters is essentially the Pr^{3+} lifetime of the fast clusters. Therefore, the emitting centers ratio of 54 in Table 3.4 is solely attributed to the fast clusters and does not take into account the ultra-fast clusters. In a similar way, the ETE calculated in section 3.5 (Table 3.2) corresponds to efficiencies within the fast clusters. The ultra-fast clusters exhibit a much higher efficiency which will be discussed in the following section.

3.8 Lifetimes and ETE in the ultra-fast clusters

3.8.1 Super-exchange interaction

The ultra-fast decay component, corresponding to the ultra-fast $\text{Pr}^{3+}\text{-Yb}^{3+}$ clusters, is observed in all the codoped samples ($0.5\%\text{Pr}^{3+}\text{-}\times\%\text{Yb}^{3+}$ with $\times=0.5, 1, 2, 4$ and 10). The time scale in the previous decay curves such as in Fig.3.10 does not allow to observe decay components of a few nanoseconds long. When choosing a suitable time scale, as displayed in Fig.3.20 for the $1\%\text{Yb}^{3+}$ and $4\%\text{Yb}^{3+}$ codoped samples, the ultra-fast component can be observed. The $^3\text{P}_0$ lifetime for the ultra-fast clusters in the different samples was again estimated using a double exponential fit as shown in Fig.3.19. In all cases, the quenching of the $^3\text{P}_0$ lifetime observed in the ultra-fast cluster is spectacular, going from $80\text{ }\mu\text{s}$ to a few nanoseconds for all the codoped samples ($0.5\%\text{Pr}^{3+}\text{-}\times\%\text{Yb}^{3+}$ with $\times=0.5, 1, 2, 4$). Furthermore, a shortening from 42 ns ($1\%\text{Yb}^{3+}$) to 34 ns ($4\%\text{Yb}^{3+}$) and then to 20 ns ($10\%\text{Yb}^{3+}$) can be observed in Fig.3.20. Consequently, ETEs higher than 99.90% are found for all samples, reaching a record value of 99.97% in $\text{CaF}_2\text{:}0.5\%\text{Pr}^{3+}\text{-}10\%\text{Yb}^{3+}$.

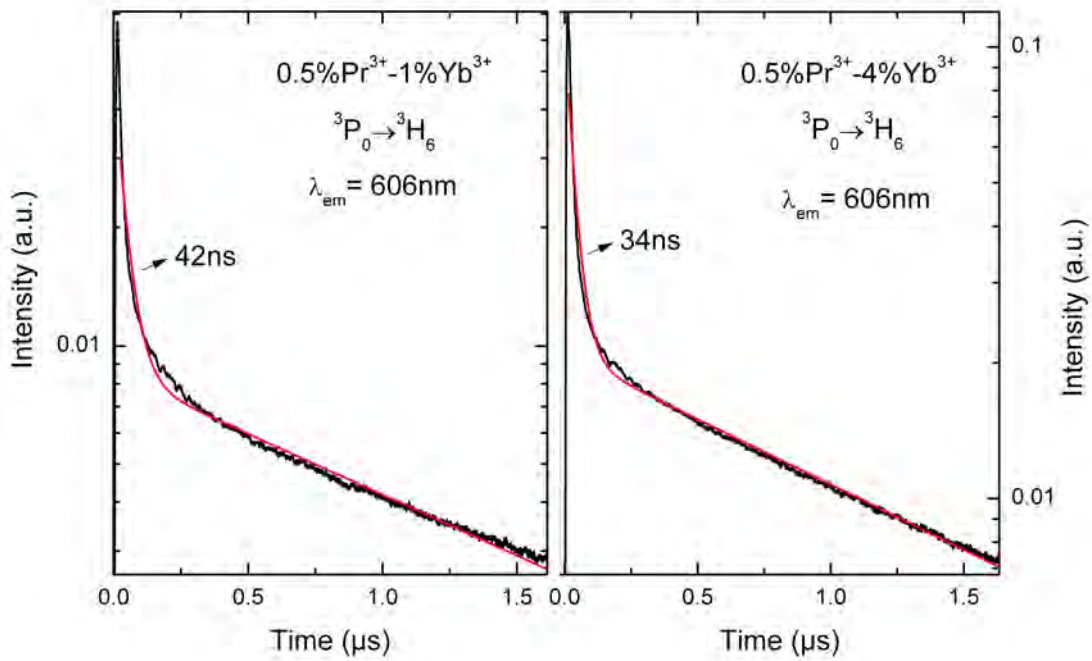


Figure 3.20: $^3\text{P}_0$ decays and double exponential fit for $\text{CaF}_2\text{:}0.5\%\text{Pr}^{3+}\text{-}1\%\text{Yb}^{3+}$ and $\text{CaF}_2\text{:}0.5\%\text{Pr}^{3+}\text{-}4\%\text{Yb}^{3+}$.

The energy transfer mechanism at play in the case of the ultra-fast cluster can hardly be explained by a dipole-dipole interaction. The energy transfer rate W_{DA} be-

tween a donor and an acceptor for a multipolar interaction W_{DA} is given by Eq.1.10 in which, the energy transfer microparameter C_{DA} depends on the spectral overlap between the emission spectrum of the donor and the absorption spectrum of the acceptor [62] (Eq.1.12). An averaged value for the C_{DA} microparameter was estimated to be $3 \times 10^9 \text{ Å}^6 \text{ s}^{-1}$ for the dipole-dipole energy transfer from $\text{Pr}^{3+} (^3\text{P}_0 \rightarrow ^1\text{G}_4)$ to $\text{Yb}^{3+} (^2\text{F}_{7/2} \rightarrow ^2\text{F}_{5/2})$ in KY_3F_{10} (Chapter 2), another fluoride host which shares structural similarities with CaF_2 . Taking this value as a reference and considering the shortest possible distance between two nearest-neighbor (NN) rare-earth ions in CaF_2 (3.86 Å in Fig.3.5), we deduce that, for a NN dimer comprising a Pr^{3+} and an Yb^{3+} ion, a maximal dipole-dipole energy transfer rate of the order of $8.7 \times 10^5 \text{ s}^{-1}$ can be expected, which is 60 times smaller than the rate of $5 \times 10^7 \text{ s}^{-1}$ observed for the ultra-fast cluster. Another type of interaction than dipole-dipole with a short range interaction is thus responsible for this very large energy transfer rate. Dipole-quadrupole and quadrupole-quadrupole interactions, while usually far less efficient than dipole-dipole, become non-negligible when the interaction distance between ions is reduced. However, quadrupole transitions are usually considered when dipole transitions are impossible [62]. On the other hand, Inokuti and Hirayama [63] showed that energy transfer by exchange interaction exhibits an exponential dependence with the distance R between ions, which makes this mechanism very efficient when the distance is very short (Eq.1.13). Therefore, energy transfer rates of the order of 10^7 s^{-1} or more have been previously studied using exchange interactions between rare-earth ions [67,245]. The energy transfer rate by exchange interaction presented in Chapter 1 is here recalled:

$$W_{ex} = \frac{1}{\tau_0} \times e^{\gamma(1-\frac{R}{R_0})} \quad (3.5)$$

where τ_0 is the intrinsic donor lifetime (i.e. without energy transfer), $\gamma = 2R_0/L$ with L the effective average Bohr radius that is usually equal to 1 Å [66]. R_0 is the critical interaction distance at which the energy transfer becomes equal to the intrinsic de-excitation rate τ_0^{-1} . This critical distance R_0 can be derived from Eq.3.5 as follows:

$$R_0 = R + \frac{L}{2} \ln(\tau_0 W_{ex}) \quad (3.6)$$

Using $R = 3.86$, $W_{ex} = 5 \times 10^7 \text{ s}^{-1}$ and $\tau_0 = 80 \text{ } \mu\text{s}$ (Table 3.3), Eq.3.6 gives a value of 8 Å for R_0 . This value is in agreement with similar calculations dealing with energy transfer

by exchange interaction ($R_0=10$ Å [66]). While exchange interaction is likely to be the mechanism at play in the ultra-fast cluster, energy transfer within the fast cluster can be easily explained by a dipole-dipole interaction since the energy transfer rate W calculated is in this case of the order of 7.6×10^5 s⁻¹ ($W = \tau^{-1} - \tau_0^{-1}$ with $\tau=1.3$ μs and $\tau_0=80$ μs as displayed in Table 3.3)). The use of the same intrinsic lifetime ($\tau_0=80$ μs) for the two types of clusters is justified by the fact that at longer times (>150 μs), the two decays in CaF₂:0.5%Pr³⁺-5%Lu³⁺ exhibit the same time constant of 80 μs (Fig.3.17) which can then be considered as their intrinsic lifetime (i.e without energy transfer).

In conclusion, the fact that the two types of clusters exhibit different types of interactions is most likely due to different arrangements of rare-earth ions within the clusters. In the case of the ultra-fast cluster, the exchange interaction could be more specifically a super-exchange interaction in which closely spaced neighboring rare-earth ions are coupled to each other by common diamagnetic ligands [65]. In that case, the position of the “bridging” ligand (in our case, a Fluorine ion) becomes crucial.

3.8.2 Fast Cluster to Ultrafast Cluster ratio

The ratio between the two types of Pr³⁺-Yb³⁺ clusters (ultra-fast and fast) is here investigated and calculated for several CaF₂:Pr³⁺-Yb³⁺ codoped samples by using the time-resolved emission spectra obtained with the ultra-fast decay component (nanosecond scale) on the one hand, and, on the other hand, with the fast component (microsecond scale). As seen in Fig.3.19 and Fig.3.20, the luminescence decays used for the time-resolved spectra can be described by a double exponential function for a given emission wavelength:

$$I(t, \lambda) = I_{uf} e^{-\frac{t}{\tau_{uf}}} + I_f e^{-\frac{t}{\tau_f}} \quad (3.7)$$

in which I_{uf} and I_f are the emission intensities at $t = 0$ for the ultra-fast cluster, and fast cluster respectively and, τ_{uf} and τ_f are the corresponding lifetime values, as for instance $\tau_{uf}=20$ ns and $\tau_f=1.3$ μs for CaF₂:0.5%Pr³⁺-10%Yb³⁺ (Fig.3.19). Integrating this expression over a (t_1 - t_2) time window one can obtain:

$$\int_{t_1}^{t_2} I(t, \lambda) dt = I_{uf} \tau_{uf} (e^{-\frac{t_1}{\tau_{uf}}} - e^{-\frac{t_2}{\tau_{uf}}}) + I_f \tau_f (e^{-\frac{t_1}{\tau_f}} - e^{-\frac{t_2}{\tau_f}}) \quad (3.8)$$

Eq.3.8 depends however on the emission wavelength for which the decay is recorded. In order to get emission intensities I_{uf} and I_f which would be independent on the emission wavelength and thus reflect the corresponding cluster concentration, we used the spectral integral of the time-resolved $^3P_0 \rightarrow ^3H_6$ emission spectrum recorded within a given time window such as in 3.18. By doing so, the ratio I_{uf}/I_f becomes directly proportional to the ratio between the two clusters concentrations. Estimating this ratio involves first of all determining I_{uf} and I_f . I_f can be easily calculated by integrating the corresponding time-resolved spectrum recorded at long time (for instance, between 400 ns and 1 μ s as displayed in Fig.3.21-left) when the emission of the ultra-fast cluster is already finished (Fig.3.19 and Fig.3.20). The value of I_f can then be derived from Eq.3.8 as:

$$I_f = \frac{\int_{t_1}^{t_2} I(t) dt}{\tau_f (\exp(-\frac{t_1}{\tau_f}) - \exp(-\frac{t_2}{\tau_f}))} \quad (3.9)$$

with $t_1 = 400$ ns et $t_2 = 1$ μ s.

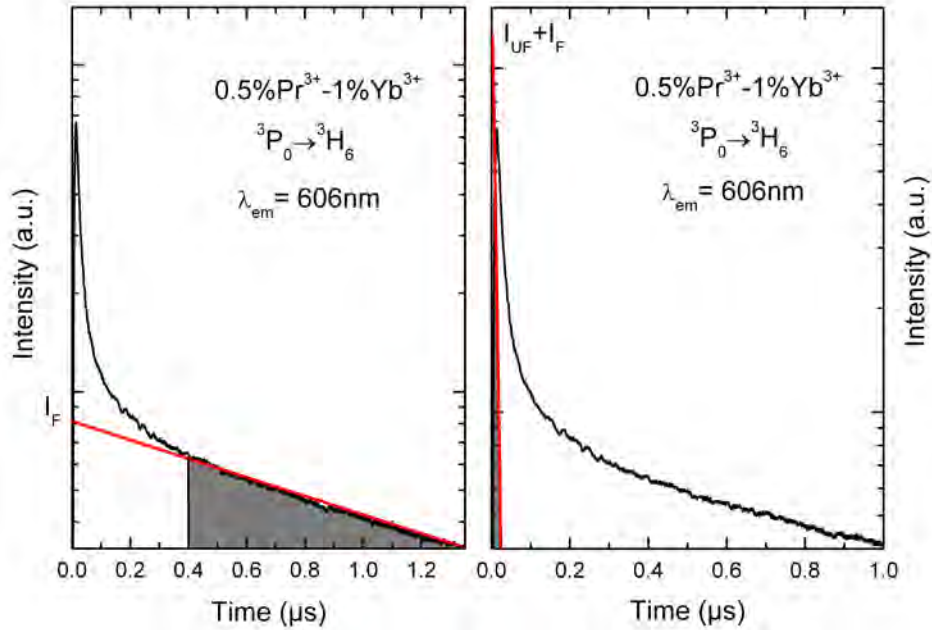


Figure 3.21: View of the integrated sections used in the calculations to determine I_f and I_{uf} in $CaF_2: 0.5\%Pr^{3+}-1\%Yb^{3+}$ at 606 nm. (Left) Step 1: determination of I_f from the integrated section between 20 ns and 1.3 μ s; (Right) Step 2: determination of I_{uf} from the integrated section between 0 and 20 ns.

In the same way, I_{uf} can be derived by integrating the time-resolved spectrum obtained from the first nanoseconds of the decay (Fig.3.21-right). Knowing the value of

I_f , I_{uf} is then easily deduced from Eq.3.10 as:

$$I_f = \frac{\int_{t_1}^{t_2} I(t)dt - I_f \tau_f (\exp(-\frac{t_1}{\tau_f}) - \exp(-\frac{t_2}{\tau_f}))}{\tau_{uf} (\exp(-\frac{t_1}{\tau_{uf}}) - \exp(-\frac{t_2}{\tau_{uf}}))} \quad (3.10)$$

with $t_1 = 0$ et $t_2 = 20$ ns.

As a result, the ratio I_{uf}/I_f between the two clusters was found to increase with the Yb^{3+} content. At low Yb^{3+} contents (0.5%, 1%) the ratio is lower than 1, or in other words, the fast clusters represent in these samples the dominant centers. When the Yb^{3+} concentration increases, the ultra-fast cluster dominates with a ratio of 3 in $\text{CaF}_2:0.5\%\text{Pr}^{3+}-4\%\text{Yb}^{3+}$ (i.e. 75% of UFC) and 5.25 in $\text{CaF}_2:0.5\%\text{Pr}^{3+}-10\%\text{Yb}^{3+}$ (i.e. 84% of UFC). Thus, the increase of the Yb^{3+} concentration clearly favors the formation of ultra-fast clusters instead of fast clusters.

3.8.3 Consequences

In conclusion, since the ultrafast clusters appear as the major centers in $0.5\%\text{Pr}^{3+}-10\%\text{Yb}^{3+}$ codoped CaF_2 , the ETE obtained for these clusters in $\text{CaF}_2:0.5\%\text{Pr}^{3+}-10\%\text{Yb}^{3+}$ i.e. 99.97% can be assumed to be the effective ETE of the sample. Table 3.5 compares this result with $\text{KY}_3\text{F}_{10}: \text{Pr}^{3+}-\text{Yb}^{3+}$ (Chapter 2) as well as other results reported in the literature. The ETE in $\text{CaF}_2:0.5\%\text{Pr}^{3+}-10\%\text{Yb}^{3+}$ appears thus to be the highest reported to the best of our knowledge. The fact that there is a much greater number of ultrafast clusters than fast clusters in $\text{CaF}_2:0.5\%\text{Pr}^{3+}-10\%\text{Yb}^{3+}$ also explains the value of 54 (Table 3.4) found for the ratio of luminescent centers N_2/N_1 (with N_2 the number of luminescent centers in $\text{CaF}_2:\text{Pr}^{3+}-\text{Yb}^{3+}$ and N_1 the number of luminescent centers in Pr^{3+} singly doped CaF_2) while the same value is about 400 for $\text{CaF}_2:0.5\%\text{Pr}^{3+}-5\%\text{Lu}^{3+}$. As pointed out earlier, this ratio of 54 only represents the emission due to the fast clusters and does not take into account the ultrafast clusters. When taking into account the fact that the ultrafast clusters represent 5.25 times the number of fast clusters, we can derive a ratio N_2/N_1 for the ultra-fast clusters equal to $54 \times 5.25 = 284$ and a total ratio of $284 + 54 = 338$ which is very close to the values of 354 and 418 found in $\text{Pr}^{3+}:\text{KY}_3\text{F}_{10}$ and $\text{CaF}_2:0.5\%\text{Pr}^{3+}-5\%\text{Lu}^{3+}$ respectively.

Table 3.5: Summary of ETEs obtained with different materials for the energy transfer $\text{Pr}^{3+}({}^3\text{P}_0 \rightarrow {}^1\text{G}_4)$ to $\text{Yb}^{3+}({}^2\text{F}_{7/2} \rightarrow {}^2\text{F}_{5/2})$. $\text{CaF}_2:0.5\%\text{Pr}^{3+}-10\%\text{Yb}^{3+}$ presents the record efficiency for the first energy transfer.

Material	Concentration	ETE (%)	Ref.
$\text{SrF}_2:\text{Pr}^{3+}-\text{Yb}^{3+}$	$0.1\%\text{Pr}^{3+}-17\%\text{Yb}^{3+}$	99	[107]
$\text{LaF}_3:\text{Pr}^{3+}-\text{Yb}^{3+}$	$0.005\%\text{Pr}^{3+}-10\%\text{Yb}^{3+}$	61.6	[108]
$\text{YF}_3:\text{Pr}^{3+}-\text{Yb}^{3+}$	$0.5\%\text{Pr}^{3+}-17\%\text{Yb}^{3+}$	2.9	[109]
$\text{GdAl}_3(\text{BO}_3):\text{Pr}^{3+}-\text{Yb}^{3+}$	$1\%\text{Pr}^{3+}-30\%\text{Yb}^{3+}$	95.4	[111]
Lanthanumborogermanate glass	$0.5\%\text{Pr}^{3+}-20\%\text{Yb}^{3+}$	65	[113]
$\text{KY}_3\text{F}_{10}:\text{Pr}^{3+}-\text{Yb}^{3+}$	$0.5\%\text{Pr}^{3+}-20\%\text{Yb}^{3+}$	96.5	[168]
$\text{CaF}_2:\text{Pr}^{3+}-\text{Yb}^{3+}$	$0.5\%\text{Pr}^{3+}-10\%\text{Yb}^{3+}$	99.97	

3.9 Summary of results

The spectroscopic study of a $0.5\%\text{Pr}^{3+}-5\%\text{Lu}^{3+}$ codoped CaF_2 sample and a series of $\text{CaF}_2: \text{Pr}^{3+}-\text{Yb}^{3+}$ codoped samples with Yb^{3+} concentrations equal to 0%, 0.5%, 1%, 2%, 4%, and 10% has provided further insight into the doping distribution, allowing the identification of three distinct Pr^{3+} centers which are single Pr^{3+} ions, Pr^{3+} clusters and $\text{Pr}^{3+}-\text{Yb}^{3+}$ clusters. Furthermore, two types of $\text{Pr}^{3+}-\text{Yb}^{3+}$ clusters denoted ultra-fast and fast clusters were identified. As a summary, a schematic representation of the evolution of the different centers with the Yb^{3+} content is displayed in Fig.3.22. Among the most remarkable points depicted in Fig.3.22, one can especially notice the large number of Pr^{3+} clusters found in singly Pr^{3+} doped CaF_2 (estimated to be 99.75% of the total number of centers); the elimination of all single Pr^{3+} ions at 4% Yb^{3+} ; the removal of all non-emitting Pr^{3+} clusters at about 5% Yb^{3+} (demonstrated by the drastic increase of the number of luminescent centers in $\text{CaF}_2:0.5\%\text{Pr}^{3+}-5\%\text{Lu}^{3+}$, result which can be extended to the $\text{Pr}^{3+}-\text{Yb}^{3+}$ codoping); and finally, the dominance of the ultra-fast $\text{Pr}^{3+}-\text{Yb}^{3+}$ clusters (UFC) at high Yb^{3+} contents ($\sim 84\%$ at 10% Yb^{3+}). At 4% Yb^{3+} , the UFC represent only 75% and the FC 25% of the total amount of clusters. This result tends to show that the number of FC saturates above 4% Yb^{3+} while the number of UFC continues to grow.

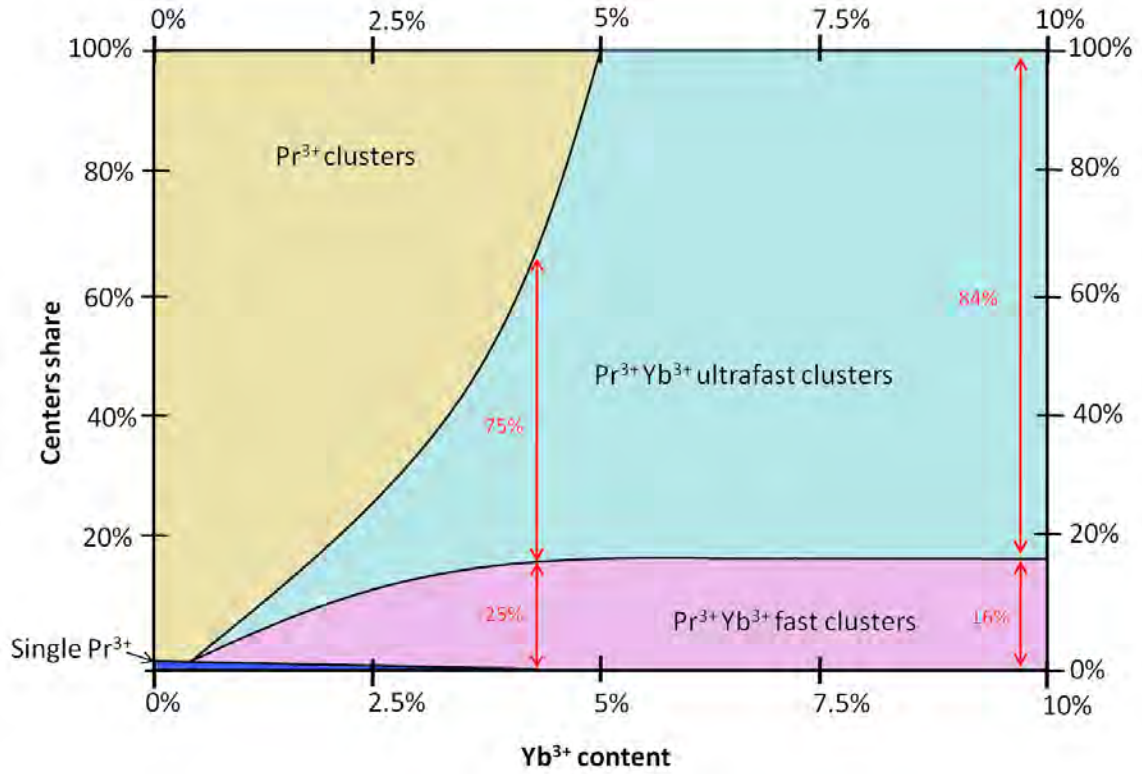


Figure 3.22: Schematic representation of the centers proportions as a function of the Yb^{3+} content.

3.10 QC with Pr^{3+} - Yb^{3+} codoped CaF_2 : Yb^{3+} emission and modeling

3.10.1 Yb^{3+} emission and lifetimes

In terms of QC applications, it is important to investigate the infrared emissions from Yb^{3+} ions and Pr^{3+} ions in the $^1\text{G}_4$ level following the first energy transfer. Fig.3.23.b shows the Yb^{3+} emission for the Pr^{3+} - $\text{Yb}^{3+}:\text{CaF}_2$ samples under Pr^{3+} excitation at 442 nm. Fig.3.23 is a first-hand evidence that there is an energy transfer between Pr^{3+} and Yb^{3+} ions. Fig.3.23.b presents the emission spectra of the different samples normalized to the shoulder at 1040 nm. One can notice that the shape of the Yb^{3+} emission spectrum changes as the main emission peak at 980 nm tends to decrease with the Yb^{3+} concentration. This effect commonly observed, which becomes stronger when increasing the Yb^{3+} concentration, is due to the reabsorption of the emitted photons [246].

A direct comparison of the Yb^{3+} emission intensity from one sample to another can be performed in Fig.3.23 since the excitation and detection geometry were kept identical for all samples which were prepared as powders with the same geometry from bulk crystals. Fig.3.24 shows the evolution of the Yb^{3+} emission at 1040 nm (in order to minimize the effect of reabsorption) with the Yb^{3+} content under Pr^{3+} excitation. The Yb^{3+} intensity increases up to 2% Yb^{3+} showing that more and more Yb^{3+} ions are excited by means of the $\text{Pr}^{3+} \rightarrow \text{Yb}^{3+}$ energy transfer. The Yb^{3+} intensity starts to decrease when the Yb^{3+} concentration reaches 4% most likely because of the back-transfer processes already observed in $\text{KY}_3\text{F}_{10}:\text{Pr}^{3+}-\text{Yb}^{3+}$ (Chapter 2). Interestingly, above 4% Yb^{3+} , the intensity again increases (Fig.3.24.b).

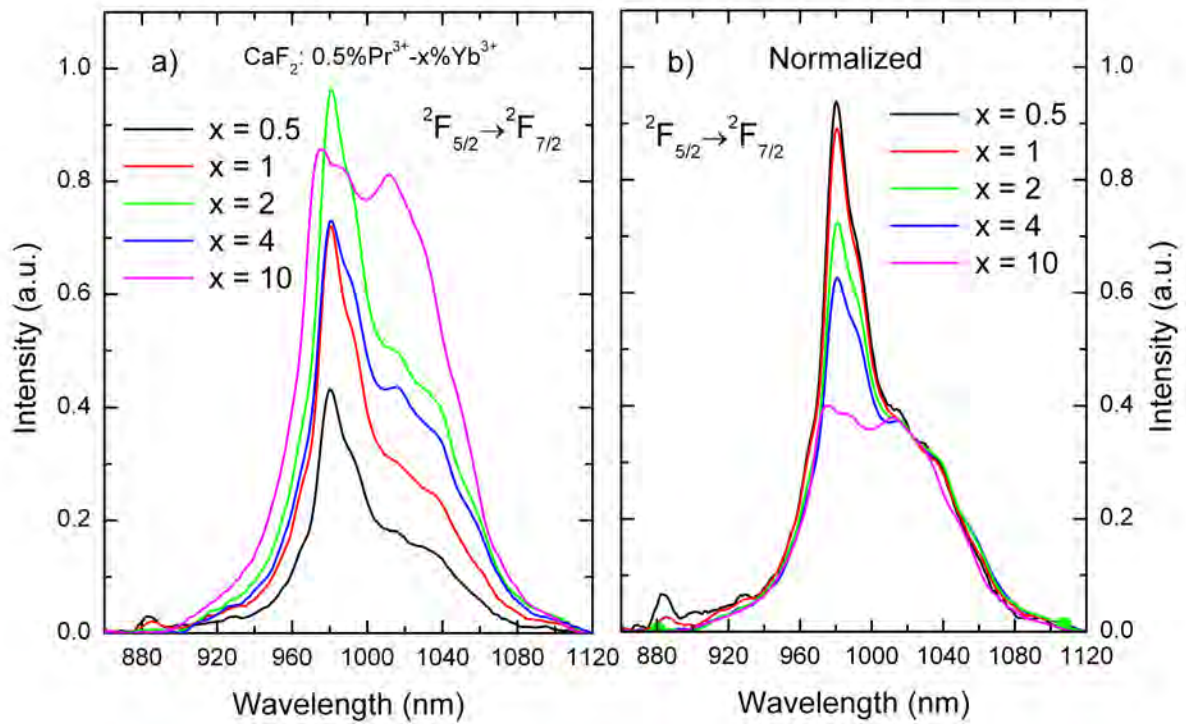


Figure 3.23: Ytterbium emission ($^2F_{5/2} \rightarrow ^2F_{7/2}$) under Pr^{3+} excitation at 442 nm (3P_2) in $\text{CaF}_2:0.5\%\text{Pr}^{3+}-x\%\text{Yb}^{3+}$ ($x = 0, 0.5, 1, 2, 4$). (a) Relative Yb^{3+} intensities of all samples recorded in the same conditions; (b) Normalized emission spectra illustrating the effect of photon reabsorption.

This increase between 4% Yb^{3+} and 10% Yb^{3+} shows that the overall number of emitting Yb^{3+} ions has increased from 4% Yb^{3+} to 10% Yb^{3+} . This can be explained first by the increasing efficiency of the first energy transfer with the Yb^{3+} content, but more importantly by the progressive elimination of the non-emitting Pr^{3+} clusters dominant

at low Yb^{3+} concentrations (Fig.3.22), which are replaced by Pr^{3+} - Yb^{3+} clusters. The formation of these Pr^{3+} - Yb^{3+} clusters increases the number of centers within which the energy transfer can take place and thus, the number of excited Yb^{3+} ions.

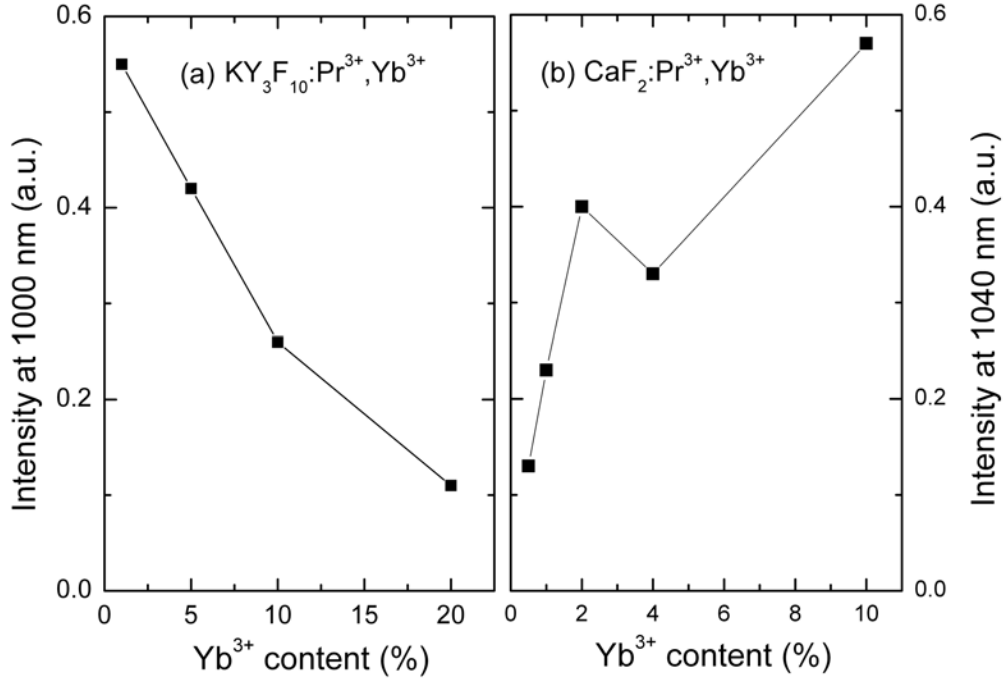


Figure 3.24: Yb^{3+} emission evolution with the Yb^{3+} content in (a) $\text{KY}_3\text{F}_{10}:\text{Pr}^{3+}\text{-Yb}^{3+}$ and (b) $\text{CaF}_2:\text{Pr}^{3+}\text{-Yb}^{3+}$.

Investigating the second energy transfer in $\text{CaF}_2:\text{Pr}^{3+}\text{-Yb}^{3+}$ requires the analysis of the $^1\text{G}_4$ and $^2\text{F}_{5/2}$ dynamics. Fig.3.25 displays the room temperature $^2\text{F}_{5/2}$ and $^1\text{G}_4$ decay curves recorded upon Pr^{3+} excitation at 442 nm ($^3\text{P}_0$) for all the codoped samples. The corresponding luminescence lifetimes were again calculated with the decay integral (Eq.2.1). The results are summarized in Table 3.6. As seen in Table 3.6, both $^1\text{G}_4$ and $^2\text{F}_{5/2}$ lifetimes are quenched when increasing the Yb^{3+} content. In the case of $^2\text{F}_{5/2}$, the quenching is remarkable, with an Yb^{3+} intrinsic lifetime of 2.4 ms [247] down to 51 μs for 10% Yb^{3+} . This quenching suggests that in spite of the increasing Yb^{3+} intensity observed in Fig.3.24, the back transfer processes are also very efficient in $\text{CaF}_2:\text{Pr}^{3+}\text{-Yb}^{3+}$. The decrease of the $^1\text{G}_4$ lifetime can be in principle associated to the effect of the second energy transfer β , $\text{Pr}^{3+}(^1\text{G}_4 \rightarrow ^3\text{H}_4)$ to $\text{Yb}^{3+}(^2\text{F}_{7/2} \rightarrow ^2\text{F}_{5/2})$.

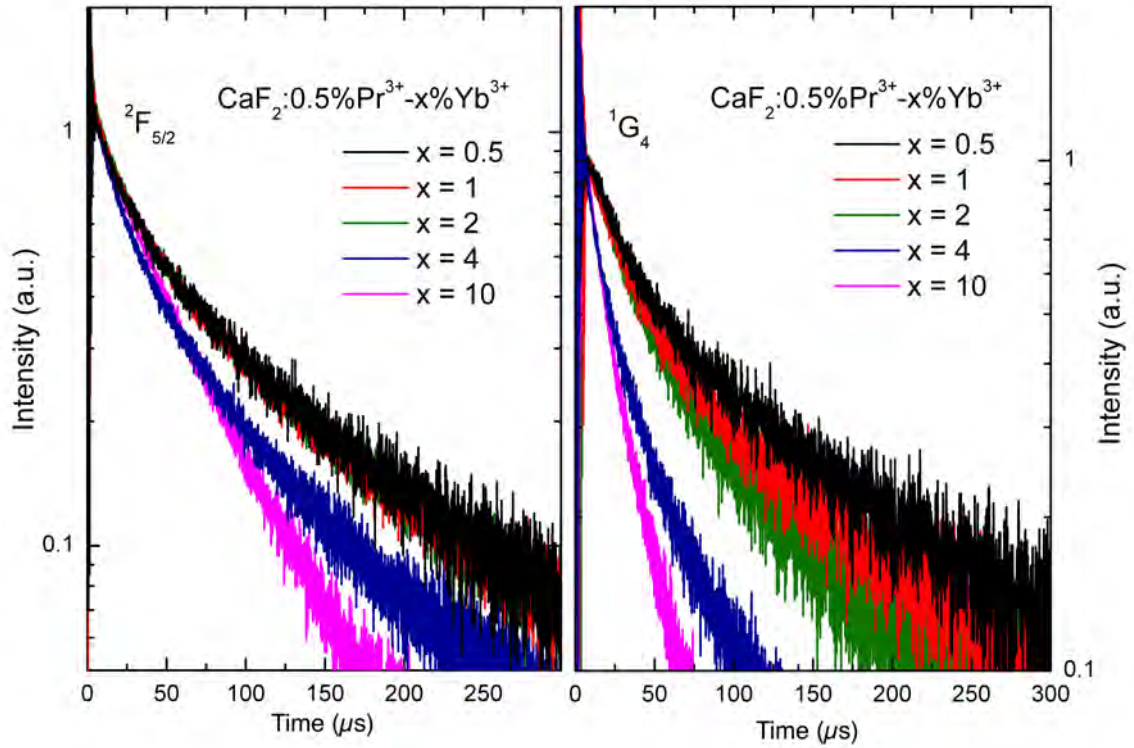


Figure 3.25: RT experimental $^2F_{5/2}$ and 1G_4 decay curves in $\text{CaF}_2: 0.5\%\text{Pr}^{3+}-x\%\text{Yb}^{3+}$ ($x = 0.5, 1, 2, 4, 10$) at 480 nm excitation.

Table 3.6: $^2F_{5/2}$ and 1G_4 experimental lifetimes upon Pr^{3+} excitation at 480 nm.

Sample	$\lambda_{exc}=480 \text{ nm}$	$\lambda_{exc}=480 \text{ nm}$
Energy level	τ_{1G4}	$\tau_{2F5/2}$
$\text{CaF}_2:0.5\%\text{Pr}^{3+}-0.5\%\text{Yb}^{3+}$	110	90
$\text{CaF}_2:0.5\%\text{Pr}^{3+}-1\%\text{Yb}^{3+}$	95	81
$\text{CaF}_2:0.5\%\text{Pr}^{3+}-2\%\text{Yb}^{3+}$	77	75
$\text{CaF}_2:0.5\%\text{Pr}^{3+}-4\%\text{Yb}^{3+}$	35	54
$\text{CaF}_2:0.5\%\text{Pr}^{3+}-10\%\text{Yb}^{3+}$	21	51

As stated in Chapter 2, the energy transfer rates associated with the second energy transfer and the back-transfer mechanisms necessitates the use of a rate-equation based modeling. However, modeling the energy transfers in $\text{CaF}_2:\text{Pr}^{3+}\text{-Yb}^{3+}$ is a really complicated task since up to 4 different centers (single Pr^{3+} ions, Pr^{3+} clusters and two types of $\text{Pr}^{3+}\text{-Yb}^{3+}$ clusters) may actually coexist at low Yb^{3+} concentrations. This complexity makes the modeling in $\text{CaF}_2:\text{Pr}^{3+}\text{-Yb}^{3+}$ nearly impossible, unless dealing with samples for which the situation is notably simplified. It is the case for $\text{CaF}_2:0.5\%\text{Pr}^{3+}\text{-}10\%\text{Yb}^{3+}$ in which the ultra-fast $\text{Pr}^{3+}\text{-Yb}^{3+}$ clusters are dominant (at 85%). Consequently, the $^2\text{F}_{5/2}$ and $^1\text{G}_4$ decay curves shown in Fig.3.25 can be supposed to exclusively arise from $\text{Pr}^{3+}\text{-Yb}^{3+}$ ultra-fast clusters for $\text{CaF}_2:0.5\%\text{Pr}^{3+}\text{-}10\%\text{Yb}^{3+}$. For this sample, a rate-equation modeling can then be used to estimate the energy transfer rates for the second transfer (β) and the Yb^{3+} quenching mechanisms (γ and δ).

3.10.2 Rate-equation modeling

The rate equation modeling uses the notation introduced in Chapter 2 (2.6.2). Within the ultra-fast clusters, the depopulation of the $^3\text{P}_0$ level is extremely fast leading in a few nanoseconds to the state displayed in Fig.3.26.b i.e. one Pr^{3+} ion excited in the $^1\text{G}_4$ level and one Yb^{3+} ion excited in the $^2\text{F}_{5/2}$ level. Therefore, one can simplify the modeling by assuming that the pumping in the $^3\text{P}_J$ multiplet (Fig.3.26.a) instantaneously leads to Fig.3.26.b. The system is then simply described by a two-equation system (3.11) in which n_2 and n_3 are initially populated:

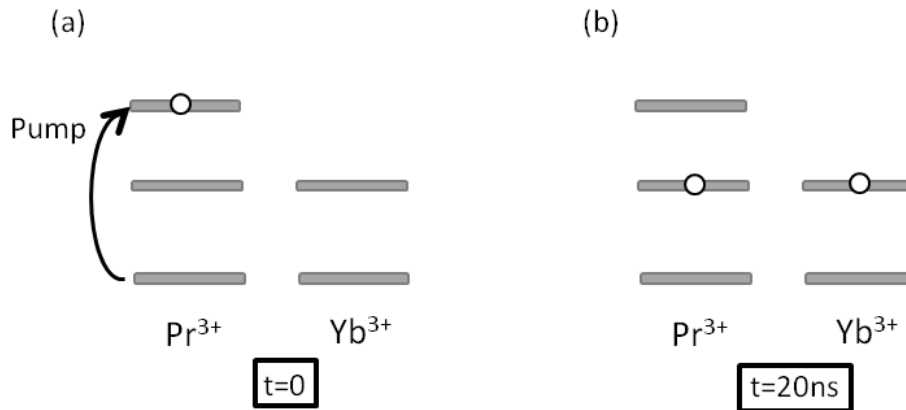


Figure 3.26: Schematic representation of the initial conditions.

$$\frac{dn_2}{dt} = -(R_2 + \beta)n_2 + \gamma n_3 \quad (3.11)$$

$$\frac{dn_3}{dt} = -(R_3 + \gamma + \delta)n_3 + \beta n_2$$

in which β , γ , δ are the energy transfer rates as defined in Chapter 2 and R_i is the radiative transition rate for level i , equal to τ_i^{-1} . n_2 , and n_3 are the populations of the 1G_4 and $^2F_{5/2}$ energy levels respectively.

The $^2F_{5/2}$ experimental luminescence decay shown in Fig.3.25 for $\text{CaF}_2:0.5\%\text{Pr}^{3+}-10\%\text{Yb}^{3+}$ were compared to the time-dependent solutions of 3.11 under initial conditions where both n_2 and n_3 have the same initial population. Contrarily to what happens with 2.7, analytical solutions can be found for 3.11:

$$n_2(t) = \frac{R_3 - R_2 + 3\gamma + \delta - \beta + \sqrt{\Delta}}{2\sqrt{\Delta}} e^{-\frac{1}{2}(R_2+R_3+\beta+\gamma+\delta-\sqrt{\Delta})t} - \frac{R_3 - R_2 + 3\gamma + \delta - \beta - \sqrt{\Delta}}{2\sqrt{\Delta}} e^{-\frac{1}{2}(R_2+R_3+\beta+\gamma+\delta+\sqrt{\Delta})t} \quad (3.12)$$

$$n_3(t) = \frac{R_3 - R_2 + \gamma + \delta - 3\beta + \sqrt{\Delta}}{2\sqrt{\Delta}} e^{-\frac{1}{2}(R_2+R_3+\beta+\gamma+\delta+\sqrt{\Delta})t} - \frac{R_3 - R_2 + \gamma + \delta - 3\beta - \sqrt{\Delta}}{2\sqrt{\Delta}} e^{-\frac{1}{2}(R_2+R_3+\beta+\gamma+\delta-\sqrt{\Delta})t} \quad (3.13)$$

in which $\sqrt{\Delta}$ takes the form defined in Eq.2.22. The numerical values used for the simulations are the Yb^{3+} radiative lifetime, $\tau_3 = R_3^{-1}$, set to 2.4 ms; the $\text{Pr}^{3+} \ ^3P_0$ radiative lifetime, $\tau_1 = R_1^{-1}$, set to 80 μs (Table 3.3), and finally, the $\text{Pr}^{3+} \ ^1G_4$ radiative lifetime, $\tau_2 = R_2^{-1}$, set to 150 μs .

Fig.3.27 presents the solution 3.13 obtained with $\beta=2.2 \times 10^7 \text{ s}^{-1}$; $\gamma=1.6 \times 10^7 \text{ s}^{-1}$ and $\delta=2.3 \times 10^4 \text{ s}^{-1}$. The theoretical decay is quite in agreement with the experimental value. As expected, the energy transfers β and γ are comparable to the energy transfer rate found experimentally for the first energy transfer. Thus, the second energy transfer and

the back-transfer most likely take place through exchange interaction within the ultra-fast clusters. Interestingly, the fact that the energy transfers occur at the nanosecond scale explains the lack of rise time in the experimental decays. In fact, the rise-time exists but is extremely short and thus invisible in the experimental decay curves. The energy transfer rate found for the transfer δ , is much lower than the other energy transfer rates. As mentioned in Chapter 2, this energy transfer δ is partially due to a non-resonant energy transfer from $^2\text{F}_{5/2}$ to $^3\text{F}_4$ (Fig.2.13). Because of the very short distances between the ions in the ultrafast cluster, a transfer rate $\delta=2.3\times 10^4 \text{ s}^{-1}$, although non-resonant, appears to be reasonable.

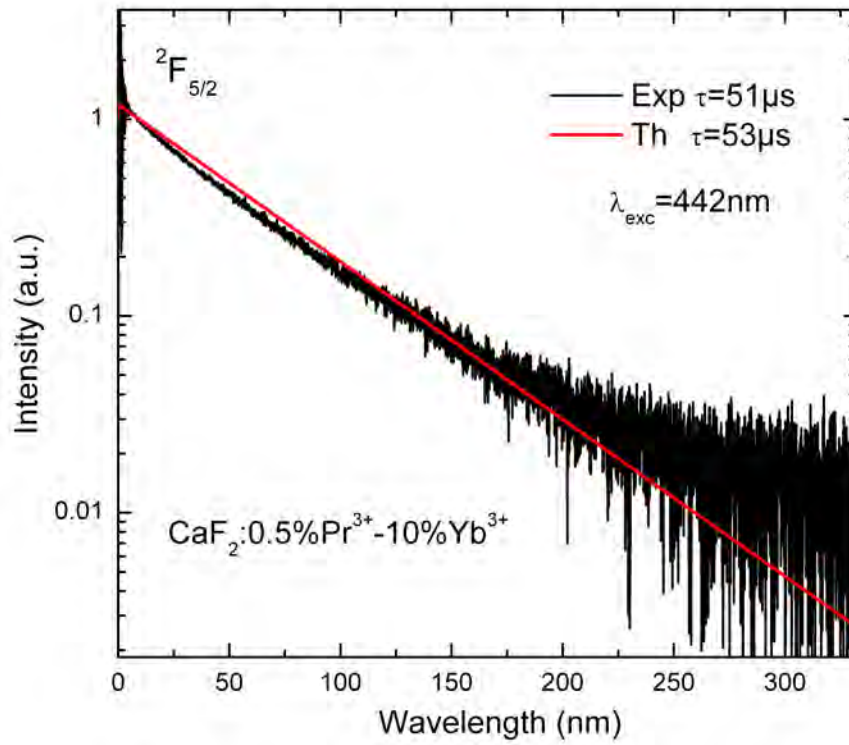


Figure 3.27: $^2\text{F}_{5/2}$ experimental decay obtained upon 442 nm excitation compared to $n_3(t)$ (3.13).

3.11 Conclusions Chapter 3

The investigation of the QC mechanism in $\text{CaF}_2:\text{Pr}^{3+}\text{-Yb}^{3+}$ revealed particularly efficient energy transfers between Pr^{3+} and Yb^{3+} ions due to the formation of $\text{Pr}^{3+}\text{-Yb}^{3+}$ clusters. In singly Pr^{3+} doped CaF_2 , the structure is dominated by non-luminescent Pr^{3+} clusters. The visible luminescence from $^3\text{P}_0$ then only comes from a minority of “isolated” ions sitting in single-ion sites, possibly with a C_{4V} symmetry. When codoping with Yb^{3+} ions, the Pr^{3+} clusters are progressively replaced by $\text{Pr}^{3+}\text{-Yb}^{3+}$ clusters. At 0.5% Pr^{3+} -5% Yb^{3+} , the Pr^{3+} clusters vanish from the structure and all Pr^{3+} ions are then embedded within two major types of $\text{Pr}^{3+}\text{-Yb}^{3+}$ clusters.

The presence of $\text{Pr}^{3+}\text{-Yb}^{3+}$ clusters replacing the initial Pr^{3+} clusters was first found by comparing emission intensities from $\text{Pr}^{3+}\text{-Lu}^{3+}$ codoped and Pr^{3+} singly doped CaF_2 samples. The drastic increase of the Pr^{3+} luminescence in $\text{CaF}_2:0.5\%\text{Pr}^{3+}\text{-5}\%\text{Lu}^{3+}$ by a factor of 400 clearly indicates that the Pr^{3+} clusters are replaced by $\text{Pr}^{3+}\text{-Lu}^{3+}$ clusters. These results open the way to other potential applications. The drastic increase of the Pr^{3+} luminescence observed in $\text{CaF}_2:0.5\%\text{Pr}^{3+}\text{-5}\%\text{Lu}^{3+}$, for instance, paves the way for a possible visible laser operation, otherwise unattainable with Pr^{3+} singly doped CaF_2 . Moreover, as displayed in Fig.3.13.b, Pr^{3+} presents an interesting orange transition at 606 nm, a laser emission wavelength which is well adapted and actively searched for quantum information processing experiments.

The exact same two types of clusters were found for both $\text{Pr}^{3+}\text{-Lu}^{3+}$ and $\text{Pr}^{3+}\text{-Yb}^{3+}$. Regarding the $\text{Pr}^{3+}\text{-Yb}^{3+}$ codoping, the first type of $\text{Pr}^{3+}\text{-Yb}^{3+}$ clusters, labeled as “fast cluster”, exhibits a fast energy transfer rate of the order of $7.6 \times 10^5 \text{ s}^{-1}$ in $\text{CaF}_2:0.5\%\text{Pr}^{3+}\text{-10}\%\text{Yb}^{3+}$. The energy transfer in the second cluster (ultra-fast cluster) is two orders of magnitude faster and contrarily to the first one, cannot be explained by a dipole-dipole interaction. This ultra-fast energy transfer is likely due to a super-exchange interaction in which the coupling between the rare-earth ions is mediated by a common Fluorine ion. The ultrafast cluster was found to dominate the structure in $\text{CaF}_2:0.5\%\text{Pr}^{3+}\text{-10}\%\text{Yb}^{3+}$ at 84% with the 16% left being “fast” clusters. The energy transfer efficiency derived for the ultra-fast clusters reaches values as high as 99.97% for the energy transfer $\text{Pr}^{3+}(^3\text{P}_0 \rightarrow ^1\text{G}_4)$ to $\text{Yb}^{3+}(^2\text{F}_{7/2} \rightarrow ^2\text{F}_{5/2})$.

The investigation of the second energy transfer and back-transfer by a rate equation modeling also shows extremely efficient interactions for all the energy transfers in the case of the ultra-fast clusters. This result explains in particular the lack of rise time

observed in the $^2F_{5/2}$ and 1G_4 experimental dynamics for $\text{CaF}_2:0.5\%\text{Pr}^{3+}-10\%\text{Yb}^{3+}$, in which the “ultra-fast” clusters dominate. The analysis of the down converted Yb^{3+} emission revealed an increase of the near-infrared luminescence with the Yb^{3+} content upon Pr^{3+} excitation around 442 nm because of the substitution of Pr^{3+} clusters by $\text{Pr}^{3+}\text{-Yb}^{3+}$ clusters. However, this increase of the Yb^{3+} emission cannot compensate the strong Yb^{3+} quenching evidenced by the short Yb^{3+} lifetime values observed even at low Yb^{3+} concentration ($\tau = 90 \mu\text{s}$ in $\text{CaF}_2:0.5\%\text{Pr}^{3+}-0.5\%\text{Yb}^{3+}$). This poor result is mainly due to back-transfer processes which quench the Yb^{3+} luminescence and favor IR emissions from the Pr^{3+} 1G_4 and 3H_6 levels.

Cooperative Quantum Cutting in $\text{CaF}_2:\text{Tb}^{3+}-\text{Yb}^{3+}$

4.1 Introduction

The cooperative energy transfer from one Tb^{3+} ion to two Yb^{3+} ions simultaneously and the consecutive emission of two NIR photons is investigated using CaF_2 as host material. The $\text{Tb}^{3+}-\text{Yb}^{3+}$ system presents an energy level scheme particularly suitable for cooperative energy transfers (Fig.1.20.a). Indeed, the Tb^{3+} ($^5\text{D}_4 \rightarrow ^7\text{F}_6$) emission energy closely matches the absorption transition energy of two ytterbium ions, and no resonant energy transfer pathway exists for Tb^{3+} ions excited in their $^5\text{D}_4$ level.

The $\text{Tb}^{3+}-\text{Yb}^{3+}$ codoping was among the first ones to be investigated for visible to NIR quantum cutting for solar applications [117] which led to a number of investigations on possible efficient $\text{Tb}^{3+}-\text{Yb}^{3+}$ quantum cutters [119-122]. The opposite path, i.e. the excitation of one Tb^{3+} ion by simultaneous energy transfer from two Yb^{3+} ions was previously studied in various host materials such as glasses [248-251] with the aim of developing blue-green lasers and optical amplifiers pumped by LD at 980 nm. Relatively good results were obtained in these investigations with up to 60% upconversion efficiency reported, for instance, in a borosilicate glass [250]. In spite of this, the $\text{Tb}^{3+}-\text{Yb}^{3+}$ system is generally considered limited in terms of efficiency, both for upconversion and downconversion quantum cutting because of the second order character of the cooperative energy transfer involved. A cooperative mechanism is only expected to take place when first-order resonant energy transfer processes are forbidden within the system and in addition it involves a three-body interaction. Therefore, the cooperative mechanism may only occur in a relatively efficient way if donors and acceptors are close enough to be able to

strongly interact. The distance between donors and acceptors must be therefore reduced by increasing the doping concentration in the host. However, increasing the rare-earth concentration usually gives rise to important concentration quenching processes which automatically limit the system performance [117].

CaF_2 has been shown, in previous chapters, to be a very attractive host for photonics applications with the particularity of forming rare-earth aggregates within which the rare-earth dopants are very close to each other. This characteristic makes CaF_2 a promising material since it favors efficient energy transfers while keeping relatively low Yb^{3+} concentrations. This advantage is particularly interesting in order to get efficient cooperative energy transfers. A detailed spectroscopic investigation of a series of $\text{CaF}_2:\text{Tb}^{3+}-\text{Yb}^{3+}$ codoped samples is presented in this chapter. Remarkable efficiency results have been found for the cooperative energy transfer between Tb^{3+} and Yb^{3+} ions in CaF_2 , and more importantly for the overall QC efficiency of the system. These promising results initiated the search of potential sensitizers for Tb^{3+} ions in order to achieve an efficient QC system with real potential for practical applications. The Tb^{3+} sensitization with trivalent Cerium on the one hand and trivalent Bismuth on the other hand, is investigated in the last part of this chapter.

4.2 Experimental methods

A series of $\text{CaF}_2:\text{Tb}^{3+}-\text{Yb}^{3+}$ codoped crystals as well as $\text{CaF}_2:\text{Tb}^{3+}-\text{Ce}^{3+}$ and $\text{CaF}_2:\text{Tb}^{3+}-\text{Bi}^{3+}$ crystals were grown in our laboratory by using the Bridgman-Stockbarger technique.

Table 4.1: $\text{CaF}_2:\text{Tb}^{3+}-\text{RE}^{3+}$ (RE= Yb, Ce or Bi) investigated samples.

Nominal concentrations	Real concentrations
2% Tb^{3+}	2% Tb^{3+}
0.5% Tb^{3+} -0.5% Yb^{3+}	0.5% Tb^{3+} -0.5% Yb^{3+}
0.5% Tb^{3+} -2% Yb^{3+}	0.5% Tb^{3+} -2% Yb^{3+}
0.5% Tb^{3+} -10% Yb^{3+}	0.5% Tb^{3+} -10.8% Yb^{3+}
0.5% Tb^{3+} -20% Yb^{3+}	0.5% Tb^{3+} -19.5% Yb^{3+}
0.5% Tb^{3+} -5% Ce^{3+}	0.5% Tb^{3+} -5% Ce^{3+}
0.5% Tb^{3+} -5% Bi^{3+}	0.5% Tb^{3+} -5% Bi^{3+}

More details about the growth technique are provided in Section 2.2. After growth, the samples were prepared as plates with a 3 mm thickness and as powders. The dopant concentrations in the crystals were assessed by absorption measurements. The composition of the investigated samples are summarized in Table 4.1.

The optical spectroscopy setups were the same as the ones used in the previous chapters with the exception of the photoluminescence excitation spectra (PLE) which were carried out with an Horiba Fluorolog-3 spectrofluorometer.

4.3 Spectroscopy of the Tb^{3+} - Yb^{3+} clusters in CaF_2

4.3.1 Tb^{3+} aggregates

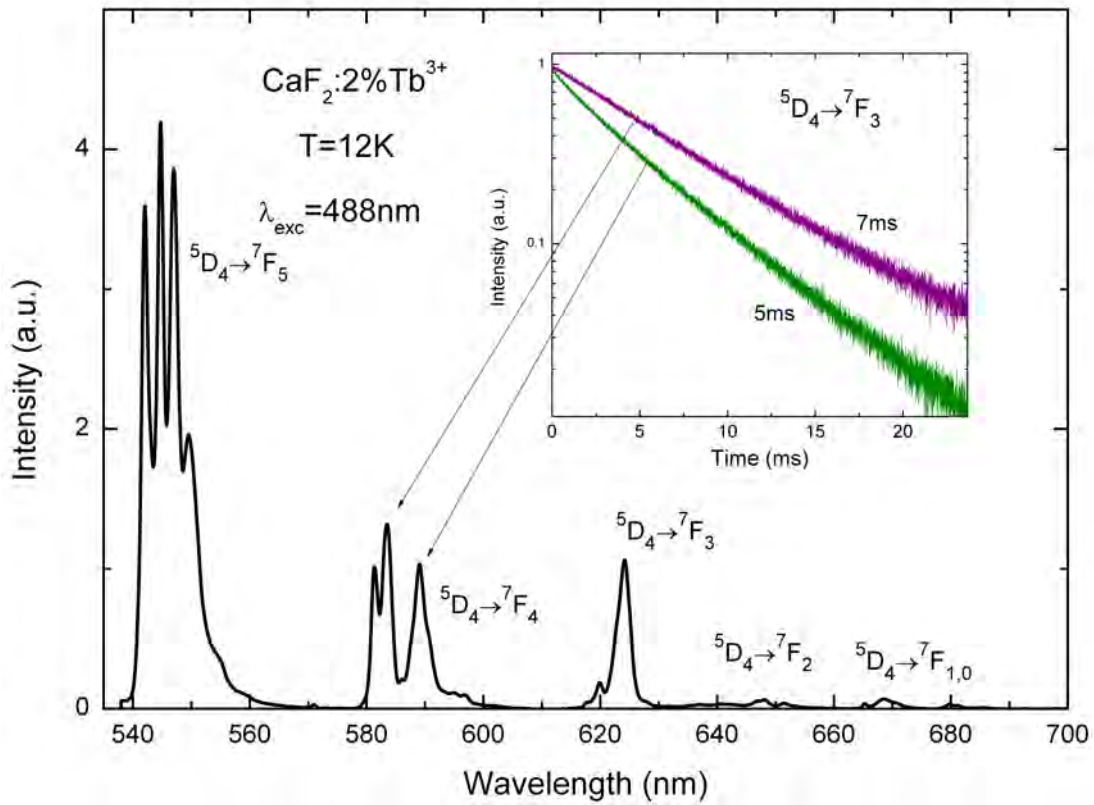


Figure 4.1: Low temperature $^5\text{D}_4$ emission spectrum in $\text{CaF}_2:2\%\text{Tb}^{3+}$. Inset: Low temperature $^5\text{D}_4$ decay curves recorded at 583 ($\tau=7$ ms) and 588 nm ($\tau=5$ ms) respectively.

Previous investigations of $\text{CaF}_2:\text{Tb}^{3+}$ [252-255] reported the existence of two different centers for Tb^{3+} ions in CaF_2 . These experimental studies were carried out with relatively low Tb^{3+} concentrations ($< 0.1\%$). Thus, the two centers were primarily as-

sociated to single ions sites of C_{4v} and C_{3v} symmetry respectively. Our investigation of higher Tb^{3+} doping and codoping with Tb^{3+} and Yb^{3+} ions reveal the existence of specific rare-earth aggregates.

The Tb^{3+} emission spectrum displayed in Fig.4.1 was recorded at low temperature (12 K) between 530 nm and 700 nm in a 2% Tb^{3+} singly doped CaF_2 sample upon Ar laser 488 nm excitation (${}^7\text{F}_6 \rightarrow {}^5\text{D}_4$). All the characteristic ${}^5\text{D}_4$ transitions, except the ${}^5\text{D}_4 \rightarrow {}^7\text{F}_6$ transition, can be clearly observed within this spectral range. As displayed in the inset of Fig.4.1, two different single exponential ${}^5\text{D}_4$ decays exist in 2% Tb^{3+} singly doped CaF_2 at 12 K depending on the emission wavelength. Under 485 nm excitation, a single exponential luminescence decay with a 7 ms fluorescence lifetime is recorded at 583 nm while a clearly different decay curve with a 5 ms lifetime is observed at 590 nm. These two decays coincide with two different emission peaks in the low temperature emission spectrum, both of them belonging to the ${}^5\text{D}_4 \rightarrow {}^7\text{F}_4$ transition, which suggests that each emission peak might originate from a different Tb^{3+} center.

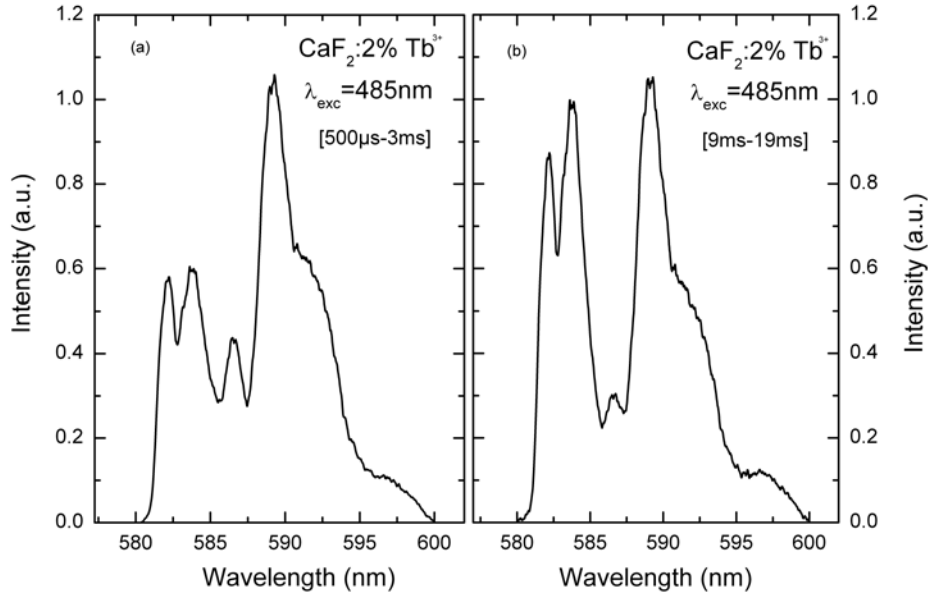


Figure 4.2: Low temperature time-resolved ${}^5\text{D}_4 \rightarrow {}^7\text{F}_3$ emission performed in the time windows (a) 500 μs - 3 ms and (b) 9-19 ms, in CaF_2 :2% Tb^{3+} .

Time-resolved spectra of the ${}^5\text{D}_4 \rightarrow {}^7\text{F}_4$ transition were recorded using the LT ${}^5\text{D}_4$ decay and by setting time-windows at shorter times between 500 μs and 3 ms; and at longer times between 9 and 19 ms. The existence of two different Tb^{3+} sites is definitely confirmed by the time-resolved spectra presented in Fig.4.2. For shorter times [500 μs -

3 ms], the peak at 588 nm is prominent while at longer times the peak at 583 nm rises since it is characteristic of a different Tb^{3+} center with a longer lifetime. These two Tb^{3+} centers are likely to be Tb^{3+} clusters first because of the rather high Tb^{3+} concentration in the sample (2%at.) and also because of the $^5\text{D}_4$ lifetimes measured for the two Tb^{3+} centers (5 ms and 7 ms) which are shorter than the $^5\text{D}_4$ lifetime associated to Tb^{3+} single ion site (11 ms) [255].

4.3.2 Tb^{3+} - Yb^{3+} spectroscopy

Room temperature fluorescence spectra were recorded between 570 and 640 nm under excitation at 488 nm for the different Tb^{3+} - Yb^{3+} codoped samples presented in Table 4.1. In Fig.4.3.a, the Tb^{3+} $^5\text{D}_4 \rightarrow ^7\text{F}_4$, and $^5\text{D}_4 \rightarrow ^7\text{F}_3$ transitions can be clearly identified. A slight change with the increasing Yb^{3+} content can be observed in the shape of the Tb^{3+} emission spectra, especially for the $^5\text{D}_4 \rightarrow ^7\text{F}_4$ transition, possibly indicating the formation of a new species in Tb^{3+} - Yb^{3+} codoped CaF_2 .

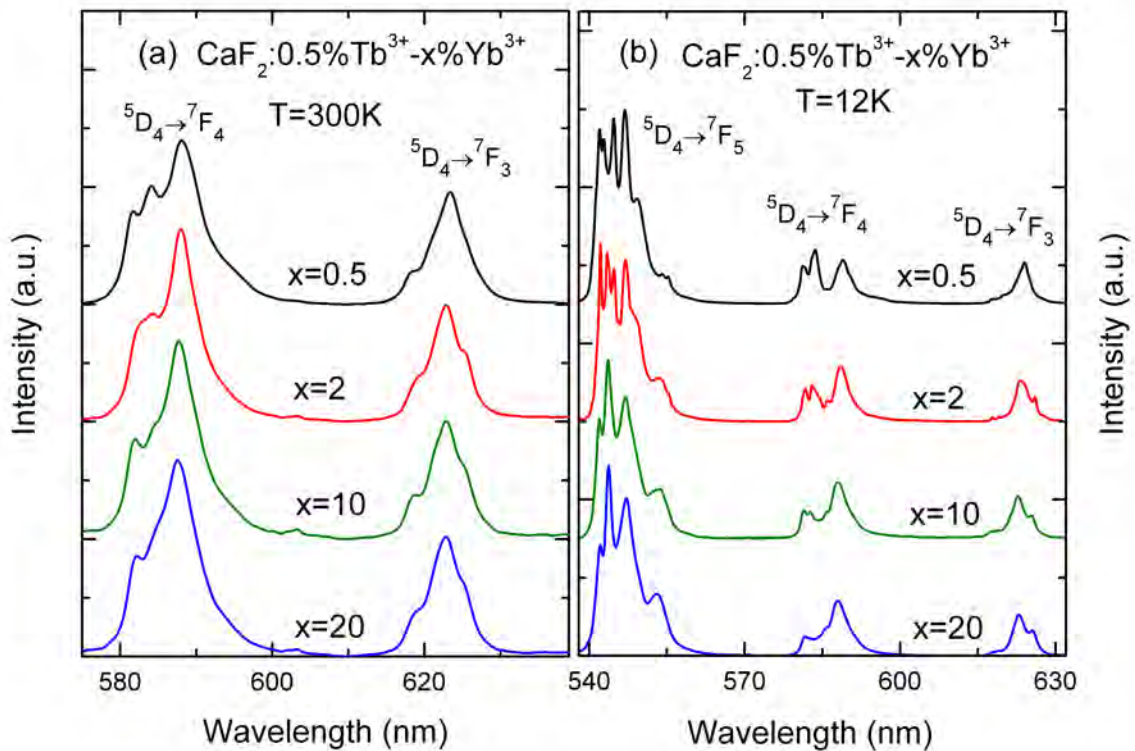


Figure 4.3: (a) Room temperature $^5\text{D}_4$ emission spectra in $\text{CaF}_2:0.5\%\text{Tb}^{3+}-x\%\text{Yb}^{3+}$ ($x=0.5, 2, 10, 20$) at 488 nm excitation (b) Low temperature $^5\text{D}_4$ emission spectra in $\text{CaF}_2:0.5\%\text{Tb}^{3+}-x\%\text{Yb}^{3+}$ ($x=0.5, 2, 10, 20$) at 488 nm excitation.

The analysis of the low temperature $^5\text{D}_4$ emission spectra for the different codoped samples is even more explicit in terms of emitting centers. As displayed in Fig.4.3.b, a clear evolution with the Yb^{3+} content is observed in the low temperature Tb^{3+} emission. The spectrum obtained at low Yb^{3+} concentrations ($x=0.5$ in Fig.4.3.b) is nearly identical to the Tb^{3+} singly doped CaF_2 emission spectrum (Fig.4.1). Thus, the emission most probably originates in this codoped sample from the Tb^{3+} clusters identified in Tb^{3+} singly doped CaF_2 . However, the shape of the spectra progressively changes when the Yb^{3+} concentration increases, indicating the formation of a new Tb^{3+} center in all likelihood associated with the Yb^{3+} codopant. This conclusion is in agreement with the evolution of the rare-earth aggregates observed for $\text{CaF}_2\text{:Pr}^{3+}\text{-Yb}^{3+}$ (Chapter 3) in which $\text{Pr}^{3+}\text{-Yb}^{3+}$ clusters progressively replace the Pr^{3+} clusters and become the dominant emitting center at relatively high Yb^{3+} concentrations.

In Chapter 3, two different types of $\text{Pr}^{3+}\text{-Yb}^{3+}$ clusters were clearly identified in $\text{CaF}_2\text{:Pr}^{3+}\text{-Yb}^{3+}$. Unlike $\text{CaF}_2\text{:Pr}^{3+}\text{-Yb}^{3+}$, the investigation of both room temperature and low temperature $^5\text{D}_4$ time-resolved spectra in the different $\text{CaF}_2\text{:Tb}^{3+}\text{-Yb}^{3+}$ codoped samples showed no sign of the existence of different types of $\text{Tb}^{3+}\text{-Yb}^{3+}$ centers in CaF_2 . On the contrary, the same emission spectrum, as the one displayed in Fig.4.3 with 10% Yb^{3+} and 20% Yb^{3+} , was recorded for all possible time windows for these two samples. This result first indicates that all the Tb^{3+} clusters are all replaced by $\text{Tb}^{3+}\text{-Yb}^{3+}$ clusters for Yb^{3+} concentrations of 10% or higher. Secondly, it shows that a single type of $\text{Tb}^{3+}\text{-Yb}^{3+}$ clusters exists at high Yb^{3+} concentrations in $\text{CaF}_2\text{:Tb}^{3+}\text{-Yb}^{3+}$.

4.3.3 Yb^{3+} emission

The occurrence of the cooperative energy transfer is clearly illustrated by the Yb^{3+} emission detected upon Tb^{3+} excitation at 488 nm ($^7\text{F}_6 \rightarrow ^5\text{D}_4$). Fig.4.4 displays the emission spectra recorded between 570 nm and 1080 nm at room temperature for the samples codoped with 0.5% Yb^{3+} and 20% Yb^{3+} . Along with the terbium $^5\text{D}_4$ transitions, a larger band around 1 μm is without any doubt assigned to the Yb^{3+} ($^2\text{F}_{5/2} \rightarrow ^2\text{F}_{7/2}$) transition in Fig.4.4. Remarkably, the Yb^{3+} emission band is much more important for the sample codoped with 0.5% Tb^{3+} -20% Yb^{3+} than for the sample codoped with 0.5% Tb^{3+} -0.5% Yb^{3+} . A further insight into the Yb^{3+} emission evolution is shown in Fig.4.5. The Yb^{3+} emission intensity increases in a remarkable way with the increasing Yb^{3+} content, while the reabsorption of emitted photons is again observed in the Yb^{3+} emission spectrum as the main emission peak at 980 nm tends to decrease with the Yb^{3+} concentration [246].

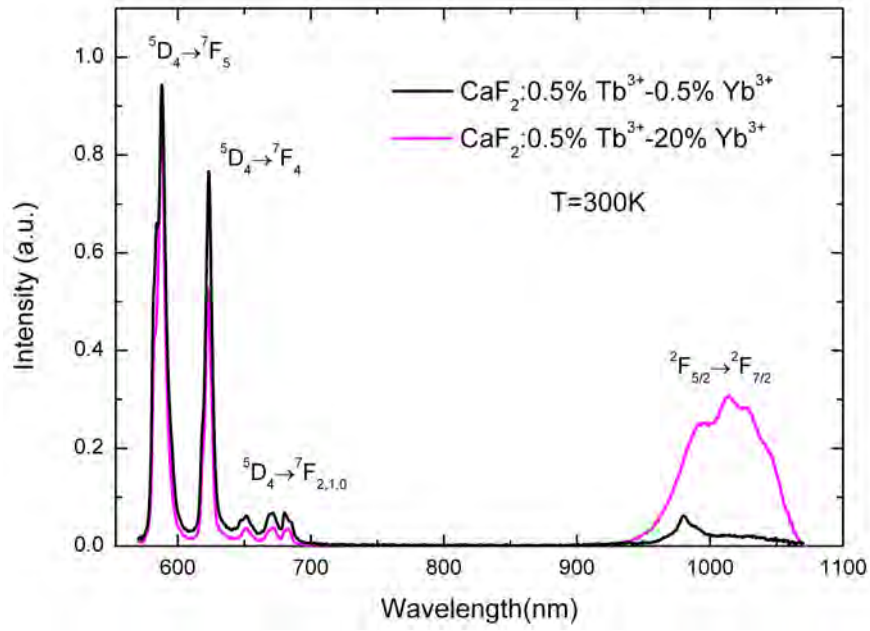


Figure 4.4: RT emission spectra in $\text{CaF}_2:0.5\%\text{Tb}^{3+}-0.5\%\text{Yb}^{3+}$ and $\text{CaF}_2:0.5\%\text{Tb}^{3+}-10\%\text{Yb}^{3+}$ recorded between 570 nm and 1100 nm at 488 nm excitation. The cooperative energy transfer is perfectly illustrated by the Yb^{3+} emission band around 1000 nm.

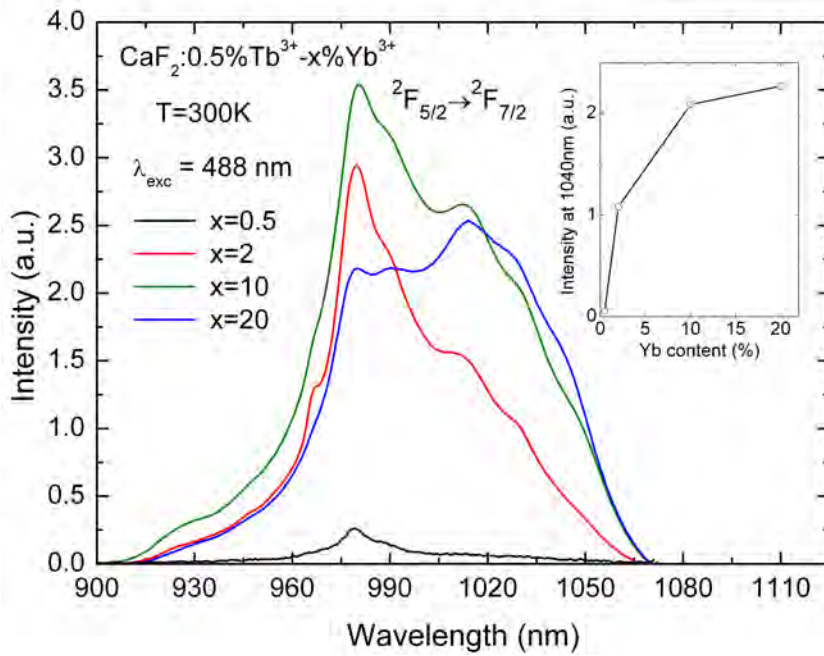


Figure 4.5: Ytterbium ${}^2\text{F}_{5/2} \rightarrow {}^2\text{F}_{7/2}$ downconverted emission at 488 nm excitation in $\text{CaF}_2:0.5\%\text{Tb}^{3+}-x\%\text{Yb}^{3+}$ ($x=0.5, 2, 10, 20$). Inset: Intensity at 1040 nm as a function of the Yb^{3+} content.

As shown in the inset of Fig.4.5, the Yb^{3+} emission intensity tends to saturate when the Yb^{3+} concentration reaches 20%. This saturation could be explained by either a saturation of the energy transfer efficiency from Tb^{3+} to Yb^{3+} or by detrimental energy transfers such as back-transfers or concentration quenching processes which would limit the Yb^{3+} emission. The following analysis of the Tb^{3+} $^5\text{D}_4$ and Yb^{3+} $^2\text{F}_{5/2}$ decay times show that these latter quenching processes are very limited in CaF_2 : Tb^{3+} - Yb^{3+} .

4.3.4 Lifetimes and ETE

Fig.4.6 displays the room temperature Tb^{3+} $^5\text{D}_4$ luminescence decays for the different samples. As seen in Fig.4.6, all the decay curves present exponential features unlike Pr^{3+} ($^3\text{P}_0$) (Fig.3.10) in CaF_2 : Tb^{3+} - Yb^{3+} , supporting the idea of a single type of Tb^{3+} - Yb^{3+} cluster in CaF_2 : Tb^{3+} - Yb^{3+} .

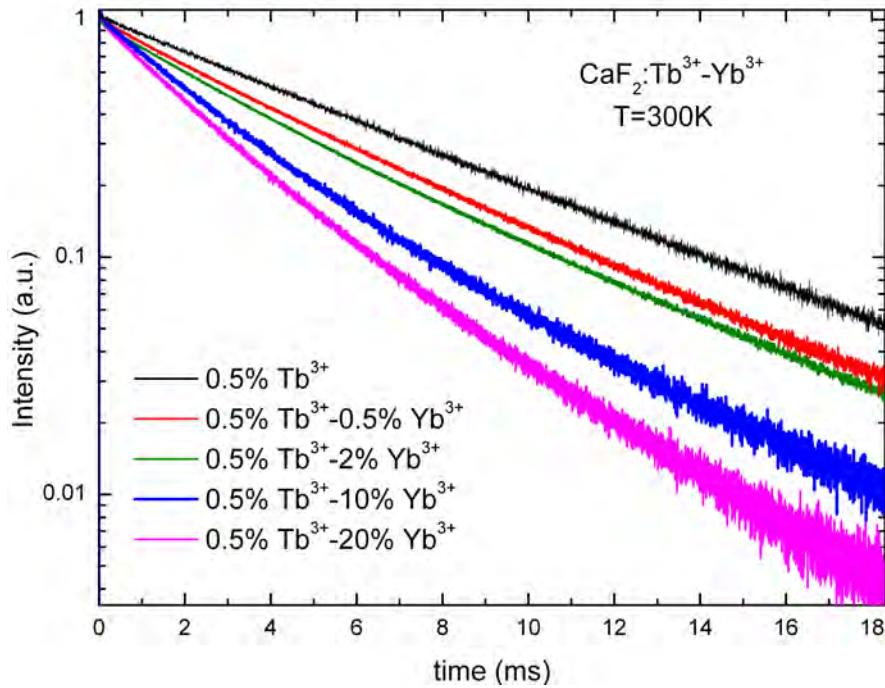


Figure 4.6: Room temperature $^5\text{D}_4$ decay curves in CaF_2 : $0.5\%\text{Tb}^{3+}$ - $x\%\text{Yb}^{3+}$ ($x=0, 0.5, 2, 10, 20$).

The luminescence lifetimes for the different samples were determined by single exponential fits. The ETE for the cooperative mechanism was afterwards calculated by using Eq.2.3. The value of the Tb^{3+} lifetime without Yb^{3+} , essential for the ETE calculation in Eq.2.3, was carefully investigated at RT. The same 6 ms decay is found at RT for all emission wavelengths in Tb^{3+} singly doped CaF_2 while the lifetimes of the two Tb^{3+} clusters

identified at 12 K were 5 ms and 7 ms respectively. As the temperature is raised to RT, the spectra of the two different aggregates merge because of homogenous broadening and exhibit a single decay of 6 ms. From the calculated ETE, the efficiency of the quantum cutting process is easily derived as:

$$\eta_{QC} = \eta_{r(5D4)}(1 - \eta_{x\%Yb}) + 2\eta_{x\%Yb} \quad (4.1)$$

in which $\eta_{x\%Yb}$ is the ETE with $x\%Yb^{3+}$ and $\eta_{r(5D4)}$ is the intrinsic 5D_4 emission QE (without Yb^{3+} ions) which is set to 1. The results are summarized in Table 4.2.

Table 4.2: Luminescence lifetimes, ETE and QC efficiency (QCE) in Tb^{3+} - Yb^{3+} codoped crystals.

Sample	τ_{5D4} (ms)	ETE (%)	QCE (%)
2% Tb^{3+}	6	-	-
0.5% Tb^{3+} -0.5% Yb^{3+}	4.9	18	118
0.5% Tb^{3+} -2% Yb^{3+}	4.7	22	122
0.5% Tb^{3+} -10% Yb^{3+}	3.2	47	147
0.5% Tb^{3+} -20% Yb^{3+}	2.8	53	153

Fig.4.7 displays the evolution of the Tb^{3+} 5D_4 emission lifetime and the efficiency of the QC mechanism as a function of the Yb^{3+} content. The evolution is rather fast from 0% Yb^{3+} to 0.5% Yb^{3+} , and can be related to the emergence of Tb^{3+} - Yb^{3+} clusters with the incorporation of Yb^{3+} ion in the host matrix. The evolution becomes slower at higher Yb^{3+} concentrations, especially between 10% Yb^{3+} and 20% Yb^{3+} . This seems logical since increasing the Yb^{3+} content from 10% Yb^{3+} to 20% Yb^{3+} does not suppose a great change in the cluster structure as demonstrated by the emission spectra in Fig.4.3.

The Yb^{3+} fluorescence decay obtained under Tb^{3+} excitation at 485 nm are displayed in Fig.4.8-left for 0.5% Tb^{3+} -10% Yb^{3+} codoped CaF_2 and consist, as expected, of a rise time followed by a decay time. The Yb^{3+} fluorescence decay upon 485 nm excitation was therefore adjusted with a double exponential fit as follows:

$$I(t) = A_1 e^{\frac{-t}{\tau_d}} - A_2 e^{\frac{-t}{\tau_r}} \quad (4.2)$$

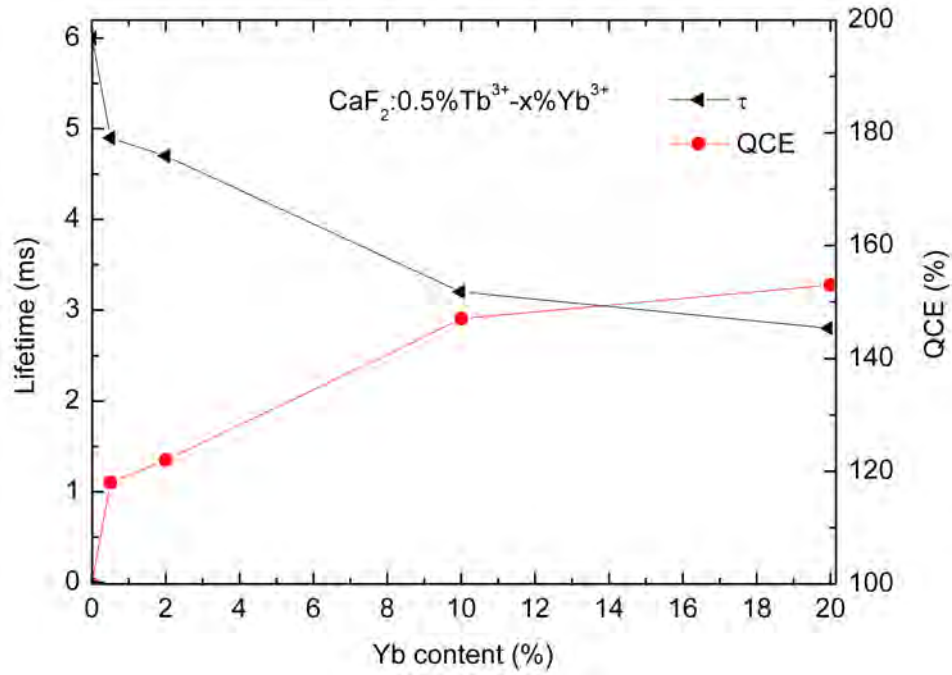


Figure 4.7: Evolution of the Tb^{3+} $^5\text{D}_4$ emission lifetime and of the efficiency of the QC mechanism (QCE) with the Yb^{3+} content.

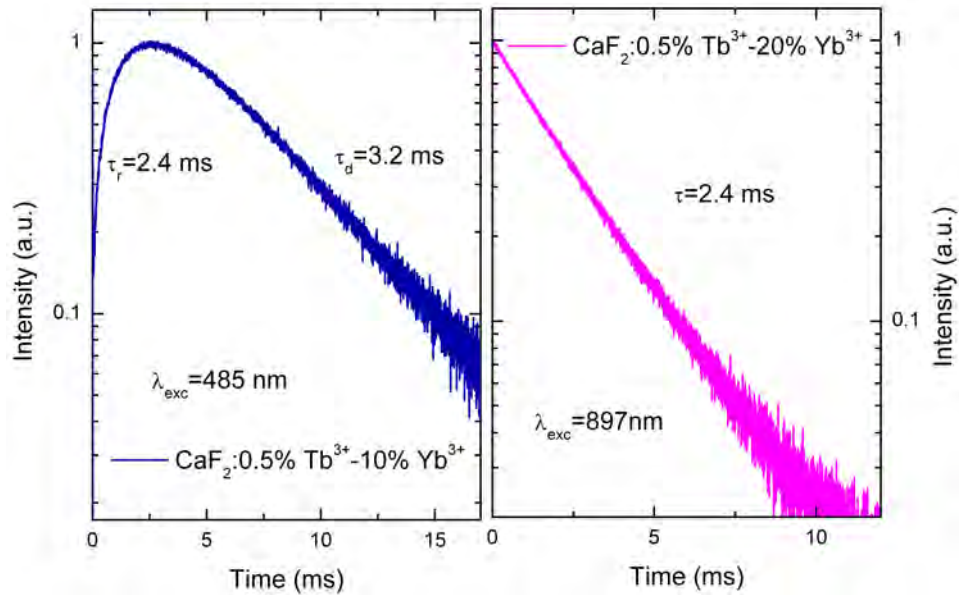


Figure 4.8: (left) Yb^{3+} fluorescence decay upon 485 nm excitation for CaF_2 : 0.5% Tb^{3+} -10% Yb^{3+} ; (right) Yb^{3+} fluorescence decay upon 897 nm excitation for CaF_2 : 0.5% Tb^{3+} -20% Yb^{3+} .

in which τ_d and τ_r are the decay and rise times respectively. The 2.4 ms rise time constant (Fig.4.8-left), can be ascribed to the $\text{Yb}^{3+} \ ^2\text{F}_{5/2}$ lifetime since 2.4 ms is exactly the Yb^{3+} lifetime value which is found in $\text{CaF}_2:\text{Yb}^{3+}$ [247]. The 3.2 ms decay in Fig.4.8-left, is consistent with the $^5\text{D}_4$ emission lifetime measured directly as shown in Table 4.2. The fact that the Yb^{3+} lifetime remains equal to 2.4 ms, which is verified by recording the Yb^{3+} lifetime under direct Yb^{3+} excitation (Fig.4.8-right) in $\text{CaF}_2:0.5\%\text{Tb}^{3+}-20\%\text{Yb}^{3+}$, indicate not only that the concentration quenching is indeed very limited in CaF_2 , but also that there is no back-transfer from Yb^{3+} to Tb^{3+} . The only back-transfer, which might take place, is the non-resonant energy transfer $\text{Yb}^{3+} ({}^2\text{F}_{5/2} \rightarrow {}^2\text{F}_{7/2})$ to $\text{Tb}^{3+} ({}^7\text{F}_6 \rightarrow {}^7\text{F}_0)$. This process is highly unlikely in a host material presenting low phonon energy like CaF_2 , since the energy gap between ${}^2\text{F}_{5/2}$ and ${}^7\text{F}_0$ is about 3800 cm^{-1} . The absence of quenching of the Yb^{3+} lifetime along with a high ETE for the cooperative process is remarkable in comparison with other hosts.

4.4 Conclusions

Based on the quenching of the Tb^{3+} lifetime, a remarkable QC efficiency, reaching a value of 153%, is obtained with $0.5\%\text{Tb}^{3+}-20\%\text{Yb}^{3+}$ codoped CaF_2 . This result can be compared to other QC results obtained with other $\text{Tb}^{3+}-\text{Yb}^{3+}$ codoped materials. The results summarized in Table 4.3 show QEs greater than unity in all cases. Even higher efficiencies than in $\text{CaF}_2:\text{Tb}^{3+}-\text{Yb}^{3+}$ were previously reported [117], however, the price to pay for such high efficiencies was an extremely high Yb^{3+} concentration. This is a major problem for the quantum cutting mechanism through cooperative energy transfer in most host materials, because of the important concentration quenching of the Yb^{3+} emission observed at high Yb^{3+} concentrations. The clustering process of rare-earth ions in CaF_2 offers the advantage of achieving high QE with a much lower Yb^{3+} content than in other hosts (Table 4.3). The clustering along with a rather low Yb^{3+} concentration lead to a very weak concentration quenching of the Yb^{3+} emission which is difficult to achieve in other hosts.

Cooperative QC has been investigated with other codopings, not presented in Table 4.3, and as a result, high efficiencies have been reported. For instance, a QC efficiency of 172% has been announced with $0.01\%\text{Tm}^{3+}-50\%\text{Yb}^{3+}$ in YPO_4 [256] based on the quenching of the $\text{Tm}^{3+} \ ^1\text{G}_4$ energy level. In the same way, a QC efficiency of 179% has been reported in $\text{YBO}_3:1\%\text{Ce}^{3+}-6\%\text{Yb}^{3+}$, based on the quenching of the $\text{Ce}^{3+} \ 4f5d$

emission lifetime [125]. The efficiencies reported are remarkable, but, these results must be handled with great care since, in these systems, contrarily to the $\text{Tb}^{3+}\text{-Yb}^{3+}$ couple, the quenching of the donor lifetime can also take place through other mechanisms than the cooperative energy transfer as for instance, non resonant-energy transfers. Finally, none of the results presented in Table 4.3 takes into account the evolution of the Yb^{3+} emission as a function of the Yb^{3+} content and thus the concentration quenching, which is extremely important for a real application of the QC mechanism.

Table 4.3: Summary of quantum cutting efficiencies (QCE) reported in the past with $\text{Tb}^{3+}\text{-Yb}^{3+}$ codoped materials.

Material	Concentration	QCE (%)	Reference
$\text{Yb}(\text{YPO}_4)\text{:Tb}^{3+}$	1% Tb^{3+} -15% Yb^{3+}	110	[117]
$\text{Yb}(\text{YPO}_4)\text{:Tb}^{3+}$	1% Tb^{3+} -100% Yb^{3+}	180	[117]
Oxifluoride glass- CaF_2	0.3% Tb^{3+} -26% Yb^{3+}	155	[121]
$\text{Y}_2\text{O}_3\text{:Tb}^{3+}, \text{Yb}^{3+}$	0.1% Tb^{3+} -20% Yb^{3+}	137	[122]
Li-Ca borate glass	4% Tb^{3+} -26% Yb^{3+}	132	[257]
$\text{Y}_2\text{O}_3\text{:Bi}^{3+}, \text{Yb}^{3+}$	0.5% Tb^{3+} -15% Yb^{3+}	139.5	[130]
$\text{CaF}_2\text{:Tb}^{3+}, \text{Yb}^{3+}$	0.5% Tb^{3+} -20% Yb^{3+}	153	-

4.5 Sensitization

The $4f$ transitions of the trivalent rare-earth ions present low absorption coefficients coming from weak f - f oscillator strengths. Thus, the development of efficient rare-earth based solar up and down converters involves not only finding rare-earth doped systems presenting efficient energy transfers, but also sensitizing the rare-earth ions along with an efficient absorption of the sunlight radiation.

The sensitization of trivalent rare earth ions is in principle possible by energy transfer from another impurity ion, or, from the host itself. The ideal sensitizer must fulfill different conditions such as presenting a wide absorption band with high absorption coefficients as well as having emission bands which match the absorption bands of the sensitized rare-earth ion in order to assure an efficient resonant energy transfer. The rare earths themselves are among the most used sensitizers. The sensitization of a rare-earth ion is indeed possible using the strong absorptions of 5d levels or charge transfer bands (CTB).

In the same way, Tl-like elements such as Pb^{2+} or transition metal ions such as Cr^{3+} can be good sensitizers since, they generally present wide absorption bands with larger absorption coefficients than the $4f$ levels of the rare-earth ions. In addition, they have been proved to easily transfer their energy to rare-earth ions in different host materials in numerous occasions [258-260].

More sophisticated approaches also suggest the sensitization of the rare earth ions by taking advantage of the special properties of a number of nanostructures. Nanocrystals or QDs for instance, are broadband absorbers presenting emission bands which can be controlled by the dot size, and well adapted to the excitation of the rare-earth ions. For instance, the sensitization of Er^{3+} ions by silicon nanocrystals has been recently investigated in silica layers [261-264] in order to optically or, eventually, electrically pump Er^{3+} ions for a $1.54 \mu\text{m}$ laser emission. In the same way, efficient sensitization and emission enhancement of several rare-earth ions embedded in different materials with various (ZnO , Cds , $\text{GaN} \dots$) nanoparticles has been recently reported [265-268].

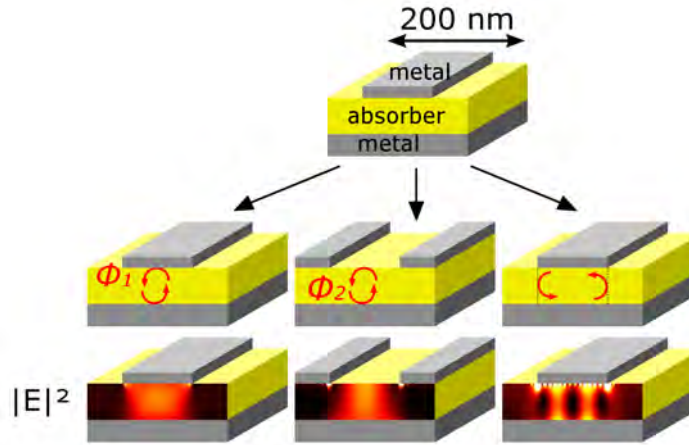


Figure 4.9: Example of plasmon rare-earth system. The SPs are generated at the boundary between the metallic films and the absorber containing the RE ions. The SP resonances enhance the rare-earth emission quantum yield.

In addition to the intrinsic absorption and emission properties of nanostructures such as QDs, surface plasmon resonances have been used to enhance the emission of different luminescent centers including rare-earth ions. Surface plasmons (SPs) are generated at the boundary between a metallic dot or thin-film and a dielectric material (so-called absorber). SPs improve the light trapping within the absorber in the whole visible range by multi-resonant mechanisms. In the case of rare-earth ions, the coupling between the

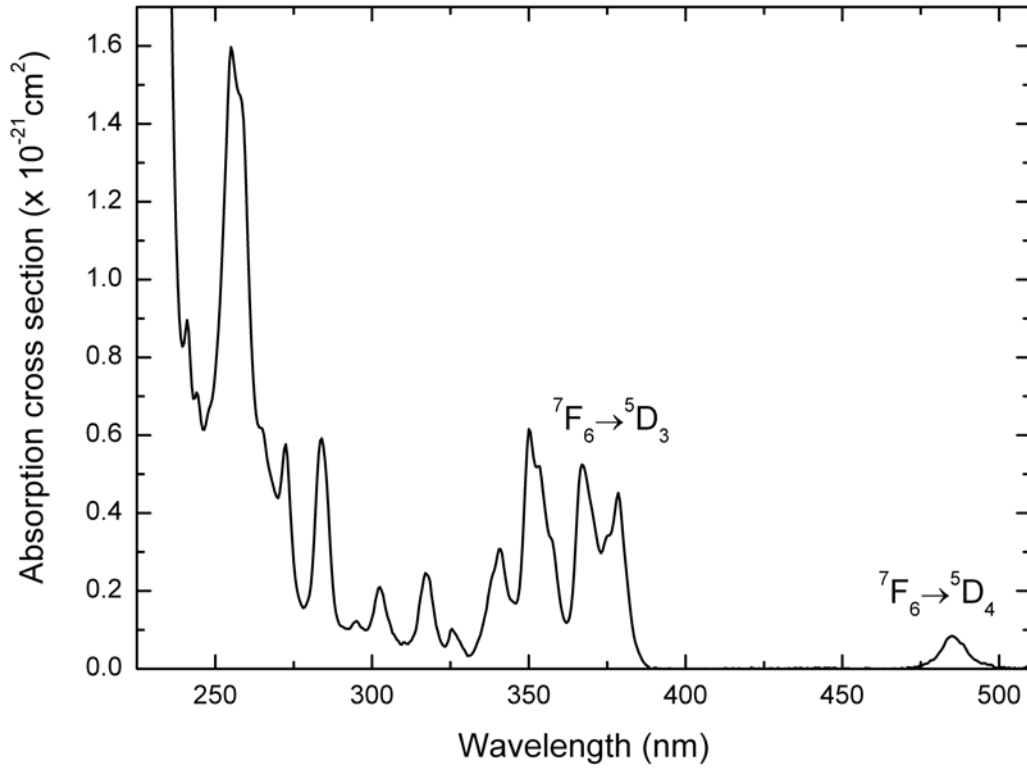
excited states of the rare earths, and the local electrical field generated by the SPs results in an increase of the rare earth luminescence quantum yield [269-271]. However, the sensitization of rare-earth ions by metal nanoparticles or nanoclusters does not seem to involve surface plasmon resonance per say. This sensitization appears to be efficient only for very tiny metal clusters (made of a few atoms) and imply an energy transfer from the metal nanocluster to the rare-earth ion [272].

The rare-earth ions sensitization by using approaches based on nanostructures or taking advantage of the metal nanoclusters present without a doubt a great potential. Nevertheless, these technologies are as of today inefficient for real practical applications since the fluorescence enhancement they provoke is still far from reaching the requirements of a viable practical application. In addition, their exploitation involves quite expensive and complex technologies. Anyway, an intense research activity exists around nanotechnologies and plasmonics so that they might become a very interesting alternative in the future.

4.5.1 Tb^{3+} ions sensitization

The promising QC efficiency results obtained with $\text{CaF}_2:\text{Tb}^{3+}-\text{Yb}^{3+}$ make the Tb^{3+} sensitization a question which deserves the highest interest. Indeed, the Tb^{3+} absorption is both weak and spectrally narrow (Fig.4.10). Among the different sensitization possibilities, codoping the $\text{Tb}^{3+}-\text{Yb}^{3+}$ system with a different luminescent center is, contrarily to other approaches, a very versatile solution which can be adopted for a large number of host materials. From this point of view, codoping the materials with Ce^{3+} ions and taking advantage of the usually efficient $\text{Ce}^{3+} \rightarrow \text{Tb}^{3+}$ energy transfer [273-278] is a very attractive alternative. In the case of CaF_2 , several $4f5d$ absorption and emission bands located in the UV region have been reported in the past literature. The absorption band so-called A, which is the lowest one in energy, is found between 280 and 320 nm peaking around 307 nm ($\sim 32500 \text{ cm}^{-1}$) [279,280]. Moreover, a broad emission between 300 and 380 nm is observed showing a good spectral overlap with the Tb^{3+} energy levels located above 26000 cm^{-1} ($^5\text{D}_3$, $^5\text{L}_{10}$, $^5\text{D}_3 \dots$) as displayed in Fig.4.11. As a matter of the fact, a sensitization of Tb^{3+} by energy transfer from Ce^{3+} to Tb^{3+} has already been reported in a host containing CaF_2 nanoparticles [278].

Besides Ce^{3+} , energy transfer to Tb^{3+} ions has been demonstrated from other luminescent centers such as Cu^+ and Sn^{2+} in SrLiPO_4 [281]. Nevertheless, finding suitable

Figure 4.10: Tb^{3+} absorption cross-section

sensitizers for Tb^{3+} in CaF_2 seems quite a difficult task. One of the most investigated is Pb^{2+} since efficient $\text{Pb}^{2+} \rightarrow \text{RE}^{3+}$ sensitization in the UV region has been demonstrated in several host materials [282,283] and particularly, efficient $\text{Pb}^{2+} \rightarrow \text{Tb}^{3+}$ energy transfer [258,284]. However, Pb^{2+} presents several absorptions and emission bands in the UV and VUV regions in the case of CaF_2 . The lowest absorption band (A band) is located around 207 nm ($\sim 48300 \text{ cm}^{-1}$) [285] and the corresponding emission band (A') is found at approximately 220 nm ($\sim 45000 \text{ cm}^{-1}$), so that no spectral overlap with Tb^{3+} ions is in principle expected. The same difficulty appears with Bi^{3+} . A good spectral overlap and efficient $\text{Bi}^{3+} \rightarrow \text{Tb}^{3+}$ energy transfer were reported in $\text{YAl}_3\text{B}_4\text{O}_{12}$ and YPO_4 [287]. In a fluoride host as NaYF_4 , Bi^{3+} has been found to absorb between 100 and 350 nm while presenting a wide emission band between 350 and 600 nm [288,289]. Thus, Bi^{3+} appears suitable for energy transfer towards the $^5\text{D}_3$ and $^5\text{D}_4$ Tb^{3+} -excited states in NaYF_4 . Nevertheless, the case of CaF_2 is very different from NaYF_4 . The lowest absorption band which can be found for Bi^{3+} in CaF_2 is expected at higher energy than in NaYF_4 , particularly between 225 and 190 nm (A band). In a similar way as Pb^{2+} , Bi^{3+} is definitely not adapted as sensitizer for Tb^{3+} ions in CaF_2 .

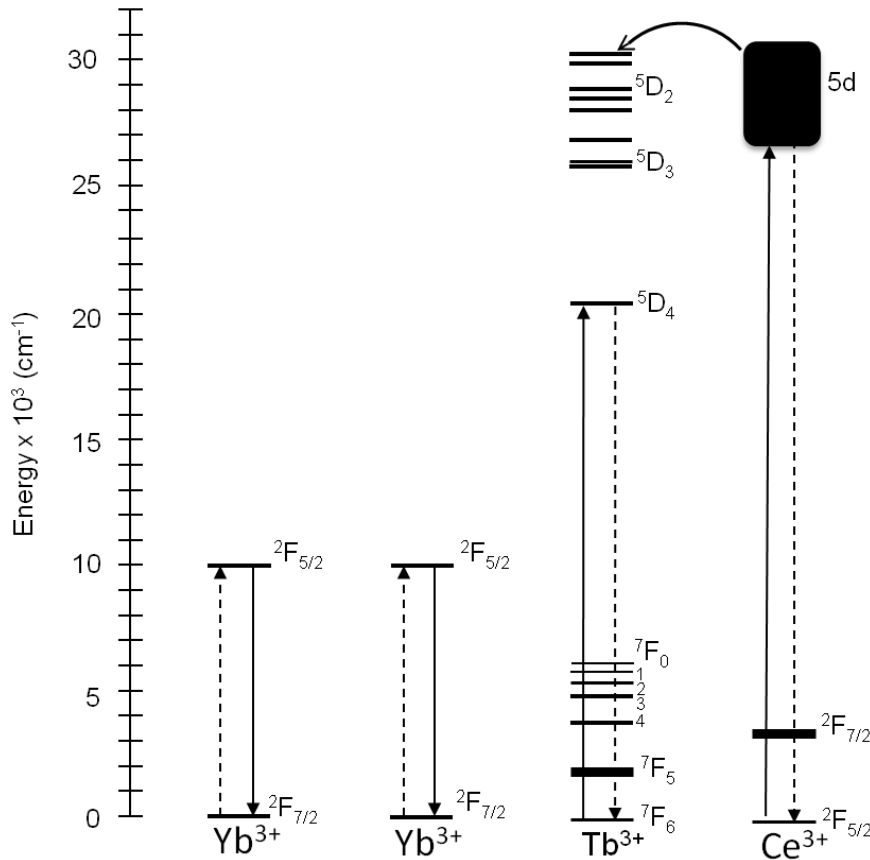


Figure 4.11: Ce^{3+} - Tb^{3+} - Yb^{3+} triply doped system

Other approaches are possible such as energy transfer from metallic dots to rare-earth ions, since interesting results have been recently reported. For instance, an enhanced emission from Tb^{3+} ions has been demonstrated by energy transfer from ZnO nanoparticles [265] and WO_3 QDs [266] in a Silica xerogel host. Moreover, a particularly remarkable result has been obtained with Tb^{3+} and Yb^{3+} doped CdS nanocrystals (4.2-5.5 nm in diameter) [290]. A wide and intense excitation band starting at 450nm and extended to the deep UV region is reported for the CdS nanocrystals. Thus, CdS nanocrystals are able to sensitize Tb^{3+} ions. In addition, the sensitization is apparently efficient since broadband emission in the visible region associated to the $^5\text{D}_4$ emissions is reported in the study as arising from the codoped Tb^{3+} - Yb^{3+} CdS nanocrystals [290].

Mechanisms based on surface plasmon resonances (SPRs) have been also investigated to enhance the Tb^{3+} luminescence in several glasses containing Ag nanoparticles [291,292]. Nevertheless, in spite of these interesting results, the Tb^{3+} luminescence enhancement remains relatively low in these materials due to quenching processes endured by the Tb^{3+} ions after sensitization.

In conclusion, several interesting candidates exist to sensitize and/or enhance the Tb^{3+} emission. Nevertheless, an efficient sensitization remains a difficult task so that further investigations are required for all these different approaches in order to develop efficient sensitized systems in the future.

4.5.2 CaF_2 codoped Tb^{3+} - Ce^{3+} and Tb^{3+} - Bi^{3+} investigation

The energy transfer from Ce^{3+} and Bi^{3+} ions to Tb^{3+} ions upon UV excitation was experimentally investigated with CaF_2 samples codoped with 0.5% Tb^{3+} -5% Ce^{3+} and 0.5% Tb^{3+} -5% Bi^{3+} respectively.

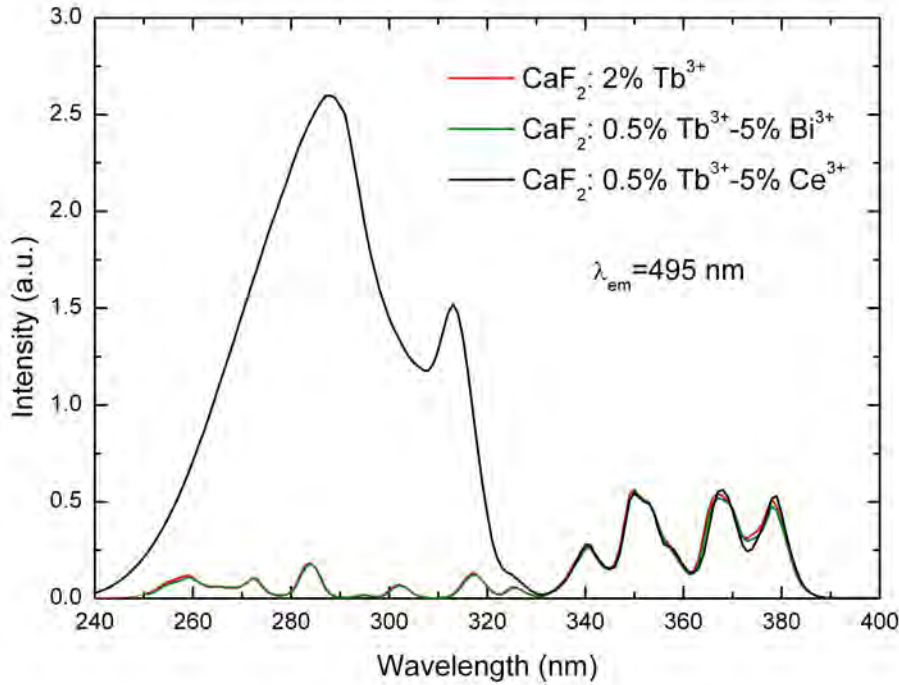


Figure 4.12: Photoluminescence excitation (PLE) spectra recorded between 240 and 400 nm monitoring the Tb^{3+} $^5\text{D}_4$ emission at 495 nm ($^5\text{D}_4 \rightarrow ^7\text{F}_6$). The spectra are normalized to the Tb^{3+} lines around 360 nm for sake of clarity.

Fig.4.12 displays the photoluminescence excitation (PLE) spectra recorded for the two samples between 240 and 400 nm compared to the PLE spectrum in Tb^{3+} singly doped CaF_2 . The detection wavelength is set at 495 nm ($^5\text{D}_4 \rightarrow ^7\text{F}_6$). As observed, a wide excitation band is observed between 240 and 330 nm for the 0.5% Tb^{3+} -5% Ce^{3+} codoped sample which is attributed to the $4f \rightarrow 5d$ Ce^{3+} absorption transition (Fig.4.11). On the contrary, the 0.5% Tb^{3+} -5% Bi^{3+} codoped sample and the 2% Tb^{3+} singly doped sample

show identical PLE spectra in which the different peaks are exclusively assigned to Tb^{3+} transitions. This result confirms, as previously mentioned, the inability of Bi^{3+} ions to sensitize Tb^{3+} in the near UV spectral region.

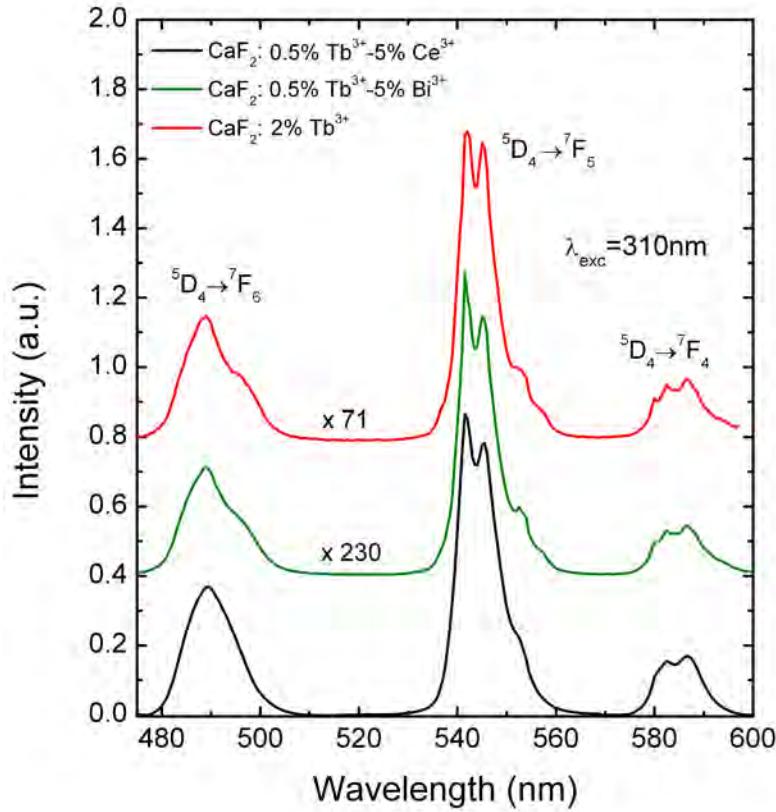


Figure 4.13: Normalized emission spectra upon 310 nm excitation in $\text{Tb}^{3+}\text{-X}^{3+}$ ($\text{X} = \text{Ce}, \text{Bi}$) codoped CaF_2 and Tb^{3+} singly doped CaF_2 .

The emission spectra recorded between 480 nm and 600 nm upon 310 nm excitation for the samples codoped with $\text{Ce}^{3+}\text{-Tb}^{3+}$ and $\text{Bi}^{3+}\text{-Tb}^{3+}$ ions; and for the Tb^{3+} singly doped sample are displayed in Fig.4.13. The same $^5\text{D}_4$ luminescence spectrum is obtained for the three samples. The normalization factors demonstrate a drastic increase of the Tb^{3+} $^5\text{D}_4$ luminescence intensity when codoping with Ce^{3+} ions. The Tb^{3+} emission is remarkably enhanced by a factor of 230 in $0.5\%\text{Tb}^{3+}\text{-}5\%\text{Ce}^{3+}$ in comparison to a sample with the same Tb^{3+} concentration ($0.5\%\text{Tb}^{3+}\text{-}5\%\text{Bi}^{3+}$). The Tb^{3+} singly doped sample in Fig.4.13 contains 4 times more Tb^{3+} ions (2%at.) which explains why the enhancement factor is only 70 in comparison to the $0.5\%\text{Tb}^{3+}\text{-}5\%\text{Ce}^{3+}$ sample. In conclusion, the $\text{Ce}^{3+}\text{-Tb}^{3+}$ codoping exhibits a very efficient sensitization of Tb^{3+} ions by Ce^{3+} ions.

4.6 Absolute QC efficiency in $\text{Pr}^{3+}\text{-Yb}^{3+}$ and $\text{Tb}^{3+}\text{-Yb}^{3+}$ doped CaF_2

The direct measurement of the absolute conversion efficiency is crucial in order to evaluate the real potential of these systems in terms of applications. As outlined in Chapter 3 for the $\text{CaF}_2\text{:Pr}^{3+}\text{-Yb}^{3+}$ samples, the modeling of the QC efficiency is not straightforward because of the complexity introduced by the rare-earth clustering. In spite of the practical importance of a direct quantum efficiency measurement, there is still a relatively small number of publications reporting absolute upconversion [72,91,97,293,294] and downconversion [295-297] yields. A method to estimate the absolute quantum cutting efficiency is presented here. The absolute quantum efficiency was measured with a setup based on a calibrated integrating sphere (IS) of 15 cm of diameter, associated to a Si detector and a mode lock-in amplifier.

4.6.1 Experimental protocol

The absolute QC efficiency was investigated for different $\text{Pr}^{3+}\text{-Yb}^{3+}$ and $\text{Tb}^{3+}\text{-Yb}^{3+}$ CaF_2 samples. The excitation beam goes through the sample placed at the sphere center before going out through a small hole which is opposite to the opening. A blue Laser Diode at 445 nm was used as excitation source to promote the Pr^{3+} ions in the $^3\text{P}_2$ level and a 488 nm argon laser line to excite the Tb^{3+} ions into the $^5\text{D}_4$ level. The experimental setup is presented in Fig.4.14.

The absolute DC efficiency is defined in a general way as:

$$\eta^{DC} = \frac{P_{em}^{DC}}{P_{abs}} = \frac{\int_{900nm}^{1100nm} p_{DC} d\lambda}{P_{abs}} \quad (4.3)$$

in which P_{abs} is the excitation power absorbed by the sample and P_{em}^{DC} the downconverted power. In this particular case, we exclusively investigate the downconverted power emitted by the Yb^{3+} ions between 900 nm and 1100 nm (Yb^{3+} emission band) as it is the spectral region of interest for Si solar cells.

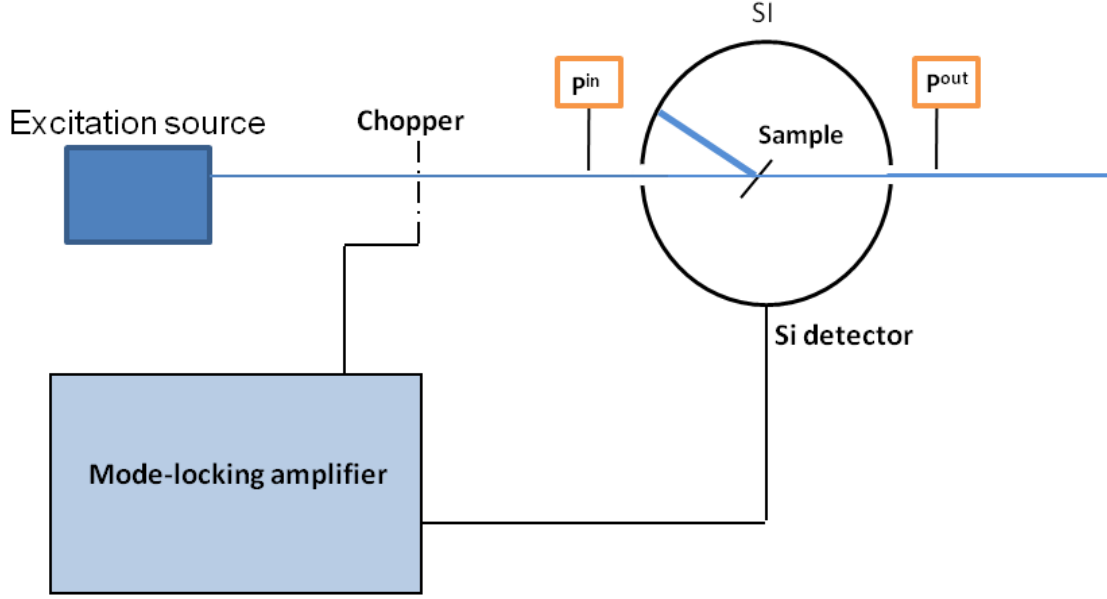


Figure 4.14: Absolute DC efficiency measurements setup.

4.6.2 Absorbed power measurement

The experimental setup shown in Fig.4.14 is firstly used to determine the portion of pump power absorbed by the different samples. The absorbed power (P_{abs}) can be estimated as:

$$P_{abs} = P_{in} - P_{rd} - P_{out} \quad (4.4)$$

in which, P_{in} is the incident power measured before the sphere, P_{rd} is the portion of the pump beam which is diffused and reflected by the sample, and P_{out} is the power transmitted by the sample, which is measured after the integrating sphere (Fig.4.14). The incident light reflected and diffused by the sample (P_{rd}) is measured by the silicon detector providing a signal denoted V_{rd} (mV). In order to get a good estimation of V_{rd} , we used a band-pass filter (FWHM=40 nm) centered at the excitation wavelength ($\sim 445\text{nm}$) which excludes the fluorescence emissions from the sample.

In order to derive the diffused and reflected power (P_{rd}) from the output signal (V_{rd}), a calibration is necessary. The excitation beam is thus sent into the sphere without the sample. The operation is repeated for different incident powers with the filter centered at 445 nm in front of the detector (Fig.4.15). As expected, the detector response is proportional to the incident power in both cases (Fig.4.15). The relationship between the

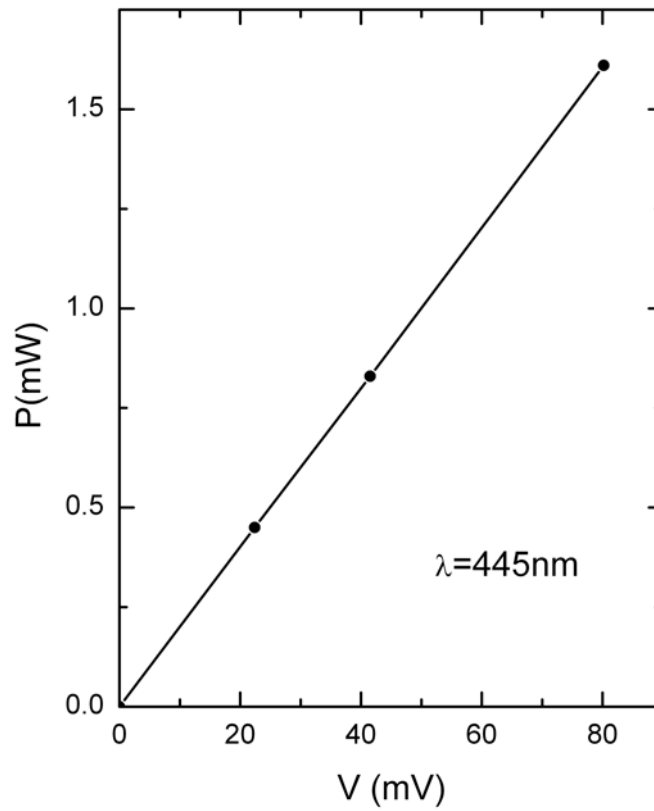


Figure 4.15: Voltage response within the integrating sphere as a function of the incident power at 445 nm.

detector output signal and the incident power are the following.

$$P(mW) = 0.02007 \times V_{445}(mV) \quad (4.5)$$

Eq.4.5 is used to determine P_{rd} knowing the values of V_{rd} . Once P_{rd} is derived from Eq.4.5, the power absorbed by the sample can be easily estimated by applying Eq.4.4. The different power values used for the DC efficiency calculation for the Pr^{3+} - Yb^{3+} samples are summarized in Table 4.4. In addition, the values of P_{abs} derived from Eq.4.4 are compared in Table 4.4 to the values of absorbed power (P_{abs}^{B-L}) obtained with the Beer-Lambert law as follows:

$$P_{abs} = P_{in}T(1 - e^{-\sigma N_P t}) \quad (4.6)$$

in which T is the transmission at the front face of the crystal ($T=96\%$) in order to take into account the Fresnel reflection, σ is the Pr^{3+} absorption cross-section at 445 nm, equal to $1.15 \times 10^{-20} \text{ cm}^2$ (Fig.3.14.d), N_{Pr} is the total Pr^{3+} concentration, in this case $1.225 \times 10^{20} \text{ ions/cm}^3$ (0.5%at. Pr^{3+}) and “ t ” is the sample thickness.

Similar absorption values are obtained by both methods showing that the two methods (direct Power measurement or Beer-Lambert calculation) are rather accurate despite instrumental uncertainties.

Table 4.4: Power values used for the DC efficiency calculation in $\text{CaF}_2:0.5\%\text{Pr}^{3+}-\times\%\text{Yb}^{3+}$ samples.

Samples	P_{in} (mW)	P_{out} (mW)	P_{rd} (mW)	P_{abs} (mW)	P_{abs}^{B-L} (mW)	t (mm)
0.5% Yb^{3+}	1.01	0.57	0.079	0.361	0.336	3.02
1% Yb^{3+}	1.01	0.30	0.345	0.365	0.336	3.03
2% Yb^{3+}	1.01	0.42	0.174	0.416	0.400	3.78
4% Yb^{3+}	1.01	0.40	0.116	0.494	0.483	4.90
10% Yb^{3+}	1.01	0.51	0.206	0.294	0.303	2.66

The estimation of the absorbed power in the $\text{CaF}_2:\text{Tb}^{3+}$ - Yb^{3+} samples is more challenging than for the Pr^{3+} - Yb^{3+} samples due to the extremely low absorption of the Tb^{3+} ions at 488 nm (Fig.4.10). The Tb^{3+} absorption cross-section is 200 times lower than the absorption of Pr^{3+} at 445 nm. Therefore, the absorbed pump power in the different Tb^{3+} - Yb^{3+} samples (<3%) is too weak to be determined experimentally by using Eq.4.4. The typical experimental error associated to the absorbed power measurement with Eq.4.4 is 0.1 mW, while only a few tens of microwatts are absorbed by the Tb^{3+} - Yb^{3+} samples. Therefore, the absorbed power had to be calculated by using the Beer-Lambert law (Eq.4.6) in which σ , the Tb^{3+} absorption cross-section at 488 nm, equals $6.46 \times 10^{-23} \text{ cm}^2$ (Fig.4.10). The results of the calculations are presented in Table 4.5.

Table 4.5: Incident and absorbed pump power at 488 nm in the Tb^{3+} - Yb^{3+} samples.

Samples	P_{in} (mW)	P_{abs} (μW)	t (mm)
$\text{CaF}_2:0.5\text{Tb}^{3+}-20\text{Yb}^{3+}$	7.5	13.1	2.3
$\text{CaF}_2:0.5\text{Tb}^{3+}-10\text{Yb}^{3+}$	7.5	15.3	2.7

4.6.3 Downconverted Yb^{3+} emission and absolute QE

The downconverted Yb^{3+} emission upon 445 nm excitation (Pr^{3+} - Yb^{3+} samples) and 488 nm (Tb^{3+} - Yb^{3+} samples) was measured for the different samples by using the experimental setup of Fig.4.14. This time, a narrow bandpass filter (FWHM=10 nm) centered at 980 nm was placed in front of the silicon detector to reject the reflected and diffused light from the excitation as well as other emission wavelengths than the Yb^{3+} emission. The downconverted power at 980 nm measured by the silicon detector is labeled V_{980} (mV). Another calibration similar to Fig.4.15 is then necessary to convert the V_{980} signal at 980 nm into the corresponding P_{980} power. For that purpose, a Ti-Sa laser tuned to 980 nm was sent into the sphere and the detector voltage was recorded for several input power values. As displayed in Fig.4.16, the detector response is again proportional to the incident power.

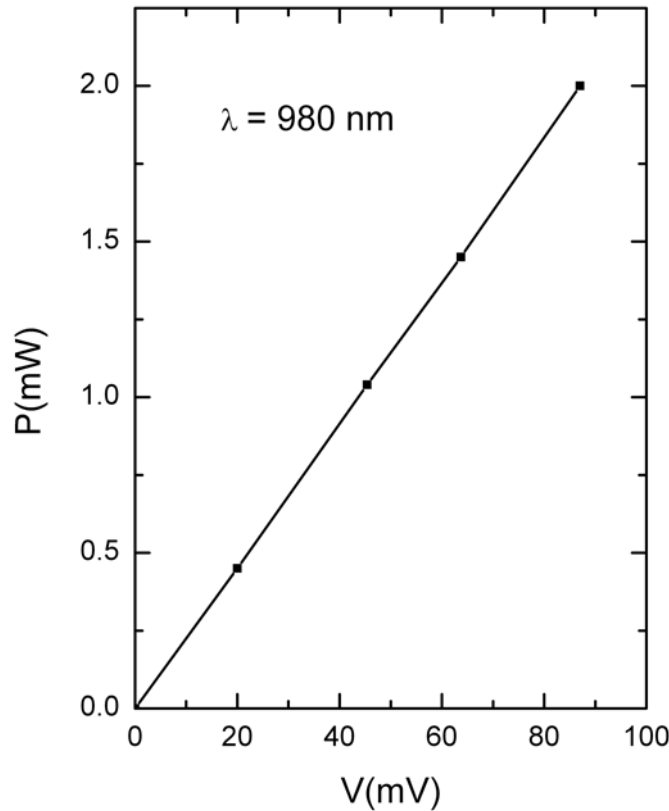


Figure 4.16: Voltage response within the integrating sphere as a function of the incident power at 980 nm.

The relationship between the detector output signal and the incident power at 980 nm with the bandpass filter centered at 980 nm (FWHM=10 nm) is the following:

$$P_{980}(mW) = 0.0230 \times V_{980}(mV) \quad (4.7)$$

One can notice that the slope in Eq.4.7 at 980 nm is almost the same as the slope obtained at 445 nm (Eq.4.5) using the same calibration procedure. This result is quite surprising as the silicon detector is supposed to have a decrease in its spectral response between 445 and 980 nm. One would expect to observe a higher slope at 980 nm than at 445 nm meaning that a given input power would lead to a smaller signal voltage at 980 nm.

Since the bandpass filter only transmits a narrow spectral window of the whole Yb^{3+} emission spectrum, the total QC power is finally determined by extrapolating the P_{980} power obtained with Eq.4.7 for the entire Yb^{3+} emission band. Table 4.6 gives the total Yb^{3+} QC power P_{Yb}^{DC} along with the corresponding absorbed power in the different samples. Knowing the downconverted power, the absolute QC efficiency values in the near-infrared Yb^{3+} band between 900 and 1100 nm can then be calculated using Eq.4.3 and are summarized in Table 4.6 for the different samples.

The QC efficiency is surprisingly low with a maximum of 0.27% for the $\text{Pr}^{3+}\text{-Yb}^{3+}$ samples while it reaches 9% for the $\text{Tb}^{3+}\text{-Yb}^{3+}$ samples. The quenching of the Yb^{3+} emission can explain partially these very poor results as will be discussed in the next section.

Table 4.6: Absolute QC efficiency results

Samples	P_{abs} (μW)	P_{DC}^{Yb} (μW)	η^{QC} (%)
$\text{CaF}_2\text{:}0.5\%\text{Pr}^{3+}\text{-}0.5\%\text{Yb}^{3+}$	361	0.50	0.14%
$\text{CaF}_2\text{:}0.5\%\text{Pr}^{3+}\text{-}1\%\text{Yb}^{3+}$	365	0.85	0.23%
$\text{CaF}_2\text{:}0.5\%\text{Pr}^{3+}\text{-}2\%\text{Yb}^{3+}$	416	1.13	0.27%
$\text{CaF}_2\text{:}0.5\%\text{Pr}^{3+}\text{-}4\%\text{Yb}^{3+}$	494	1.02	0.21%
$\text{CaF}_2\text{:}0.5\%\text{Pr}^{3+}\text{-}10\%\text{Yb}^{3+}$	294	0.63	0.21%
$\text{CaF}_2\text{:}0.5\%\text{Tb}^{3+}\text{-}10\%\text{Yb}^{3+}$	15.3	1.32	8.6%
$\text{CaF}_2\text{:}0.5\%\text{Tb}^{3+}\text{-}20\%\text{Yb}^{3+}$	13.1	1.19	9.0%

4.6.4 discussion

The very good agreement between the Beer-Lambert law and the measured absorbed pump power indicate that the impact of experimental errors (calibrations, power measurements and so on) on the absorbed pump power value should be low.

However, the calculations reveal extremely low QC values comprised between 0.14% and 0.27% for the $\text{CaF}_2:\text{Pr}^{3+}\text{-Yb}^{3+}$ samples with the best result obtained with $\text{CaF}_2:0.5\%\text{Pr}^{3+}\text{-}2\%\text{Yb}^{3+}$. These very low values appear rather suspicious. The quenching of the Yb^{3+} emission evidenced by the decrease of the Yb^{3+} lifetime explains only to some extent these very low numbers. The QC efficiencies in Table 4.6 might be in fact underestimated. An indication that the QC efficiencies are underestimated can be found in the calibration we used in Fig.4.16 to convert the detector voltage into the corresponding power at 980 nm. As mentioned earlier, the slope of this calibration is rather small in comparison with the calibration performed at 445 nm as one would expect the slope to be larger at 980 nm than at 445 nm. With a larger calibration slope value the downconverted signal voltage at 980 nm would lead to higher DC power values and thus to higher QC efficiency.

Nevertheless, the low efficiency results indicate that the visible excitation is clearly not efficiently converted into NIR light around 1 μm . The mechanisms leading to the quenching of the $\text{Yb}^{3+} {}^2\text{F}_{5/2}$ level play a fundamental role in this poor performance, impairing the downconverted emissions at 1 μm and favoring instead IR emissions from the $\text{Pr}^{3+} {}^1\text{G}_4$ and ${}^3\text{H}_6$ levels along with non-radiative relaxations. The very good efficiency of the first energy transfer observed in the $\text{Pr}^{3+}\text{-Yb}^{3+}$ clusters assures the downconversion of the absorbed visible emission. However, the downconversion process does not lead to the emission of two photons by two Yb^{3+} ions per visible photon absorbed but rather to the emission of infrared photons which would eventually go through the solar cells. These photons become then useless unless an efficient upconverter layer is used at the rear face of the cell, which would however make the whole system more complicated.

The QE of the QC mechanism in the $\text{CaF}_2:\text{Tb}^{3+}\text{-Yb}^{3+}$ samples confirms the results derived from the spectroscopic studies (4.3) revealing a much higher quantum yield than in the $\text{Pr}^{3+}\text{-Yb}^{3+}$ samples with a maximum of 9% in $\text{CaF}_2:0.5\%\text{Tb}^{3+}\text{-}20\%\text{Yb}^{3+}$ which would correspond to an overall efficiency of 109% in terms of photons. As mentioned earlier, this efficiency value is most likely underestimated. The expected efficiency for $\text{CaF}_2:0.5\%\text{Tb}^{3+}\text{-}20\%\text{Yb}^{3+}$ is 53% (with an overall efficiency of 153% in photons) according to the spectroscopic investigations which especially showed that the Yb^{3+} quenching is

very limited since the Yb^{3+} lifetime remains unchanged in the codoped samples.

While the absolute value of QC efficiency in Table 4.6 are probably underestimated, a direct comparison of the quantum efficiency in the two types of codopings is possible since the same detection and calibration procedure was used for all samples. When considering samples with the same codopants concentrations such as $10\%\text{Yb}^{3+}\text{-}0.5\%\text{Tb}^{3+}/\text{Pr}^{3+}$, the QC efficiency of the $\text{Tb}^{3+}\text{-Yb}^{3+}$ samples is about 40 times larger ($8.6/0.21=40$ in Table 4.6) than the efficiency derived from the $\text{Pr}^{3+}\text{-Yb}^{3+}$ samples confirming the superiority of the $\text{Tb}^{3+}\text{-Yb}^{3+}$ codoping over $\text{Pr}^{3+}\text{-Yb}^{3+}$ for a practical application as solar downconverter.

4.7 Conclusions Chapter 4

Tb^{3+} - Yb^{3+} codoped CaF_2 has been shown to be efficient for visible to infrared down-conversion quantum cutting. The emission of two photons by Yb^{3+} ions after absorption of a visible photon is possible through a single cooperative energy transfer from Tb^{3+} ions in the case of the Tb^{3+} - Yb^{3+} codoping. The cooperative mechanisms generally give rise to low efficient energy transfers. In the case of CaF_2 , the formation of Tb^{3+} - Yb^{3+} clusters strongly reduces the distance between donors and acceptors which improves in a remarkable way the efficiency of the cooperative mechanism with a rather low Yb^{3+} concentration in comparison with other host materials. Quantum efficiencies up to 153% are found with $\text{CaF}_2:0.5\%\text{Tb}^{3+}-20\%\text{Yb}^{3+}$ which is one of the best results among cooperative systems.

The investigation of the Yb^{3+} downconverted emission intensity shows an increase of the Yb^{3+} emission with the Yb^{3+} content. This result provides a first evidence of the low impact of the Yb^{3+} emission quenching in $\text{CaF}_2:\text{Tb}^{3+}$ - Yb^{3+} . This result was confirmed by the study of Yb^{3+} dynamics which shows that the Yb^{3+} lifetime remains equal to 2.4 ms and does not suffer from concentration quenching effects. This result appears logical as the Yb^{3+} ions tend to form clusters in CaF_2 . In consequence, the distance between clusters is rather large and the concentration quenching becomes therefore limited in comparison with a host with the same doping concentration but a uniform distribution of dopants. In spite of these good results derived from the spectroscopic investigations, the efficient sensitization of Tb^{3+} ions is a necessary condition for a real exploitation of $\text{CaF}_2:\text{Tb}^{3+}$ - Yb^{3+} as quantum cutter. In a general way, the RE^{3+} sensitization is still challenging, while several solutions are proposed. As a result of our experimental investigation, an enhanced $\text{Tb}^{3+} \ ^5\text{D}_4$ emission is observed upon UV excitation in CaF_2 when codoping with Ce^{3+} ions, which establishes the potential of trivalent cerium to act as an efficient Tb^{3+} sensitizer in CaF_2 .

General conclusions

The research of efficient rare earth based quantum cutters for third generation photovoltaic applications has been here explored. With this aim, the $\text{Pr}^{3+}\text{-Yb}^{3+}$ codoping has been investigated using KY_3F_{10} and CaF_2 as host materials. This codoping presents a level scheme allowing a two-step quantum cutting mechanism since two resonant $\text{Pr}^{3+} \rightarrow \text{Yb}^{3+}$ energy transfers are possible, i.e. $\text{Pr}^{3+}({}^3\text{P}_0 \rightarrow {}^1\text{G}_4)$ to $\text{Yb}^{3+}({}^2\text{F}_{7/2} \rightarrow {}^2\text{F}_{5/2})$ and $\text{Pr}^{3+}({}^1\text{G}_4 \rightarrow {}^3\text{H}_4)$ to $\text{Yb}^{3+}({}^2\text{F}_{7/2} \rightarrow {}^2\text{F}_{5/2})$. The efficiency of the two energy transfers involved in the process was demonstrated to depend on several parameters, with the most important being the distance between the donor and acceptor ions, their intrinsic radiative efficiency and the existence of quenching processes detrimental to the intended application.

The choice of fluorides, particularly KY_3F_{10} and CaF_2 , as host lattices favors in a general way the efficiency of the energy transfers between rare-earth ions since this kind of hosts presents low phonon energy which notably limits multiphonon relaxation processes. In spite of this common feature, however, remarkably higher energy transfer rates are obtained in $\text{CaF}_2\text{:Pr}^{3+}\text{-Yb}^{3+}$ than in KY_3F_{10} . Thus, even when energy transfer efficiencies as high as 97% are demonstrated for the first energy transfer with $\text{KY}_3\text{F}_{10}\text{:0.5\%Pr}^{3+}\text{-20\%Yb}^{3+}$, the efficiency in the $\text{CaF}_2\text{:Pr}^{3+}\text{-Yb}^{3+}$ samples for the same energy transfer is notably higher. This is primarily explained by the existence of a drastically different dopant distribution between the two hosts. Indeed, the codoping with rare-earth ions in KY_3F_{10} creates a random distribution of dopants while, in the case of CaF_2 , a process

of rare-earth clustering takes place giving rise to extremely efficient $\text{Pr}^{3+} \rightarrow \text{Yb}^{3+}$ energy transfers due to the short distance (a few Å) between the rare-earth ions forming the cluster.

The clusters resulting from the codoping of CaF_2 with Pr^{3+} and Yb^{3+} were thus investigated in details. The spectroscopic studies revealed the presence of three different Pr^{3+} centers, which were identified as single Pr^{3+} ions (isolated); Pr^{3+} clusters (enduring strong cross-relaxation processes) and $\text{Pr}^{3+}\text{-Yb}^{3+}$ clusters (presenting extremely efficient $\text{Pr}^{3+} \rightarrow \text{Yb}^{3+}$ energy transfers). In addition, the $\text{Pr}^{3+}\text{-Yb}^{3+}$ clusters were found to be divided into two different categories characterized by different emission spectra and energy transfer rates. Energy transfer rates of 10^5 s^{-1} are observed for one of these $\text{Pr}^{3+}\text{-Yb}^{3+}$ clusters, denoted “fast” clusters, while, on the contrary, energy transfer rates of 10^7 s^{-1} are demonstrated for the second ones, thus denoted “ultra-fast” clusters. Consequently, while the energy transfer efficiencies can be explained by dipole-dipole inter-ionic interactions in the case of the “fast” clusters, super-exchange interactions most likely account for the energy transfer efficiencies associated with the “ultra-fast” clusters. This result assumes that a structural difference exists between the two types of $\text{Pr}^{3+}\text{-Yb}^{3+}$ clusters, the distances rare-earth ions forming the clusters being likely shorter in the case of the “ultra-fast” clusters.

The evolution of the different centers (single Pr^{3+} ions, Pr^{3+} clusters and $\text{Pr}^{3+}\text{-Yb}^{3+}$ clusters) as a function of the Yb^{3+} concentration was also assessed in details. The $\text{Pr}^{3+}\text{-Yb}^{3+}$ clusters were found to be the dominant centers at Yb^{3+} concentrations of 4% and higher, and in particular, the $\text{Pr}^{3+}\text{-Yb}^{3+}$ “ultra-fast” clusters represent 84% of the overall number of luminescent centers at 10% Yb^{3+} . On the contrary, the non-luminescent Pr^{3+} clusters were found to dominate along with a minority of single Pr^{3+} ions in the samples presenting low Yb^{3+} concentrations. This analysis allowed us to conclude that only the $\text{CaF}_2\text{:Pr}^{3+}\text{-Yb}^{3+}$ samples presenting Yb^{3+} concentrations higher than 4% are really interesting for quantum cutting applications since it is within the $\text{Pr}^{3+}\text{-Yb}^{3+}$ clusters that the most efficient energy transfers take place in CaF_2 .

Interestingly, the different investigations into the $\text{Pr}^{3+}\text{-Yb}^{3+}$ cluster structures revealed a very strong spectroscopical equivalence between the $\text{Pr}^{3+}\text{-Yb}^{3+}$ and the $\text{Pr}^{3+}\text{-Lu}^{3+}$ codoping in CaF_2 . The $\text{Pr}^{3+}\text{-Lu}^{3+}$ codoping is demonstrated to give rise to the same two types of rare-earth clusters than the $\text{Pr}^{3+}\text{-Yb}^{3+}$ codoping, and vice-versa, which is primarily explained by the strong similarities (notably in size and mass), exhibited by Yb^{3+} and Lu^{3+} ions. The codoping of Pr^{3+} ions with Lu^{3+} ions leads to a replacement

of non-luminescent Pr^{3+} clusters by $\text{Pr}^{3+}\text{-Lu}^{3+}$ clusters. Since no energy transfer between Pr^{3+} and Lu^{3+} ions is possible, a drastic increase of the Pr^{3+} luminescence is thus observed in $\text{Pr}^{3+}\text{-Lu}^{3+}$ codoped CaF_2 in comparison to singly doped $\text{CaF}_2\text{:Pr}^{3+}$. In particular, the Pr^{3+} luminescence is 400 times brighter in $0.5\%\text{Pr}^{3+}\text{-}5\%\text{Lu}^{3+}$ codoped CaF_2 than in $0.5\%\text{Pr}^{3+}$ singly doped CaF_2 . Indeed, the Pr^{3+} luminescence is strongly quenched in singly Pr^{3+} doped CaF_2 due to the efficient cross-relaxation energy transfer processes endured by the Pr^{3+} ions in the Pr^{3+} clusters, which prevents any possibility of laser operation with singly Pr^{3+} doped CaF_2 . Therefore, the possibility of visible laser operation with $\text{CaF}_2\text{:Pr}^{3+}\text{-Lu}^{3+}$ is now opened and is currently undertaken. This laser operation is particularly interesting since the Pr^{3+} emission spectrum in $\text{CaF}_2\text{:Pr}^{3+}\text{-Lu}^{3+}$ reveals the existence of an important transition at approximately 606 nm, which is especially desirable for quantum information processing applications.

The investigation of the second step of the quantum cutting process as well as the assignment of an accurate value of quantum efficiency for the whole mechanism is particularly complicated both in $\text{Pr}^{3+}\text{-Yb}^{3+}$ codoped KY_3F_{10} and CaF_2 . This difficulty appears very clearly in the case of $\text{KY}_3\text{F}_{10}\text{:Pr}^{3+}\text{-Yb}^{3+}$ when modeling the system through different approaches. A classical rate-equation modeling was carried out from which, energy transfer rates values were finally derived for the different energy transfer mechanisms involved in the system. More sophisticated approaches were also developed by combining the rate-equations with Monte-Carlo computational methods. One of the main results of this modeling is the existence of a thermal equilibrium between the $^1\text{G}_4$ and the $^2\text{F}_{5/2}$ levels because of the energy transfers going back and forth in between the two levels. The modeling also confirms the presence of efficient quenching mechanisms which affect the Yb^{3+} luminescence. As a result, the downconversion mechanism for the emission of two photons from Yb^{3+} ions per photon absorbed by Pr^{3+} ions is very inefficient in spite of the relatively efficient first and second energy transfers $\text{Pr}^{3+} \rightarrow \text{Yb}^{3+}$. Instead, the quantum cutting mechanism appears to lead to emissions at lower energies ($1.3\ \mu\text{m}$ and $2\ \mu\text{m}$) from the $^1\text{G}_4$ and $^3\text{H}_6$ levels. The same type of conclusion can be drawn in the case of $\text{CaF}_2\text{:Pr}^{3+}\text{-Yb}^{3+}$ despite the complex multisite structure following the rare-earth clustering process. Indeed, a strong quenching of the Yb^{3+} lifetime is observed showing that the Yb^{3+} emission cannot meet the requirements for a practical solar application.

The quantum cutting mechanism was finally investigated in $\text{Tb}^{3+}\text{-Yb}^{3+}$ codoped CaF_2 . The excitation of two Yb^{3+} ions takes place in this system through a single cooperative energy transfer from Tb^{3+} . The cooperative mechanism is known to be several

orders of magnitude less efficient than any first order system presenting resonant energy transfer paths. Nevertheless, the spectroscopic investigations carried out in $\text{Tb}^{3+}\text{-Yb}^{3+}$ doped CaF_2 show the formation of $\text{Tb}^{3+}\text{-Yb}^{3+}$ clusters within which the cooperative energy transfer is particularly efficient. In addition, the analysis of the evolution of the Yb^{3+} emission with the increasing Yb^{3+} content reveals a promising low impact of the Yb^{3+} quenching processes in this material. Absolute quantum cutting efficiency measurements reveal a 40 times higher efficiency in $\text{CaF}_2\text{:Tb}^{3+}\text{-Yb}^{3+}$ in comparison to $\text{Pr}^{3+}\text{-Yb}^{3+}$. These promising results open the door to the next challenge in the pursuit of efficient quantum cutters for practical applications. This next challenge is without a doubt the rare-earth sensitization, and in this particular case, the Tb^{3+} sensitization. The most promising Tb^{3+} sensitizers were reviewed and finally, an efficient sensitization of Tb^{3+} ions is demonstrated by using trivalent cerium as sensitizer.



Bibliography

- [1] “Key World Statistics”, International Energy Agency (2010)
- [2] “IPCC Fourth Assessment Report: Climate Change” (2007)
- [3] G. Hering, “Year of the tiger”, *Photon International* 3 (2011)
- [4] “Solar Energy Perspectives: Executive Summary”, International Energy Agency (2011).
- [5] R. Ohl, *Bell #1*, U.S. Patent 2402662.
- [6] M. A. Green, “Third Generation Photovoltaics: Ultra-high conversion efficiency at low cost”, *Prog. Photovoltaics* 9 (2) (2001), 123
- [7] M. D. Chapin, C. S. Fuller et M. A. Green, “A New Silicon p-n Junction Photocell for Converting Solar Radiation into Electrical Power”, *J. Appl. Phys.* 25 (1954) 676
- [8] J. Zhao, A. Wang, et M. A. Green, “24.5% Efficiency silicon PERT cells on MCZ substrates and 24.7% efficiency PERL cells on FZ substrates”, *Prog. Photovoltaics* 7 (6) (1999), 471
- [9] D. Niinobe, K. Nishimura, S. Matsuno, Fujioka H, T. Katsura, T. Okamoto, T. Ishihara, H. Morikawa, et S. Arimoto, “Honeycomb structured multi-crystalline silicon solar cells with 18.6% efficiency via industrially applicable laser-process”, *23rd*

- European Photovoltaic Solar Energy Conference and Exhibition*, Session Reference: 2CV.5.74 (2008)
- [10] K. Knapp et T. Jester, “Empirical investigation of the energy payback time for photovoltaic modules”, *Solar Energy* 71 (3) (2001), 165
- [11] M. A. Green, K. Emery, Y. Hishikawa, W. Warta, et E. D. Dunlop, “Solar cell efficiency tables (Version 38)”, *Prog. Photovoltaics* 19 (5) (2011), 565
- [12] D. E. Carlson et C. R. Wronski, “Amorphous silicon solar cell”, *Appl. Phys. Lett.* 28 (11) (1976), 671
- [13] D. L. Staebler et C. R. Wronski, “Reversible conductivity changes in discharge-produced amorphous Si”, *Appl. Phys. Lett.* 31 (4) (1977), 292
- [14] S. Benagli, D. Borrello, E. Vallat-Sauvain, J. Meier, U. Kroll, J. Hötzel, J. Spitznagel, J. Steinhäuser, L. Castens, et Y. Djeridane, “High-efficiency amorphous silicon devices on LPCVD-ZnO TCO prepared in industrial KAI-M R&D reactor”, *24th European Photovoltaic Solar Energy Conference*, Hamburg (2009)
- [15] J. Meier, F. L. Fliückiger, H. Keppner, et A. Shah, “Complete microcrystalline p-i-n solar cell-Crystalline or amorphous cell behavior”, *Appl. Phys. Lett.* 65 (7) (1994), 860
- [16] J. Löffler, A. Gordijn, R. L. Stolk, H. Li, J. K. Rath, et R. E. I. Schropp, “Amorphous and *micromorph* silicon tandem cells with high open-circuit voltage”, *Sol. Energy Mater. & Sol. Cells* 87 (1-4) (2005), 251
- [17] B. Yan , G. Yue, et S. Guha, “Status of nc-Si:H solar cells at united solar and roadmap for manufacturing a-Si:H and nc-Si:H based solar panels. In Amorphous and Polycrystalline Thin-Film Silicon Science and Technology”, *Materials Research Society Symposium Proceedings* 989 (2007), 0989-A15-01
- [18] M. Taguchi, K. Kawamoto, S. Tsuge, T. Baba, H. Sakata, M. Morizane, K. Uchihashi, N. Nakamura, S. Kiyama, et O. Oota, “HIT (TM) cells - High-efficiency crystalline Si cells with novel structure”, *Prog. Photovoltaics* 8 (5) (2000), 503
- [19] M. Tanaka, M. Taguchi, T. Matsuyama, T. Sawada, S. Tsuda, S. Nakano, H. Hanafusa, et Y. Kuwano, “Development of new a-Si c-Si heterojunction solar cells ACJ-

- HIT (artificially constructed junction-heterojunction with intrinsic thin layer)", *Jpn. J. Appl. Phys. Part I* 31 (11) (1992), 3518
- [20] Y. Tsunomura, Y. Yoshimine, M. Taguchi, T. Baba, T. Kinoshita, H. Kanno, H. Sakata, E. Maruyama, et M. Tanaka, "Twenty-two percent efficiency HIT solar cell", *Sol. Energy Mater. & Sol. Cells* 93 (6-7) (2009), 670
- [21] M. Taguchi, A. Terakawa, E. Maruyama, et M. Tanaka, "Obtaining a higher V_{oc} in HIT cells", *Prog. Photovoltaics* 13 (6) (2005), 481
- [22] S. Guha, "Can your roof provide your electrical needs? The growth prospect of building-integrated photovoltaic", *Conference Record of the Thirty-First IEEE Photovoltaic Specialists Conference* (2005), 12
- [23] A. Favier, D. Muñoz, S. Martín de Nicolás, et P.-J. Ribeyron, "Boron-doped zinc oxide layers grown by metal-organic CVD for silicon heterojunction solar cells applications", *Sol. Energy Mater. & Sol. Cells* 95 (4) (2011), 1057
- [24] R. Bube, "Temperature dependence of the width of the band gap in several photoconductors", *Phys. Rev.* 98 (2) (1955), 431
- [25] D. Cunningham, K. Davies, L. Grammond, E. Mopas, N. O'Connor, M. Rubcich, M. Sadeghi, D. Skinner, et T. Trumbly, "Large area Apollo (R) module performance and reliability", *Conference Record of the twenty-eight IEEE Photovoltaic Specialists Conference* (2000), 13
- [26] S. Wagner, J. L. Shay, P. Migliorato, et H. M. Kasper, "CuInSe₂/CdS heterojunction photovoltaic detectors", *Appl. Phys. Lett.* 25 (8) (1974), 434.
- [27] P. Jackson, D. Hariskos, E. Lotter, S. Paetel, R. Wuerz, R. Menner, W. Wischmann, et M. Powalla, "New world record efficiency for Cu(In,Ga)Se₂ thin-film solar cells beyond 20%", *Prog. Photovoltaics* 19 (7) (2011), 894
- [28] M. Kaelin, D. Rudmann, et A. N. Tiwari, "Low cost processing of CIGS thin film solar cells", *Solar Energy* 77 (2004), 749
- [29] H. Spanggaard et F. C. Krebs, "A brief history of the development of organic and polymeric photovoltaics", *Sol. Energy Mater. & Sol. Cells* 83 (2004), 125
- [30] M. Grätzel, "Photoelectrochemical cells", *Nature* 414 (6861) (2001), 338

- [31] Y. Chiba, A. Islam, Y. Watanabe, R. Komiya, N. Koide, et L. Han, "Dye-sensitized solar cells with conversion efficiency of 11.1%", *Jpn. J. Appl. Phys. Part 2 - Express Letter* 45 (24-28) (2006), L638
- [32] L. L. Kazmerski, "Solar photovoltaics R&D at the tipping point: A 2005 technology overview", *Journal of Electron Spectroscopy and Related Phenomena* 150 (2006), 105
- [33] M. A. Green, "Third generation photovoltaics: advanced solar energy conversion: Advanced Solar Energy Conversion". Springer-Verlag (2006)
- [34] W. Shockley et H. J. Queisser, "Detailed Balance Limit of Efficiency of p-n Junction Solar Cells", *J. Appl. Phys.* 32 (3) (1961), 510
- [35] J. Zahler, A. Morral, C. Ahn, H. Atwater, M. Wanlass, C. Chu, et P. Iles, "Wafer bonding and layer transfer processes for 4-junction. high efficiency solar cells", New York: IEEE (2002)
- [36] H. Yoon, J. E. Granata, P. Hebert, R. R. King, C. M. Fetzer, P. C. Colter, K. M. Edmondson, D. Law, G. S. Kinsey, D. D. Krut, J. H. Ermer, M. S. Gillanders, et N. H. Karam, "Recent advances in high-efficiency III-V multi-junction solar cells for space applications: ultra triple junction qualification", *Prog. Photovoltaics* 13 (2) (2005), 133
- [37] Y. Xia, P. Yang, Y. Sun, Y. Wu, B. Mayers, B. Gates, Y. Yin, F. Kim, et Y. Yan, "One-dimensional nanostructures: Synthesis, characterization, and applications", *Adv. Mater.* 15 (5) (2003), 353
- [38] C. Burda, X. Chen, R. Narayanan, et M. El-Sayed, "Chemistry and properties of nanocrystals of different shapes", *Chem. Rev.* 105 (4) (2005), 1025
- [39] M. Paxman, J. Nelson, B. Braun, J. Connolly, K. W. J. Barnham, C. T. Foxon, et J. S. Roberts, "Modeling the spectral response of the quantum well solar cell", *J. Appl. Phys.* 74 (1) (1993), 614
- [40] M. Mazzer, K. W. J. Barnham, I. M. Ballard, A. Bessiere, A. Ioannides, D. C. Johnson, M. C. Lynch, T. N. D. Tibbits, J. S. Roberts, G. Hill, et C. Calder, "Progress in quantum well solar cells", *Thin Solid Films* 511-512 (2006), 76
- [41] C. Strümpel, M. McCann, G. Beaucarne, V. Arkhipov, A. Slaoui, V. Svrcek, C. del Canizo, et I. Tobias, "Modifying the solar spectrum to enhance silicon solar cell

- efficiency. An overview of available materials”, *Sol. Energy Mater. & Sol. Cells* 91 (2007), 238
- [42] J. de Wild, A. Meijerink, J. K. Rath, W. G. J. H. M. van Sark, et R. E. I. Schropp, “Upconverter solar cells: materials and applications”, *Energy Environ. Sci.* 4 (12) (2011), 4835
- [43] T. Trupke et M. A. Green, “Improving solar cell efficiencies by down-conversion of high-energy photons”, *J. Appl. Phys.* 92 (3) (2002), 1668
- [44] T. Trupke et M. A. Green, “Improving solar cell efficiencies by up-conversion of sub-band-gap light”, *J. Appl. Phys.* 92 (7) (2002), 4117
- [45] T. Trupke, A. Shalav, B. S. Richards, P. Würfel, et M. A. Green, “Efficiency enhancement of solar cells by luminescent up-conversion of sunlight”, *Sol. Energy Mater. & Sol. Cells* 90 (2006), 3327
- [46] G. Seybold et G. Wagenblast, “New perylene and violanthrone dyestuffs for fluorescent collectors”, *Dyes and Pigments* 11 (4) (1989), 303
- [47] A. A. Earp, G. B. Smith, J. Franklin, et P. Swift, “Optimisation of a three-colour luminescent solar concentrator daylighting system”, *Sol. Energy Mater. & Sol. Cells* 84 (1-4) (2004), 411
- [48] B. A. Swartz, T. Cole, et A. H. Zewail, “Photon trapping and energy transfer in multiple-dye plastic matrices: an efficient solar-energy concentrator”, *Opt. Lett.* 1 (2) (1977), 73
- [49] A. M. Hermann, “Luminescent solar concentrators-A review”, *Sol. Energy* 29 (4) (1982), 323
- [50] A. Zastrow, “On the conversion of solar radiation with fluorescent planar concentrators (FPCs)”, *Proc. 3rd Int. Photovoltaic Solar Energy Conf.* Cannes, France (1980), 413
- [51] R. E. Sah, G. Baur, et H. Kelker, “Influence of the solvent matrix on the overlapping of the absorption and emission bands of solute fluorescent dyes”, *Appl. Phys.* 23 (4) (1980), 369

- [52] W. van Sark, A. Meijerink, R. Schropp, J. van Roosmalen, et E. Lysen, "Modeling improvement of spectral response of solar cells by deployment of spectral converters containing semiconductor nanocrystals RID C-5009-2009 RID C-4897-2009 RID C-6410-2009", *Semiconductors* 38 (8) (2004), 962
- [53] V. Svrcek, A. Slaoui, et J. Muller, "Silicon nanocrystals as light converter for solar cells", *Thin Solid Films* 451 (2004), 384
- [54] D. J. Norris et M. G. Bawendi, "Structure in the lowest absorption feature of CdSe quantum dots", *J. Chem. Phys.* 103 (13) (1995), 5260
- [55] A. Shabaev, A. L. Efros, et A. J. Nozik, "Multiexciton Generation by a Single Photon in Nanocrystals", *Nano Lett.* 6 (12) (2006), 2856
- [56] R. D. Schaller et V. I. Klimov, "High Efficiency Carrier Multiplication in PbSe Nanocrystals: Implications for Solar Energy Conversion", *Phys. Rev. Lett.* 92 (18) (2004) 186601
- [57] D. H. Dieke et H. M. Crosswhite, "The spectra of the Doubly and Triply Rare Earths", *Appl. Opt.* 2 (7) (1963), 675
- [58] B. C. Rowan, L. R. Wilson, et B. S. Richards, "Advanced Material Concepts for Luminescent Solar Concentrators", *IEEE Journal of Selected topics in quantum electronics* 14 (5) (2008), 1312
- [59] S. Wojtczuk, P. Chiu, X. Zhang, D. Derkacs, C. Harris, D. Pulver, et M. Timmons, "InGaP/GaAs/InGaAs concentrators using Bi-facial epigrowth", *35th IEEE PVSC*, Honolulu (2010)
- [60] C. Cohen-Tannoudji, B. Diu, et F. Laloë, "Quantum mechanics" Wiley (1977)
- [61] B. Henderson et G. F. Imbusch, "Optical Spectroscopy of Inorganic Solids". Oxford University Press (2006)
- [62] D. L. Dexter, "A Theory of sensitized Luminescence in Solids", *J. Chem. Phys.* 21 (5) (1953), 833
- [63] M. Inokuti et F. Hirayama, "Influence of Energy Transfer by the Exchange Mechanism on Donor Luminescence", *J. Chem. Phys.* 43 (6) (1965), 1978

- [64] W. P. Wolf et R. J. Birgeneau, "Electric Multipole Interactions between Rare-Earth Ions", *Phys. Rev.* 166 (2) (1968), 376
- [65] P. W. Anderson, "New Approach to the Theory of Superexchange Interactions", *Phys. Rev.*, 115 (1) (1959), 2
- [66] W. B. Smith et R. C. Powell, "Energy transfer in $\text{CaWO}_4\text{: Sm}^{3+}$ ", *J. Chem. Phys.* 76 (2) (1982), 854
- [67] V. S. Mironov, "Superexchange Mechanism of Energy Transfer between Neighboring Lanthanide Ions in Dielectric Crystals", *Optics and Spectroscopy* 88 (3) (2000), 372
- [68] R. B. Barthem, R. Buisson, et J. C. Vial, "Coexistence of two excitation transfer mechanisms in $\text{LiYF}_4\text{:Pr}$ ", *J. Lum.* 38 (1987), 190
- [69] R. T. Wegh, H. Donker, et A. Meijerink, "Vacuum-ultraviolet spectroscopy and quantum cutting for Gd^{3+} in LiYF_4 ", *Phys. Rev. B* 56 (21) (1997), 13841
- [70] L. Beuzamy et B. Moine, "Quantum cutting effect in $\text{KY}_3\text{F}_{10}\text{:Tm}^{3+}$ ", *Phys. Rev. B* 78 (2008), 184302
- [71] A. Lezama, M. Oria, et C. B. de Araujo, "Site-selective spectroscopy via energy up-conversion in $\text{CaF}_2\text{: Pr}^{3+}$ ", *Phys. Rev. B* 33 (7) (1986), 4493
- [72] F. Auzel, "Upconversion and Anti-Stokes Processes with f and d Ions in Solids", *Chem. Rev.* 104 (2004), 139
- [73] J. P. R. Wells, G. D. Jones, et R. J. Reeves, "Energy transfer and laser spectroscopy of Eu^{3+} co-doped $\text{CaF}_2\text{: Sm}^{3+}$ ", *J. Lum.* 72-74 (1997), 977
- [74] F. Auzel et Pecile D., "Comparison and efficiency of materials fir summation of photons assisted by energy transfer", *J. Lum.* 8 (1973), 32
- [75] X. Wu, J. P. Denis, G. Özen, et F. Pellé, "Infrared-to-visible conversion luminescence of Tm^{3+} and Yb^{3+} ions in glass ceramics", *J.Lum* 60-61 (2004), 212
- [76] F. Auzel, "Compteur quantique par transfert d'énergie entre deux ions de terres rares dans un tungstate dnas un verre", *C. R. Acad. Sci. Paris*, 262 (1966), 1016
- [77] F. Auzel, D. Meichenin, F. Pellé, et P. Goldner, "Cooperative luminescence as a defining process for RE-ions clustering in glasses and crystals", *Opt. Mat.* 4 (1994), 35

- [78] F. Auzel, “Upconversion processes in coupled ion systems”, *J. Lum.* 45 (1990), 341
- [79] E. Osiac, S. Kuck, E. Heumann, G. Huber, E. Sani, A. Toncelli, et M. Tonelli, “Spectroscopic characterisation of the upconversion avalanche mechanism in $\text{Pr}^{3+}, \text{Yb}^{3+}:\text{BaY}_2\text{F}_8$ ”, *Opt. Mat.* 24 (2003), 537
- [80] V. Lupei, E. Osiac, T. Sandrock, E. Heumann, et G. Huber, “Excited state dynamics in sensitized photon avalanche processes”, *J. Lum.* 76 & 77 (1998), 441
- [81] S. Kuck, A. Dening, E. Heumann, E. Mix, T. Sandrock, K. Sebal, et G. Huber, “Avalanche up-conversion processes in Pr, Yb-doped materials”, *J. Alloys and Comp.* 300-301 (2000), 65
- [82] S. Kuck, I. Sokolska, M. Henke, M. Doring, et T. Scheffler, “Photon cascade emission in Pr^{3+} -doped fluorides”, *J. Lum.* 102-103 (2003), 176
- [83] P. Goldner, O. Guillot-Noël, G. Dantelle, M. Mortier, T. H. My, et F. Bretenaker, “Orange avalanche upconversion for high-resolution laser spectroscopy”, *EPJ Applied Physics* (2006), 1
- [84] P. Goldner et F. Pellé, “Photon avalanche fluorescence and lasers”, *Opt. Mat.* 5 (1996), 239
- [85] K. J. Kim, A. Jouini, A. Yoshikawa, R. Simura, G. Boulon, et T. Fukuda, “Growth and optical properties of Pr,Yb-codoped KY_3F_{10} fluoride single crystals for up-conversion visible luminescence”, *Journal of Crystal Growth* 299 (2007), 171
- [86] O. Hellmig, S. Salewski, A. Stark, J. Schwenke, P. E. Toschek, K. Sengstock, et V. M. Baev, “Multicolor diode-pumped upconversion fiber laser”, *Opt. Lett.* 35 (13) (2010), 2263
- [87] R. Balda, J. Fernández, A. Mendioroz, M. Voda, et M. Al-Saleh, “Infrared-to-visible upconversion processes in $\text{Pr}^{3+}/\text{Yb}^{3+}$ -codoped KPb_2Cl_5 ”, *Phys. Rev.* 68 (2003), 165101
- [88] H. Zellmer, P. Riedel, et A. Tünnermann, “Visible upconversion lasers in praseodymium-ytterbium-doped fibers”, *Appl. Phys. B* 69 (1999), 417
- [89] S. R. Lüthi, M. Pollnau, H. U. Güdel, et M. P. Hehlen, “Near-infrared to visible upconversion in Er^{3+} -doped $\text{Cs}_3\text{Lu}_2\text{Cl}_9$, $\text{Cs}_3\text{Lu}_2\text{Br}_9$, and $\text{Cs}_3\text{Y}_2\text{I}_9$ excited at $1.54\ \mu\text{m}$ ”, *Phys. Rev. B* 60 (1) (1999), 162

- [90] F. Pellé et P. Goldner, "Pair processes in $\text{CsCdBr}_3\text{:Er}^{3+}$, a study by up-conversion and excited-state absorption of efficient uv and blue anti-Stokes emission", *Phys. Rev. B* 48 (14) (1993), 9995
- [91] R. H. Page, K. I. Schaffers, P. A. Waide, J. B. Tassano, S. A. Payne, W. F. Krupke, et W. K. Bischel, "Upconversion-pumped luminescence efficiency of rare-earth-doped hosts sensitized with trivalent ytterbium", *J. Opt. Soc. Am. B* 15 (3) (1998), 996
- [92] A. Rapaport, J. Milliez, F. Szipocs, M. Bass, A. Cassanho, et H. Jenssen, "Properties of a new, efficient, blue-emitting material for applications in upconversion displays: $\text{Yb, Tm:KY}_3\text{F}_{10}$ ", *Appl. Opt.* 43 (35) (2004), 6477
- [93] J. P. van der Ziel, L. G. Van Uitert, W. H. Grodkiewicz, et R. M. Mikulyak, " $1.5\ \mu\text{m}$ infrared excitation of visible luminescent in $\text{Y}_{1-x}\text{Er}_x\text{F}_3$ and $\text{Y}_{1-x-y}\text{Er}_x\text{Tm}_y\text{F}_3$ via resonant energy transfer", *J. Appl. Phys.* 60 (12) (1986), 4262
- [94] S. A. Pollack et D. B. Chang, "Ion-pair upconversion pumped laser emission in Er^{3+} ions in YAG, YLF, SrF_2 , and CaF_2 crystals", *J. Appl. Phys.* 64 (6) (1988), 2885
- [95] P. Xie et S. C. Rand, "Continuous wave, fourfold upconversion laser", *Appl. Phys. Lett.* 63 (23) (1993), 3125
- [96] S. Ivanova, F. Pellé, A. Tkachuk, M. F. Joubert, Y. Guyot, et V. P. Gapontzev, "Upconversion luminescence dynamics of Er-doped fluoride crystals for optical converters", *J. Lum.* 128 (5-6) (2008), 914
- [97] S. Ivanova et F. Pellé, "Strong $1.53\ \mu\text{m}$ to NIR-VIS-UV upconversion in Er-doped fluoride glass for high-efficiency solar cells", *J. Opt. Soc. Am. B* 26 (10) (2009), 1930
- [98] A. Shalav, B. S. Richards, et T. Trupke, "Application of $\text{NaYF}_4\text{:Er}^{3+}$ up-converting phosphors for enhanced near-infrared silicon solar cell response", *Appl. Phys. Lett.* 86 (2005), 013505
- [99] B. C. Hong et K. Kawano, "PL and PLE studies of $\text{KMgF}_3\text{:Sm}$ crystal and the effect of its wavelength conversion on CdS/CdTe solar cell", *Sol. Energy Mater. & Sol. Cells* 80 (2003), 417
- [100] K. Kawano, B. C. Hong, K. Sakamoto, T. Tsuboi, et H. J. Seo, "Improvement of the conversion efficiency of solar cell by rare earth ion", *Opt. Mat.* 31 (2009), 1353

-
- [101] D. L. Dexter, "Possibility of quantum yields greater than unity", *Phys. Rev.* 108 (3) (1957), 630
- [102] C. R. Ronda, "Phosphors for lamps and displays: an applicational view", *Journal of Alloys and Compounds* 225 (1995), 534
- [103] K. D. Oskam, R. T. Wegh, H. Donker, E. V. D. van Loef, et A. Meijerink, "Downconversion: a new route to visible quantum cutting", *Journal of Alloys and Compounds* 300-301 (2000), 421
- [104] R. T. Wegh, H. Donker, E. V. D. van Loef, K. D. Oskam, et A. Meijerink, "Quantum cutting through downconversion in rare-earth compounds", *J. Lum.* 87-89 (2000), 1017
- [105] J. L. Sommerdijk, A. Bril, et A. W. de Jager, "Luminescence of Pr^{3+} -Activated fluoride", *J. Lum.* 9 (1974), 288
- [106] J. L. Sommerdijk, A. Bril, et A. W. Jager, "Two photon luminescence with ultraviolet excitation of trivalent praseodymium", *J. Lum.* 8 (1974), 341
- [107] B. M. van der Ende, L. Aarts, et A. Meijerink, "Near-Infrared Quantum Cutting for Photovoltaics", *Adv. Mat.* (2009), 3073
- [108] K. Deng, X. Wei, X. Wang, Y. Chen, et M. Yin, "Near-infrared quantum cutting via resonant energy transfer from Pr^{3+} to Yb^{3+} in LaF_3 ", *App. Phys. B* 102 (2011), 555
- [109] L. Aarts, B. van der Ende, M. F. Reid, et A. Meijerink, "Downconversion for Solar Cells in $\text{YF}_3\text{:Pr}^{3+}$, Yb^{3+} ", *Spectroscopy Letters* 43 (5) (2010), 373
- [110] J. T. van Wijngaarden, S. Scheidelaar, T. J. H. Vlugt, M. F. Reid, et A. Meijerink, "Energy transfer mechanism for downconversion in the (Pr^{3+} , Yb^{3+}) couple", *Phys. Rev. B* 81 (2010), 155112
- [111] Q. Y. Zhang et G. F. Yang, "Cooperative downconversion in $\text{GdAl}_3(\text{BO}_3)_4\text{:RE}^{3+}, \text{Yb}^{3+}$, RE=Pr, Tb, and Tm", *Appl. Phys. Lett.* 91 (2007), 051903
- [112] A. Jaffrès, B. Viana, et E. van der Kolk, "Photon management in $\text{La}_2\text{BaZnO}_5\text{:Tm}^{3+}, \text{Yb}^{3+}$ and $\text{La}_2\text{BaZnO}_5\text{:Pr}^{3+}, \text{Yb}^{3+}$ by two step cross-relaxation and energy transfer", *Chem. Phys. Lett.*, 527 (2012), 42

- [113] X. Liu, Y. Qiao, G. Dong, S. Ye, B. Zhu, G. Lakshminarayana, D. Chen, et J. Qiu, “Cooperative downconversion in Yb^{3+} - RE^{3+} ($\text{RE}=\text{Tm}$ or Pr) codoped lanthanum borogermanate glasses”, *Opt. Lett.* 33 (23) (2008), 2858
- [114] L. Aarts, B. M. van der Ende, et A. Meijerink, “Downconversion for solar cells in $\text{NaYF}_4:\text{Er},\text{Yb}$ ”, *J. Appl. Phys.* 106 (2009), 023522
- [115] J. J. Eilers, D. Biner, J. T. van Wijngaarden, K. Krämer, H. U. Güdel, et A. Meijerink, “Efficient visible to infrared quantum cutting through downconversion with the Er^{3+} - Yb^{3+} couple in $\text{Cs}_3\text{Y}_2\text{Br}_9$ ”, *Appl. Phys. Lett.* 96 (2010), 151106
- [116] J. M. Meijer, L. Aarts, B. M. van der Ende, T. J. H. Vlugt, et A. Meijerink, “Downconversion for solar cells in $\text{YF}_3:\text{Nd}^{3+}, \text{Yb}^{3+}$ ”, *Phys. Rev. B* 81 (2010), 035107
- [117] P. Vergeer, T. J. H. Vlugt, M. H. F. Kox, M. I. den Hertog, J. P. J. M. van der E., A. Meijerink, M. I. den Hertog, J.P.J.M. van der Eerden, et A. Meijerink, “Quantum cutting by cooperative energy transfer in $\text{Yb}_x\text{Y}_{1-x}\text{PO}_4:\text{Tb}^{3+}$ ”, *Phys. Rev. B* 71 (2005), 014119
- [118] Q. Y. Zhang, C. H. Yang, et Z. H. Jiang, “Concentration-dependent near-infrared quantum cutting in $\text{GdBO}_3:\text{Tb}^{3+}, \text{Yb}^{3+}$ nanophosphors”, *Appl. Phys. Lett.* 90 (2007), 061914
- [119] Q. Y. Zhang et C. H. Yang, “Cooperative quantum cutting in one-dimensional $\text{Yb}_x\text{Gd}_{1-x}\text{Al}_3(\text{BO}_3)_4:\text{Tb}^{3+}$ nanorods”, *Appl. Phys. Lett.* 90 (2007), 021107
- [120] X. Y. Huang, D. C. Yu, et Q. Y. Zhang, “Enhanced near-infrared quantum cutting in $\text{GdBO}_3:\text{Tb}^{3+}, \text{Yb}^{3+}$ phosphors by Ce^{3+} codoping”, *J. Appl. Phys.* 106 (2009), 113521
- [121] S. Ye, B. Zhu, J. Chen, J. Luo, et J. R. Qiu, “Infrared quantum cutting in $\text{Tb}^{3+}, \text{Yb}^{3+}$ codoped transparent glass ceramics containing CaF_2 nanocrystals”, *Appl. Phys. Lett.* 92 (2008), 141112
- [122] J. L. Yuan, X. Y. Zeng, J. T. Zhao, Z. J. Zhang, H. H. Chen, et X. X. Yang, “Energy transfer mechanisms in $\text{Tb}^{3+}, \text{Yb}^{3+}$ codoped Y_2O_3 downconversion phosphor”, *J. Phys. D: Appl. Phys.* 41 (2008), 105406
- [123] X. Liu, Y. Teng, Y. Zhuang, J. Xie, Y. Qiao, G. Dong, D. Chen, et J. Qiu, “Broad-band conversion of visible light to near-infrared emission by $\text{Ce}^{3+}, \text{Yb}^{3+}$ -codoped yttrium aluminum garnet”, *Opt. Lett.* 34 (22) (2009), 3565

- [124] D. Chen, Y. Wang, Y. Yu, P. Huang, et F. Weng, “Near-infrared quantum cutting in transparent nanostructured glass ceramics”, *Opt. Lett.* 33 (16) (2008), 1884
- [125] J. Chen, H. Guo, Z. Li, H. Zhang, et Y. Zhuang, “Near-infrared quantum cutting in Ce^{3+} , Yb^{3+} co-doped YBO_3 phosphors by cooperative energy transfer”, *Opt. Mat.* 32 (2010), 998
- [126] H. Zhang, C. Jindeng, et G. Hai, “Efficient near-infrared quantum cutting by Ce^{3+} - Yb^{3+} couple in GdBO_3 phosphors”, *Journal of rare earths* 29 (9) (2011), 822
- [127] H. Lin, S. Zhou, H. Teng, Y. Li, W. Li, X. Hou, et T. Jia, “Near infrared quantum cutting in heavy Yb doped $\text{Ce}_{0.03}\text{Yb}_{3x}\text{Y}_{(2.97-3x)}\text{Al}_5\text{O}_{12}$ transparent ceramics for crystalline silicon solar cells”, *J. Appl. Phys.* 107 (4) (2010), 043107
- [128] X. Y. Huang et Q. Y. Zhang, “Near-infrared quantum cutting via cooperative energy transfer in $\text{Gd}_2\text{O}_3:\text{Bi}^{3+}, \text{Yb}^{3+}$ phosphors”, *J. Appl. Phys.*, 107 (2010), 063505
- [129] X. Y. Huang, J. X. Wang, D. C. Yu, S. Ye, Q. Y. Zhang, et X. W. Sun, “Spectral conversion for solar cell efficiency enhancement using $\text{YVO}_4:\text{Bi}^{3+}, \text{Ln}^{3+}$ ($\text{Ln}=\text{Dy}, \text{Er}, \text{Ho}, \text{Eu}, \text{Sm}, \text{and Yb}$) phosphors”, *J. Appl. Phys.*, 109 (2011), 113526
- [130] W. Xian-Tao, Z. Jiang-Bo, C. Yong-Hu, Y. Min, et L. Yong, “Quantum cutting downconversion by cooperative energy transfer from Bi^{3+} to Yb^{3+} in Y_2O_3 phosphor”, *Chin. Phys. B* 19 (7) (2010), 077804
- [131] P. Dorenbos, “Systematic behavior in trivalent lanthanide charge transfer energies”, *J. Phys.: Condens. Matter* (2003), 8417
- [132] K. Friese, H. Krüger, V. Kahlenberg, T. Balic-Zunic, H. Emerich, J. Y. Gesland, et A. Grzechnik, “Study of the temperature dependence of the structure of KY_3F_{10} ”, *J. Phys.: Condens. Matter* 18 (9) (2006), 2677
- [133] E. Boulma, M. Diaf, J. P. Jouart, M. Bouffard, J. L. Doualan, et R. Moncorgé, “Anti-Stokes emissions and determination of Stark sub-level diagram of Er^{3+} ions in KY_3F_{10} ”, *J. Phys: Condens. Matter*, 18 (29), (2006), 6721
- [134] M.A. Dubinskii, N. M. Khaidukov, I. G. Garipov, L. N. DemYanets, A. K. Naumov, V. V. Semashko, et V. A. Malyusov, “Spectral-kinetic and Lasing Characteristics of New Nd^{3+} -activated Laser Hosts of the KF-YF_3 System”, *Journal of Modern Optics* 37 (8) (1990), 1355

- [135] M. Laroche, A. Braud, S. Girard, J. Doualan, R. Moncorge, M. Thuau, et L. Merkle, "Spectroscopic investigations of the $4f5d$ energy levels of Pr^{3+} in fluoride crystals by excited-state absorption and two-step excitation measurements", *J. Opt. Soc. Am. B-Opt. Phys.* 16 (12) (1999), 2269
- [136] J. P. R. Wells, M. Yamaga, T. P. J. Han, et H. G. Gallagher, "Infrared absorption, laser excitation and crystal-field analyses of the C_{4v} symmetry centre in KY_3F_{10} doped with Pr^{3+} ", *J. Phys.: Condens. Matter* 12 (2000), 5297
- [137] A. Yoshikawa, K. Kamada, M. Nikl, K. Aoki, H. Sato, J. Pejchal, et T. Fukuda, "Growth and luminescent properties of $\text{Pr}:\text{KY}_3\text{F}_{10}$ single crystal", *Journal of Crystal Growth* 285 (2005), 445
- [138] P. Camy, J. L. Doualan, R. Moncorgé, J. Bengoechea, et U. Weichmann, "Diode-pumped $\text{Pr}^{3+}:\text{KY}_3\text{F}_{10}$ red laser", *Opt. Lett.* 32 (11) (2007), 1462
- [139] S. Khiari, M. Velazquez, R. Moncorgé, J. L. Doualan, P. Camy, A. Ferrier, et M. Diaf, "Red-luminescence analysis of Pr^{3+} doped fluoride crystals", *Journal of Alloys and Compounds* 451 (2008), 128
- [140] A. Toncelli, L. Bonelli, R. Faoro, D. Parisi, et M. Tonelli, "Investigation of Pr-doped fluoride crystals as possible white-light emitters", *Opt. Mat.* 31 (2009), 1205
- [141] B. Xu, P. Camy, J. L. Doualan, Z. Cai, et R. Moncorgé, "Visible laser operation of Pr^{3+} -doped fluoride crystals pumped by a 469 nm blue laser", *Opt. Exp.* 19 (2) (2011), 1191
- [142] P. Porcher et P. Caro, "Crystal field parameters for Eu^{3+} in KY_3F_{10} ", *J. Chem. Phys.* 65 (1) (1976), 189
- [143] P. Porcher et P. Caro, "Crystal field parameters for Eu^{3+} in KY_3F_{10} . II. Intensity parameters", *J. Chem. Phys.* 68 (9) (1978), 4176
- [144] P. Porcher et P. Caro, "Crystal field parameters for Eu^{3+} in KY_3F_{10} . III. Radiative and nonradiative transition probabilities", *J. Chem. Phys.* 68 (9) (1978), 4183
- [145] K. Heyde, K. Binnemans, et C. Görller-Walrand, "Spectroscopic properties of $\text{KY}_3\text{F}_{10}:\text{Er}^{3+}$ ", *J. Chem. Soc., Faraday Trans.* 94 (12) (1998), 1671

- [146] A. Braud, P. Y. Tigreat, J. L. Doualan, et R. Moncorgé, “Spectroscopy and cw operation of a 1.85 μm Tm: KY₃F₁₀ laser”, *Appl. Phys. B: Laser and Optics* 72 (2001), 909
- [147] M. Mujaži et J. P. R. Wells, “Spectroscopy and crystal-field analysis of KY₃F₁₀:Ho³⁺”, *J. Phys.: Condens. Matter* 21 (2009), 255402
- [148] M. Ito, G. Boulon, A. Bensalah, Y. Guyot, C. Goutaudier, et H. Sato, “Spectroscopic properties, concentration quenching, and prediction of infrared laser emission of Yb³⁺-doped KY₃F₁₀ cubic crystal”, *J. Opt. Soc. Am. B* 24 (12) (2007), 3023
- [149] M. Ito, S. Hraiech, C. Goutaudier, K. Lebbou, et G. Boulon, “Growth of Yb³⁺-doped KY₃F₁₀ concentration gradient crystal fiber by laser-heated pedestal growth (LHPG) technique”, *Journal of Crystal Growth* 310 (1) (2008), 140
- [150] C. Andraud, A. Vedrine, F. Pellé, et B. Blanzat, “Energy-transfer processes between Eu³⁺ and Tb³⁺ in KY₃F₁₀”, *Journal of the Less-Common Metals* 93 (1) (1983), 239
- [151] A. Braud, S. Girard, J. L. Doualan, M. Thuau, et R. Moncorgé, “Energy-transfer processes in Yb:Tm-doped KY₃F₁₀, LiYF₄, and BaY₂F₈ single crystals for laser operation at 1.5 and 2.3 μm ”, *Phys. Rev. B* 61 (8) (2000), 5280
- [152] P. Y. Tigreat, J. L. Doualan, C. Budasca, et R. Moncorgé, “Energy transfer processes in (Yb³⁺, Dy³⁺) and (Tm³⁺, Dy³⁺) codoped LiYF₄ and KY₃F₁₀ single crystals”, *J. Lum.* 94-95 (0) (2001), 23
- [153] M. F. Joubert, G. Boulon, et F. Gaume, “Energy transfer between the Eu²⁺ sites in KY₃F₁₀ single crystals”, *Chem. Phys. Lett.* 80 (2) (1981), 367
- [154] H. Marconi da Silva M. D. Linhares, A. Felipe Henriques Librantz, L. Gomes, L. Coronato Courrol, S. L’cia Baldochi, et I. Marcia Ranieri, “Energy transfer rates and population inversion investigation of ¹G₄ and ¹D₂ excited states of Tm³⁺ in Yb:Tm:Nd:KY₃F₁₀ crystals”, *J. Appl. Phys.* 109 (8) (2011), 083533
- [155] M. Y. Sharonov, A. L. Bratus, B. K. Sevastyanov, Z. I. Zhmurova, A. A. Bystrova, E. A. Krivandina, L. N. Demianets, et B. P. Sobolev, “The amplification and excited state absorption of Nd-doped nonstoichiometric crystals with fluorite structure in the 1.3 μm region”, *Optics Communications* 111 (3-4) (1994), 245

- [156] M. Y. Sharonov, Z. I. Zhmurova, E. A. Krivandina, A. A. Bystrova, I. I. Buchinskaya, et B. . P. Sobolev, "Improved by Yb^{3+} sensitizer fluorite crystals, doped with Pr^{3+} , for 1.3 μm optical amplifiers", *Optics Communications* 124 (1996), 595
- [157] S. Tanabe, T. Kouda, et T. Hanada, "Energy transfer and 1.3 μm emission in $\text{Pr}\pm\text{Yb}$ codoped tellurite glasses", *Journal of Non-Crystalline Solids* 274 (2000), 55
- [158] P. V. dos Santos, M. V. D. Vermelho, E. A. Gouveia, M. T. de Araujo, A. S. Gouveia-Neto, F. C. Cassanjes, S. J. L. Ribeiro, et Y. Messaddeq, "Infrared-to-visible frequency upconversion in Pr/Yb and Er/Yb - codoped tellurite glasses", *Journal of Alloys and Compounds* 344 (2002), 304
- [159] R. A. Laudise, "The growth of single crystals". Prentice-Hall (1970)
- [160] M. Ito, G. Boulon, A. Bensalah, Y. Guyot, G. Goutaudier, and H. Sato, "Spectroscopic properties, concentration quenching, and prediction of infrared laser emission of Yb^{3+} -doped KY_3F_{10} ", *J. Opt. Soc. Am. B* 24 (12) (2007), 3023
- [161] M. Yokota et O. Tanimoto, "Effects of Diffusion on Energy Transfer by Resonance", *J. Phys. Soc. Jpn.* 22 (1967), 779
- [162] A. I. Burshtein, "The influence of the migration mechanism of approaching particles on the energy transfer between them", *J. Lum.* 21 (3) (1980), 317
- [163] I. R. Martín, V. D. Rodríguez, U. R. Rodríguez-Mendoza, et V. Lavín, "Energy transfer with migration. Generalization of the Yokota-Tanimoto model for any kind of multipole interaction", *J. Chem. Phys.* 111 (3) (1999), 1191
- [164] S. A. Payne, L. K. Smith, W. L. Kway, J. B. Tassano, et W. F. Krupke, "The mechanism of Tm to Ho energy transfer in LiYF_4 ", *J. Phys.: Condens. Matter* 4 (44) (1992), 8525
- [165] B. M. Walsh, N. P. Barnes, et B. D. Bartolo, "On the distribution of energy between the $\text{Tm } ^3\text{F}_4$ and $\text{Ho } ^5\text{I}_7$ manifolds in Tm -sensitized Ho luminescence", *J. Lum.* 75 (1997), 89
- [166] B. M. Walsh, N. P. Barnes, et B. D. Bartolo, "The temperature dependence of energy transfer between the $\text{Tm } ^3\text{F}_4$ and $\text{Ho } ^5\text{I}_7$ manifolds of Tm -sensitized Ho luminescence in YAG and YLF", *J. Lum.* 90 (2000), 39

- [167] T. Kushida, "Energy Transfer and Cooperative Optical Transitions in Rare-Earth Doped Inorganic Materials. III. Dominant Transfer Mechanism", *J. Phys. Soc. Jpn.* 34 (1973), 1334
- [168] D. Serrano, A. Braud, J.-L. Doualan, P. Camy, A. Benayad, V. Ménard, et R. Moncorgé, "Ytterbium sensitization in KY_3F_{10} : Pr^{3+} , Yb^{3+} for silicon solar cells efficiency enhancement", *Opt. Mat.* 33 (2011), 1028
- [169] E. van der Kolk, O. M. T. Kate, J. W. Wiegman, D. Biner, et K. W. Krämer, "Enhanced $^1\text{G}_4$ emission in NaLaF_4 : Pr^{3+} , Yb^{3+} and charge transfer in NaLaF_4 : Ce^{3+} , Yb^{3+} studied by fourier transform luminescence spectroscopy", *Opt. Mat.* 33 (2011), 1024
- [170] R. K. Watts et H. J. Richter, "Diffusion and Transfer of Optical Excitation in YF_3 : Yb, Ho", *Phys. Rev. B* 6 (4) (1972), 1584
- [171] J. Hegarty, D. L. Huber, et W. M. Yen, "Fluorescence quenching by cross-relaxation in LaF_3 : Pr^{3+} ", *Phys. Rev. B* 25 (9) (1982), 5638
- [172] P. Kabro, J. A. Capobianco, F. S. Ermeneux, R. Moncorgé, M. Bettinelli, et E. Cavalli, "Excited state dynamics and energy transfer processes in YVO_4 : Er^{3+} crystals", *J. Appl. Phys.* 82 (8) (1997), 3983
- [173] B. Savoini, J. Santiuste, et R. Gonzalez, "Optical characterization of Pr^{3+} -doped yttria-stabilized zirconia single crystals", *Phys. Rev. B* 56 (10) (1997), 5856
- [174] S. R. Rotman, "Nonradiative energy transfer in Nd:YAG - evidence for the correlated placement of ions", *Appl. Phys. Lett.* 54 (21) (1989), 2053
- [175] A. Eyal et S. R. Rotman, "The determination of acceptor distribution from the donor decay time response in co-doped crystals", *Chem. Phys. Lett.* 206 (1-4) (1993), 113
- [176] O. Barbosa-García et C. W. Struck, "Monte Carlo treatment of the nonradiative energy transfer process for nonrandom placements of dopants in solids", *J. Chem. Phys.* 100 (6) (1994), 4554
- [177] J. T. Vega-Durán, O. Barbosa-García, L. A. Díaz-Torres, M. A. Meneses-Nava, et D. S. Sumida, "Effects of energy back transfer on the luminescence of Yb and Er ions in YAG", *Appl. Phys. Lett.* 76 (15) (2000), 2032

- [178] S. K. Lyo, T. Holstein, et R. Orbach, "Spectral and spatial diffusion in a disordered system", *Phys. Rev. B* 18 (4) (1978), 1637
- [179] H. C. Chow et R. C. Powell, "Models for energy transfer in solids", *Phys. Rev. B* 21 (9) (1980), 3785
- [180] C. N. Fleming, K. A. Maxwell, J. M. DeSimone, T. J. Meyer, et J. M. Papanikolas, "Ultrafast Excited-State Energy Migration Dynamics in an Efficient Light-Harvesting Antenna Polymer Based on Ru(II) and Os(II) Polypyridyl Complexes", *J. Am. Chem. Soc.* 123 (42) (2001), 10336
- [181] L. B. A. Johansson, S. Engström, et M. Lindberg, "Electronic energy transfer in anisotropic systems. III. Monte Carlo simulations of energy migration in membranes", *J. Chem. Phys.* 96 (5) (1992), 3844
- [182] L. E. Bausa, G. Lifante, E. Daran, et P. L. Pernas, "CaF₂:Er³⁺ molecular beam epitaxial layers as optical waveguides", *Appl. Phys. Lett.* 68 (23) (1996), 3242
- [183] A. Peña, P. Camy, A. Benayad, J. L. Doualan, C. Maurel, M. Olivier, V. Nazabal, et R. Moncorgé, "Yb:CaF₂ grown by liquid phase epitaxy", *Optical Materials* 33 (11) (2011), 1616
- [184] P. Camy, J. L. Doualan, S. Renard, A. Braud, V. Ménard, et R. Moncorgé, "Tm³⁺:CaF₂ for 1.9 μ m laser operation", *Optics Communications* 236 (4-6) (2004), 395
- [185] M. Siebold, M. Hornung, S. Bock, J. Hein, M. C. Kaluza, J. Wemans, et R. Uecker, "Broad-band regenerative laser amplification in ytterbium-doped calcium fluoride (Yb:CaF₂)", *Appl. Phys. B* 89 (2007), 543
- [186] M. Siebold, M. Hornung, R. Boedefeld, S. Podleska, S. Klingebiel, C. Wandt, F. Krausz, S. Karsch, R. Uecker, A. Jochmann, J. Hein, et M. C. Kaluza, "Terawatt diode-pumped Yb:CaF₂ laser", *Opt. Lett.* 33 (23) (2008), 2770
- [187] S. A. Payne, J. A. Caird, L. L. Chase, L. K. Smith, N. D. Nielsen, et W. F. Krupke, "Spectroscopy and gain measurements of Nd³⁺ in SrF₂ and other fluorite-structure hosts", *J. Opt. Soc. Am. B* 8 (4) (1991), 726
- [188] B. Bleaney, P. M. Llewellyn, et D. A. Jones, "Paramagnetic Resonance of Uranium Ions", *Proceedings of the Royal Society B* 69 (1956), 858

-
- [189] M. Dvir et W. Low, "Paramagnetic Resonance Spectra of Impurities in Calcium Fluoride", *Proc. Roy. Soc.* 75 (1959), 136
- [190] J. Sierro, "ESR Detection of the Hydrolysis of Solid CaF_2 ", *J. Chem. Phys.* 34 (1961), 2183
- [191] S. D. McLaughlan, "Paramagnetic Resonance of Pr^{3+} and U^{4+} ions in CaF_2 ", *Phys. Rev.* 150 (1) (1966), 118
- [192] K. Sasaki et J. Maier, "Re-analysis of defect equilibria and transport parameters in YO-stabilized ZrO using EPR and optical relaxation", *Solid State Ionics* 134 (2000), 303.
- [193] G. K. Miner, T. P. Graham, et G. T. Johnson, "Effect of a CeH Codopant on the GdH EPR Spectrum of SrF_2 at Room Temperature", *J. Chem. Phys.* 57 (3) (1972), 1263
- [194] M. L. Falin, K. I. Gerasimov, V. A. Latypov, A. M. Leushin, H. Bill, et D. Lovy, "EPR and optical spectroscopy of Yb^{3+} ions in CaF_2 and SrF_2 ", *J. Lum.* 102-103 (2003), 239
- [195] S. A. Kazanskii, A. I. Ryskin, A. E. Nikiforov, A. Y. Zaharov, M. Y. Ougrumov, et G. S. Shakurov, "EPR spectra and crystal field of hexamer rare-earth clusters in fluorites", *Phys. Rev. B* 72 (2005), 014127
- [196] G. Leniec, S. M. Kaczmarek, et G. Boulon, "EPR and optical properties of $\text{CaF}_2\text{:Yb}$ single crystals", *Proc. SPIE-Int. Soc. Opt. Eng.* 5958 (2005), 595825
- [197] S. A. Kazanskii et A. I. Ryskin, "EPR spectra and crystal field of hexamer rare-earth clusters in fluorites", *Phys. Rev. B* 72 (2005), 014127
- [198] Booth, M. R. Mustafa, et B. R. McGarvey, "Clustering and defect structure of CaF_2 crystals doped with YbF_3 and ErF_3 as determined by ^{19}F nuclear magnetic resonance", *Phys. Rev. B* 17 (11) (1978), 4150
- [199] J. Fontanella et C. Andeen, "The dielectric spectrum of erbium doped CaF_2 ", *Phys. Rev. B* 16 (8) (1977), 3762
- [200] C. Andeen, D. Link, et J. Fontanella, "Cluster-associated relaxations in rare-earth-doped calcium", *Phys. Rev. B* 16 (8) (1977), 3762

- [201] J. Fontanella, C. Andeen, et D. Schuele, "The dielectric spectrum of erbium doped CaF_2 ", *J. Phys. C: Solid State Phys.* 9 (1976), 1055
- [202] R. D. Shelley et G. R. Miller, "Ionic thermocurrent study of the dipole-dipole interaction in CaF_2 doped with NaF ", *Journal of Solid State Chemistry* 1 (2) (1970), 218
- [203] J. Wagner et S. Mascarenhas, "Ionic-Thermocurrent Study of Rare-Earth-Doped CaF_2 and SrF_2 ", *Phys. Rev. B* 6 (12) (1972), 4867
- [204] E. L. Kitts et J. H. Crawford, "Relaxation of type-I dipolar complexes in calcium fluoride containing trivalent rare-earth impurities", *Phys. Rev. B* 9 (12) (1974), 5264
- [205] T. R. Reddy, E. R. Davies, J. M. Baker, D. N. Chambers, R. C. Newman, et B. Özbay, "Identification of trigonal rare earth centres in calcium fluoride using endor of ^{19}F ^{1}H ^{17}O ", *Phys. Lett.* 36 (1971), 231
- [206] S. Schweizer et J. M. Spaeth, "EPR and ENDOR investigation of single crystalline and powdered $\text{NaCl}:\text{Rh}^{2+}$ and $\text{AgCl}:\text{Rh}^{2+}$ ", *Journal of Physics and Chemistry of Solids* 58 (6) (1997), 859
- [207] S. S. Batsanov, L. I. Kobets, V. P. Kazakov, et L. R. Batsanova, "Optical spectra of $\text{CaF}_2:\text{Tb}$ crystals", *Journal of applied spectroscopy* 4 (2) (1966), 111
- [208] D. W. Pack, W. J. Manthey, et D. S. McClure, " $\text{Ce}^+:\text{Na}^+$ pairs in CaF_2 and SrF_2 . Absorption and laser-excitation spectroscopy, and the observation of hole burning", *Phys. Rev. B* 40 (14) (1989), 40
- [209] M. Yamaga, S. Yabashi, Y. Masui, M. Honda, H. Takahashi, M. Sakai, N. Sarukura, J. P. R. Wells, et G. D. Jones, "Optical, infrared and EPR spectroscopy of $\text{CaF}_2:\text{Ce}^{3+}$ crystals co-doped with Li^+ or Na^+ ", *J. Lum.* 108 (1-4) (2004), 307
- [210] N. J. Cockroft, D. Thompson, G. D. Jones, et R. W. G. Syme, "Site-selective spectroscopy of hydrogenic sites in $\text{CaF}_2:\text{Er}^{3+}$ crystals", *J. Chem. Phys.* 86 (2) (1987), 521
- [211] B. M. Tissue et J. C. Wright, "Site-selective laser spectroscopy of $\text{CaF}_2:\text{Pr}^{3+}$ and $\text{CaF}_2:\text{Pr}^{3+}, \text{R}^{3+}$ ($\text{R}^{3+} = \text{Y}^{3+}, \text{Gd}^{3+}, \text{Nd}^{3+}$)", *Phys. Rev. B* 36 (18) (1987), 9781

- [212] R. J. Reeves, G. D. Jones, et W. G. Syme, "Site-selective laser spectroscopy of Pr^{3+} C_{4v} symmetry centers in hydrogenated CaF_2 : Pr^{3+} and SrF_2 : Pr^{3+} crystals", *Phys. Rev. B* 46 (10) (1992), 5939
- [213] T. P. J. Han, G. D. Jones, et R. W. G. Syme, "Site-selective spectroscopy of Nd^{3+} centers in CaF_2 : Nd^{3+} and SrF_2 : Nd^{3+} ", *Phys. Rev. B* 47 (22) (1993), 14706
- [214] L. van Pieterson, R. P. A. Dullens, P. S. Peijzel, et A. Meijerink, "Site-selective laser spectroscopy of $4f^n-4f^n-15d$ transitions in CaF_2 : Pr^{3+} with F^- , D^- , H^- , Li^+ , or Na^+ charge compensation", *J. Chem. Phys.* 115 (20) (2001), 9393
- [215] C. R. A. Catlow, L. M. Moroney, A. V. Chadwick, et G. N. Greaves, "The use of exafs in the study of defect clusters in doped CaF_2 ", *Radiation Effects* 75 (1-4) (1983), 159
- [216] G. Drazic, S. Kobe, A. C. Cefalas, E. Sarantopoulou, et Z. Kollia, "Observation of nanostructured cluster formation of Tm ions in CaF_2 crystals", *Materials Science and Engineering B* 152 (2008), 119
- [217] J. Corish, C. R. A. Catlow, P. W. M. Jacobs, et S. H. Ong, "Defect aggregation in anion-excess fluorites. Dopant monomers and dimers", *Phys. Rev. B* 25 (10) (1982), 6425
- [218] P. J. Bendall, C. R. A. Catlow, J. Corish, et P. W. M. Jacobs, "Defect Aggregation in Anion-Excess Fluorites II. Clusters Containing More than Two Impurity Atoms", *Journal of Solid State Chemistry* 51 (1984), 159
- [219] V. A. Chernyshev, A. E. Nikiforov, V. P. Volodin, et G. S. Slepukhin, "Electronic Structure of Yb^{3+} Impurity Centers in Fluorites", *Fizika Tverdogo Tela* 52 (9) (2010), 1746
- [220] E. Friedman et W. Low, "Effect of Thermal Treatment of Paramagnetic Resonance Spectra of Rare Earth Impurities in Calcium Fluoride", *J. Chem. Phys.* 33 (1960), 1275
- [221] M. J. Weber et R. W. Bierig, "Parametric Resonance and Relaxation of Trivalent Rare-Earth Ions in Calcium Fluoride. I. Resonance Spectra and Crystal Fields", *Phys. Rev.* 134 (6A) (1964), 1492

- [222] G. D. Jones et R. J. Reeves, “ Na^+ , Li^+ and cubic centres in rare-earth-doped CaF_2 and SrF_2 ”, *J. Lum.* 87-89 (0) (2000), 1108
- [223] S. P. Jamison, R. J. Reeves, P. P. Pavlichuk, et G. D. Jones, “Sharp resonance modes of cubic symmetry rare-earth ions in CaF_2 -type crystals”, *J. Lum.* 83-84 (1999), 429
- [224] P.P. Feofilov, *Dokl. Akad. Nauk. SSSR* 99 (1954), 731
- [225] J. Kirton et S. D. McLaughlan, “Correlation of Electron Paramagnetic Resonance and Optical-Absorption Spectra of $\text{CaF}_2\text{:Yb}^{3+}$ ”, *Phys. Rev.* 155 (2) (1967), 279
- [226] D. N. Chambers et R. C. Newman, “Complexes of low symmetry involving hydride ions paired with trivalent rare earth ions in calcium fluoride. (IR absorption and EPR)”, *J. Phys. C: Solid State Phys.* 5 (1972), 997
- [227] U. Ranon et A. Yaniv, “Charge compensation by interstitial F^- ions in rare-earth-doped SrF_2 and BaF_2 ”, *Phys. Lett.* 9 (1) (1964), 17
- [228] C. Andeen, J. Fontanella, M. C. Wintersgill, P. J. Welcher, R. J. Kimble, et G. E. Matthews, “Clusters in rare-earth-doped alkaline earth fluorides”, *J. Phys. C: Solid State Phys.*, 14 (1981), 3557
- [229] E. Mahlab, V. Volterra, et W. Low, “Orthorhombic electron Spin Resonance Spectrum of U^{3+} in CaF_2 ”, *Phys. Rev.* 131 (3) (1963), 920
- [230] D. R. Tallant, D. S. Moore, et J. C. Wright, “Defect equilibria in fluorite structure crystals”, *J. Chem. Phys.* 67 (6) (1977), 2897
- [231] J. B. Fenn, J. C. Wright, et F. K. Fong, “Optical study of ion-defect clustering in $\text{CaF}_2\text{:Er}^{3+}$ ”, *J. Chem. Phys.* 59 (10) (1973), 5591
- [232] C. R. A. Catlow, A. V. Chadwick, J. Corish, L. M. Moroney, et A. N. O'Reilly, “Defect structure of doped CaF_2 at high temperatures”, *Phys. Rev. B* 39 (3) (1989), 1897
- [233] J. Chrysochoos, “Laser induced multisite emission of Pr^{3+} in CaF_2 at low and room temperature”, *J. Lum.* 31-32 (1984), 172
- [234] E. Radzhabov, “Photon cascade emission of Pr^{3+} ion in alkaline-earth fluorides”, *J. Lum.* 129 (2009), 1581

- [235] D. S. Moore et J. C. Wright, "Laser spectroscopy of defect chemistry in $\text{CaF}_2\text{:Er}$ ", *J. Chem. Phys.* 74 (3) (1981), 1626
- [236] K. H. Petit, P. Evesque, et J. Duran, "Dimers and clusters in $\text{CaF}_2\text{:Pr}^{3+}$. Laser selective excitation and time-resolved spectroscopy", *J. Phys. C: Solid State Phys.* 14 (1981), 5081
- [237] M. B. Seelbinder et J. C. Wright, "dentification of higher order clusters in charge compensated materials using three-body energy transfer", *J. Chem. Phys.* 75 (1981), 5070
- [238] R. Balda, J. Fernandez, A. de Pablos, et J. M. Fdez-Navarro, "Spectroscopic properties of Pr^{3+} ions in lead germanate glass", *J. Phys.: Condens. Matter* 11 (1999), 7411
- [239] W. A. Hargreaves, "Energy Levels of Tetragonally sited Pr^{3+} ions in Calcium Fluoride Crystals", *Phys. Rev. B* 6 (9) (1972), 3417
- [240] J. P. Laval, A. Mikou, et B. Frit, "Short-Range order in heavily doped $\text{CaF}_2\text{:Ln}^{3+}$ fluorites a powder neutron diffraction study", *Solid State Ionics* 28-30 (1988), 1300
- [241] D. Serrano, A. Braud, J. L. Doualan, P. Camy, et R. Moncorgé, "Highly efficient energy transfer in Pr^{3+} , Yb^{3+} codoped CaF_2 for luminescent solar converters", *J. opt. Soc. Am. B* 28 (7) (2011), 1760
- [242] J. Hormadaly et R. Reisfeld, "Intensity parameters and laser analysis of Pr^{3+} and Dy^{3+} in oxide glasses", *Journal of Non-Crystalline Solids* 30 (3) (1979), 337
- [243] M. Eyal, E. Greenberg, R. Reisfeld, et N. Spector, "Spectroscopy of praseodymium(III) in zirconium fluoride glass", *Chem. Phys. Lett.* 117 (2) (1985), 108
- [244] L. Su, J. Xu, H. Li, W. Yang, Z. Zhao, J. Si, Y. Dong, et G. Zhou, "Codoping Na^+ to modulate the spectroscopy and photoluminescence properties of Yb^{3+} in CaF_2 laser crystal", *Opt. Lett.* 30 (9) (2005), 1003
- [245] V. Lupei et A. Lupei, "Emission dynamics of the $^4\text{F}_{3-2}$ level of Nd^{3+} in YAG at low pump intensities", *Phys. Rev. B* 61 (12) (2000), 8087

- [246] V. Petit, P. Camy, J.-L. Doualan, X. Portier, et R. Moncorgé, “Spectroscopy of $\text{Yb}^{3+}:\text{CaF}_2$: From isolated centers to clusters”, *Phys. Rev. B* 78 (2008), 085131
- [247] V. Petit, J.-L. Doualan, P. Camy, X. Portier, et R. Moncorgé, “CW and tunable laser operation of Yb^{3+} doped CaF_2 ”, *Appl. Phys. B* 78 (2004), 681
- [248] G. M. Salley, R. Valiente, et H. U. Gudel, “Luminescence upconversion mechanisms in Yb^{3+} - Tb^{3+} systems”, *J. Lum.* 94-95 (2001), 305
- [249] T. Yamashita et Y. Ohishi, “Cooperative energy transfer between Tb^{3+} and Yb^{3+} ions co-doped in borosilicate glass”, *J. Non-Cryst. Solids* 354 (2008), 1883
- [250] T. Yamashita et Y. Ohishi, “Analysis of energy transfers between Tb^{3+} and Yb^{3+} codoped in borosilicate glasses”, *J. Opt. Soc. Am. B* 26 (4) (2009), 819
- [251] B. Lai, J. Wang, et Q. Su, “Ultraviolet and visible upconversion emission in $\text{Tb}^{3+}/\text{Yb}^{3+}$ co-doped fluorophosphate glasses”, *Appl. Phys. B* 98 (2010), 41
- [252] P. A. Forrester et C. F. Hempstead, “Paramagnetic Resonance of Tb^{3+} Ions in CaWO_4 and CaF_2 ”, *Phys. Rev.* 126 (3) (1962), 923
- [253] R. W. Bierig, M. J. Weber, et S. I. Warshaw, “Paramagnetic Resonance and Relaxation of Trivalent Rare-Earth Ions in Calcium Fluoride. II. Spin-Lattice Relaxation”, *Phys. Rev.* 134 (6A) (1964), A1504
- [254] G. D. Jones et K. M. Murdoch, “Laser site-selective spectroscopy of Tb^{3+} ions in CaF_2 and SrF_2 ”, *J. Lum.* 60 (1994), 131
- [255] J. Chrysochoos, “Laser-induced emission of $\text{CaF}_2\text{-Tb}^{3+}$ at room and low temperatures”, *Journal of the Less Common Metals* 93 (1) (1983), 73
- [256] L. Xie, Y. Wang, et H. Zhang, “Near-infrared quantum cutting in $\text{YPO}_4\text{:Yb}^{3+}, \text{Tm}^{3+}$ via cooperative energy transfer”, *Appl. Phys. Lett.* 94 (2009), 061905
- [257] I. A. A. Terra, L. J. Borrero-González, T. R. Figueredo, J. M. P. Almeida, A. C. Hernandes, L. A. O. Nunes, et O. L. Malta, “Down-conversion process in Tb^{3+} - Yb^{3+} co-doped Calibo glasses”, *J. Lum.* 132 (7) (2012), 1678
- [258] J. Lin et Q. Su, “Luminescence of Pb^{2+} and Energy Transfer from Pb^{2+} to Rare Earth Ions in Silicate Oxyapatites”, *Phys. stat. sol. (b)* 196 (261), (1996)

- [259] B. Viana, C. Garapon, A. M. Lejus, et D. Vivien, “ $\text{Cr}^{3+} \rightarrow \text{Nd}^{3+}$ energy transfer in the $\text{LaMgAl}_{11}\text{O}_{19}$: Cr, Nd laser material”, *J. Lum* 47 (3) (1990), 73
- [260] M. D. Shinn et A. A. Tesar, “Observation of temperature-dependent Cr^{3+} - Nd^{3+} sensitization in fluoride glasses”, *J. Lum* 51(4) (1992), 189
- [261] M. Fujii, M. Yoshida, Y. Kanzawa, S. Hayashi, et K. Yamamoto, “1.54 μm photoluminescence of Er^{3+} doped into SiO_2 films containing Si nanocrystals: Evidence for energy transfer from Si nanocrystals to Er^{3+} ”, *Appl. Phys. Lett.* 71 (9) (1997), 1198
- [262] G. Franzo, V. Vinciguerra, et F. Priolo, “The excitation mechanism of rare-earth ions in silicon nanocrystals”, *Appl. Phys. A-Mater. Sci. Process.* 69 (1) (1999), 3
- [263] F. Iacona, D. Pacifici, A. Irrera, M. Miritello, G. Franzo, F. Priolo, D. Sanfilippo, G. Di Stefano, et P. G. Fallica, “Electroluminescence at 1.54 μm in Er-doped Si nanocluster-based devices”, *Appl. Phys. Lett.* 81 (17) (2002), 3242
- [264] V. Y. Timoshenko, D. M. Zhigunov, P. K. Kashkarov, O. A. Shalygina, S. A. Teterukov, R. J. Zhang, M. Zacharias, M. Fujii, et S. Hayashi, “Photoluminescence properties of erbium-doped structures of silicon nanocrystals in silicon dioxide matrix”, *Journal of Non-Crystalline Solids* 352 (9-20) (2006), 1192
- [265] A. M. Klonkowski, M. Zalewska, et B. Koscielska, “Emission enhancement of Eu(III) and/or Tb(III) ions entrapped in silica xerogels with ZnO nanoparticles by energy transfer”, *J. Non-Cryst. Solids* 352 (40-41) (2006), 4183
- [266] M. Zalewska, B. Lipowska, et A. M. Klonkowski, “Improvement of luminescent materials composed of Tb(III) ions, WO_3 nanoparticles and silica xerogel as a matrix”, *Journal of Non-Crystalline Solids* 354 (35-39) (2008), 4388
- [267] T. Hayakawa, S. T. Selvan, et M. Nogami, “Energy Transfer Between Eu^{3+} Ions and CdS Quantum Dots in Sol-Gel Derived CdS/ SiO_2 : Eu^{3+} Gel”, *Journal of Sol-Gel Science and Technology*, 19 (1) (2000), 779
- [268] Y. Hori, X. Biquard, E. Monroy, D. Jalabert, F. Enjalbert, L. S. Dang, M. Tanaka, O. Oda, et B. Daudin, “GaN quantum dots doped with Eu”, *Applied Physics Letters* 84 (2) (2004), 206
- [269] A. F. Campos, A. Meijerink, C. de M. Donega, et O. L. Malta, “A theoretical calculation of vibronic coupling strength: the trend in the lanthanide ion series and

- the host-lattice dependence”, *Journal of Physics and Chemistry of Solids* 61 (2000), 1489
- [270] T. Hayakawa, S. Tamil Selvan, et M. Nogami, “Enhanced fluorescence from Eu^{3+} owing to surface plasma oscillation of silver particles in glass”, *Journal of Non-Crystalline Solids* 259 (1-3) (1999), 16
- [271] J. Ueda et S. Tanabe, “Surface plasmon excited fluorescence of Er^{3+} -Doped Y_2O_3 thin film fabricated by Pulsed Laser Deposition”, *IOP Conference Series: Materials Science and Engineering* 1 (2009), 012005
- [272] C. Maurizio, E. Trave, G. Perotto, V. Bello, D. Pasqualini, P. Mazzoldi, G. Battaglin, T. Cesca, C. Scian, and G. Mattei, “Enhancement of the Er^{3+} luminescence in Er-doped silica by few-atom metal aggregates”, *Phys. Rev. B* 83 (2011), 195430
- [273] J. Lin, Q. Su, H. Zhang, et S. Wang, “Crystal structure dependence of the luminescence of rare earth ions (Ce^{3+} , Tb^{3+} , Sm^{3+}) in Y_2SiO_5 ”, *Materials Research Bulletin* 31 (2) (1996), 189
- [274] M. Jose et A. Lakshmanan, “ Ce^{3+} to Tb^{3+} energy transfer in alkaline earth (Ba, Sr or Ca) sulphate phosphors”, *Optical Materials* 24 (4) (2004), 651
- [275] K. Y. Jung et H. W. Lee, “Enhanced luminescent properties of $\text{Y}_3\text{Al}_5\text{O}_{12}:\text{Tb}^{3+}, \text{Ce}^{3+}$ phosphor prepared by spray pyrolysis”, *J. Lum.* 126 (2) (2007), 469
- [276] Z.-L. Wang, H. L. W. Chan, H.-L. Li, et J. H. Hao, “Highly efficient low-voltage cathodoluminescence of spherical particles”, *Appl. Phys. Lett.* 93 (14) (2008), 141106
- [277] C. Guo, H. Jing, et T. Li, “Green-emitting phosphor $\text{Na}_2\text{Gd}_2\text{B}_2\text{O}_7:\text{Ce}^{3+}, \text{Tb}^{3+}$ for near-UV LEDs”, *RSC Adv.* 2 (5) (2012), 2119
- [278] L. Song et L. Xue, “Efficient fluorescence of dissolved $\text{CaF}_2:\text{Tb}^{3+}$ and $\text{CaF}_2:\text{Ce}^{3+}$, Tb^{3+} nanoparticles through surface coating sensitization”, *Appl. Surf. Sci.* 258 (8) (2012), 3497
- [279] U. Caldiño G.C. de la Cruz, G. Muñoz H., et J. Rubio O., “ $\text{Ce}^{3+} \rightarrow \text{Eu}^{2+}$ energy transfer in CaF_2 ”, *Solid State Communications* 69 (4) (1989), 347

- [280] Peter Dorenbos, “The 5d level positions of the trivalent lanthanides in inorganic compounds”, *J. Lum.* 91 (2000), 155
- [281] W. L. Wanmaker, A. Bril, et J. W. ter Vrugt, “Sensitization of Tb^{3+} luminescence by Sn^{2+} and Cu^+ in alkaline earth-phosphates”, *Appl. Phys. Lett.* 8 (10) (1966), 260
- [282] V. Babin, K. D. Oskam, Peter Vergeer, et Andries Meijerink, “The role of Pb^{2+} as a sensitizer for Gd^{3+} - Eu^{3+} downconversion couple in fluorides”, *Radiation Measurements* 38 (2004), 767
- [283] J. Lin et Q. Su, “Luminescence of Pb^{2+} and energy transfer from Pb^{2+} to rare earth ions in silicate oxyapatites”, *physica status solidi (b)* 196 (1) (2006), 261
- [284] C. Shen, Z. Hao, et Z. Gong, “Energy transfer phenomena in $\text{GdMgB}_5\text{O}_{10}:\text{Pb}^{2+}$, $\text{Mn}^{2+}/\text{Tb}^{3+}$ ”, *J. Lum.* 40-41 (0) (1988), 663
- [285] K. P. Oboth, F. J. Lohmeier, et F. Fischer, “VUV and UV Spectroscopy of Pb^{2+} and Bi^{3+} Centres in Alkaline-Earth Fluorides”, *physica status solidi (b)* 154 (2) (2006), 789
- [286] M. Paraschiva, I. Nicoara, M. Stef, et O.M. Bunoiu, “Distribution of Pb^{2+} Ions in PbF_2 -Doped CaF_2 Crystals”, *Acta Physica Polonica A* 117 (3) (2010), 466
- [287] G. Blasse, “Study of Energy Transfer from Sb^{3+} , Bi^{3+} , Ce^{3+} to Sm^{3+} , Eu^{3+} , Tb^{3+} , Dy^{3+} ”, *J. Chem. Phys.* 47 (6) (1920), 1920
- [288] T. Hirai, K. Chong, N. Ohno, T. Kawai, et S. Hashimoto, “Luminescence of Bi^{3+} Ions Doped in NaYF_4 ”.
- [289] K. Chong, T. Hirai, T. Kawai, S. Hashimoto, et N. Ohno, “Optical properties of Bi^{3+} ions doped in NaYF_4 ”, *J. Lum.* 122-123 (2007), 149
- [290] S. Das et K. C. Mandal, “Optical downconversion in rare earth (Tb^{3+} and Yb^{3+}) doped CdS nanocrystals”, *Materials Letters* 66 (1) (2012), 46
- [291] P. Piasecki, A. Piasecki, Z. Pan, R. Mu, et S. H. Morgan, “Formation of Ag nanoparticles and enhancement of Tb^{3+} luminescence in Tb and Ag co-doped lithium-lanthanum-aluminosilicate glass”, *J. Nanophotonics* 4 (2010)

- [292] L. R. P. Kassab, R. de Almeida, D. M. da Silva, et C. B. de Araújo, “Luminescence of Tb^{3+} doped $\text{TeO}_2\text{-ZnO-Na}_2\text{O-PbO}$ glasses containing silver nanoparticles”, *J. Appl. Phys.* 104 (9) (2008), 093531
- [293] Q. Nie, L. Lu, T. Xu, S. Dai, X. shen, X. Liang, X. Zhang, et X. Zhang, “Upconversion luminescence of $\text{Er}^{3+}/\text{Yb}^{3+}$ -codoped natrium-germanium-bismuth glasses”, *J. Phys. Chem. Solids* 67 (11) (2006), 2345
- [294] V. K. Rai, K. Kumar, et S. B. Rai, “Upconversion in Pr^{3+} doped tellurite glass ”, *Opt. Mat* 29 (7) (2007), 873
- [295] T. Jüstel, J.-C. Krupa, et D. U. Wiechert, “VUV spectroscopy of luminescent materials for plasma display panels and Xe discharge lamps”, *J. Lum.* 93 (13) (2001), 173
- [296] B. Moine, G. Bizarri, B. Varrel, et J.Y. Rivoire, “VUV-extended measurements of quantum efficiency of sodium salicylate and of some NBS standard phosphors”, *Opt. Mat.* 29 (9) (2007), 1148
- [297] J. Ueda et S. Tanabe, “Visible to near infrared conversion in $\text{Ce}^{3+}\text{-Yb}^{3+}$ co-doped YAG ceramics”, *J. Appl. Phys*, 106 (2009), 043101

List of Figures

1	Cellule silicium avec convertisseur “basse-fréquence”	2
2	Schéma du quantum cutting avec le système $\text{Pr}^{3+}\text{-Yb}^{3+}$	3
3	Evolution des espèces avec la concentration en Yb^{3+}	6
4	Schéma du quantum cutting avec le système $\text{Tb}^{3+}\text{-Yb}^{3+}$	7
1.1	First Silicon cell by Bell laboratory	14
1.2	PV second generation: thin films	15
1.3	HIT cell	17
1.4	Gratzel-type DSSC scheme	18
1.5	Efficiency and cost projections for the three PV generations	20
1.6	Loss mechanisms in a p-n junction	21
1.7	AM1.5 Solar spectrum	22
1.8	Absorption mechanism in a triple-junction solar cell	23
1.9	QDs solar cell	24
1.10	Solar cell with added upconverter and downconverter	25
1.11	$4f$ energy levels splitting under the effect of different interactions	30
1.12	Overview of energy transfer processes	32
1.13	Overview of upconversion mechanisms	34
1.14	Er^{3+} upconverted emissions	35
1.15	Upconversion mechanism with Er^{3+} and Yb^{3+} ions	36

1.16	Silicon cell response	38
1.17	Overview of downconversion mechanisms	39
1.18	Quantum cutting with Pr^{3+} - Yb^{3+}	40
1.19	Quantum cutting with Er^{3+} - Yb^{3+} and QC Nd^{3+} - Yb^{3+} ions	41
1.20	Cooperative QC with Tb^{3+} - Yb^{3+} ions and Tm^{3+} - Yb^{3+} ions	42
1.21	Research cells efficiency (updated results).	44
2.1	KY_3F_{10} primitive cell	48
2.2	Selection of energy transfer processes within the Pr^{3+} - Yb^{3+} system	49
2.3	Room temperature absorption spectra in $\text{KY}_3\text{F}_{10}:\text{Pr}^{3+}$ - Yb^{3+}	50
2.4	RT emission spectra under laser diode excitation at 442 nm in KY_3F_{10} . .	52
2.5	RT $^3\text{P}_0$ emission spectra under blue excitation in KY_3F_{10}	53
2.6	$\text{KY}_3\text{F}_{10}:0.5\%\text{Pr}^{3+}-\times\%\text{Yb}^{3+}$ ($\times=5, 10, 20$) normalized emission spectra . .	55
2.7	Experimental $^3\text{P}_0$, $^1\text{G}_4$ and $^2\text{F}_{5/2}$ decay curves	57
2.8	Energy levels and processes involved in DC QC with Pr^{3+} and Yb^{3+} ions .	61
2.9	Calculation of P_α from Eq.2.18.	65
2.10	Experimental intensity ratios compared to the simulated curves	66
2.11	Comparison between experimental and simulated decay curves	68
2.12	Evaluation of Eq.2.26 with β and γ	69
2.13	Room temperature Pr^{3+} emission spectra in the range 1-2.5 μm	71
2.14	Experimental $^3\text{P}_0$ decays compared to the rate-equation solutions	74
2.15	$^3\text{P}_0$ decays compared to the IH model and MC simulations	77
2.16	Spectral overlap between the Pr^{3+} emission and Yb^{3+} absorption	78
2.17	MC simulations	79
3.1	CaF_2 crystal structure	85
3.2	Cubic simmetry site	86
3.3	C_{4v} symmetry	86
3.4	C_{3v} symmetry sites	87
3.5	NN and NNN dimers	88
3.6	Trimer structure	88
3.7	Hexameric cluster	89
3.8	RT Pr^{3+} emission spectra in $\text{CaF}_2:\text{Pr}^{3+}$ - Yb^{3+}	92
3.9	$^3\text{P}_0$ and $^1\text{D}_2$ decay curves	93
3.10	RT $^3\text{P}_0$ decay curves in $\text{CaF}_2:0.5\% \text{Pr}^{3+}-\times\%\text{Yb}^{3+}$ ($\times=0, 0.5, 1, 2, 4, 10$) .	93

3.11	RT Pr^{3+} emission spectra around $1.3 \mu\text{m}$	95
3.12	$^3\text{P}_0$ decay curve recorded at 607 nm. Inset: time-resolved spectra	96
3.13	Pr^{3+} $^3\text{P}_0$ emission spectra when exciting at 442 nm	101
3.14	RT Pr^{3+} absorption spectra recorded between 420 and 490 nm	104
3.15	Pr^{3+} $^3\text{P}_0$ decay curves under pulsed excitation at 468 nm	105
3.16	LT absorption spectra between 450 and 490 nm	109
3.17	$^3\text{P}_0$ decays in $\text{CaF}_2:0.5\%\text{Pr}^{3+}-5\%\text{Lu}^{3+}$	110
3.18	Pr^{3+} time-resolved spectra: Fast cluster and Ultra-fast cluster	111
3.19	Ultra-fast $^3\text{P}_0$ decay and setup transient response	112
3.20	$^3\text{P}_0$ decays and double exponential fit	114
3.21	View of the integrated sections used in the calculations	117
3.22	Schematic representation of the centers proportions	120
3.23	Ytterbium emission under Pr^{3+} excitation at 442 nm	121
3.24	Yb^{3+} emission evolution	122
3.25	RT experimental $^2\text{F}_{5/2}$ and $^1\text{G}_4$ decay curves at 480 nm excitation	123
3.26	Schematic representation of the initial conditions.	124
3.27	$^2\text{F}_{5/2}$ experimental decay compared to $n_3(t)$	126
4.1	LT Tb^{3+} $^5\text{D}_4$ emission spectrum	131
4.2	LT time-resolved Tb^{3+} $^5\text{D}_4 \rightarrow ^7\text{F}_3$ emission	132
4.3	RT and LT $^5\text{D}_4 \rightarrow ^7\text{F}_3$ emission spectra	133
4.4	RT emission spectra in $\text{CaF}_2:\text{Tb}^{3+}-\text{Yb}^{3+}$	135
4.5	Yb^{3+} $^2\text{F}_{5/2} \rightarrow ^2\text{F}_{7/2}$ downconverted emission	135
4.6	RT $^5\text{D}_4$ decay curves in $\text{CaF}_2:0.5\%\text{Tb}^{3+}-\times\%\text{Yb}^{3+}$ ($\times=0, 0.5, 2, 10, 20$)	136
4.7	Evolution of the Tb^{3+} $^5\text{D}_4$ lifetime and the QE	138
4.8	$^2\text{F}_{5/2}$ decay curves upon 488 nm and 897 nm excitation	138
4.9	Example of plasmon sensitized system	141
4.10	Tb^{3+} absorption cross-section	143
4.11	$\text{Ce}^{3+}-\text{Tb}^{3+}-\text{Yb}^{3+}$ triply doped system	144
4.12	PLE spectra recorded between 240 and 400 nm	145
4.13	Normalized emission spectra upon 310 nm excitation	146
4.14	Absolute DC efficiency measurements setup	148
4.15	Voltage response within the IS as a function of the incident power at 445 nm	149
4.16	Voltage response as a function of the incident power at 980 nm	151

List of Tables

1	Concentrations disponibles	4
2	Efficacité du premier transfert d'énergie dans $\text{KY}_3\text{F}_{10}:\text{Pr}^{3+}-\text{Yb}^{3+}$	4
3	Taux de transfert déduits de la modélisation	5
4	Efficacité du premier transfert d'énergie dans $\text{CaF}_2:\text{Tb}^{3+}-\text{Yb}^{3+}$	8
1.1	Main PV semiconductors bandgap energies	22
1.2	Comparison of the potential energy converters main properties	27
1.3	Expected splitting for a $^{2S+1}\text{L}_J$ level with J integer	31
2.1	$\text{KY}_3\text{F}_{10}:\text{Pr}^{3+}-\text{Yb}^{3+}$ investigated samples	51
2.2	Experimental lifetimes in KY_3F_{10}	56
2.3	Experimental $^3\text{P}_0$ lifetimes and ETEs	58
2.4	Reported ETEs.	59
2.5	Compared theoretical and experimental lifetimes.	70
2.6	Energy transfer rates derived by modeling	72
2.7	Simulated and experimental $^3\text{P}_0$ lifetimes.	78
3.1	$\text{CaF}_2:\text{Pr}^{3+}-\text{X}^{3+}$ ($\text{X}=\text{Yb}^{3+}$ or Lu^{3+}) investigated samples.	90
3.2	$^3\text{P}_0$ lifetime and ETE for the first ET	97
3.3	Spectroscopic parameters used for the calculations	103
3.4	Emission intensities and luminescent centers ratio	106

3.5	Summary of ETEs obtained with different materials	119
3.6	$^2F_{5/2}$ and 1G_4 experimental lifetimes	123
4.1	$\text{CaF}_2\text{:Tb}^{3+}\text{-RE}^{3+}$ (RE= Yb, Ce or Bi) investigated samples	130
4.2	Luminescence lifetimes, ETE and QE	137
4.3	Summary of QE reported results with $\text{Tb}^{3+}\text{-Yb}^{3+}$ codoped materials	140
4.4	Power values used for the DC efficiency calculation in $\text{CaF}_2\text{:Pr}^{3+}\text{-Yb}^{3+}$. .	150
4.5	Incident and absorbed pump power at 488 nm in the $\text{Tb}^{3+}\text{-Yb}^{3+}$ samples .	150
4.6	Absolute QC efficiency results	152

La succession de transferts d'énergie peut aboutir à la conversion d'un photon de haute énergie en plusieurs photons d'énergie inférieure à celle du photon original. Ce mécanisme, connu sous le nom de quantum cutting, est étudié dans ce travail de thèse pour la fabrication de convertisseurs luminescents capables de transformer les photons solaires dans le domaine visible et UV en plusieurs photons autour de $1\mu\text{m}$. Le couple de terres rares $\text{Pr}^{3+}\text{-Yb}^{3+}$ présente une structure de niveaux d'énergie particulièrement adaptée pour le mécanisme du quantum cutting. Après l'absorption d'un photon visible par le Pr^{3+} (donneur), deux transferts d'énergie résonants peuvent avoir lieu vers deux ions Yb^{3+} (accepteurs). L'efficacité des transferts $\text{Pr}^{3+}\rightarrow\text{Yb}^{3+}$ est ici évaluée dans les matériaux hôtes KY_3F_{10} et CaF_2 . L'étude des transferts d'énergie dans KY_3F_{10} révèle des taux de transfert élevés, mais aussi, une importante chute de l'émission de l' Yb^{3+} . Contrairement à KY_3F_{10} , l'étude des transferts d'énergie dans CaF_2 est particulièrement prometteur du fait de la formation d'agrégats de terres rares au sein du cristal. La courte distance qui sépare les ions dopants dans les agrégats favorise en effet l'apparition de transferts d'énergie extrêmement efficaces. Le quantum cutting est également étudié avec le codopage de terres rares $\text{Tb}^{3+}\text{-Yb}^{3+}$ dans CaF_2 . Dans ce cas, l'excitation simultanée de deux ions Yb^{3+} a lieu par le biais d'un seul transfert d'énergie, dit coopératif, à partir des ions Tb^{3+} . Le mécanisme coopératif est connu pour être moins efficace que les transferts d'énergie résonants. Néanmoins, la formation d'agrégats dans CaF_2 dopé $\text{Tb}^{3+}\text{-Yb}^{3+}$ permet d'obtenir une efficacité de transfert supérieure à celle qui peut-être observée dans d'autres matériaux.

The occurrence of a series of consecutive energy transfers can lead to the conversion of a high-energy photon into several photons with an energy lower than the incident one. This mechanism, usually referred to as quantum cutting, is investigated in this PhD work in order to develop luminescent solar converters able to transform the visible and UV solar photons into several photons with energy around $1\mu\text{m}$. The rare-earth couple $\text{Pr}^{3+}\text{-Yb}^{3+}$ presents a level structure particularly suitable for the quantum cutting mechanism since, upon absorption of a visible photon by Pr^{3+} (donor), two resonant energy transfers can take place with two neighboring Yb^{3+} ions (acceptors). The efficiency of the $\text{Pr}^{3+}\rightarrow\text{Yb}^{3+}$ energy transfers is here investigated within the host materials KY_3F_{10} and CaF_2 . The study of the energy transfers in KY_3F_{10} reveals a high transfer rate but also, a remarkable quenching of the Yb^{3+} emission. On the other hand, the investigation of the KY_3F_{10} energy transfers using CaF_2 as host material is particularly promising because of the formation of rare-earth aggregates. The short distance between the dopants within the clusters favors the apparition of extremely efficient energy transfers in this material. The quantum cutting process is finally studied with the rare-earth ions codoping Tb^{3+} and Yb^{3+} in CaF_2 . In this case, the simultaneous excitation of two Yb^{3+} ions takes place through a single cooperative energy transfer from Tb^{3+} ions. The cooperative mechanism is known to be less efficient than resonant energy transfers. Nevertheless, the rare-earth clustering in CaF_2 codoped $\text{Tb}^{3+}\text{-Yb}^{3+}$ gives rise to energy transfer efficiencies notably higher than that observed with other materials.

Mots clés:

Quantum Cutting; Downconversion; Cellules Solaires; Terres Rares; Transfert d'énergie; Spectroscopie Optique; CaF_2 ; KY_3F_{10}

Discipline: Milieux Dilués et Optique Fondamentale

Centre de Recherche sur les ions, les matériaux et la Photonique (CIMAP)
6, boulevard du Maréchal Juin 14050 Caen Cedex 04, France
Equipe Matériaux et Instrumentation Laser (MIL)

